Fundamentals of Hydrogen Safety Engineering I

Vladimir Molkov

Vladimir Molkov

Fundamentals of Hydrogen Safety Engineering I

Fundamentals of Hydrogen Safety Engineering I

ISBN 978-87-403-0226-4

Contents

Disclaimer. Author does not make any warranty or assumes any legal liability or responsibility for the accuracy, completeness, or any third party's use of any information, product, procedure, or process disclosed, or represents that its use would not infringe privately owned rights. Any electronic website link in this book is provided for user convenience and its publication does not constitute or imply its endorsement, recommendation, or favouring by the author.

1 Introduction

High priority research directions for the hydrogen economy include safety as a technological, a psychological and sociological issue (US Department of Energy, 2004). This book provides the state-of-the-art in hydrogen safety as a technological issue and introduces a reader to the subject of hydrogen safety engineering. Hydrogen safety engineering is defined as application of scientific and engineering principles to the protection of life, property and environment from adverse effects of incidents/accidents involving hydrogen. The use of hydrogen as an energy carrier presents several unusual hazards. The best investment in hydrogen safety is educated and trained personnel, informed public. This book is a contribution to hydrogen safety knowledge transfer and education of all stakeholders including technology developers and safety engineers, consultants and users, policy makers and investors, etc. It can be used as a textbook for higher education programmes in hydrogen safety, e.g. MSc in Hydrogen Safety Engineering course at the University of Ulster.

1.1. Why hydrogen?

The scarcity of fossil fuel reserves, geopolitical fears associated with fossil fuel depletion, and issues of environment pollution and climate change as well as the need to ensure independence of energy supply make the low-carbon economy with an essential hydrogen vector inevitable in the coming decades. Today first series of hydrogen-fuelled buses and cars are already on the road and refuelling stations are operating in different countries around the world. How safe are hydrogen technologies and fuel cell products? This book will help to understand the state-of-the-art in hydrogen safety engineering and assist to make this fast emerging market inherently safer. Global fuel cell demand will reach $8.5 billion in 2016 (PennWell Corporation, 2007).

1.2. Public perception of hydrogen technologies

Public perception of hydrogen technologies is still affected by the 1937 *Hindenburg* disaster. The catastrophe is often associated with hydrogen as a reason even there is an opinion that the difference in electrical potential between the zeppelin "landing" rope and the ground during descending had generated electrical current that ignited the dirigible canopy made of extremely combustible material. This was followed by diffusive combustion of hydrogen in air without generation of a significant blast wave able to injure people. Figure 1–1 shows a photo of burning *Hindenburg* dirigible fire demonstrating that there was no "explosion" (Environmental graffiti alpha, 2010).

Figure 1–1. Photo of the *Hindenburg* dirigible fire demonstrating that there was no "explosion" (Environmental graffiti alpha, 2010).

Contrary to popular misunderstanding hydrogen helped to save 62 lives in the *Hindenburg* disaster. The NASA research has demonstrated (Bain and Van Vorst, 1999) that the disaster would have been essentially unchanged even if the airship were lifted not by hydrogen but by non-combustible helium, and that probably nobody aboard was killed by a hydrogen fire. The 35% who died were killed by jumping out, or by the burning diesel oil, canopy, and debris (the cloth canopy was coated with what nowadays would be called rocket fuel). The other 65% survived, riding the flaming dirigible to earth as the clear hydrogen flames swirled harmlessly above them.

1.3. The importance of hydrogen safety

There is a clear understanding by all stakeholders of the role of hydrogen safety for emerging hydrogen and fuel cell technologies, systems and infrastructure. This is supported by investment to safety of about 5–10% of the total funding of hydrogen and fuel cell programmes both in USA and in Europe. Hydrogen safety studies were initiated decades ago as a result of accidents in the process industries, and were supported by safety research for nuclear power plants and aerospace sector. For example, a study of the Three Mile Island nuclear plant (USA) accident in 1979 (Henrie and Postma, 1983) demonstrated that almost homogeneous 8% by volume of hydrogen in air mixture deflagrated. Fortunately, the deflagration pressure increases to about 190 kPa only that was considerably below the strength of the large concrete containment building.

Recent disasters involving hydrogen, i.e. the Challenger Space Shuttle explosion (1986) and the Fukushima nuclear tragedy (2011), demonstrated that our knowledge and engineering skills to deal safely with hydrogen even within these industries require more investment, from both intellectual and financial perspective.

Nowadays dealing with hydrogen is getting out of hands of highly trained professionals in industry and become everyday activity for public. This implies a need in establishment of a new safety culture in society, development of innovative safety strategies and breakthrough engineering solutions. It is expected that the level of safety and risk at the consumer interface with hydrogen must be similar or exceeds that present with fossil fuel usage. Thus, safety parameters of hydrogen and fuel cell products will directly define their competitiveness on the market.

Hydrogen safety engineers, technology developers and infrastructure designers, scientists using research facilities, technical staff at maintenance workshops and refuelling stations, first responders should be professionally educated to deal with hydrogen systems at pressures up to 100 MPa and temperatures down to -253°C (liquefied hydrogen) in open and confined spaces. Regulators and public officials should be provided with the state-of-the-art knowledge and a guidance to professionally support the safe introduction of hydrogen and fuel cell systems to everyday life of public. Engineers, including those who have handled hydrogen in different industries for several decades, need to undergo periodic retraining through continuous professional development courses to acquire the latest knowledge and skills for using hydrogen in the public domain. Indeed, emerging hydrogen systems and infrastructure *will create in a close future entirely new environment of hydrogen usage, which is not covered by industrial experience or through existing codes and recommended practice* (Ricci et al., 2006).

Hydrogen-powered vehicles are one of the main applications of hydrogen and fuel cell technologies. Hazards and associated risks for hydrogen-fuelled cars should be understood and interpreted in a professional way with full comprehension of consequences by all stakeholders starting from system designers through regulators to users. Probably the first comparison of the "severity" of a hydrogen and gasoline fuel leak and ignition was performed by Swain (2001). Figure 1–2 shows snapshots of hydrogen jet fire and gasoline fire at 3 s (left) and 60 s (right) after car fire initiation.

Figure 1–2. Hydrogen jet fire and gasoline fire: 3 (left) and 60 (right) seconds after car fire initiation (Swain, 2001).

The scenario with hydrogen-fuelled car presented in Fig. 1–2 is rare, e.g. it can be realised at a false self-initiation of a pressure relief device (PRD). Indeed, a release of hydrogen through the PRD from the onboard storage would be in majority of cases initiated by an external fire. A scenario with the external fire drastically changes hazards and associated risks compared to the situation shown in Fig. 1–2.

Figures 1–3 and 1–4 demonstrate results of a study on hydrogen-powered cars fire performed in Japan (Tamura et al., 2011). The hydrogen fuel cell vehicle (HFCV) was equipped with a thermal pressure relief device (TPRD) with vent pipe internal diameter of 4.2 mm. In a test shown in Fig. 1–3 the compressed hydrogen gas tank was installed exactly at the position of the removed gasoline tank. By this reason, there was no chance to install a larger storage vessel and a small tank of 36 litres volume at pressure 70 MPa was used.

The fire spread from a gasoline vehicle to HFCV was investigated to address scenarios when different types of vehicles are catching fire in car collision or natural disaster like earthquake. The experiment revealed that when the TPRD of HFCV is activated by gasoline fire a fireball of more than 10 m diameter is formed (Fig. 1–3, right).

Figure 1–3. A HFCV gasoline pool fire test: (left) – gasoline fire just before initiation of TPRD, (right) – 1 second after TPRD initiation (Tamura et al., 2011).

In another test of Tamura et al. (2011) two vehicles were parked approximately 0.85 m apart and the spread of fire from HFCV to the gasoline vehicle was investigated. Figure 1–4 shows two vehicles after the TPRD initiation in the HFCV. It can be concluded that self-evacuation from the car or safeguarding by first responders with such design of hydrogen release system is impossible and car manufacturers yet have to address this customer safety issue.

Figure 1–4. The HFCV with initiated TPRD (left) and the gasoline car (right) (Tamura et al., 2011).

In test conditions (Tamura et al., 2011) the cause of fire spread from the HFCV to the adjacent gasoline vehicle, in authors' opinion, is the flame spreading from the interior and exterior fittings of the HFCV but not the hydrogen flame from the TPRD (it is worth noting that the small storage tank of only 36 litres with a shorter hydrogen release time was used in the study by Tamura et al. (2011) instead of a larger tank that is needed to provide competitive driving range). Authors concluded that in car carrier ships and other similar situations with closely parked HFCVs, the test results point to the possibilities of a fire in an HFCV to activate its TPRD and thereby to generate hydrogen flames which in turn may cause the under floor TPRD activation in adjoining HFCV.

To minimize damage by HFCV fire, therefore, authors suggested that it is important to early detect and extinguish fire before the TPRD activation. It is known that hydrogen fire is difficult if not possible to extinguish in many practical situations. Hopefully, car manufacturers will develop appropriate safety engineering solutions, including reduction of flame length from hydrogen-powered vehicle in a mishap, thus excluding the "domino" effect in accident development and assisting first responders to control such fires and successfully perform rescue operations. Experiments by Tamura et al. (2011) have clearly demonstrated that hydrogen-powered vehicle fire consequences can be very "challenging" both from life safety and property loss points of view.

Hydrogen is not more dangerous nor safer compared to other fuels (Ricci et al., 2006). Safety of hydrogen and fuel cell systems and infrastructure fully depends on how professionally it is handled at the design stage and afterwards. The safe and successful use of hydrogen starts with knowing of and adhering to the state-of-the-art knowledge in hydrogen safety engineering, appropriate regulation for the design of the systems and facilities. Safety shall be considered at all stages of a hydrogen system of infrastructure life cycle, beginning with its initial design and continuing through its manufacturing, construction, operation, maintenance, and ending with its decommissioning.

1.4. Hazards, risk, safety

Hazard can be defined as a chemical or physical condition that has the potential for causing damage to people, property and the environment. Hydrogen accident could have different hazards, e.g. asphyxiation due to release in closed space, frostbite by liquefied hydrogen, thermal hazards from jet fire, pressure effects from deflagrations and detonations, etc. Hazard could lead to no damage, if the proper safety measures are applied, or could lead to costly consequences up to fatalities if the system or infrastructure has been designed and used without professional knowledge in hydrogen safety.

The modern definition of risk is provided by ISO/IEC Guide 73:2002 (2002) stating that it is the "*combination of the probability of an event and its consequence*" while safety is defined as the *"freedom from unacceptable risk"*. This means that safety is a societal category and cannot be numerically defined while risk is a technical measure that can be calculated (LaChance et al., 2009). Society, in consequence, establishes acceptable levels of risk or risk acceptance criteria.

The general requirement is that the risk associated with hydrogen-fuelled vehicles should be the same or below the risk for today's vehicles using fossil fuels. Currently this requirement is not yet achieved throughout the whole range of hydrogen and fuel cell systems. Indeed, consequences of hydrogen-powered car fire to life safety and property loss, e.g. in confined spaces such as garages and tunnels, are more "costly" compared to consequences of fossil fuel vehicle fire at a current level of fire resistance of hydrogen onboard storage and design of pressure relief devices. In fact, the probability of external to vehicle fire, e.g. at home garages and general vehicle parking garages will be the same independent of a vehicle type.

The garage fires statistics from National Fire Protection Association (NFPA) is as follows. During the four-year period of 2003–2006 an estimated average of 8,120 fires per year that started in the vehicle storage areas, garages, or carports of one or two-family homes (Ahrens, 2009). These fires caused an average of 35 civilian deaths, 367 civilian injuries, and $425 million in direct property damage. Further to this NFPA estimated (Ahrens, 2006) that during 1999–2002, an average of 660 structure fires and 1,100 vehicle fires in or at general vehicle parking garages were reported per year (include bus, fleet, or commercial parking structures). 60% of the vehicle fires and 29% of the structure fires in these properties resulted from failures of equipment or heat source. Vehicles were involved in the ignition of 13% of these structure fires. Exposure to another fire was a factor in roughly one-quarter of both structure and vehicle fires. The data does not distinguish between open and enclosed garages.

This statistics makes it clear that safety strategies and solutions, including those developed by car manufacturers, yet have to be improved to rely on a firm engineering design rather than a general risk assessment of which uncertainties are impossible to define for emerging technologies.

The general approach to consideration of hazards and associated risks can be based on the former NASA (1997) guidelines. An analysis shall be conducted to identify all fire and explosion hazards and accomplish the following:

- Significant hazards shall be eliminated or reduced to acceptable risk levels;
- Where the hazard cannot be eliminated or reduced, the system components associated with the hazard shall be relocated to an area less threatening to people and property as directed by the Authority Having Jurisdiction (AHJ);
- Where the hazard cannot be eliminated, reduced, or removed, the system components associated with the hazard shall be isolated within the facility so as not to pose a danger to the remainder of the structure or its occupants;
- Where the hazard cannot be eliminated, reduced, relocated, or isolated, protection shall be provided to ensure adequate levels of human and structural safety. Should an incident/accident occur, the occupants of the facility shall be provided with protection to enable them to leave the area safely and the structure will be protected to ensure its continued integrity.

1.5. Hydrogen safety communication

The European network of excellence (NoE) HySafe "Safety of Hydrogen as an Energy Carrier" (2004–2009. www.hysafe.org) with €12M of the European Community funding paved the way to defragmentation of hydrogen safety research in Europe and beyond, and closing knowledge gaps in the field. Since 2009, when the HySafe project was formally finished, the coordination of international hydrogen safety activities is led by the International Association for Hydrogen Safety (http://www.hysafe.org/IAHySafe) that brings together experts in hydrogen safety science and engineering from industry, research organizations, and academia from all over the globe.

The International Energy Agency's Hydrogen Implementation Agreement Task 31 "Hydrogen Safety" is also contributing to the prioritization of problems to be solved, discussions of work-in-progress, and the cross-fertilization of safety strategies and engineering solutions developed in different countries around the globe.

The main sources of published knowledge in hydrogen safety include at the moment the Biennial Report on Hydrogen Safety (2008) initiated by NoE HySafe, Proceedings of the International Conference on Hydrogen Safety, and the International Journal of Hydrogen Energy.

The main educational/training activities in the area of hydrogen safety include the European Summer School on Hydrogen Safety and other technical and summer schools, the International Short Course and Advanced Research Workshop (ISCARW) series "Progress in Hydrogen Safety", and the World's first postgraduate course in hydrogen safety, i.e. MSc in Hydrogen Safety Engineering at the University of Ulster. However, the need in an increasing stream of highly qualified university graduates to underpin the emerging industry and early markets is obvious.

The Workgroup on Cross Cutting Issues of the European HFC Technology Platform (Wancura et al., 2006) indicated that educational and training efforts are key instrument in lifting barriers imposed by the safety of hydrogen. This Workgroup has estimated that during the FP7 period (2007–2013), the educated staff needed may amount to 500 new graduates from postgraduate studies on an annual basis in all of Europe. In a study of the European e-Academy of Hydrogen Safety performed within the NoE HySafe, it was estimated that the subset of these necessary graduates specialising in hydrogen safety would amount to 100 on an annual basis (Dahoe and Molkov, 2007).

Unfortunately, to describe all recent progress made in the field of hydrogen safety science and engineering by the international hydrogen safety community is a difficult if not impossible task. The materials presented here are mainly results of the Hydrogen Safety Engineering and Research (HySAFER, http://hysafer.ulster.ac.uk/) Centre at the University of Ulster studies performed as a seeding research and within projects funded by the European Commission and the Fuel Cell and Hydrogen Joint Undertaking.

1.6. The subject and scope of hydrogen safety engineering

The subject of hydrogen safety engineering (HSE) is defined as the application of scientific and engineering principles to the protection of life, property and environment from adverse effects of incidents/accidents involving hydrogen. The scope of hydrogen safety engineering is reflected in the updated HySafe activities matrix (Fig. 1–5) developed by the HySafe consortium (www.hysafe.org). "Vertical" activities are relevant to key phenomena, hazards and risks, including but not limited to releases and dispersion, spontaneous ignition and thermal effects from fires, pressure effects from deflagrations and detonations, mitigation technologies and safety devices, etc. "Horizontal" activities are relevant to safety of various applications and infrastructure, including hydrogen production and distribution, automotive and other transportation, storage, fuel cell components, portable and micropower applications, infrastructure such as refuelling stations, garages, tunnels , etc. The intersection of these vertical and horizontal activities defines the scope of hydrogen safety engineering. Both knowledge of phenomena and engineering safety solutions for hydrogen and fuel cell systems are expected to feed relevant regulations, codes and standards (RCS).

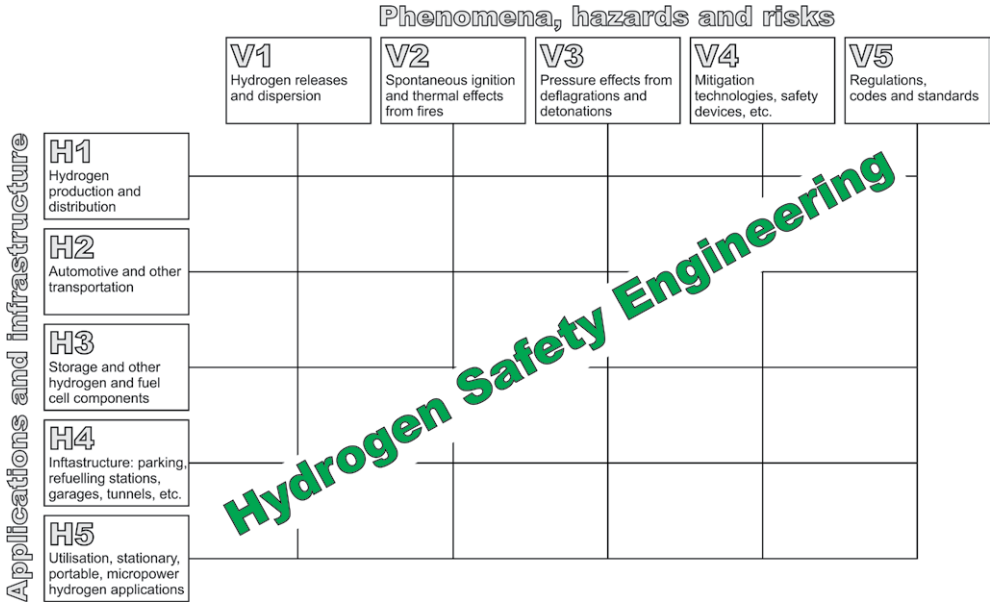

Figure 1–5. The HySafe activity matrix.

The HSE can be applied to existing and new hydrogen systems, including but not limited to stationary, e.g. combined heat and power systems, or portable, e.g. mobile phone and computers, applications for indoor and outdoor use, hydrogen transportation and refuelling infrastructure, power generation, hydrogen production and distribution units, storage, infrastructures such as garages, parking, tunnels, pipelines networks, etc. A hydrogen system could be defined as an equipment dealing with hydrogen e.g. storage, production, delivery, distribution, consumption, etc. Hydrogen should remain contained within hydrogen system from its production/delivery to its final use.

1.7. The emerging profession of hydrogen safety engineering

The higher education of researchers and engineers is a key to surmount challenges of hydrogen safety. The development of an International Curriculum on Hydrogen Safety Engineering (www.hysafe.org/Curriculum) was the first step in the establishment of the profession undertaken by the European e-Academy of Hydrogen Safety in collaboration with partners around the globe. About 70 renowned international experts contributed to the draft for development of the Curriculum. The Curriculum has been already implemented into the World's first postgraduate course in hydrogen safety, i.e. MSc in hydrogen safety engineering at the University of Ulster (http://www.ulster.ac.uk/elearning/programmes/view/course/10139), continuous professional development course at Warsaw University of Technology, hydrogen technology and safety course at the HECTOR School of the Karlsruhe Institute of Technology. The main contributor to the establishment of the profession through a closing of knowledge gaps and educational/training programmes is the international hydrogen safety community led by the International Association for Hydrogen Safety (IA HySafe).

The HSE discipline is developing on the experience and lessons learnt by fire safety engineering, which is today a well-established profession focused mainly on building fires. Unfortunately, graduates of fire safety engineering courses are not taught currently to tackle specific problems of hydrogen safety such as high pressure leaks and dispersion, spontaneous ignition and thermal effects of under-expanded jet fires, pressure loads of hydrogen-air deflagrations/detonations and blast waves, emergency services intervention at an accident scene with a hydrogen system, etc. However, there are common problems, knowledge and experience which HSE can utilise to some extent, such as fire resistance of structures and life safety.

Fire safety was originally regulated by prescriptive codes, aiming to protect societies from adverse effects of fires in traditional buildings with low hazard occupancies (Croce et al., 2008). However, for more complex buildings, the prescriptive approach didn't meet the needs of designers or approval bodies. Those prescriptive codes didn't offer flexibility for innovation, they didn't necessarily provide optimum solution for a particular project, they provided requirements without statement of objectives, they might lag many years behind modern design practice and their use unable to anticipate all eventualities (BSI, 2001; Hadjisophocleous and Benichou, 2002).

In the late 1980s, a project led by the Warren Centre in Australia made a significant contribution by proposing fundamental improvements to fire safety. The purpose was to define a basis for a new generation of RCS. Among the numerous recommendations of the Warren Centre Report (1989), some are directly applied to hydrogen safety systems:

- design for safety should be treated as "*an engineering responsibility rather than as a matter for detailed regulatory control*";
- designers should develop a greater understanding of fire phenomena and human behaviour and adopt appropriate engineering techniques in their design of fire safety systems;
- fire engineering design courses and training strategies should be developed and implemented, up to and including postgraduate level, etc.

This report led to a worldwide attention towards fire safety engineering. The methodology highlighted by this approach was dedicated to measure design's performance using different tools, e.g. simple engineering calculations and contemporary computer-based models.

There was an intention to implement non-complex documents (Hadjisophocleous and Benichou, 2002) in performance-based fire safety regulations to provide greater flexibility when designing and evaluating a project, and to promote innovation in building design, materials, products, and fire protection systems (Croce et al., 2008). This approach nevertheless requires education of professionals and the validation of tools and methods used for quantification (Hadjisophocleous and Benichou, 2002).

The developments in hydrogen safety engineering are greatly inspired by and based on the developments of fire safety engineering, including performance-based RCS, educational programmes and freely available contemporary CFD (Computational Fluid Dynamics) tools like Fire Dynamics Simulator (http://fire.nist.gov/fds/).

The framework for fire safety engineering is described by Deakin and Cooke (1994). Some of their statements can be directly transferred to define the HSE framework:

- **Provide a systematic approach.** The process used to undertake HSE and evaluate the performance of a design, should be clearly defined and explained.
- **Define acceptance criteria.** The performance of a design is evaluated by comparison with deterministic, comparative or probabilistic criteria.
- **Simplify the problem.** The HSE process is separated into analysis of Technical Sub-Systems (TSS) that can be used individually to address specific issues or together to address all aspects.
- **Illustrate interactions.** The complexity of phenomena and interactions between elements of hydrogen system, people and the built environment in a case of incident/accident requires a simplified approach by underlining interactions between different TSS.
- **Ensure adequate consideration of all those factors relevant to any aspect of the design.** In order to identify all significant variables in a quantification process, it is essential to list relevant scenarios. Doing this, it is possible for each scenario to inventory critical factors from hydrogen system/infrastructure, e.g. parameters of accident scenario including occupancy, etc.

- **Insist on clear presentation and comment on calculation methods and data sources.** As the application of HSE might be subject to review and approval, it is essential that findings, calculations and assumptions, are presented in a report that can be clearly and readily understood.

1.8. Knowledge gaps and future progress

In Europe the priorities in hydrogen safety research are formulated by industry through calls of the Fuel Cell and Hydrogen Joint Undertaking (FCH JU, http://www.fch-ju.eu/) mainly as a part of cross-cutting issues. The international hydrogen safety community contributes to the prioritization of research through different activities of the International Association for Hydrogen Safety (www.hysafe.org). The International Energy Agency Hydrogen Implementation Agreement Task 31 "Hydrogen Safety" (http://www.ieah2safety.com/) is actively involved in the process too. A gap analysis of CFD modelling of accidental hydrogen release and combustion has been performed recently by an expert group led by JRC, Institute for Energy, The European Commission (Baraldi et al., 2010).

In spite of indubitable progress in hydrogen safety in the last decade, there are still numerous gaps of knowledge and a need in science-intensive tools, based on contemporary theories and thorough validation against a series of experiments carried out at different conditions. The non-exhaustive list of research topics has been prioritized by the hydrogen safety community, including but not limited to the following items grouped by phenomena or application. Based on the report by Baraldi et al. (2010) author updated the list of knowledge gaps in hydrogen safety as follows.

***Release and dispersion phenomena*:** hydrogen leak source characterization and modelling; shape of leak source effects; dispersion and accumulation in enclosed areas in presence of natural and mechanical ventilation; surface effects on jet release and separation distance; criteria for uniform or layered distribution of hydrogen in vented enclosure; liquid hydrogen release behaviour; behaviour of cold jets released in humid air; releases in complex geometries; effect of wind on indoor (natural ventilation) and outdoor releases in areas with complex surroundings; behaviour of expanded and under-expanded plane jets compared to round jets; interaction of multiple jets; transient effects in high momentum jets; transition from momentum- to buoyancy-controlled flow; flammable envelope for downward free and impinging jets; dynamics of unsteady releases (blow-downs and hydrogen puff, etc.); initial stage of release and dispersion in ventilated enclosure; applicability limits for pressure peaking phenomenon; etc.

***Ignition phenomena*:** mechanisms of hydrogen ignition during release; CFD modelling and validation of the membrane rupture and the associated transient processes; CFD modelling of transition from spontaneous ignition to jet fires and/or the quenching of the spontaneous ignition; development and validation of sub-grid scale models accounting for interaction of turbulence and chemistry; ignition in complex geometries like pressure relief devices; extinction of spontaneous ignition in piping; jet ignition delay time and position of ignition source for simulations of deflagration overpressure; effect of spontaneous ignition on deflagration overpressure as compared to spark ignition at different distances from the release source; ignition in complex geometries like pressure relief devices; etc.

***Hydrogen fires*:** behaviour of free jet flames, e.g. thermal radiation in the presence of a crosswind and surface effects on flame jet propagation; development of models and validation of CFD tools for large-scale hydrogen jet fires, including under transient conditions of decreasing notional nozzle diameter and temperature during a blowdown; thermal and pressure effects of indoor hydrogen fires; understanding of under-ventilated fires, self-extinction and re-ignition phenomena; impinging jet fires and heat transfer to structural elements, storage vessels, etc.; predictive simulations of blow-off, lift-off, and blow-out phenomena; expanded and under-expanded plane jet flames; predictive simulations of micro-flame quenching and blow-off; effect of micro-flames on materials degradation; etc.

***Deflagrations and detonations*:** effect of hydrogen jet ignition delay time and position of ignition source on predictive simulation of deflagration overpressure; flammability and detonability limits of gaseous mixtures containing hydrogen; modelling of coherent deflagration during venting of deflagration in low-strength equipment accounting for Rayleigh-Taylor instability; effect of inertia of vent cover on deflagration dynamics, including DDT; partially premixed flames, in particular triple flames in hydrogen-air layers and their pressure effects in enclosed space; development of SGS models of DDT at large industrial scales accounting for Richtmyer-Meshkov instability; etc.

***Storage*:** fire resistance of onboard storage vessels and effect of PRD; metal hydride dust cloud deflagration hazard; engineering solutions to reduce heat transfer to storage tanks from external fire scenarios (localized and engulfing fires); etc.

***High pressure electrolysers*:** an explosion of a pressurized electrolyser at operational pressure 40 MPa happened on December 7, 2005 at a demonstration hydrogen stand at Kyushu University (http://www.kyushuu.ac.jp/news/hydrogen/hydrogensummary0330.pdf; http://www.nsc.go.jp/senmon/shidai/kasai/kasai004/ssiryo4-1.pdf). Possibly after the membrane leak an internal hydrogen-oxygen jet fire resulted in metal (titanium) fire and explosion or rupture of the electrolyzer shell. Internal fluid and combustion products were released into surrounding including parking area around the laboratory building. Several vehicle glass damages occurred due to the exposure to hydrogen fluoride which formed by the decomposition of polymer materials of the membrane. A French-Russian study (Millet et al., 2011) reports the analysis of the failure mechanisms of PEM water electrolysis cells which can ultimately lead to the destruction of the electrolyser. A two-step process involving firstly the local perforation of the solid polymer electrolyte followed secondly by the catalytic recombination of hydrogen and oxygen stored in the electrolysis compartments has been evidenced. Photographs of a stainless steel fitting and nut drilled by a hydrogen-oxygen flame formed inside the PEM stack are presented (Millet et al., 2011). Millet et al. (2011) concluded that the internal hydrogen-oxygen combustion prevails over "explosion".

***Hazard and risk identification and analysis for early markets*:** data collection from new hydrogen-based operating devices, systems and facilities; failure statistics of new hydrogen applications; systems safety analysis of hydrogen applications; engineering correlations, etc. Since new technologies are penetrating densely populated urban environment, special attention should be paid to hazards and risk mitigation technologies and methods such as sensors, barriers/walls and separation distances.

2 Hydrogen properties and hazards

As a unique gas hydrogen was discovered by Henry Cavendish in 1766. It was given the name "water forming" by Antoine Lavoisier seven years later, who proved that water was composed of hydrogen and oxygen. The word "hydrogen"originates from the Greek words *hydōr* (water) and *gignomai* (forming). However, it has to be mentioned that hydrogen was observed and collected by Robert Boyle in 1671, who dissolved iron in diluted hydrochloric acid, i.e. long before it was recognized as a unique gas by Henry Cavendish.

Hydrogen is one of the main compounds of water and of all organic matter, and it's widely spread not only in The Earth but also in the entire Universe. It is the most abundant element in the Universe representing 75% by mass or 90% by volume of all matter (BRHS, 2009). Hydrogen forms 0.15% of The Earth crust.

This chapter presents selected properties of hydrogen that are relevant to safety provisions and associated hazards. Safety of hydrogen and fuel cell systems and infrastructure at the user interface will be provided when the technology developers, designers, regulators, operational personnel, first responders and finally public are aware through education and training of the specific hazards associated with the handling and use of hydrogen and understand how to prevent the incident/accident or mitigate/control it if happened.

2.1. Physical and chemical properties

2.1.1. Atomic and molecular hydrogen, ortho- and para-hydrogen

Atomic number of hydrogen (symbol H) in the periodic table is one, and atomic mass is 1.008 g/mol (approximated by four digits). The hydrogen atom is formed by a nucleus with one unit of positive charge (proton) and one electron. The electron carries a negative charge and is usually described as occupying a "probability cloud" surrounds the nucleus somewhat like a fuzzy, spherical shell. Charges of the proton and electron of each hydrogen atom cancel each other out, so that individual hydrogen atom is electrically neutral. The mass of a hydrogen atom is concentrated in its nucleus. Indeed, the proton is more than 1800 times more massive than the electron. Neutron can be present in the nucleus. Neutron has almost the same mass as proton and does not carry a charge. The radius of the electron's orbit, which defines the size of the atom, is approximately 100,000 times as large as the radius of the nucleus. Size of hydrogen atom in its ground state is 10^{-10} m (1 angstrom).

There are three hydrogen isotopes: protium (found in more than 99,985% of the natural element; only a proton in the nucleus), deuterium (found in nature in 0.015% approximately; a proton and a neutron in the nucleus), and tritium (appears in small quantities in nature, but can be artificially produced by various nuclear reactions; a proton and two neutrons in the nucleus) with atomic mass 1, 2 and 3 respectively (approximated by one digit). Tritium is unstable and radioactive (generates β rays – fast moving electrons as a result of neutron conversion into a proton, 12.3 years half-decay time).

In normal conditions hydrogen is a gas formed by diatomic molecules, H_2 (molecular mass 2.016), in which two hydrogen atoms have formed a covalent bond. This is because the atomic arrangement of a single electron orbiting a nucleus is highly reactive. For this reason, hydrogen atoms naturally combine into pairs. Hydrogen is colourless, odourless and insipid. That is why its leak is difficult to detect. Compounds such as mercaptans, which are used to scent natural gas, cannot be added to hydrogen for use in PEM (proton exchange membrane) fuel cells as they contain sulphur that would poison the fuel cells.

The hydrogen molecule exists in two forms, distinguished by the relative rotation of the nuclear spin of the individual atoms in the molecule. Molecules with spins in the same direction (parallel) are called ortho-hydrogen; and those with spins in the opposite direction (anti-parallel), para-hydrogen (NASA, 1997). These molecules have slightly different physical properties but are chemically equivalent. The chemistry of hydrogen, and in particular the combustion chemistry, is little altered by the different atomic and molecular forms.

The equilibrium mixture of ortho- and para-hydrogen at any temperature is referred to as equilibrium hydrogen. The equilibrium ortho-para-hydrogen mixture with a content of 75% ortho-hydrogen and 25% para-hydrogen at room temperature is called normal hydrogen. At lower temperatures, equilibrium favours the existence of the less energetic para-hydrogen (liquid hydrogen at 20 K is composed of 99,8% of para-hydrogen). The ortho-para-hydrogen conversion is accompanied by a release of heat, 703 kJ/kg at 20 K for ortho- to para-hydrogen conversion, or 527 kJ/kg for normal to para-hydrogen conversion (NASA, 1997).

This feature of hydrogen underpins inherently safer storage of hydrogen as cryo-compressed rather than liquefied fluid (fluids with temperatures below –73°C are known as cryogenic fluids) in automotive applications due to essential reduction if not exclusion at all of the hydrogen boil-off phenomenon at day-to-day normal driving. In fact, due to conversion of para- to ortho-hydrogen during "consumption" of external heat the release of hydrogen from storage tank as a result of boil-off phenomenon is practically excluded for cryo-compressed storage with clear safety implications.

The process of hydrogen liquefaction includes the removal of the energy released by the ortho-para state conversion. The heat of conversion is 715.8 kJ/kg. This is 1.5 times of the heat of vaporization (ISO/TR 15916:2004). The liquefaction is a very slow exothermic process that can take several days to complete, unless it is accelerated with the use of a paramagnetic catalyst.

2.1.2. Gas, liquid, and solid phases

The phase diagram of hydrogen is presented schematically in Fig. 2–1. There are three curves. One curve shows change of boiling (condensation for the opposite phase transition) temperature with pressure, another gives change of melting (freezing) temperature with pressure, and the third indicates pressures and temperatures when *sublimation* is possible. The process of condensation is also known as liquefaction.

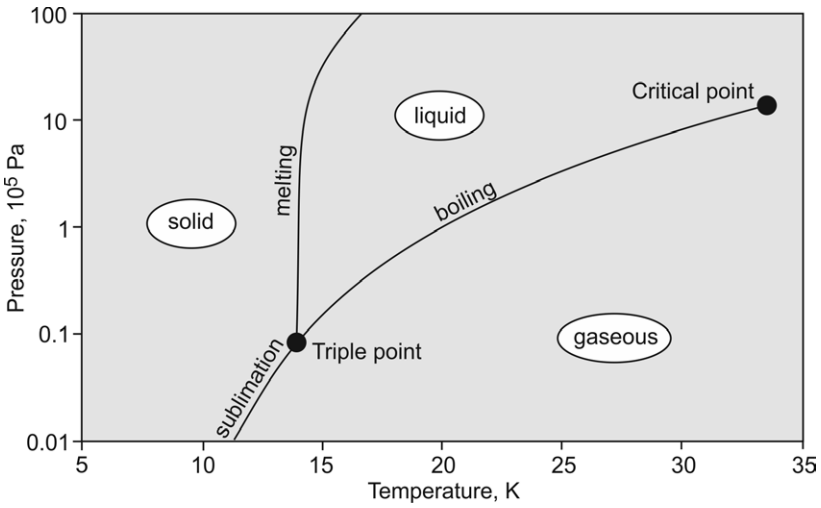

Figure 2–1. Phase diagram of hydrogen.

Hydrogen is used in gaseous, liquid, or slush forms. Liquid hydrogen is transparent with a light blue tint. Slush hydrogen is a mixture of solid and liquid hydrogen at the triple point temperature. The phase transition of hydrogen is dominated by the low temperatures at which transitions between gas, liquid, and solid phases occur. The *triple point* (see phase diagram), which is the condition under which all three phases can coexist, is temperature 13.8 K and pressure 7.2 kPa. The vapour pressure of slush hydrogen can be as low as 7.04 kPa (NASA, 1997) and safety measures must be taken during operations to prevent air leakage into the system that could create flammable mixture.

The highest temperature, at which a hydrogen vapour can be liquefied, is the critical temperature, which is 33.145 K (see "critical point" on the phase diagram). The corresponding critical pressure is 1.3 MPa (density at critical point is 31.263 kg/m^3). Above the critical temperature it is impossible to condense hydrogen into liquid just by increasing the pressure. All you get is cryo-compressed gas. The molecules have too much energy for the intermolecular forces to hold them together as a liquid.

The normal boiling point (NBP, boiling temperature at absolute pressure of 101,325 kPa) of hydrogen is 20.3 K. The normal melting point is 14.1 K (101,325 kPa). Hydrogen has the second lowest boiling and melting points of all substances (helium has lowest value of boiling temperature of 4.2 K and melting temperature of 0.95 K). All these temperatures are extremely low and below the freezing point of air. It is worth reminding that at absolute zero temperature of 0 K (–273.15 °C), which is the lowest temperature in the universe, all molecular motion stops.

Liquid para-hydrogen (NBP) has a density of 70.78 kg/m^3. The corresponding *specific gravity* is 0.071 (the reference substance is water with specific gravity of 1). Thus, liquid hydrogen is approximately 14 times less dense than water. Ironically, every cubic meter of water (made up of hydrogen and oxygen) contains 111 kg of hydrogen whereas a cubic meter of liquid hydrogen contains only 70.78 kg of hydrogen (College of the Desert, 2001). Thus, water packs more mass of hydrogen per unit volume, because of its tight molecular structure, than hydrogen itself. This is true of most other liquid hydrogen-containing compounds such as hydrocarbons as well. The higher density of the saturated hydrogen vapour at low temperatures may cause the cloud to flow horizontally or downward immediately upon release if liquid hydrogen leak occurs. These facts have to be accounted for by first responders during intervention at an accident scene.

An essential safety concern of liquid hydrogen's low temperature is that, with the exception of helium, all gases will be condensed and solidified should they be exposed to it. Leaks of air or other gases into direct exposure with liquid hydrogen can lead to several hazards (ISO/TR 15916:2004). The solidified gases can plug pipes and orifices and jam valves. In a process known as cryo-pumping the reduction in volume of the condensing gases may create a vacuum that can draw in yet more gas, e.g. oxidiser like air. Large quantities of material can accumulate displacing the liquid hydrogen if the leak persists for long periods. At some point, should the system be warmed for maintenance, these frozen materials will re-gasify possibly resulting in high pressures or explosive mixtures. These other gases might also carry heat into the liquid hydrogen and cause enhanced evaporation losses or "unexpected" pressure rise.

Liquid hydrogen is usually transferred in vacuum insulated lines. However, cold hydrogen flowing through tubes which are not sufficiently thermally insulated can easily cool the system below 90 K so that condensed air with an oxygen content of up to 52 % is present (NBP of nitrogen is 77.36 K, NBP of oxygen is 90.15 K, NBP of carbon dioxide is 216.6 K). The liquid condensate flows and looks like liquid water. This oxygen-enriched condensate enhances the flammability of materials and makes materials combustible that normally are not. This includes for example bituminous road covers. This is of particular concern when transferring large quantities of hydrogen. If a piece of equipment cannot be insulated, the area underneath should be free of any organic material.

Oxygen enrichment can increase the flammability and even lead to the formation of shock-sensitive compounds. Oxygen particulate in cryogenic hydrogen gas may even detonate. Vessels with liquid hydrogen have to be periodically warmed and purged to keep the accumulated oxygen content in the vessel to less than 2% (ISO/TR 15916:2004). Caution should be exercised if carbon dioxide is used as a purge gas. It may be difficult to remove all carbon dioxide from the system low points where the gas can accumulate.

2.1.3. Heat of vaporization, melting, and sublimation

Heat of vaporization (condensation) at NBP is 445.6 kJ/kg. Heat of melting (fusion) at melting (freezing) point is 58.8 kJ/kg. Heat of *sublimation* is 379.6 kJ/kg.

2.1.4. Hydrogen expansion ratio

The volume of liquid hydrogen expands with the addition of heat significantly more than can be expected based on our experience with water. The coefficient of thermal expansion at NBP is 23 times that of water at ambient conditions (ISO/TR 15916:2004). The significance for safety arises when cryogenic storage vessels have insufficient ullage space to accommodate expansion of the liquid. This can lead to an over pressurisation of the vessel or penetration of the liquid hydrogen into transfer and vent lines.

A considerable increase in volume is associated with the phase change of liquid to gaseous hydrogen, and yet another volume increase occurs for gaseous hydrogen that is allowed to warm from the NBP to NTP. The ratio of the final volume to the initial volume for the phase change from liquid to gaseous hydrogen and expansion of heated gas is 847 (ISO/TR 15916:2004). This total volume increase can result in a final pressure of 177 MPa (starting with an initial pressure of 0.101 MPa) if the gaseous hydrogen is in a closed vessel. Pressure relief devices should be installed as a safety measure in any volume in which liquid hydrogen or cold gaseous hydrogen could be trapped, to prevent overpressure from expansion of the liquid hydrogen or cold gaseous hydrogen.

When hydrogen is stored as a high pressure gas at 25 MPa (gauge) and atmospheric temperature, its expansion ratio to atmospheric pressure is 1:240 (College of the Desert, 2001). While a higher storage pressure increases the expansion ratio somewhat, gaseous hydrogen under any conditions cannot approach the expansion ratio of liquid hydrogen.

2.1.5. Buoyancy as safety asset

The main hydrogen safety asset, i.e. its highest on The Earth buoyancy, confers the ability to rapidly flow out of an incident scene, and mix with the ambient air to a safe level below the lower flammability limit (LFL) of 4% by volume of hydrogen in air. Indeed, hydrogen has a density of 0.0838 kg/m^3 (NTP) which is far below than air density of 1.205 kg/m^3 at the same conditions. The unwanted consequences of hydrogen releases into the open atmosphere, and in partially confined geometries, where no conditions to allow hydrogen to accumulate exist, are drastically reduced by buoyancy.

Contrary, heavier hydrocarbons are able to form a huge combustible cloud, as in cases of disastrous Flixborough in 1974 (Health and Safety Executive, 1975) and Buncefield in 2005 (Buncefield Investigation, 2010) explosions. In many practical situations, hydrocarbons may pose stronger fire and explosion hazards than hydrogen. Hydrogen high buoyancy affects its dispersion considerably more than its high diffusivity.

Pure hydrogen is positively buoyant above a temperature of 22 K, i.e. over almost the whole temperature range of its gaseous state (BRHS, 2009). Buoyancy provides comparatively fast dilution of released hydrogen by surrounding air below the lower flammability level. In unconfined conditions only small fraction of released hydrogen would be able to deflagrate. Indeed, a hydrogen-air cloud evolving from the inadvertent release upon the failure of a storage tank or pipeline liberates only a small fraction of its thermal energy in case of a deflagration, which is in the range 0.1-10% and in most cases below 1% of the total energy of released hydrogen (Lind, 1975; BRHS, 2009). This makes safety considerations of hydrogen accident with large inventory at the open quite different from that of other flammable gases with often less or no harmful consequences at all.

Caution should be taken in applying gaseous hydrogen buoyancy observations to releases of hydrogen vapours at cryogenic temperatures. Hydrogen vapours at low temperature can be denser than air at NTP. Usually the condensation of atmospheric humidity will also add water to the mixture cloud, firstly making it visible, and secondly increasing the molecular mass of the mixture even more.

2.1.6. Diffusivity and viscosity

Diffusivity of hydrogen is higher compared to other gases due to small size of the molecule. Data on the diffusion coefficient of hydrogen in air are ranging from 6.1E-05 m^2/s (Alcock et al., 2001) to 6.8E-05 m^2/s (Baratov et al., 1990).

Helium and hydrogen effective diffusion coefficients through gypsum panels were measured by Yang et al. (2011). The estimated average diffusion coefficients are found to be D_e=1.3-1.4E-05 m^2/s for helium (3.3E-06 m^2/s for painted gypsum panel), and D_e=1.4E-05 m^2/s for hydrogen at room temperature 22 C. Authors underlined that since the interior of most garages in the U.S. have large surface areas covered with gypsum panels together with the fact that hydrogen can readily diffuse through gypsum panels, this diffusion process should not be overlooked in the hazard assessment of accidental release of hydrogen in garages or enclosures lined with gypsum panels. The quasi-steady diffusive molar flux ($mol/m^2/s$) through the unit area of a panel of thickness δ (m) can be approximated by $D_e(C\text{-}C_S)/\delta$, where C (mol/m^3) is the molar concentration of hydrogen in enclosure and C_S (mol/m^3) is the concentration in the surrounding.

The low viscosity of hydrogen and the small size of the molecule cause a comparatively high flow rate if the gas leaks through fittings, seals, porous materials, etc. This negative effect is to a certain extent offset by the low energy density (volumetric) of hydrogen in comparison with e.g. methane or other hydrocarbon gases. Viscosity of gaseous hydrogen (μPoise): 89.48 (NTP) and 11.28 (NBP). Viscosity of liquid hydrogen at NBP is 132.0 μPoise (BRHS, 2009).

2.1.7. Interaction with materials

Hydrogen can cause a significant deterioration in the mechanical properties of metals (NASA, 1997). This effect is referred to as hydrogen embrittlement. Hydrogen embrittlement involves a large number of variables such as the temperature and pressure of the environment; the purity, concentration, and exposure time of the hydrogen; and the stress state, physical and mechanical properties, microstructure, surface conditions, and nature of the crack front of the material. Many hydrogen material problems involve welds or the use of an improper material.

The selection of a structural material for use in liquid or slush service is based primarily on the mechanical properties of the material such as yield and tensile strength, ductility, impact strength, and notch insensitivity (NASA, 1997). The material must have certain minimum values of these properties over the entire temperature range of operation, with appropriate consideration for non-operational conditions such as a fire. The material must be metallurgically stable so phase changes in the crystalline structure do not occur with time or repeated thermal cycling.

Hydrogen is non-corrosive. Many metals absorb hydrogen, especially at high pressures. Hydrogen absorption by steel can result in embrittlement, which can lead to fails in the equipment. There is an atomic solution of hydrogen in metals. Permeated through a metal atomic hydrogen recombines to molecules on the external surface of storage to diffuse into surrounding gas afterwards. The choice of material for hydrogen system is an important part of hydrogen safety.

2.1.8. Specific heat and thermal conductivity

Non-nuclear energy applications typically use material data that applies to normal hydrogen, i.e. two protium atoms arranged in 75% as ortho-hydrogen and 25% as para-hydrogen molecules. The only exception occurs for cryogenic applications such as liquid and cryo-compressed hydrogen storage, in which heat is an important parameter. The larger property differences between ortho- and para-hydrogen occur in those properties for which heat is important, that is enthalpy, specific heat capacity and thermal conductivity, whereas other properties, such as density, vary little between ortho-hydrogen and para-hydrogen.

On a molar basis, the heat capacity of hydrogen is similar to that of other diatomic gases despite its low molecular mass (ISO/TR 15916:2004). Specific heat of gaseous hydrogen at constant pressure c_p (kJ/kg/K): 14.85 (NTP), 14.304 (STP), 12.15 (NBP). Specific heat of liquid hydrogen at boiling point is 9.66 kJ/kg/K (BRHS, 2009). The specific heat at constant pressure of liquid para-hydrogen is c_p=9.688 kJ/kg/K. This is more than double that of water and greater than 5 times that of liquid oxygen at its NBP. Gas constant of hydrogen is 4.1243 kJ/kg/K (this is the universal gas constant divided by the molecular mass). The specific heats ratio of hydrogen at NTP conditions (293.15 K and 101.325 kPa) is γ=1.39 and STP conditions (273.15 K and 101.325 kPa) is γ =1.405.

Thermal conductivity of hydrogen is significantly higher than that of other gases. Gaseous hydrogen (W/m/K): 0.187 (NTP), 0.01694 (NBP). Liquid hydrogen (W/m/K): 0.09892 (NBP).

2.1.9. The Joule-Thomson effect

In 1843 Joule investigated the dependence of energy of gases on pressure using the simple apparatus that included a copper bulb N1 filled with air under pressure, isolated from an evacuated similar bulb N2 by a valve. The bulbs were immersed in a well-stirred water bath equipped with a sensitive thermometer. After thermal equilibrium had been established, the valve was opened to allow the gas to expand into bulb N2. No change in temperature was detected and Joule concluded that "no change of temperature occurs when air is allowed to expand in such a manner as not to develop mechanical power", i.e. do no external work, $\Delta W = 0$. Since "no change of temperature" was observed, $\Delta Q = 0$, and therefore

$$\Delta W = \Delta Q = \Delta U = 0. \tag{2–1}$$

Thus, Joule concluded that the expansion of gas occurred at constant internal energy U.

Unfortunately, the system used by Joule for this experiment had a very large heat capacity compared with the heat capacity of air, and the small change of temperature that took place was not observed. In fact, the gas in bulb N1 warmed up slightly and the one which had expanded into bulb N2 was somewhat cooler and when thermal equilibrium was finally established the gas was at a slightly different temperature from that before the expansion.

Later Joule in association with Thomson, who devised a different experimental procedure, performed another study of the dependence of the energy and enthalpy of real gases during expansion. The gas in new experiment freely expanded from a pressure *P1* to pressure *P2* by the throttling action of the porous plug. The system was thermally insulated, thus the expansion occurred adiabatically. Gas was allowed to flow continuously through the porous plug, and when steady state conditions have been reached the temperatures of the gas before and after expansion, *T1* and *T2*, were measured by sensitive thermocouples.

It can be shown that throttling (the expansion of fixed mass flow rate of gas) occurs at constant enthalpy. Indeed, if two imaginary pistons introduced into the system with parameters *V1, P1, T1* upstream of the plug and *V2, P2, T2* downstream of the plug then the work done by the surroundings on the system downstream and upstream of the plug is respectively $+P1V1$ and $-P2V2$. Thus, the overall change in internal energy of the gas during the adiabatic expansion ($\Delta Q=0$) following the second law of thermodynamics is $\Delta U= P1V1-P2V2$. By definition $\Delta H=\Delta U+\Delta PV$ and thus this expansion is isenthalpic ($\Delta H=0$)

$$H_2 = H_1 \tag{2–2}$$

It is worth noting that this is done in an assumption that the difference in the specific kinetic energy of gas before and after the plug can be neglected (Moran and Shapiro, 2006). However, this is not the case when there is a release from the storage with practically zero flow velocity through the small orifice where velocity can reach supersonic values.

The throttling experiment by Joule and Thomson measures directly the change in temperature of a gas with pressure at constant enthalpy which is called the Joule-Thomson coefficient

$$\mu_{JT} = \left(\frac{\partial T}{\partial P}\right)_H . \tag{2–3}$$

For expansion, the change of pressure is negative and therefore a positive value for Joule-Thomson coefficient corresponds to gas cooling on expansion and negative coefficient corresponds to gas heating.

For an ideal gas and isenthalpic process

$$\left(\frac{\partial H}{\partial P}\right)_T = \left(\frac{\partial H}{\partial T}\right)_P \left(\frac{\partial T}{\partial P}\right)_H = -c_P \cdot \mu_{JT} = 0 . \tag{2–4}$$

Because the heat capacity at constant pressure c_p is not zero, Joule-Thomson coefficient must be zero for an ideal gas.

For real gases, if Joule-Thomson experiments are performed with different conditions downstream of the porous plug, a curve with constant enthalpy can be drawn in coordinates temperature-pressure *T-P* (see Fig. 2–2). A series of curves could be generated by performing experiments at different conditions upstream of the plug. Figure 2–2 is typical of all real gases.

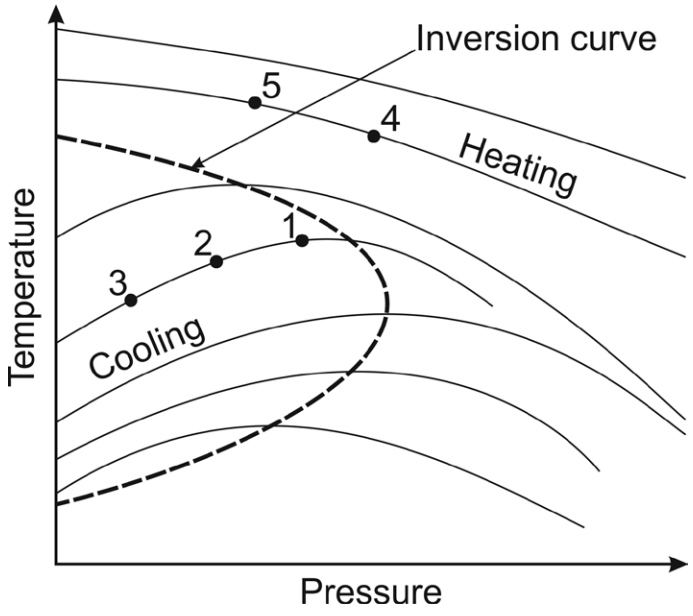

Figure 2–2. Isenthalpic curves (solid lines) and inversion curve (dash line).

If the temperature is quite low the curves pass through a maximum called the inversion point. The locus of the inversion points is called the inversion curve. The slope of an isenthalpic curve at any point is equal to Joule-Thomson coefficient and at the maximum of the curve, or the inversion point, it is equal to 0. It is evident that when the Joule-Thomson effect is to be used in the liquefaction of gases by expansion, the conditions must be chosen so that the temperature will decrease. For example, a drop in temperature would be produced by an expansion from point 1 to point 2 and then to point 3. However, a temperature rise would result in an expansion from point 4 to point 5.

At higher temperatures or lower temperatures coupled with high pressures expansion will heat the gas (see Fig. 2–2). In a Joule-Thomson process, starting at ambient temperature, the temperature of hydrogen will not drop but rise. Most gases at ambient temperatures cool when expanded across a porous plug. However, the temperature of hydrogen increases when the gas is expanded at a temperature above its inverse Joule-Thomson temperature 193 K. Yet, the inverse Joule-Thomson effect cannot be the primary cause of any ignition that occurs when hydrogen is vented from a high-pressure storage. The temperature increase from the Joule-Thomson effect is only a few degrees Kelvin at the most. It would not raise the gas temperature to its ignition value unless the gas was already near the ignition temperature after mixing with surrounding gas.

2.1.10. Ideal and real gas equations

The ideal gas equation that is applied to hydrogen at moderate pressures can be written in the form

$$p = \rho \cdot R_{H2} \cdot T, \tag{2–5}$$

where p is the pressure, Pa; ρ is the density, kg/m^3; T is the temperature, K; R_{H2} is the hydrogen gas constant (4124.24 J/kg/K) that is equal to the ratio of the universal gas constant R (8.3145 J/mol/K) to the molecular mass of hydrogen M=2.016 kg/kmol.

The ideal gas equation is not applicable to hydrogen storage pressures above 10–20 MPa when effects of non-ideal gas are essential. The Abel-Noble equation of state for real hydrogen gas is (Chenoweth, 1983)

$$p = Z \cdot \rho \cdot R_{H2} \cdot T, \tag{2–6}$$

where the compressibility factor Z is

$$Z = \frac{1}{1 - b\rho}, \tag{2–7}$$

in which b=7.69E-03 m^3/kg is the co-volume constant for the Abel-Noble equation.

Use of the ideal gas law equation instead of the real gas equation has an important safety implications. The ideal gas law if applied for a release from high pressure storage would overestimate the mass flow rate of the leak and the total mass discharged. The compressibility factor Z gives a value of this overestimation. The compressibility factor for arbitrary storage pressure and temperature can be calculated by the following equation derived from the previous two

$$Z = 1 + \frac{b \cdot p}{R_{H2} \cdot T}. \tag{2–8}$$

For example, it is equal to Z=1.01 at 1.57 MPa, Z=1.1 at 15.7 MPa, and Z=1.5 at 78.6 MPa (temperature 293.15 K). This means that at storage pressure of 78.6 MPa the amount of released hydrogen would be overestimated by 50% if the ideal gas equation of state is applied for carrying out hydrogen safety engineering calculations.

2.1.11. Speed of sound in ideal gases

Speed of sound in ideal gases is

$$C = \sqrt{\gamma \frac{p}{\rho}}, \tag{2–9}$$

where p is the pressure, Pa; ρ is the density, kg/m^3; $\gamma = c_p / c_v$ is the ratio of specific heats at constant pressure c_p and constant volume c_v respectively (both in J/mol/K). Using the ideal gas law equation in the form

$$p = \rho \frac{R \cdot T}{M}, \tag{2–10}$$

where M is the molecular mass, kg/mol, and R is the universal gas constant, the speed of sound equation can be rewritten as

$$C = \sqrt{\gamma \frac{R \cdot T}{M}}. \tag{2–11}$$

Speed of sound in gaseous hydrogen is 1294 m/s at NTP and 355 m/s at NBP (normal boiling point – boiling temperature of hydrogen 20.3 K at pressure 101,325 Pa). Speed of sound in liquid hydrogen is 1093 m/s (boiling point). Speed of sound in stoichiometric hydrogen-air mixture is 404 m/s (BRHS, 2009).

2.2. Combustion properties

At normal temperature hydrogen is a not very reactive substance, unless it has been activated somehow, e.g. by an appropriate catalyser. Hydrogen reacts with oxygen to form water at ambient temperature extraordinarily slow. However, if the reaction is accelerated by a catalyser or a spark, it proceeds with high rate and "explosive" violence. Molecular hydrogen dissociates into free atoms at high temperatures. Atomic hydrogen is a powerful reductive agent, even at ambient temperature e.g. when it diffuses from a high temperature zone of a flame front into its pre-heating low temperature zone. The heat released when the hydrogen atoms recombine to the hydrogen molecule is used for example to obtain high temperatures in the atomic hydrogen welding.

Hydrogen burns in a clean atmosphere with an invisible flame. It has a somewhat higher adiabatic premixed flame temperature for a stoichiometric mixture in air of 2403 K compared to other fuels (BRHS, 2009). This temperature can be a reason for serious injure at an accident scene, especially at clean laboratory environment where the hydrogen flame is practically invisible. However, hydrogen combustion and hot currents will cause changes in the surroundings that can be used to detect the flame. Although the non-luminous hydrogen flame makes visual detection difficult, there is a strong effect of heat and turbulence on the surrounding atmosphere and raising plume of hot combustion products. These changes are called the signature of the fire.

2.2.1. Stoichiometric mixture, equivalence ratio, and mixture fraction

Stoichiometric mixture is a mixture in which both fuel and oxidiser are fully consumed (complete combustion) to form combustion product(s). For example, the two diatomic gases, hydrogen (H_2) and oxygen (O_2), can combine to form water as the only product of an exothermic reaction between them, as described by the equation

$$2H_2 + O_2 = 2H_2O. \tag{2–12}$$

Thus, the stoichiometric hydrogen-oxygen mixture is composed of 66.66% by volume of hydrogen and 33.33% of oxygen. Let us calculate a stoichiometric concentration of hydrogen in mixture with air composed of 21% by volume of oxygen and 79% of nitrogen (actually ambient air is a mixture of nitrogen, at about 78%, oxygen, at about 21%, with the remaining 1% composed of carbon dioxide, methane, hydrogen, argon, and helium; there can be some water vapour present depending on the humidity)

$$2H_2 + (O_2 + 3.76N_2) = 2H_2O + 3.76N_2 . \tag{2–13}$$

Thus, the stoichiometric concentration of hydrogen in air (assuming 21% of oxygen and 79% of nitrogen) is 29.59% by volume (2/(2+1+3.76)=0.2959) with air content of 70.41%.

The equivalence ratio is the ratio of the actual fuel-to-oxidizer ratio to the fuel-to-oxidiser ratio in the stoichiometric mixture

$$\phi = \frac{m_f / m_{ox}}{(m_f / m_{ox})_{st}} = \frac{n_f / n_{ox}}{(n_f / n_{ox})_{st}}, \tag{2–14}$$

where m is mass and n is number of moles, subscripts "f", "ox", "st" denotes fuel, oxidiser, and stoichiometric mixture respectively. The equivalence ratio is 1.0 at stoichiometry, the ratios are less than 1.0 for lean by fuel mixtures, and are greater than 1.0 for rich mixtures.

There is essential advantage of using the equivalence ratio over a fuel–oxidiser ratio. The equivalence ratio does not have the dependence on the units being used, i.e. it is the same value either mass or number of moles are used. Contrary, the fuel–oxidiser ratio based on mass of fuel and oxidiser is not same as the fuel-oxidiser ratio based on number of moles. Let us consider for example a mixture of one mole of hydrogen (H_2) and one mole of oxygen (O_2). Indeed, two different fuel-oxidizer ratio (*FOR*), one based on mass and another on number of moles, are different

$$FOR_m = \frac{2}{32} = 0.0625 \quad \text{and} \quad FOR_n = \frac{1}{1} = 1. \tag{2–15}$$

At the same time the equivalence ratio calculated by mass is

$$\phi = \frac{m_f / m_{ox}}{(m_f / m_{ox})_{st}} = \frac{2/32}{(4/32)_{st}} = 0.5 \tag{2–16}$$

and by number of moles is

$$\phi = \frac{n_f / n_{ox}}{(n_f / n_{ox})_{st}} = \frac{1/1}{(2/1)_{st}} = 0.5 \tag{2–17}$$

i.e. exactly the same (0.5) for the mixture composed of 1 mole of hydrogen and 1 mole of oxygen.

The ratio of actual air-fuel ratio (*AFR*) to stoichiometric mixture ratio is denoted by lambda (λ). The relationship between λ and *AFR* is

$$\lambda = \frac{AFR}{(AFR)_{st}}. \tag{2–18}$$

The equivalence ratio and lambda are relates as

$$\phi = \frac{1}{\lambda}. \tag{2–19}$$

Dealing with *FOR* or *AFR* is not always convenient especially for computer simulations as they have a value of infinity at either the pure air (oxidiser) or pure fuel side (computers get extremely upset when they try to tackle calculations with infinity), or they do not map the complete mixture spectrum (Wikipedia). Thus, for simulations in many cases a property is needed which is bounded. The mixture fraction, ξ, is usually taken as unity in the fuel stream and is nil in the oxidizer stream. It varies linearly between this two bounds such that at any point of a frozen flow the fuel mass fraction is $Y_F = \xi Y_{F0}$ and the oxidizer mass fraction is $Y_O = (1-\xi) Y_{O0}$, where Y_{F0} and Y_{O0} are the fuel and oxidizer mass fractions in the fuel and oxidizer streams, respectively.

All of the atoms present at the unburned mixture are present in the combustion products although they may be reorganized into different molecules. The mixture fraction that is independent of element *i* can be defined as

$$\xi = \frac{Z_i - Z_{i,O0}}{Z_{i,F0} - Z_{i,O0}}, \tag{2–20}$$

with an element mass fraction Z_i, i.e. the ratio of the mass of element *i* to the total mass, equal to

$$Z_i = \sum_{j=1}^{S} \mu_j w_j \text{ , } i=1...E \text{ ,} \tag{2–21}$$

where μ_{ij} is the mass fraction of the element i in the species j, w_j is the species mass fraction in the mixture, S is the number of different species, and E is the number of different elements in the mixture. It can be shown that the stoichiometric mixture fraction, that is where diffusion flame front is located, is equal to

$$\xi_s = \frac{1}{1+\phi} = \frac{\lambda}{1+\lambda}. \quad (2\text{–}22)$$

2.2.2. Heat of combustion

The lower heating value (heat of combustion) of hydrogen is 241.7 kJ/mol and the higher heating value is 286.1 kJ/mol (BRHS, 2009). The difference of about 16% is due to the heat of condensation of water vapour, and this value is larger compared to other gases.

2.2.3. Flammability limits

The flammability range of hydrogen is wider compared to most hydrocarbons, i.e. 4% to 75% by volume in air at NTP. The flammability range of hydrogen expands with temperature, e.g. the lower flammability limit drops from 4% at NTP to 3% at 100°C (for an upward propagating flame), and depends on pressure (see below). In addition to this, the flammability limits of hydrogen depend on a direction of flame propagation. Ranges of the flammability limits for different direction of flame propagation referenced in (Coward and Jones, 1952) are presented in Table 2–1. For example, in an initially quiescent mixture a conservative value of LFL changes from 3.9% by volume for upward propagation, through 6% for horizontally propagating flames, to 8.5% for downward propagating flames.

Upward propagation		**Horizontal propagation**		**Downward propagation**	
LFL	UFL	LFL	UFL	LFL	UFL
3.9–5.1%	67.9–75%	6.0–7.15%	65.7–71.4%	8.5–9.45%	68–74.5%

Table 2–1. Flammability limits of hydrogen-air for upward, horizontal, and downward (spherical) propagation in hydrogen concentration by volume (Coward and Jones, 1952).

The flammability limits depend on the apparatus applied to determine them. For example, the highest value of LFL (5.1% by volume) and the lowest value of UFL (67.9%) for upward propagating flame were observed in the narrowest throughout the entire spectrum of tube used of only 8 mm.

Coward and Jones (1952) describe an initial stage of flame propagation after ignition of 4% by volume hydrogen-air mixture as follows: a vortex ring of flame was seen just above the spark gap; it rose, expanded for about 40 cm, then broke and disappeared. Upward flame propagation at concentrations close to LFL of 4% is in a form of a collection of small balls of flame, which travel steadily to the top of the vessel. For hydrogen concentrations in the range 4.4–5.6%: similarly a vortex ring rose about 40 cm, then broke into segments each subdivided into balls of flame that travel to the top.

There is unburnt mixture in between of these small ball flames. An increasing fraction of the hydrogen present was burned as the amount of it was increased. The mixture with 5.6% of hydrogen showed about 50% combustion. This observation explains why burning of a quiescent hydrogen-air mixture near LFL of 4% by volume in a closed vessel can generate negligible in a practical sense overpressure. It is worth noting that a quiescent hydrogen-air mixture in the range of concentration 4–6% could burn practically without overpressure for a number of scenarios, e.g. if ignited at the top of an enclosure, as in such conditions it cannot propagate flame in any direction and thus no heat is released accompanied by pressure build up can be observed.

Table 2–2 shows the scattering of the flammability limits (measured in % by volume) determined by different standard apparatuses and procedures applied (Schröder and Holtappels, 2005).

Limit	DIN 51649	EN 1839 (T)	EN 1839 (B)	ASTM E 681
LFL	3.8%	3.6%	4.2%	3.75%
UFL	75.8%	76.6%	77.0%	75.1%

Table 2–2. The flammability limits of hydrogen-air mixture at NTP determined by different standards (Schröder and Holtappels, 2005).

The flammability range expands with increase of temperature. The lower flammability limit for upward flame propagation (% by volume) as a function of temperature (K) at ambient pressure can be calculated by the modified Burgess-Wheeler equation (Zabetakis, 1967; Verfondern, 2008)

$$LFL(T) = LFL(300\,K) + \frac{3.14}{\Delta H_C}(T - 300) = 4.0 + 0.013 \cdot (T - 300), \quad (2\text{–}23)$$

where ΔH_C is the lower heat of combustion, 241.7 kJ/mol. For hydrogen at the boiling point LFL is 7.7% by volume (Verfondern, 2008). The upper flammability limit dependence on mixture temperature in the range of temperature 150-300 K can be represented by the following equation (Eichert, 1992)

$$UFL(T) = 74.0 + 0.026 \cdot (T - 300). \quad (2\text{–}24)$$

Figure 2–3 shows dependence of LFL and UFL on mixture temperature for upward flame propagation (Schröder and Holtappels, 2005) and downward flame propagation (Coward and Jones, 1952). The flammability range expands practically linearly with temperature. While LFL decreases by about 2.5% by volume (from 4% to 1.5% by volume) with increase of temperature from 20°C to 400°C, UFL increases more significantly – by about 12.5% by volume for the same change of mixture temperature.

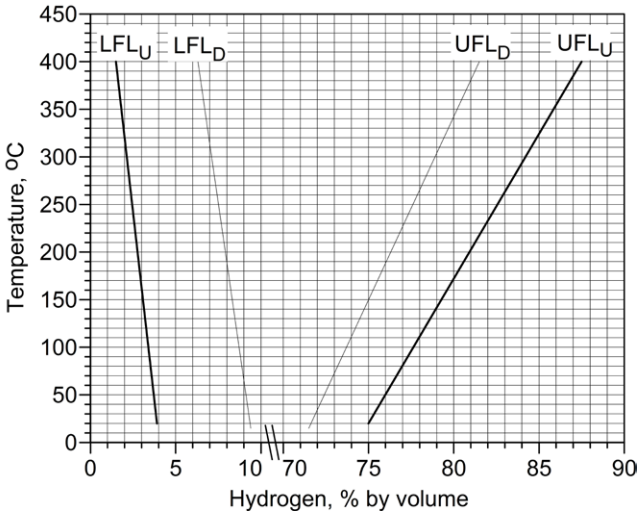

Figure 2–3. LFL and UFL of hydrogen-air mixture as a function of temperature: thick lines – upward flame propagation (Schröder and Holtappels, 2005); thin lines – downward flame propagation (Coward and Jones, 1952).

Dependences of LFL and UFL for upward flame propagation on pressure are shown in Fig. 2–4 (Schröder and Holtappels, 2005). LFL monotonically decreases in the range 0.1–5.0 MPa to 5.6% by volume and then is constant up to pressure of 15 MPa. UFL changes not monotonically: decreases from 76.6% to 71% with pressure growth from 0.1 to 2.0 MPa, then increases from 71% to 73.8% with pressure increase from 2.0 to 5.0 MPa, and again decreases insignificantly from 73.8% to 72.8% with pressure raise from 5.0 to 15.0 MPa.

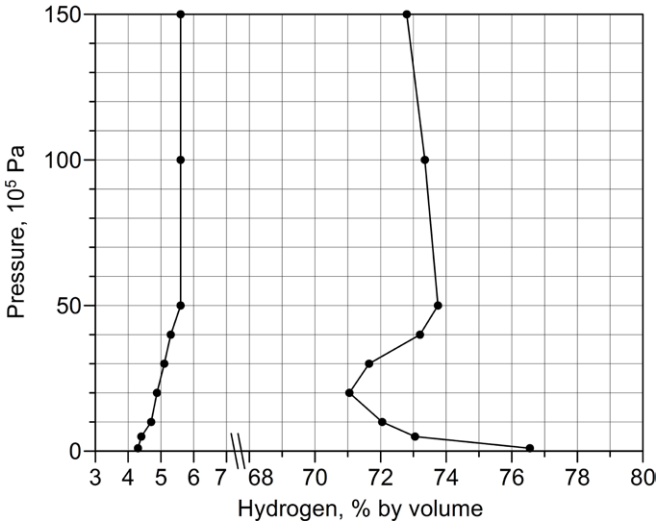

Figure 2–4. LFL and UFL of hydrogen-air mixture as a function of pressure (Schröder and Holtappels, 2005).

2.2.4. Limiting oxygen index

The limiting oxygen index is the minimum concentration of oxygen that will support flame propagation in a mixture of fuel, air, and nitrogen. No mixture of hydrogen, air, and nitrogen at NTP conditions will propagate flame if the mixture contains less than 5% by volume oxygen (NASA, 1997).

2.2.5. Ignition properties

Experience shows that escaped hydrogen is very easily ignited (NASA, 1997). Ignition sources include mechanical sparks from rapidly closing valves, electrostatic discharges in ungrounded particulate filters, sparks from electrical equipment, catalyst particles, heating equipment, lightning strikes near the vent stack, etc. Ignition sources must be eliminated or isolated in appropriate way and operations should be conducted as if unforeseen ignition sources could occur.

The ignition energy of hydrogen-air mixture varies with its composition, and becomes infinite at the flammability limits. Less energy is needed to ignite a mixture that is closer to its stoichiometric composition. Over the flammable range of hydrogen-air mixtures, the ignition energy varies by almost three orders of magnitude. The minimum ignition energy (MIE) is 0.017 mJ for the most ignitable mixture (Baratov et al., 1990). The ignition energy depends in addition to the mixture composition on other factors such as the initial pressure and temperature. Since most ignition sources generate more than 10 mJ, practically all common fuels would be ignited in mixture with air if their concentration exceeds the lower flammability limit. Ignition sources capable of forming shocks, for example high-energy spark discharges and high explosives, can directly initiate detonation.

The energy stored as static electricity on an object varies depending on the size of the object and its capacitance, the voltage to which it is charged, and the dielectric constant of the surrounding medium (Wikipedia). For modelling the effect of static discharge, a human being is represented as a capacitor of 100 picofarads, charged to a voltage of 4,000 to 35,000 volts. The total energy is of the order of millijoules. Larger objects will store more energy. This energy is typically discharged in less than a microsecond and sufficient to ignite not only near stoichiometric mixtures yet mixtures close to the flammability limits. Insulation materials such as wood, paper, and some fabrics will typically form a conductive layer that can prevent static build-up by absorbing water from the air in environments where the relative humidity is greater than 50% (ISO/TR 15916:2004).

Hydrogen is essentially an electrical insulator in both gaseous and liquid phases. The flow or agitation of hydrogen gas or liquid may generate charges of static electricity similar to all non-conductive liquids or gases (for this reason, all hydrogen conveying equipment must be thoroughly grounded). Only above some critical "breakdown" voltage, where ionization occurs, does it become an electrical conductor (BRHS, 2009). When high velocity hydrogen flow accompanies high-pressure vessel blowdown this property can potentially be responsible for the generation of static electrical charge of present in piping particulates by triboelectricity, which is a type of contact electrification in which certain materials become electrically charged after they come into contact with another different material and are then separated (Wikipedia). The probability of hydrogen ignition by this mechanism increases with increase of the blowdown time (time to empty a storage tank) with the same other conditions.

The standard auto-ignition temperature of hydrogen in air is above 510°C (Baratov et al., 1990). It is relatively high compared to hydrocarbons having long molecules. However, it can be lowered by catalytic surfaces. Objects at temperatures from 500 to 580°C can ignite hydrogen-air or hydrogen-oxygen mixtures at atmospheric pressure. Substantially cooler objects of about 320°C can cause ignition under prolonged contact at less than atmospheric pressure (NASA, 1997). Hot air jet ignition temperature is 670°C (BRHS, 2009).

2.2.6. Laminar burning velocity and flame propagation speed

The laminar burning velocity S_u (stretched value, i.e. accounting for both spherical flame curvature and strain) of a stoichiometric hydrogen-air mixture can be calculated as an experimental propagation velocity S_v of spherical flame, e.g. observed by schlieren photography – a method to register the flow of fluids of varying density (see for instance Wikipedia), divided by the expansion coefficient of combustion products E_i

$$S_u = S_v / E_i, \tag{2–25}$$

where E_i is the expansion coefficient (ratio) equal to the ratio of the unburned mixture density to the density of combustion products at the same pressure.

The dependence of expansion coefficient E_i on hydrogen concentration in air is shown in Fig. 2–5 for the entire flammability range. The expansion coefficient E_i was calculated in the HySAFER Centre by using the software Cantera (GRI mechanism) for a composition of air 79% by volume of N_2 and 21% of O_2, and the combustion products comprising the following species: H_2, H, O, O_2, OH, H_2O, HO_2, H_2O_2, N, NH, NH_2, NH_3, NNH, NO, NO_2, N_2O, HNO and N_2.

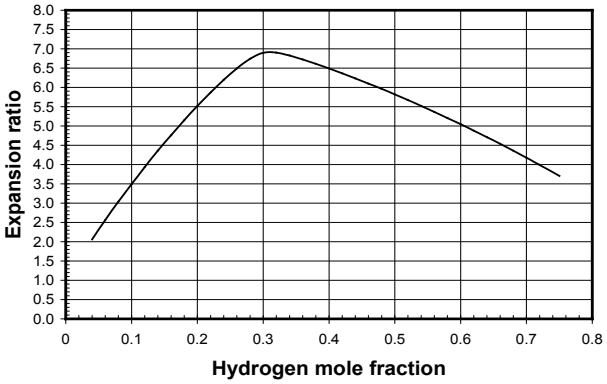

Figure 2–5. Expansion coefficient of combustion products E_i as a function of hydrogen mole fraction in air.

Values of stretched, i.e. actual strained and curved spherical flame, laminar burning velocities are accepted in the HySAFER Centre numerical studies following the experimental study by Lamoureux et al. (2003). It is worth noting that the maximum burning velocity for a hydrogen-air mixture is reached not at a near stoichiometric mixture of 29.5% (by volume) hydrogen but in a mixture with hydrogen concentration in air 40.1% (BRHS, 2009). It increases from about 2 m/s for 29.5% hydrogen-air mixture to about 2.45 m/s for 40.1% hydrogen-air mixture. This effect of shifting of the maximum laminar burning velocity is due to the high molecular diffusivity of hydrogen in air. Thus, the maximum burning velocity for a hydrogen-air premixed flame occurs at an equivalence ratio of 1.6 while for hydrocarbon-air flames it occurs at around 1.1.

The laminar burning velocity as a function of hydrogen concentration in air is presented in Fig. 2–6 for studies by Zimont and Lipatnikov (1995), based on experiments by Karpov and Severin, Tse et al. (2000), Lamoureux et al. (2003). Data by Lamoureux et al. (2003) for stretched flames were used to get values of the laminar burning velocity presented on the graph (application of stretched values in HySAFER simulations explains why these data a below of that by other researchers). Zero burning rates at flammability limits shown in Fig. 2–6 is an approximation. The near-limit "burning velocity" (quotes are used to indicate that flame propagation at the limit is not in the form of continuous flame rather as separate flame balls) for 5% by volume hydrogen-air flame measured in zero-gravity conditions can be estimated as 2.5–3.5 cm/s (Ronney, 1990).

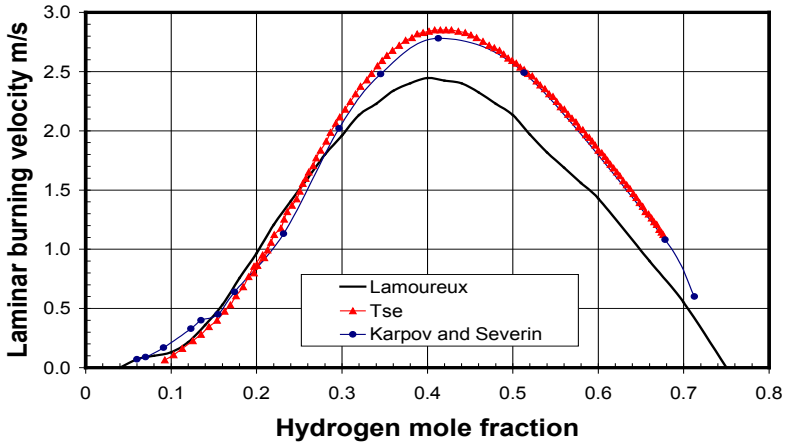

Figure 2–6. Laminar burning velocity of hydrogen-air mixture as a function of hydrogen mole fraction in air.

The maximum possible flame propagation speed, i.e. deflagration front velocity relative to a fixed observer, is given by the speed of sound in the combustion products, which is 975 m/s for a stoichiometric hydrogen-air mixture (BRHS, 2009).

2.2.7. Quenching

Hydrogen flames are difficult to quench. For example, premixed hydrogen-air combustion can be aggravated by heavy sprays of water due to induced turbulence and ability of mixture to burn around the droplets. Hydrogen has the lowest quenching distance compared to other flammable gases. Quenching of any flame occurs when heat losses from flame are comparable with heat generation due to combustion, and then the chemical reactions cannot be sustained. Published data are quire scattered and terminology used can complicate the problem further.

Usually quenching distance is reported as the minimum pipe diameter through which a premixed flame can pass. For example, Kanury (1975) measured the quenching distance as 0.51 mm. Technical report of ISO (ISO/TR 15916:2004) states that the quenching gap in air (NTP) for hydrogen is 0.64 mm.

Hydrogen has the narrowest maximum experimental safe gap (MESG) of 0.08 mm (BRHS, 2009) to prevent premixed flame propagation out of a shell, composed of two hemispherical parts, through the gap between flanges of these hemispheres. It is worth noting that pressure within the shell during the test approaches the maximum explosion (deflagration) pressure in closed vessel. Because of difference in the experimental set up (high deflagration pressures between hemispheres in MESG testing), the MESG is always smaller than the quenching gap. The lowest reported quenching distance for hydrogen is 0.076 mm (Wionsky, 1972).

The quenching distance decreases with increase of pressure and temperature, depends of mixture composition, etc. This is probably the main reason of the published data scattering. Hydrogen-air mixture with higher burning rate generally has smaller quenching gap, and flame arresters for faster burning gases require smaller apertures. To author's knowledge there are flame arresters only for hydrogen-air not for hydrogen-oxygen mixtures at the moment.

There is another limit for "quenching" of hydrogen flames. This is the blow-off limit which occurs when the flow rate is reached beyond which the flame blows off the nozzle.

2.2.8. Detonability limits

Detonation is the worst case scenario for hydrogen accident (Zbikowski et al., 2008). The detonation wave is a complex of precursor shock and combustion wave propagates with a speed of von Neumann spike. Detonation front thickness is a distance from the precursor shock to the end of reaction zone where the Chapman-Jouguet condition (sonic plane) condition is reached.

The detonability range mentioned in technical report ISO/TR 15916:2004 is 18–59% by volume of hydrogen in air. The detonation range of 13–70% is reported for hydrogen-air in a 43 cm diameter tube (Tieszen et al., 1986). A lower detonability limit of 12.5% by volume was observed in the Russian detonation test facility RUT, the largest of its kind. The widest detonability range of hydrogen in air 11–59% by volume is recommended by Alcock et al. (2001).

A conservative generalisation of available data gives the detonability range of hydrogen in air 11–70% by volume. This is narrower and as expected within the flammability range of 4–75%. The detonability limits are not fundamental characteristics of the mixture as they strongly depend on the size of the experimental set up where they are measured. Indeed, a diameter of the tube, where detonation can propagate, should be of the order of a detonation cell size. A detonation cell size increases with approaching the detonability limits. Thus, the larger is the scale of an experimental apparatus the smaller is the lower detonability limit (the larger is the upper detonability limit). The detonability limits of hydrogen-air mixture of the same concentration expand with the scale of a flammable cloud. This explains the difference between the lower detonability limit of hydrogen 11% by volume reported by Alcock et al. (2001) and the underestimated value of 18% suggested by the international standard (ISO/TR 15916:2004). Experimental values of detonation cell size for a stoichiometric hydrogen-air mixture are 1.1–2.1 cm (Gavrikov et al., 2000).

2.2.9. Run-up distance for deflagration-to-detonation transition (DDT)

The experimentally observed run-up distance for transition from deflagration to detonation (DDT) in stoichiometric hydrogen-air mixture in a tube has typical length to diameter ratio of approximately 100. The DDT phenomenon is still one of the challenging subjects for combustion research. Different mechanism are responsible for a flame front acceleration to a velocity close to the speed of sound in an unburned mixture, including but not limited to increase of laminar burning velocity with pressure in conditions of adiabatic compression, increase of burning rate due to preferential diffusion phenomenon, turbulence in an unburned mixture, turbulence generated by flame front itself, fractal type of flame front area growth with flame radius and decrease of inner cut-off, and various instabilities such as hydrodynamic, Rayleigh-Taylor, Richtmyer-Meshkov, Kelvin-Helmholtz, etc. Then, there is a jump from the maximum deflagrative flame propagation velocity, which is about the speed of sound in combustion products for near stoichiometric hydrogen-air mixture, to the detonation velocity that is about twice of the maximum deflagration velocity.

The presence of obstacles in a tube can essentially reduce run-up distance for DDT. This is thought to be due to significant contribution of the Richtmyer-Meshkov instability just before the DDT. Indeed, the Richtmyer-Meshkov instability increases a flame front area in both directions of a shock passage through the flame front. This is opposite to the Rayleigh-Taylor instability, where only one direction is unstable to the pressure gradient (acceleration of flow in the direction from lighter combustion products to heavier unburned mixture). The DDT is thought to happen in a so-called hot spot(s), which potentially could be located within the turbulent flame brush or ahead of it, e.g. in a focus of a strong shock reflection. The peculiarities of DDT mechanisms do not affect the steady-state detonation wave following DDT.

Safety measures to exclude the potential DDT are very important. Indeed, while the deflagration of quiescent stoichiometric hydrogen-air cloud in the open atmosphere generates pressure wave of only 0.01 MPa (below a level of eardrum injury), the detonation of the same mixture would be accompanied by a blast of more than two orders of magnitude higher pressure of about 1.5 MPa (far above the fatal pressure of about 0.08–0.10 MPa).

2.3. Comparison with other fuels

Hydrogen is an unusual fuel. Indeed, hydrogen leaks support combustion at flow rates much lower than leaks of other fuels (Butler et al., 2009), and hydrogen flames cause much faster corrosion than methane flames when the flames impinge on samples of aluminium, stainless steel, and silicon carbide fibres (Sunderland, 2010). Hydrogen flames are the dimmest of any fuel, and its mass flow rate blow-off limits are higher than similar limits for methane and propane. Volumetric flow rate of hydrogen through the same leak path at the same supply pressure were found to be significantly higher than for methane and propane (Swain and Swain, 1992). Hydrogen has smallest molecular mass, lowest density, and lowest viscosity. The thermal conductivity of hydrogen is significantly higher than that of other gases. The diffusion coefficient in air is highest among all gases.

2.3.1. Physical parameters

Parameters of hydrogen in comparison with other fuels, as well as with water and air are summarised in Tables 2–3 and 2–4.

Substance	MM, g/mol	Density, kg/m3	Viscosity, μPoise	Diffusivity in air*, cm^2/s	Thermal conductivity, mW/(m.K)
Hydrogen (H2)	2.016	70.78 (L, NBP) 1.312 (G, NBP) 0.0838 (G, NTP)	132.0 (L, NBP) 89.48 (G, NTP) 11.28 (G, NBP)	0.68	168.35 (G)
Methane (CH4)	16.043	422.62 (L, NBP) 1.819 (G, NBP) 0.668 (G, NTP)	200 (G, NTP) 102.7 (G, STP)	0.196	32.81 (STP)
Propane (C3H8)	44.096	582 (L, NBP) 2.423 (G, NBP) 1.882 (G, NTP)	1,100 (300 K)	0.0977	15.198 (STP)
Gasoline (C4-C12)	100–105	677–798*	~6,000** (L, NTP)	-	~130**
Diesel (C8-C25)	~200	788–920*	~25,000** (L, NTP)	-	-
Methanol (CH3OH)	32.04	786.9 (L, 25°C)*	5,900 (L, NTP)	0.162	250
Water (H2O)	18.016	1000 (NTP)	10,000 (L, NTP) 130 (G, NTP)	-	670
Air	28.9**	1.205 (NTP)	180 (G, NTP)		26

Note: MM – molecular mass; TC – thermal conductivity; L – liquid; G – gas or vapour; * – Baratov et al. (1990); ** – approximated.

Table 2–3. Properties of hydrogen compared to other substances (Part 1).

The dynamic viscosity of hydrogen, methane, and propane measured in [g/m/s] is $8.76x10^{-3}$, $1.09x10^{-2}$, and $7.95x10^{-3}$ respectively (Weast and Astle, 1979; Butler et al., 2009).

Substance	NBP, °C	Critical point	Critical density, kg/m^3	HV (SBP), kJ/kg	γ	SW, v/v
Hydrogen (H2)	-252.8	-240°C 1.3 MPa	31.263	451.9	1.384 (25°C)	0.0214 (Poor)
Methane (CH4)	-161.58	-82.7°C 4.596 MPa	162	760	1.305 (25°C)	0.054 (2°C)
Propane (C3H8)	-42.06	96.6°C 4.25 MPa	217	356	1.134 (25°C)	0.039 (NTP)
Gasoline (C4-C12*)	37-204	-	-	~349 (15.6°C)	-	Poor
Diesel (C12H23*)	180-340	-	-	~233 (15.6°C)	-	Poor
Methanol (CH3OH)	64.9	239.45°C 8.09 MPa	272	1004	1.2	Infinitely
Water (H2O)	100	373.946°C 22.064 MPa	322	2257 (NBP)	1.33 (steam)	-
Air	- (183–196)	-140.8°C 3.77 MPa	-	-	1.4	-

Note: NBP – boiling temperature (point) at normal pressure of 101,325 Pa; HV – latent heat of vaporisation; SBP – standard boiling point (at 0.1 MPa); SW – solubility in water; γ – specific heats ratio.

Table 2–4. Properties of hydrogen compared to other substances (Part 2).

Only helium has lower than hydrogen NBP. Hydrogen is slightly more soluble in organic solvents than in water.

2.3.2. Heating values

The higher and lower heating values of different fuels per gram of fuel are indicated in Table 2–5 (College of the Desert, 2001). Although the term heating value does not apply to batteries, the energy density of a lead acid battery is significantly lower – approximately 0.108 kJ/g. The water that results from both combustion of hydrogen in air and the electrochemical reaction within a fuel cell occurs as steam, therefore the lower heating value represents the amount of energy available to do external work. Hydrogen has the highest heating value per unit of mass and lowest per unit volume. To provide competitive driving range hydrogen has to be stored as gas under pressure or liquid. This has obvious safety implications.

Fuel	Higher Heating Value (25 °C, 0.101 MPa)	Lower Heating Value (25 °C, 0.101 MPa)	Lower Heating Value (volumetric) (15 °C)
Hydrogen	141.86 kJ/g	119.93 kJ/g	10,050 kJ/m3 (gas, 0.101 MPa) 1,825,000 kJ/m3 (gas, 20.2 MPa) 4,500,000 kJ/m3 (gas, 69.7 MPa) 8,491,000 kJ/m3 (liquid)
Methane	55.53 kJ/g	50.02 kJ/g	32,560 kJ/m3 (gas, 0.101 MPa) 6,860,300 kJ/m3 (gas, 20.2 MPa) 20,920,400 kJ/m3 (liquid)
Propane	50.36 kJ/g	45.6 kJ/g	86,670 kJ/m3 (gas, 0.101 MPa) 23,488,800 kJ/m3 (liquid)
Gasoline	47.5 kJ/g	44.5 kJ/g	31,150,000 kJ/m3 (liquid)
Diesel	44.8 kJ/g	42.5 kJ/g	31,435,800 kJ/m3 minimum (liquid)
Methanol	19.96 kJ/g	18.05 kJ/g	15,800,100 kJ/m3 (liquid)

Table 2–5. Heating values of different fuels (College of the Desert, 2001).

2.3.3. Fire and explosion indices

Comparison of key fire and explosion indices for hydrogen and other fuels is presented in Table 2–6 based on the selection of conservative values from Baratov et al. (1990), College of the Desert (2001).

Fuel	Flashpoint, °C	AIT, °C	Flammability range, % vol.	P_{max}*, kPa	MIE*, mJ	MESG, mm
Hydrogen	< -253	510*	4-75	730	0.017	0.08
Methane	-188	537*	5.28*-15	706	0.28	-
Propane	-96*	470*	2.2-9.6	843	0.25	0.92*
Gasoline	-(11-45)*	230-480	0.79-8.1*	-	0.23-0.46	0.96-1.02
Diesel	37-110*	210-370*	0.6-6.5	-	-	-
Methanol	6*	385	6-36.5	620	0.14	-

Note: AIT – auto-ignition temperature; * - Baratov et al. (1990); P_{max} – maximum pressure of deflagration in closed vessel; MIE – mimimum ignition energy; MESG – maximum experimental safe gap.

Table 2–6. Fire and explosion indices of different fuels.

The lower flammability limit of hydrogen is high compared to most hydrocarbons. The near-stoichiometric concentration of hydrogen is air (29.5% by volume) is very much higher than that of hydrocarbons (only a few percent). At the lower flammability limit the ignition energy requirement of hydrogen is similar to that of methane, and weak ignition sources such as electrical equipment sparks, electrostatic sparks or sparks from striking objects typically involve more energy than is required to ignite these flammable mixtures (Dryer et al., 2007).

This laminar burning velocity of stoichiometric hydrogen-air mixture of about 2 m/s is far greater compared to most of hydrocarbons when velocities are in the range 0.30–0.45 m/s. Hydrogen is more prone to deflagration-to-detonation transition (DDT) compared to most other flammable gases.

Compared to other fuels hydrogen is the most prone to spontaneous ignition during sudden releases to air by the so-called diffusion mechanism, when high temperature air, heated by a shock, mixes with cold hydrogen at the contact surface between these two gases and chemical reactions can be initiated, when critical conditions are reached. Indeed, sudden hydrogen releases into piping filled with air, after a safety burst disk ruptures, can be spontaneously ignited at pressures as low as about 2 MPa (Dryer et al., 2007).

On the other hand, the standard auto-ignition temperature of hydrogen in air is above 520°C which is higher than for hydrocarbons. Another swing - the hot air jet ignition temperature is lowest for hydrogen compared to all hydrocarbons decreasing further with increasing jet diameter.

The performance of octane (hydrocarbon) is used as a standard to measure resistance to knock in internal combustion engines, and is assigned a relative octane rating of 100. Fuels with an octane number over 100 have more resistance to auto-ignition than octane itself. Hydrogen has a very high research octane number and is therefore resistant to knock (combustion under lean conditions), i.e. 130+ (lean combustion) compared to other fuels: methane (125), propane (105), gasoline (87), diesel (30). The octane number has no relevance for use of hydrogen with fuel cells.

The quenching distance (the minimum pipe diameter through which a premixed flame can propagate) for hydrogen, methane, and propane are 0.51 mm, 2.3 mm, and 1.78 mm respectively (Kanury, 1975). Thus, hydrogen has the lowest quenching distance.

2.3.4. Extinction of diffusion flames

Hydrogen fires normally are not extinguished until the supply of hydrogen has been shut off because of the danger of re-ignition and "explosion".

Creitz (1961) published results on extinction of diffusion flames on a burner placed in a Pyrex jacket for six fuels. The difference in extinguishing effectiveness of an inhibitor introduced on the two sides of the reaction zone of diffusion flames has been measured as a function of oxygen concentration in the O_2-N_2 mixture supplied to the flames. Comparison of extinguishment characteristics of nitrogen (N_2), methyl bromide (CH_3Br), trifluoromethyl bromide (CF_3Br) for various fuels burning in air is shown in Table 2–7 in percentage by volume.

Fuel	Percentage of inhibitor in air or fuel at extinction						Efficiency relative to nitrogen			
	When added to air			When added to fuel			Added to air		Added to fuel	
	N_2	CH_3Br	CF_3Br	N_2	CH_3Br	CF_3Br	CH_3Br	CF_3Br	CH_3Br	CF_3Br
H2	94.1	11.7	17.7	52.4	58.1	52.6	8.0	5.3	0.9	1.0
CH4	83.1	2.5	1.5	51.0	28.1	22.9	33.2	55.4	1.8	2.2
C2H6	85.6	4.0	3.0	57.3	36.6	35.1	21.4	28.5	1.6	1.6
C3H8	83.7	3.1	2.7	58.3	34.0	37.6	27.0	31.0	1.7	1.6
C4H10	83.7	2.8	2.4	56.8	40.0	37.9	29.9	34.9	1.4	1.5
CO	90.0	7.2	0.8	42.8	19.9	-	12.5	112	2.2	-

Table 2–7. Comparison of extinguishment characteristics of nitrogen, N_2, methyl bromide, CH_3Br, and trifluoromethyl bromide, CF_3Br (Creitz, 1961).

It was found that when the inhibitor was added to the fuel, the volume percentage required for extinguishment was much greater than when added to the oxygen side of the reaction zone, with the single exception of CO flames inhibited by trifluoromethyl bromide. Author assumes that this result of Craitz (1961) can be explained by the entrainment law stating that a mass flow rate of entrained into plume surrounding gas grows with distance from the source of fuel and with momentum flux of the plume. It is well known from fire safety science that the amount of air entrained into fire at flame height is about two orders of magnitude greater than amount of released fuel.

Above oxygen concentrations on the order of 25% by volume, methyl bromide was completely ineffective when added to the oxygen side of the reaction zone, and above about 32% oxygen it was ineffective when added to the fuel, since at this oxygen concentration it burns without additional fuel.

Extinction of a diffusion flame may be affected by a number of factors, among them being the rate at which the fuel is supplied to the burner and the velocity of the secondary air past the flame (Craitz, 1961). The latter effect was found to be important at rather low or very high flow rates. When the rate of fuel supply was too low, for a given burner size, the flame would not burn, and conversely, when the rate was too high, lifting occurred and the flame tended to float off and be extinguished . In author's opinion the latter observation of Craitz (1961) could be due to shielding effect of Pyrex jacket that limits oxidiser entrainment to the flame. This particular test condition limits the importance of conclusions of such experiments.

In test by Craitz (1961) conditions the extinction of hydrogen is the most difficult among fuels tested and requires more inhibitor. Methyl bromide is more efficient to extinguish hydrogen diffusion flame in air compared to trifluoromethyl bromide. Work of Craitz (1961) can be considered as a comparative study of extinction efficiency of selected inhibitors for different fuels rather than quantitative recommendation on inhibitor concentrations for extinction of real flames, especially non-premixed turbulent flames which are characteristic for hydrogen technologies.

2.4. Health hazards

Hydrogen is not expected to cause mutagenicity, teratogenicity, embryotoxicity or reproductive toxicity. There is no evidence of adverse effects if skin or eyes are exposed to hydrogen, it cannot be ingested (unlikely route). However, inhaled hydrogen can result in a flammable mixture within the body.

Hydrogen is classified as a simple asphyxiant, has no threshold limit value (TLV), and it is not a carcinogen (NASA, 1997). High concentrations of hydrogen in air can cause an oxygen-deficient environment. Individuals breathing such an atmosphere may experience symptoms which include headaches, dizziness, drowsiness, unconsciousness, nausea, vomiting, depression of all the senses, etc. A victim may have a blue colour skin, and under some circumstances, death may occur. If hydrogen is inhaled and above symptoms observed then remove a person to fresh air, give oxygen if breathing is difficult, or apply artificial respiration if not breathing.

The system design shall prevent any possibility of asphyxiation of personnel in adjacent areas (NASA, 1997). The system design shall provide for prevention of personnel entering the enclosure unless confined space entry procedures are strictly followed. It is recommended to check oxygen content before entering an incident/accident area (no odour warning available if dangerous concentrations are present). Hydrogen concentrations have to be measured with a suitable detector.

Oxygen concentration levels below 19.5% by volume are biologically inactive for humans, and no effects of oxygen deficiency are usually observed. At concentrations below 12%, immediate unconsciousness may occur with no prior warning symptoms. Stages of asphyxiation have been noted based on the oxygen concentration (NASA, 1997):

- 15–19% by volume – decreased ability to perform tasks; may induce early symptoms in persons with heart, lung, or circulatory problems;
- 12–15% – deeper respiration, faster pulse, poor coordination;
- 10–12% – giddiness, poor judgment, slightly blue lips;
- 8–10% – nausea, vomiting, unconsciousness, ashen face, fainting, mental failure;
- 6–8% – death in 8 min (50% death and 50% recovery with treatment in 6 min, 100% recovery with treatment in 4 to 5 min);
- 4% – coma in 40 s, convulsions, respiration ceases, death.

Contact with liquid hydrogen or its splashes on the skin or in the eyes can cause serious burns by frostbite or hypothermia. Inhaling vapour or cold hydrogen produces respiratory discomfort and can result in asphyxiation. Direct physical contact with liquid hydrogen, cold vapour, or cold equipment can cause serious tissue damage. Momentary contact with a small amount of the liquid may not pose as great a danger of a burn because a protective film may form (NASA, 1997). Danger of freezing occurs when large amounts are spilled and exposure is extensive. Cardiac malfunctions are likely when the internal body temperature drops to 27°C, and death may result when the internal body temperature drops to 15°C. It is safest in the field to do nothing other than to protect the involved area with a loose cover.

2.5. Concluding remark

It can be concluded that hydrogen is not more dangerous or safer compared to other fuels. Hydrogen is different and has to be professionally handled with knowledge of underpinning science and engineering to provide public safety and competitiveness of hydrogen and fuel cell products and infrastructure.

3 Regulations, codes and standards and hydrogen safety engineering

The quality of hydrogen safety provisions directly depends on availability of an overall performance-based hydrogen safety engineering (HSE) methodology rather than a group of codes and standards, which are often prescriptive in nature and out of date. The HSE methodology must be in compliance with current regulations as well as with standards and codes which are explicitly mentioned in the regulations. Besides regulations, codes and standards (RCS) the HSE needs a highly educated workforce and contemporary engineering tools, including freely available to hydrogen safety engineers Computational Fluid Dynamics (CFD) software.

There is an overestimation to some extent of expectations from the role of RCS in safety design of hydrogen and fuel cell (HFC) systems and infrastructure from the author's point of view. Indeed, standards are at least three years old compares to the current level of knowledge in the field due to the procedure of their development and approval. They can be quite narrowed by a particular topic or include only general statements without concrete information for safety engineering. Standards cannot account for all possible situations to be resolved in real life, especially for new and developing technologies. Safety information in standards relevant to hydrogen and fuel cell systems is "naturally" fragmented throughout a constantly growing number of standards in the area.

Standards are written from the perspective of the industry and reflect mainly the interests of the industry rather than all stakeholders, including public. Some statements of standards are at least questionable if not leading to potentially catastrophic consequences. For example, all three parts of the draft standard ISO 11119 "Gas cylinders of composite construction – Specification and test methods" contain the following criteria for fire resistance test: "The cylinder shall not burst during a period of two minutes from the start of the fire test. It may vent through the pressure relief device or leak through the cylinder wall or other surfaces". There are clear safety concerns for public if such criteria are applied to products on the market. The requirement of "no burst" in two minutes implies fast blowdown of hydrogen from the storage vessel through PRD with comparatively large aperture area. This in turn would create large separation distances due to long jet flame (flame length is proportional to the PRD diameter as will be shown later) and thus prevent first responders from intervention at the accident scene. Besides, in a case of accident initiation in an enclosure like garage the typical structure will be destroyed in seconds by so called pressure peaking effect explained later.

Some standards can include information derived from risk assessment methods. Risk-informed methodology and quantitative risk assessment require statistical data. In the author's opinion they can compliment but not substitute innovative safety engineering design of hydrogen and fuel cell systems. Indeed, emerging technologies can hardly be characterized by availability of statistical data. This, at the moment, makes the use of probabilistic methods in hydrogen safety less valuable. The public is keen to know that everything possible has been done by engineers to make hydrogen-powered systems safe, rather than be satisfied by information that a probability of personal fatality is 10^{-4} or 10^{-6} or 10^{-8}. The same is valid for court proceedings as presented at the 2003 AIChE Loss Prevention Symposium in New Orleans (USA).

There is another implication that risk assessment methods "oversell", i.e. resources are diverted away from a creative engineering, including hydrogen safety engineering, and practical problem solving to everlasting discussions on acceptable risk level of which uncertainty is often unacceptably high and questionable. In spite of knowledge about uncertainties, often only "averaged" value goes to industry to open the market for their products. Unfortunately, the Fukushima disaster (Shepherd, 2011) proved these author's doubts once again and stressed the need in an overarching safety-oriented standard for hydrogen safety engineering, which gives a methodology to carry out HSE, and that systemizes and maintains the knowledge in this field.

A list of *international Regulations*, which are international laws to be complied with, relevant to hydrogen safety is presented in Table 3–1. Currently hydrogen is not yet considered as a fuel but still as one of "dangerous goods" and it will take time to update regulations for the emerging hydrogen and fuel cell systems and infrastructure.

Commission Regulation (EU) No 406/2010 of 26 April 2010 implementing Regulation (EC) No 79/2009 of the European Parliament and of the Council on type-approval of hydrogen-powered motor vehicles: http://eur-lex.europa.eu/JOHtml.do?uri=OJ:L:2010:122:SOM:EN:HTML
IMO International Code for the Construction and Equipment of Ships Carrying Liquefied Gases in Bulk (IGC Code): http://www.imo.org/environment/mainframe.asp?topic_id=995
ADR UN ECE Agreement concerning the International Carriage of Dangerous Goods by Road: http://www.unece.org/trans/danger/publi/adr/adr_e.html
RID is the European Agreement on the International Carriage of Dangerous Goods by Rail. The regulations appear as Appendix C to the Convention concerning International Carriage by Rail (COTIF) concluded at Vilnius on 3 June 1999: http://www.otif.org/en/law.html
ADN is the European Agreement concerning the International Carriage of Dangerous Goods by Inland Waterways concluded at Geneva on 26 May 2000: http://www.unece.org/trans/danger/publi/adn/adn_e.html
The rules related to transport of dangerous goods, regulated in Europe by the international agreements, mentioned in the three items above, that is, the ADR, RID, and ADN, have also been extended to national transport in the EU under the Inland transport of dangerous goods Directive 2008/68/EC: http://europa.eu/legislation_summaries/transport/rail_transport/tr0006_en.htm
The International Maritime Dangerous Goods (IMDG) Code covers the transport of dangerous goods by sea: http://www.imo.org/safety/mainframe.asp?topic_id=158

UN Recommendations on the Transport of Dangerous Goods, Model Regulations. These are updated every two years. Recommendations relevant to hydrogen are UN 1049 (Hydrogen, Compressed), UN 1066 (Hydrogen, refrigerated liquid) and UN 3468 (hydrogen in a metal hydride storage system): http://www.unece.org/trans/danger/publi/unrec/12_e.html
Dangerous Substances Directive: 67/548/EEC: http://ec.europa.eu/environment/chemicals/dansub/home_en.htm http://eur-lex.europa.eu/JOHtml.do?uri=OJ:L:2009:011:SOM:EN:HTML
Low Voltage Directive (LVD) 2006/95/EC: http://ec.europa.eu/enterprise/sectors/electrical/lvd/ http://ec.europa.eu/enterprise/sectors/electrical/files/lvdgen_en.pdf
Electromagnetic Compatibility Directive (EMC) 2004/108/EC: http://ec.europa.eu/enterprise/sectors/electrical/emc/ http://ec.europa.eu/enterprise/sectors/electrical/files/emc_guide__updated_20100208_v3_en.pdf
Pressure Equipment Directive (PED) 97/23/EC: http://ec.europa.eu/enterprise/sectors/pressure-and-gas/documents/ped/index_en.htm http://www.bsigroup.com/en/ProductServices/About-CE-Marking/EU-directives/Pressure-Equipment-Directive-PED/
Simple Pressure Vessels Directive (SPVD) 2009/105/EC : http://ec.europa.eu/enterprise/sectors/pressure-and-gas/documents/spvd/index_en.htm
Transportable Pressure Equipment Directive (TPED) 1999/36/EC: http://ec.europa.eu/transport/tpe/index_en.html
Gas Appliances Directive 2009/142/EC Includes fuel cells (where the primary function is heating): http://ec.europa.eu/enterprise/sectors/pressure-and-gas/gas_appliances/index_en.htm
Equipment and protective systems for potentially explosive atmosphere Directive (ATEX 95) 94/9/EC: http://ec.europa.eu/enterprise/sectors/mechanical/atex/index_en.htm
Directive on minimum requirements for improving the safety and health protection of workers potentially at risk from explosive atmospheres (ATEX 137) 99/92/EC: http://eur-lex.europa.eu/LexUriServ/LexUriServ.do?uri=CELEX:31999L0092:en:NOT
Machinery Directive (MD) 2006/42/EC: http://ec.europa.eu/enterprise/sectors/mechanical/files/machinery/guide_application_directie_2006-42-ec-2nd_edit_6-2010_en.pdf http://ec.europa.eu/enterprise/sectors/mechanical/machinery/
Seveso II Directive: http://ec.europa.eu/environment/seveso/index.htm
The integrated pollution prevention and control Directive (IPPC) 2008/1/EC: http://ec.europa.eu/environment/air/pollutants/stationary/ippc/summary.htm
Measures to encourage improvements in the safety and health of workers 89/391/EEC: http://europa.eu/legislation_summaries/employment_and_social_policy/health_hygiene_safety_at_work/c11113_en.htm
Personal protective equipment Directive 89/686/EEC: http://ec.europa.eu/enterprise/sectors/mechanical/documents/legislation/personalprotectiveequipment/

Note: Japan has a national regulation in force covering fuel cell passenger cars with compressed hydrogen storage. An unofficial English version is available (http://www.unece.org/trans/main/wp29/wp29wgs/wp29grsp/sgs_legislation.html). The International Fire Code (IFC) and the International Building Code (IBC), both produced by the International Code Council (ICC) in the USA, are likely to be used in other countries.

Table 3–1. International regulations relevant to hydrogen safety.

Four technical committees (TC) of the International Organization for Standardization (ISO) produce standards relevant to hydrogen and fuel cell technologies, systems, and infrastructure. Technical Committee 197 "Hydrogen Technologies" published a number of documents including:

- ISO/TR 15916:2004 Basic considerations for the safety of hydrogen systems;
- ISO 14687 Hydrogen fuel - Product specification;
- ISO 16110-1:2007 Hydrogen generators using fuel processing technologies – Part 1: Safety;
- ISO/TS 20100:2008 Gaseous hydrogen - Fuelling stations;
- ISO 17268:2006 Compressed hydrogen surface vehicle refuelling connection devices;
- ISO 22734-1:2008 Hydrogen generators using water electrolysis process – Part 1: Industrial and commercial applications;
- ISO 26142:2010 Hydrogen detection apparatus – Stationary applications.

Technical Committee 22, sub-committee (SC) 21, on electric road vehicles issued standards with safety specifications:

- ISO 23273-2:2006 Fuel cell road vehicles – Safety specifications – Part 2: Protection against hydrogen hazards for vehicles fuelled with compressed hydrogen;
- ISO 23273-3:2006 Fuel cell road vehicles – Safety specifications – Part 3: Protection of persons against electric shock, etc.

Technical Committee 58 on gas cylinders published several parts of standard ISO 11114 Transportable gas cylinders – Compatibility of cylinder and valve materials with gas contents, etc. Technical Committee 220 on cryogenic vessels published a number of standards related to large transportable vacuum-insulated vessels, gas/materials compatibility, and valves for cryogenic service, etc.

The International Electrotechnical Commission (IEC) publishes standards relevant to fuel cell technologies. These include:

- IEC 62282-2 (2007-03) Fuel Cell Modules;
- IEC 62282-3-1 (2007-04) Stationary Fuel Cell Power Systems – Safety;
- IEC 62282-3-200 (2011-10) Stationary Fuel Cell Power Systems – Performance Test Methods;
- IEC 62282-3-3 (2007-11) Stationary Fuel Cell Power Systems – Installation;
- IEC 62282-5-1 (2007-02) Portable Fuel Cell Appliances – Safety;
- IEC 62282-6-100 (2010-03) Micro Fuel Cell Power Systems – Safety.

Working Group #8 / IEC/PAS 62282-6-150 Micro Fuel Cells – Safety – Water reactive (UN Division 4.3) compounds in indirect PEM fuel cells

Working Group #9 / IEC 62282-6-200 (2007-11) Micro Fuel Cell Power Systems – Performance

Working Group #10 / IEC 62282-6-300 (2009-06) Micro Fuel Cell Power Systems – Fuel Cartridge Interchangeability

Working Group #11 / IEC 62282-7-1 Single Cell Test Method for Polymer Electrolyte Fuel Cells

The USA National Fire Protection Association (NFPA) has a number of relevant standards:

- NFPA 2 Hydrogen Technologies Code; NFPA 52 Vehicular Gaseous Fuel Systems Code;
- NFPA 55 Compressed Gases and Cryogenic Fluids Code; NFPA 50A Standard for Gaseous Hydrogen Systems at Consumer Sites;
- NFPA 50B Standard for Liquefied Hydrogen Systems at Consumer Sites;
- NFPA 221 Standard for High Challenge Fire Walls, Fire Walls, and Fire Barrier Walls;
- NFPA 853 Standard for the Installation of Stationary Fuel Cell Power Systems.

The USA Society of Automotive Engineers (SAE) relevant standards include:

- J2578 Recommended Practice for General Fuel Cell Vehicle Safety;
- J2601 Fuelling Protocols for Light Duty Gaseous Hydrogen Surface Vehicles;
- J2719 Information Report on the Development of a Hydrogen Quality Guideline for Fuel Cell Vehicles;
- J2799 70 MPa Compressed Hydrogen Surface Vehicle Fuelling Connection Device and Optional Vehicle to Station Communications, etc.

The European Industrial Gas Association (EIGA) produced the following documents among others:

- IGC Document 122/04 Environmental impacts of hydrogen plants;
- IGC Document 15/06 Gaseous hydrogen stations;
- IGC Document 121/04 Hydrogen transportation pipelines;
- IGC Document 6/02 Safety in storage, handling and distribution of liquid hydrogen;
- IGC Document 23/00 Safety training of employees;
- IGC Document 75/07 Determination of Safety Distances;
- IGC Document 134/05 Potentially explosive atmosphere – EU Directive 1999/92/EC, etc.

The Compressed Gas Association (CGA) documents include:

- G-5.3 Commodity Specification for Hydrogen;
- G-5.4 Standard for Hydrogen Piping Systems at User Locations;
- G-5.5 Hydrogen Vent Systems;
- G-5.8 High Pressure Hydrogen Piping Systems at Consumer Locations;
- C-6.4 Methods for External Visual Inspection of Natural Gas Vehicle (NGV) and Hydrogen Vehicle (HV) Fuel Containers and Their Installations, etc.

The American Society of Mechanical Engineers (ASME) standards include:

- ASME B31.12: Hydrogen piping and pipelines;
- ASME PTC 50: Performance Test Code for Fuel Cell Power Systems Performance;
- ASME BPVC Boiler and Pressure Vessel Code, etc.

The Canadian Standards Association (CSA) published standards: Stationary Fuel Cell Power Requirements:

- ANSI/CSA AMERICA FC 1-2004 – Stationary Fuel Cell Power Systems;
- ANSI/CSA AMERICA FC 3-2004 – Portable Fuel Cell Power Systems;
- CSA America HPRD1, Standards for Basic Requirements for Pressure Relief Devices for Compressed Hydrogen Vehicle Fuel Containers, etc.

The website http://www.fuelcellstandards.com/ tracks the world-wide development of over 300 hydrogen and fuel cell standards, and its matrix can be searched by the following applications or geographic areas: Stationary Fuel Cells, International, Hydrogen & Fuel Cell Vehicles, The Americas, Portable & Micro Fuel Cells, Europe, Hydrogen Infrastructure, Pacific Rim.

There are a number of useful guidelines in the field that are compiled in Table 3–2.

Installation Permitting guidance for small stationary hydrogen and fuel cell systems (HYPER) interactive handbook and PDF document: http://www.hyperproject.eu/
US installation guidelines for refuelling stations and stationary applications: http://www.pnl.gov/fuelcells/permit_guide.stm
HyApproval handbook: European handbook for the approval of hydrogen refuelling stations: http://www.hyapproval.org/
NASA: Safety standard for hydrogen and hydrogen systems: Guidelines for Hydrogen System Design, Materials Selection, Operations, Storage, and Transportation: http://www.hq.nasa.gov/office/codeq/doctree/canceled/871916.pdf (cancelled on 25.07.2005)
NASA/TM—2003–212059 Guide for Hydrogen Hazards Analysis on Components and Systems: http://ston.jsc.nasa.gov/collections/TRS/_techrep/TM-2003-212059.pdf
American Institute of Aeronautics and Astronautics (AIAA) guide to Safety of Hydrogen and Hydrogen Systems (G-095-2004e): http://www.AIAA.org

Table 3–2. Guidelines relevant to hydrogen safety.

4 Hydrogen safety engineering: framework and technical subsystems

4.1. Framework

Hydrogen safety engineering (HSE) is defined as an application of scientific and engineering principles to the protection of life, property and environment from adverse effects of incidents/accidents involving hydrogen (Molkov and Saffers, 2012). Despite the progress in hydrogen safety science and engineering during the last decade, especially through the HySafe partnership (BRHS, 2009), an overarching performance-based methodology to carry out HSE is still formally absent.

HSE comprises a design framework and technical sub-systems. A design framework for HSE, developed at the University of Ulster, is similar to British standard BS7974 for application of fire safety engineering to the design of buildings (BSI, 2001) and is expanded to reflect specific hydrogen safety related phenomena, including but not limited to high pressure under-expanded leaks and dispersion, spontaneous ignition of sudden hydrogen releases to air, high momentum jet fires, deflagrations and detonations, mitigation techniques, e.g. venting of deflagration and natural/forced ventilation, etc.

The HSE process includes three main steps (see Fig. 4–1). *Firstly*, a qualitative design review (QDR) is undertaken by a team that can include owner, hydrogen safety engineer, architect, representative of authorities having jurisdiction, e.g. emergency services, and other stakeholders. The team defines accident scenarios, suggests trial safety designs, and formulates acceptance criteria. *Secondly*, a quantitative safety analysis of selected scenarios and trial designs is carried out by qualified hydrogen safety engineer(s) using the state-of-the-art knowledge in hydrogen safety science and engineering and validated models and tools. *Thirdly*, the performance of a hydrogen and/or fuel cell system under the trial safety designs is assessed against predefined acceptance criteria.

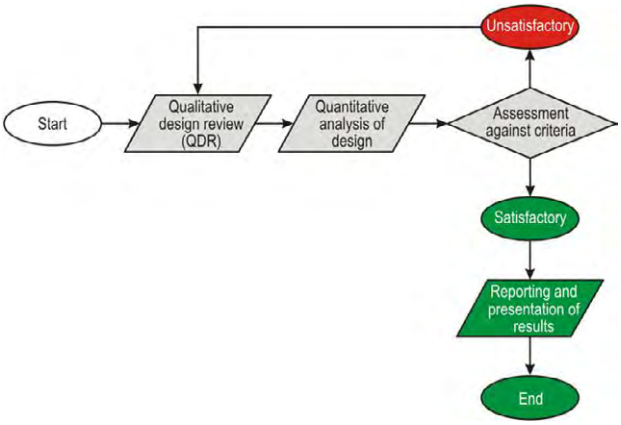

Figure 4–1. Hydrogen safety engineering process (Molkov and Saffers, 2012).

The QDR is a qualitative process based on the team's experience and knowledge. It allows its members to establish a range of *safety strategies*. Ideally, QDR has to be carried out early in the design process and in a systematic way, so that any substantial findings and relevant items can be incorporated into the design of HFC application or infrastructure before the working drawings are developed. In practice however, the QDR process is likely to involve some iterations as the design process moves from a broad concept to greater detail.

Safety objectives should be defined during the QDR. They should be appropriate to the particular aspects of the system design, as HSE may be used either to develop a complete hydrogen safety strategy or to consider only one aspect of the design. *The main hydrogen safety objectives* are safety of life, loss control and environmental protection. The QDR team should establish one or more *trial safety designs* taking into consideration *selected accident scenario(s)*. The different designs could satisfy the same safety objectives and should be compared with each other in terms of cost-effectiveness and practicability. At first glance, it is essential that trial designs should limit hazards by implementing prevention measures and ensuring the reduction of severity and frequency of consequences. Although HSE provides a degree of freedom, it is mandatory to fully respect relevant regulations when defining trial designs.

The QDR team has to establish the *acceptance criteria* against which the performance of a design can be judged. Three main methods can be used: *deterministic, comparative, and probabilistic*. The QDR team can, depending on trial designs, define acceptance criteria following all three methods. The QDR team should provide a set of qualitative outputs to be used in the quantitative analysis: results of the architectural review; hydrogen safety objectives; significant hazards and associated phenomena; specifications of the scenarios for analysis; one or more trial designs; acceptance criteria and suggested methods of analysis. Following QDR the team should decide which trial design(s) is likely to be optimum. The team should then decide whether quantitative analysis is necessary to demonstrate that the design meets the hydrogen safety objective(s).

Following the QDR a *quantitative analysis* may be carried out using Technical Sub-Systems (TSS) where various aspects of the analysis can be quantified by a deterministic study or a probabilistic study. The quantification process is preceded by the QDR procedure for two main reasons: to ensure that the problem is fully understood and that the analysis addresses the relevant aspects of the hydrogen safety system; and to simplify the problem and minimise the calculation effort required. In addition, the QDR team should identify appropriate methods of analysis among: simple engineering calculations; CFD simulations; simple probabilistic study; full probabilistic study, etc. A deterministic study using comparative criteria will generally require fewer data and resources than a probabilistic approach and is likely to be the simplest method of achieving an acceptable design. A full probabilistic study is only likely to be justified when a substantially new approach to hydrogen system design or hydrogen safety practice is being adopted. The analysis may be a combination of some deterministic and some probabilistic elements.

Following the quantitative analysis, the results should be compared with the *acceptance criteria* identified during the QDR exercise. Three basic types of approach can be considered to access the performance of safety system against criteria:

- Deterministic approach shows that on the basis of the initial assumptions a defined set of conditions will not occur;
- Comparative approach shows that the design provides a level of safety equivalent to that in similar systems and/or conforms to prescriptive codes (as an alternative to performance-based HSE);
- Probabilistic approach shows that the risk of a given event occurring is acceptably low, e.g. equal or below the established risk for similar existing systems.

If none of the trial designs developed by the QDR team satisfies the specified acceptance criteria, QDR and quantification process should be repeated until a hydrogen safety strategy satisfies acceptance criteria and other design requirements. Several options can be considered when re-conducting QDR following recommendations (BSI, 2001): development of additional trial designs; adoption of more discriminating design approach, e.g. using deterministic techniques instead of a comparative study; re-evaluation of design objectives, e.g. if the cost of hydrogen safety measures for property loss prevention outweighs the potential benefits. When a satisfactory solution has been identified, the resulting HSE strategy should be fully documented.

Depending on particularities and scope of the HSE study, the reporting of the results and findings could contain the following information (BSI, 2001):

- Objectives of the study;
- Full description of the HFC system/infrastructure;
- Results of the QDR;
- Quantitative analysis (assumptions; engineering judgments; calculation procedures; validation of methodologies; sensitivity analysis);
- Assessment of analysis results against criteria;
- Conclusions (hydrogen safety strategy; management requirements; any limitations on use);
- References (e.g. drawings, design documentation, technical literature, etc.).

4.2. Technical sub-systems

To simplify the evaluation of a HSE design, the quantification process is broken down into several technical sub-systems (TSSs). The following requirements should be accounted for development of individual TSS:

- TSS should together, as reasonably as possible, cover all possible aspects of hydrogen safety engineering;
- TSS should be balanced between their uniqueness or capacity to be used individually, and their complementarities and synergies with other TSSs;
- TSS should be a selection of the state-of-the-art in the particular field of hydrogen safety, validated engineering tools, including empirical and semi-empirical correlations and contemporary tools such as CFD models and codes;
- TSS should be flexible to allow update of existing or use of new appropriate and validated methods, reflecting recent progress in hydrogen safety science and engineering.

The following TSSs are currently suggested and under development for HSE (Molkov and Saffers, 2012):

- TSS1: Initiation of release and dispersion;
- TSS2: Ignitions;
- TSS3: Deflagrations and detonations;
- TSS4: Fires;
- TSS5: Impact on people, structures, and environment;
- TSS6: Mitigation techniques;
- TSS7: Emergency services intervention.

Hydrogen safety engineering is a key to the success of the hydrogen economy. It is the powerful tool for provision of hydrogen safety by qualified specialists in the growing market of HFC systems and infrastructure. Last not least the HSE can secure high level of competitiveness for hydrogen and fuel cell products.

5 Unignited releases

5.1. Expanded and under-expanded jets

Hydrogen-powered vehicles have onboard storage at pressures up to 70 MPa, and refuelling infrastructure operates at pressures up to 100 MPa. Unscheduled release at such pressures creates a highly under-expanded (pressure at the nozzle exit is above atmospheric pressure) turbulent jet that behaves differently from expanded jets (pressure at the nozzle exit is equal to atmospheric pressure) extensively studied previously. The majority of leaks from hydrogen storage and equipment will be in a form of an under-expanded jet at least at the beginning.

In an under-expanded a pressure at the nozzle exit has not fully dropped to the atmospheric. At high pressures a velocity at the exit from the nozzle remains locally sonic, but the exit pressure rises above ambient. As the result the expansion down to ambient conditions takes place outside the nozzle. The critical pressure ratio for sonic (choked) flow of compressible gas is about 1.9 at STP (γ =1.405) and 1.89 at NTP (γ =1.39) according to the theoretical equation for choked flow conditions

$$\frac{P_R}{P_N} = \left(\frac{\gamma+1}{2}\right)^{\gamma/(\gamma-1)}, \tag{5–1}$$

where P_R and P_N are pressure in the reservoir and the nozzle exit respectively, and γ is the ratio of specific heats. This equation can be applied to estimate the pressure at the leak (nozzle) exit by the storage pressure at the reservoir.

Ishii et al. (1999) reported that jets of diatomic gas (γ=7/5) exhausted from the open end of their test tube tend to be subsonic matched jets for ratios of pressures in the high-pressure and the low-pressure chambers (the only parameter controlling the jet strength) between 1 and 4.1, sonic under-expanded jets for pressure ratios in the range from 4.1 to 41.2, and supersonic under-expanded jets for pressure ratios above 41.2. Pressure ratio 4.1 is above the critical ratio 1.9 for sonic (choked) flow. However, there is no contradiction. Indeed, each of two pressure ratios (high-pressure chamber to tube exit, and tube exit to low-pressure chamber) can be p_R/p_N=2.05 that is close to the theoretical critical pressure ratio of 1.9 for sonic flow. The difference could be attributed to losses between high-pressure and low-pressure chambers.

For under-expanded jet the flow expansion occurs near the nozzle exit and is characterised by the complex shock structure, which is well documented and published elsewhere (Dulov and Luk'yanov, 1984). The schematic presentation of an under-expanded shock structure is given in Fig. 5–1 (left) (Dulov and Luk'yanov, 1984), and distribution of the Mach number (dimensionless number equal to ratio of a local flow velocity to the local speed of sound) in a numerically simulated under-expanded jet (initial stage of release) for pressure ratio in a storage tank and the atmosphere 160 is shown in Fig. 5–1 (right).

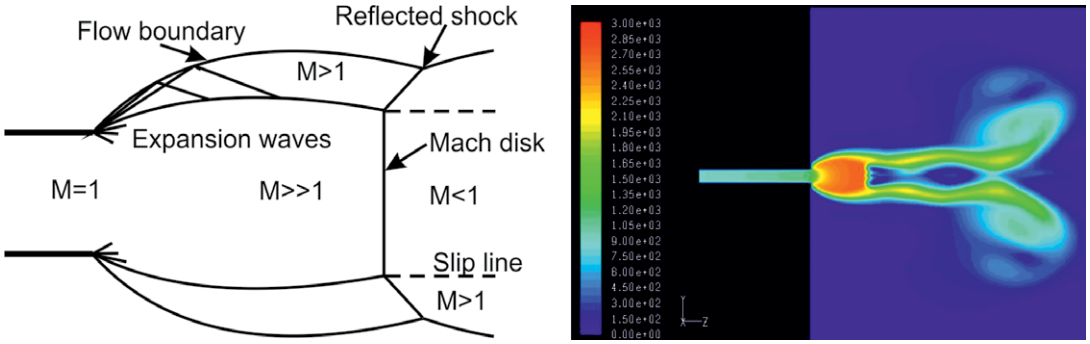

Figure 5–1. The schematic presentation of an under-expanded jet structure (left) (Dulov and Luk'yanov, 1984), and an initial stage of under-expanded jet release at 16.1 MPa through a channel of 0.25 mm (mass flow rate 0.46 g/s).

Figure 5–1 shows that local sonic velocity is established at the nozzle exit with Mach number M=1. Then, out flowing gas undergoes rapid expansion and quickly accelerates to high Mach numbers (up to M=8 for 70 MPa storage pressure) with decrease in pressure and density. A series of expansion waves are formed at the nozzle exit edge. These expansion waves are reflected as compression waves from the free surface at the jet flow boundary, coalesce and form a barrel shock and a Mach disk. As gas with very high Mach number crosses the Mach disk, it undergoes an abrupt decrease in velocity to subsonic speeds and increases in pressure (to the atmospheric) and density. The resulting flow structure after the Mach disk comprises of subsonic core (M<1) surrounded by supersonic shell (M>1) with a turbulent eddy producing shear layer called slip line dividing these two regions.

For high ratios of nozzle exit to atmospheric pressure above 40 the barrel shock culminates with a strong Mach disk without a diamond structure, and below this critical pressure ratio of 40 – with the diamond structure. This estimate of the critical pressure ratio is based on simulations of hydrogen under-expanded jets carried out at the HySAFER Centre. The ratio of a storage pressure in a vessel to a nozzle pressure can be roughly estimated as 2 for cases without losses (short nozzles). This means that no diamond structure can be expected for under-expanded hydrogen jets to the atmosphere at storage pressures below about 8 MPa. This preliminary conclusion yet has to be confirmed by experiments.

Hydrogen under-expanded jet exit shock structure was qualitatively imaged using schlieren photography by Ruggles and Ekoto (2011). Figure 5–2 shows a mean image of the Mach disk structure (left), and a mean image of Mach disk and diamond shock structure (right). Nominal pressure ratio was 10:1 and nozzle diameter was 0.75 mm.

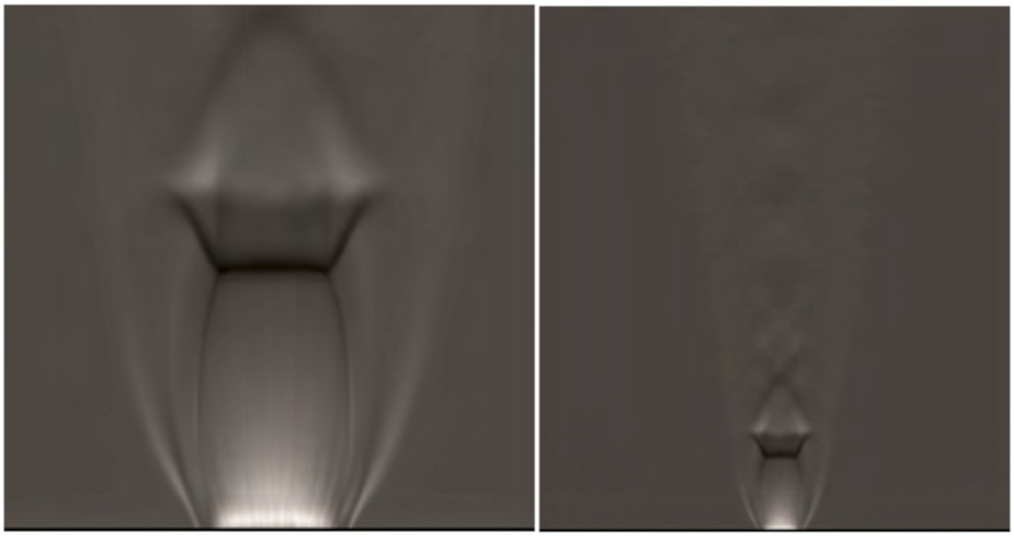

Figure 5–2. Images of the Mach disk structure (left), and Mach disk and diamond shock structure (right) (Ruggles and Ekoto, 2011).

Ruggles and Ekoto (2011) used corrected instantaneous images of flow to create a root-mean-square (r.m.s.) image of the flow fluctuations, which is shown in Fig. 5–3 and illustrates the downstream mixing layers. They noted that the schlieren image results should be interpreted with caution. Their measurements were a path averaged integration of the refractive index gradient, which may have been caused by differences in mixture fraction due to scalar mixing, but also may have been the result of changes in pressure and temperature. In the region surrounding the barrel shock structure, however, it is feasible that refractive index gradients were the result of the air entrainment ahead of the Mach disk. This would then require the inclusion of an entrainment correction in the current notional nozzle models (Ruggles and Ekoto, 2011).

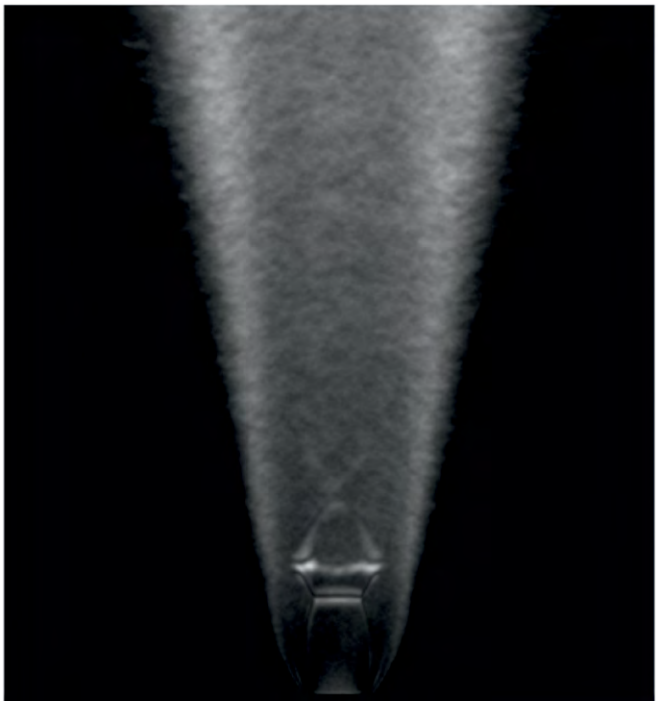

Figure 5–3. R.m.s. image of the Mach disk and diamond structure (Ruggles and Ekoto, 2011).

5.2. Under-expanded jet theories

It is convenient for some engineering calculations to substitute an under-expanded jet from actual nozzle by an expanded jet from so-called effective or notional nozzle. There are a number of notional nozzle theories. One of the most cited is the model by Birch et al. (1984). However, these former models are built on the ideal gas equation of state and thus not applicable to gas storage pressures above 10-20 MPa when effects of gas non-ideality must be accounted for. Indeed, the Abel-Noble equation of state $p=Z\rho R_{H2}T$, where $Z=1/(1-b\rho)$ is the compressibility factor, has Z=1.01 at 1.57 MPa, Z=1.1 at 15.7 MPa, and Z=1.5 at 78.6 MPa (at temperature 293.15 K).

The first theory of under-expanded jet that accounts for non-ideal behaviour of highly compressed hydrogen has been published by Schefer et al. (2007). The notional nozzle diameter calculations by Schefer et al. (2007) are similar to Birch et al. (1984) yet the Abel-Noble equation is applied and the assumption by Birch et al. about the speed of sound at the notional nozzle is relaxed. As a result the theory of Schefer et al. (2007) predicts uniform super-sonic velocities at the notional nozzle exit at high storage pressures.

In 2009 author and colleagues developed the alternative to Schefer et al. (2007) under-expanded theory that is presented here. This theory (Molkov et al., 2009) is based on mass and energy conservation equations rather than mass and momentum (Schefer et al., 2007). Similar to Birch et al. (1984) the developed model (Molkov et al., 2009) is based on the assumption of uniform sonic flow through the notional nozzle. The under-expanded jet scheme is shown in Fig. 5–4.

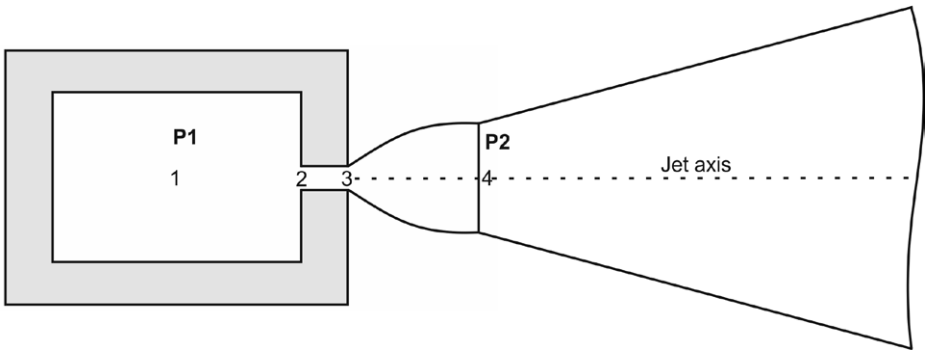

Figure 5–4. The under-expanded jet scheme: 1 – storage vessel, 2 – nozzle entrance, 3 – nozzle exit, 4 – notional nozzle exit.

It is assumed that flow velocity in the storage reservoir, 1, is zero. The flow parameters at the entrance to the leak channel are referred to by subscript 2, and at the actual nozzle exit by subscript 3. For sonic and super-sonic flows the parameters at the nozzle exit, 3, are those for choked flow and therefore the nozzle exit velocity is equal to the local speed of sound (Mach number M=1). The notional nozzle is between the actual nozzle exit, 3, and the notional nozzle exit, 4. The notional nozzle exit, 4, parameters correspond to fully expanded jet with the pressure equal to ambient and uniform flow velocity equal to local speed of sound. In some cases there can be essential minor and friction losses in the flow pathway 2–3 that cannot be neglected, e.g. the case of very narrow crack.

In this section two under-expanded jet theories will be presented – first without and then with losses. Both exploit the Abel-Noble equation of state for real hydrogen gas is applied (Chenoweth, 1983) described in Chapter 2

$$p = Z \cdot \rho \cdot R_{H2} \cdot T\,, \tag{5–2}$$

where the compressibility factor is $Z = 1/\,(\,1 - b\rho)$.

5.2.1. Theory without losses

It is assumed that the expansion of the Abel-Noble gas from the reservoir, 1, to the nozzle exit, 3, is isentropic, without losses in the flow between nozzle entrance, 2, and nozzle exit, 3. It is assumed that there is no air entrainment to an expanding jet between the actual nozzle exit, 3, and the notional nozzle exit, 4. The system of nine equations with nine unknown parameters ($\rho_{1,}$ ρ_3, u_3, T_3, p_3, ρ_4, u_4, T_4, A_4) is as follows (known parameters are: p_1, T_1, A_3, p_4 and constants c_p, R_{H2}, b, γ). Here ρ is the density (kg/m^3), u is the gas velocity (m/s), A is the cross-section area (m^2), c_p is the specific heat capacity at constant pressure (J/kg/K). Subscripts "1" through to "4" denote gas parameters at locations "1" to "4" shown in Fig. 5–4.

Three equations of state for gas parameters at the reservoir, 1, the real nozzle exit, 3, and the notional nozzle exit, 4, are

$$\rho_1 = \frac{p_1}{bp_1 + R_{H2}T_1}\,, \quad \rho_3 = \frac{p_3}{bp_3 + R_{H2}T_3}\,, \quad \rho_4 = \frac{p_4}{R_{H2}T_4}\,. \tag{5–3}$$

Two equations of energy conservation, one between the reservoir, 1, and the actual nozzle exit, 3, and another between the actual nozzle exit, 3, and the notional nozzle exit, 4, are

$$c_pT_1 = c_pT_3 + \frac{u_3^2}{2},\ c_pT_3 + \frac{u_3^2}{2} = c_pT_4 + \frac{u_4^2}{2}\,. \tag{5–4}$$

Two equations for the speed of sound, one for choked flow in the nozzle exit, 3, and another for the assumption of the speed of sound at the notional nozzle exit, 4, are

$$u_3^2 = a_3^2 = \frac{\gamma p_3}{\rho_3(1-b\rho_3)},\ u_4 = a_4 = \sqrt{\gamma R_{H2}T_4}\,. \tag{5–5}$$

The mass conservation equation between entrance to the notional nozzle, 3, and exit from the notional nozzle, 4, is

$$\rho_3 u_3 A_3 = \rho_4 u_4 A_3. \tag{5–6}$$

The isentropic expansion equation between the reservoir, 1, and the actual nozzle exit, 3, is

$$p_1\left(\frac{1}{\rho_1} - b\right)^{\gamma} = p_3\left(\frac{1}{\rho_3} - b\right)^{\gamma}\,. \tag{5–7}$$

Let us rewrite the equation (5-4) for energy conservation between the reservoir, 1, and the actual nozzle exit, 3, in the form

$$\frac{T_1}{T_3} = 1 + \frac{u_3^2}{2c_pT_3}\,, \tag{5–8}$$

and multiply numerator and denominator in the second term of the right-hand side by square of the speed of sound that is for Abel-Noble gas is

$$a^2 = \frac{\gamma P}{\rho(1-b\rho)} \tag{5–9}$$

to obtain the equation

$$\frac{T_1}{T_3} = 1 + \frac{\gamma P_3}{\rho_3(1-b\rho_3)} \frac{R_{H2} M_3^2}{2 c_p R_{H2} T_3} \tag{5–10}$$

in which $M_3 = u_3 / a_3$ is Mach number of the flow in state 3. Taking into account that $\frac{R_{H2}}{c_p} = \frac{\gamma - 1}{\gamma}$

$$\frac{T_1}{T_3} = 1 + \frac{\gamma P_3}{\rho_3(1-b\rho_3)} \frac{\gamma - 1}{\gamma} \frac{M_3^2}{2 R_{H2} T_3} = 1 + \frac{(\gamma-1) M_3^2}{2(1-b\rho_3)} \left[\frac{P_3}{\rho_3 R_{H2} T_3} \right]. \tag{5–11}$$

By substitution $\frac{P_3}{\rho_3 R_{H2} T_3} = \frac{1}{1-b\rho_3}$ and accounting for chocked flow in the actual nozzle exit 3 (M_3=1) the following equation is derived

$$\frac{T_1}{T_3} = 1 + \frac{\gamma - 1}{2(1-b\rho_3)^2} M_3^2 = 1 + \frac{\gamma - 1}{2(1-b\rho_3)^2}. \tag{5–12}$$

Let us rewrite (5–7) with use of the Abel-Noble equation of state as

$$\left(\frac{\rho_1}{1-b\rho_1} \right)^{\gamma} = \left(\frac{\rho_3}{1-b\rho_3} \right)^{\gamma} \frac{\rho_1 R T_1}{1-b\rho_1} \cdot \frac{1-b\rho_3}{\rho_3 R T_3} \tag{5–13}$$

By uniting the density terms in (5-13) and substituting for the temperature ratio from (5-12) we obtain

$$\left(\frac{\rho_1}{1-b\rho_1} \right)^{\gamma-1} = \left(\frac{\rho_3}{1-b\rho_3} \right)^{\gamma-1} \left(1 + \frac{\gamma - 1}{2(1-b\rho_3)^2} \right). \tag{5–14}$$

The procedure for the notional nozzle diameter (d_3=d_e) calculation is as follows (Molkov et al., 2009). Calculate hydrogen density in the reservoir from the Abel-Nobel equation. $\rho_1 = P_1 / Z R_{H2} T_1$. Solve a transcendental equation of isentropic expansion to find density at the actual nozzle exit (5–14). Find temperature T_3 at the actual nozzle exit from the equation (5–12) and then pressure P_3 from the Abel-Noble equation (5–2). At the actual nozzle exit, 3, the flow is chocked and hydrogen velocity can be calculated using the equation for the speed of sound (5–9). From the energy conservation equation between the actual nozzle exit and the notional nozzle exit (5–4) written per unit mass, and with the assumption that at the notional nozzle exit hydrogen velocity is equal to the local speed of sound $a_4^2 = \gamma R_{H2} T_4$, it is easy to derive that the temperature at the notional nozzle exit is

$$T_4 = \frac{2T_3}{(\gamma+1)} + \frac{(\gamma-1)}{(\gamma+1)} \frac{P_3}{\rho_3 (1-b\rho_3) R_{H2}}. \tag{5–15}$$

Then, hydrogen density at the notional nozzle can be calculated with P_4 equal to the ambient pressure as well as the velocity of gas $u_4=a_4$. Finally, from the continuity equation it follows that the notional nozzle exit diameter is

$$d_4 = d_3\sqrt{\frac{\rho_3 u_3}{\rho_4 u_4}}. \qquad (5\text{–}16)$$

The under-expanded jet theory (Molkov et al., 2009) was used to build and validate described further in this manuscript the universal similarity law that is valid for both expanded and under-expanded jets in the momentum-controlled regime, the novel correlation for hydrogen jet flame length, blow down time of hydrogen release from the storage vessel, etc. The theory is an essential tool to carry out hydrogen safety engineering.

5.2.2. Theory with losses

Minor losses in gas flow represent entrance to the channel, abrupt reduction or increase in channel cross-section area, presence of valves, elbows, etc. They are described in this theory through the minor losses factor K. Frictional losses are considered to be due to friction on walls. They are described through equation $F=fL/d$, where f is the friction factor, L is the channel/nozzle length, and d is channel diameter. The system of 12 equations describing this process is given in Table 5–1 following paper (Molkov and Bragin, 2009).

$P_2 - P_1 + \rho_2 u_2^2 \left(K/4+1\right) = 0$	$\rho_2 u_2 = \rho_3 u_3$
$c_P T_1 = c_P T_2 + \left(K+1\right)\cdot u_2^2/2$	$u_3 = \sqrt{\gamma R_{H2} T_3}\,(1 - b\rho_3)$
$\rho_2 = P_2/(bP_2 + R_{H2}T_2)$ or $P_2 = \rho_2 R_{H2} T_2/(1-b\rho_2)$	$u_4 = a_4 = \sqrt{\gamma R_{H2} T_4}$
$P_3 - P_2 + \rho_2 u_2^2 \left(F/4-1\right) + \rho_3 u_3^2 \left(F/4+1\right) = 0$	$\rho_4 = P_4/(R_{H2}T_4)$
$c_p T_2 + u_2^2/2 = c_p T_3 + (F/4+1)\cdot u_3^2/2$	$c_p T_3 + u_3^2/2 = c_p T_4 + u_4^2/2$
$\rho_3 = P_3/(bP_3 + R_{H2}T_3)$	$\rho_3 u_3 A_3 = \rho_4 u_4 A_4$

Table 5–1. The system of equations for the model of under-expanded jet with losses (Molkov and Bragin, 2009).

The system of equations in Table 5–1 can be reduced to the following two equations with two unknown parameters, i.e. u_3 and T_3,

$$\frac{u_3}{b}\left(1-\frac{\sqrt{\gamma R_{H2}T_3}}{u_3}\right)\cdot\left[\sqrt{\frac{R_{H2}T_3}{\gamma}}+\left(\frac{K+F}{4}\right)\cdot\sqrt{\frac{2}{K}\left(C_P T_1 - C_P T_3 - \frac{u_3^2}{2}\left(\frac{F}{4}+1\right)\right)}+u_3\left(\frac{F}{4}+1\right)\right]-P_1=0;$$

$$\frac{u_3}{b}\left(1-\frac{\sqrt{\gamma R_{H2}T_3}}{u_3}\right)\left[\frac{R_{H2}\left(T_1-\left(T_1-T_3-\frac{u_3^2}{2c_P}\left(\frac{F}{4}+1\right)\right)\frac{K+1}{K}\right)}{\sqrt{\frac{2}{K}\left(c_P T_1 - c_P T_3 - \frac{u_3^2}{2}\left(\frac{F}{4}+1\right)\right)}-u_3+\sqrt{\gamma R_{H2}T_3}}+\right.$$

$$\left.+\left(\frac{K}{4}+1\right)\sqrt{\frac{2}{K}\left(c_P T_1 - c_P T_3 - \frac{u_3^2}{2}\left(\frac{F}{4}+1\right)\right)}\right]-P_1=0. \qquad (5\text{-}17)$$

After u_3 and T_3 are found by solving the system of two equations (5–17), the rest of parameters in the under-expanded jet can be easily calculated.

Both under-expanded jet theory without losses (Molkov et al., 2009) and under-expanded jet theory with losses (Molkov and Bragin, 2009) are applied to calculate parameters of under-expanded hydrogen jet exiting from a narrow channel of 0.75 mm diameter and 15 mm length at pressures up to 40 MPa (see Table 5–2). The results of predictions by the under-expanded jet theories are compared against numerical simulations (LES model). The ambient temperature is assumed 287.65 K. The correlation by Nikuradse for friction factor ($1/\sqrt{f} = 0.869\cdot\ln\left(\mathrm{Re}\sqrt{f}\right)-0.8$) is applied. The Reynolds number in this formula is taken as an average of values at flow states 2 and 3. Predictions by the theory with losses are found to closely reproduce the numerical simulations whereas the theory without losses essentially over predicts the mass flow rate. The last has direct economical implication due to unjustifiably increased separation distance.

Method of calculation	0.53 MPa	10.5 MPa	40 MPa
Under-expanded theory without losses	1.44	2.80	9.56
Under-expanded theory with losses	1.05	2.08	7.76
Large Eddy Simulation	1.05	2.10	8.10

Table 5–2. Mass flow rates (g/s) through 15 mm length and 0.75 mm diameter channel at different storage pressures (Molkov and Bragin, 2009).

There is somewhat over prediction by LES of mass flow rate at high pressures (see Table 5–2). It is thought due to the fact that LES results obtained in simulations with the ideal gas equation of state that is known to over predict mass flow rate compared to the Abel-Noble equation of state.

5.3. The similarity law for concentration decay in momentum-dominated jets

Unscheduled hydrogen releases from high pressure equipment and infrastructure will create highly under-expanded jets. This could lead to formation of a large flammable hydrogen-air envelope. The size of the flammable envelope is the deterministic separation distance from the release source. Indeed, if the flammable envelope (hydrogen concentration in air equal to the lower flammability limit of 4% by volume) reaches a location of air intake into high-rise buildings, then consequences for occupants and building structure can be catastrophic.

Presence of ignition source within the envelope could initiate severe jet fires, deflagration, and potentially deflagration-to-detonation transition. It has to be noted that thermal effects of jet fires and pressure effects of deflagration or detonation could override the separation distance determined by the size of flammable envelope. Thus, knowledge of laws describing hydrogen dispersion and flammable cloud formation, including axial concentration decay, for arbitrary jets with various parameters is essential for reliable hydrogen safety engineering.

In this section an overview of previous studies on non-reacting hydrogen jets emerging into the still atmosphere is given. The similarity law for prediction of axial concentration decay of a leaking gas for sub-sonic, sonic, and super-sonic jets is presented. The similarity law is shown to be valid in a wide range of conditions from expanded to highly under-expanded jets. It can be applied for calculation of deterministic separation distances informed by the size of the flammable envelope. The non-ideal behaviour of hydrogen at high pressures and the under-expansion of flow in a nozzle exit are taken into account.

5.3.1. Expanded jets

Ricou and Spalding (1961) demonstrated by using the dimensional analysis that when the fluid density is uniform, the Reynolds number is high, and the distance x from the nozzle along the jet axis is much larger the diameter of the orifice D, then the total mass flow rate $m(x)$, including entrained surrounding gas, through a cross-section at right angle to the jet axis, is proportional to x

$$m(x) = K_1 M_0^{½} \rho_s^{½} x, \tag{5–18}$$

where the momentum flux of the jet at orifice is $M_0 = \rho_N U^2 \pi D^2 / 4$, ρ_N and ρ_S are the densities of the nozzle and the surrounding gas respectively, U is the velocity in the nozzle.

It was found experimentally (Ricou and Spalding, 1961): the equation for mass flow rate holds for non-uniform density without modification provided that buoyancy effects are negligible; a numerical constant K_1 has the value 0.282 irrespective of the density ratio; and the presence of combustion reduces K_1. The experimental data for isothermal injection of different gases (hydrogen, air, propane, carbon dioxide) into stagnant air can be held to obey the following simple relation that can be derived from (5–18)

$$\frac{m(x)}{m_N} = 0.32 \frac{x}{D} \sqrt{\frac{\rho_S}{\rho_N}}, \tag{5–19}$$

where m_N is the mass flow rate of the gas in the nozzle.

A mass fraction of fuel averaged through the jet cross-section area can be calculated as a reciprocal to the left-hand side of equation (5–19)

$$C_{av} = 3.1 \sqrt{\frac{\rho_N}{\rho_S}} \frac{D}{x}. \tag{5–20}$$

A mean mass fraction fuel on a jet axis is higher compared to the fuel mass fraction averaged through the jet cross-section. The axial concentration can be calculated by similarity laws (Chen and Rodi, 1980) for round and plane jets respectively

$$\frac{C_{ax}}{C_N} = 5.4\sqrt{\frac{\rho_N}{\rho_S}}\frac{D}{x} \text{ (round jet),} \tag{5–21}$$

$$\frac{C_{ax}}{C_N} = 2.13\sqrt{\frac{\rho_N}{\rho_S}}\sqrt{\frac{D}{x}} \text{ (plane jet),} \tag{5–22}$$

where C_N is the mass fraction of hydrogen in the nozzle (C_N =1 for pure hydrogen release).

Two important conclusions can be drawn from the similarity laws (5–21) and (5-22). The first conclusion is that for hydrogen jets to stagnant air the ratio of a distance, x=L, to a fixed concentration expressed in percents by mass, C_{ax}, to the nozzle diameter is a constant, i.e. L/D=const. This means, for example, that the distance to the lower flammability limit (separation distance) is proportional to the leak diameter. Thus, the design of hydrogen and fuel cell systems has to be carried out bearing in mind the requirement to minimise the internal diameter of piping to satisfy technological requirements to mass flow rate. The second conclusion is that a plane jet decays slower ($\propto \sqrt{D}$) compared to a round jet of the same size ($\propto D$). It is worth noting that this conclusion is valid for "infinite" plane jets. Plane jets with limited length to width ratio do not follow the similarity law (5-22) as has been demonstrated in recent research at the HySAFER Centre, at least at a far field where they are decaying similar to round jets (Molkov et al., 2010).

The mass fraction, C_M, can be calculated by the volumetric (mole) fraction, C_V, by equation

$$\frac{1}{C_M} = 1 + \left(\frac{1}{C_V} - 1\right)\cdot\frac{M_S}{M_N} \tag{5–23}$$

where M_S and M_N are molecular masses of surrounding gas (28.84 g/mol is accepted for air in calculations) and nozzle gas respectively. For example, mass fraction 0.0282 corresponds to volumetric fraction 0.295 (29.5% by volume of hydrogen in air – stoichiometric mixture), mass fraction 0.0.044365 corresponds to volumetric fraction 0.401 (40.1% – mixture with maximum burning velocity), 0.013037 – 0.16 (16%), 0.008498 – 0.11 (11%), 0.005994 – 0.08 (8%), 0.00288 – 0.04 (4%), 0.00141 – 0.02 (2%), 0.0007 – 0.01 (1%).

For expanded jets the similarity laws (5–21) and (5–22) give for round (plane) jet the following ratios of a distance to particular axial hydrogen concentration (in percents by volume), L, to the characteristic nozzle size, D (with density ratio ρ_S/ρ_N=14.45): $(L/D)_{30\%}$=49.3 (379); $(L/D)_{8.5\%}$=222 (7689); $(L/D)_{4\%}$=493 (37854); $(L/D)_{2\%}$=1008 (157926); $(L/D)_{1\%}$=2029 (640760). For example, the distance to the lower flammability limit of hydrogen in air (4% by volume) in momentum-controlled expanded jets is equal to 493 nozzle diameters.

It is worth noting that the correlations (5–21) and (5–22) by Chen and Rodi (1980) were validated by concentration measurements in vertical jets up to value L/D=50 only. Their applicability above this range should be confirmed.

Shevyakov et al. (1980) published theoretical and experimental study on hydrogen concentration decay in unignited hydrogen jets into stagnant air. It was shown, in particular, that for momentum-controlled jets (at high nozzle Froude numbers $Fr=U^2/gD>10^5$) the dimensionless distance to 30% by volume of hydrogen $(L/D)_{30\%}$ is a constant 47.9. This is an excellent agreement with published independently at the same year 1980 work by Chen and Rodi (1980) that gives value 49.3. The theoretical formula derived by Shevyakov et al. (1980) gives an estimate for the flammable envelope length $(L/D)_{4\%}$=410, which is close to the Chen and Rodi's value of $(L/D)_{4\%}$=493.

5.3.2. Previous studies of under-expanded jets

Thring and Newby (1953) were probably the first to introduce the pseudo-diameter (or notional source/nozzle diameter). They suggested that the pseudo-diameter is equal to $D_{eff} = D\sqrt{\rho / \rho_{eff}}$, where D_{eff} is the aperture of a jet through which the same mass flow rate of nozzle fluid would have emerged with the same jet momentum but with density ρ_{eff} instead of ρ. However, this relationship is valid only if flow velocity at the real and the notional nozzles are equal, which is not an obvious assumption.

Birch et al. (1984) assumed that the similarity law by Chen and Rodi (1980) could work not only for expanded but also for under-expanded jets. The behaviour of under-expanded jets was expected to be similar to classical free jets provided that an appropriate scaling factor is employed to describe the effective size of the jet source.

Authors stated that the resultant concentration field behaves as if it was produced by a larger source than the actual nozzle. Birch et al. (1984) demonstrated that for a 2.7 mm diameter round nozzle and pressures from 0.35 to 7.1 MPa the data for mean concentration of natural gas decay along the centreline, when plotted against the non-dimensional coordinate $x/(D\sqrt{p_R / p_S})$, where p_R is the pressure in storage tank, collapse onto a single curve.

The range of validation was L/D=30-170 (Birch et al., 1984). It was underlined that the notional nozzle does not necessarily exist in the physical sense – it is merely postulated to agree with chosen definition. The model by Birch et al. is built on the ideal gas law, the equation for conservation of mass between choked flow through an actual nozzle exit and a sonic flow through a notional nozzle exit. Other assumptions applied are: uniform sonic velocity after jet expansion to ambient pressure, and expanded flow temperature equal to initial temperature in the reservoir. Three years later Birch et al. (1987) published another paper that contributed to conclusions of the previous study.

Unfortunately, an incorrect form of the similarity law was reproduced by Birch et al. (1984, 1987). This error regrettably generated a number of misinterpretations of the similarity law in the hydrogen safety community. The incorrect equation (Birch et al., 1984, 1987) casts as

$$C_{ax}^{V} = 5.4\sqrt{\frac{\rho_S}{\rho_N}}\frac{D_{eff}}{x}. \qquad (5–24)$$

There are three essential differences with the Chen and Rodi correlation for expanded jets (5–21) and equation (5–24) suggested by Birch et al. (1984, 1987) for under-expanded jets. Firstly, the volumetric fraction, C_{ax}^{V}, was used instead of original mass fraction, C_{ax}, as in the original correlation (Chen and Rodi, 1980; Wang et al., 2008). Secondly, the density ratio applied by Birch et al. is reciprocal to the original. Thirdly, the notional nozzle exit diameter or effective diameter (D_{eff}) is applied instead of the actual nozzle diameter (D). These three critical differences with the original similarity law have generated inconsistencies in a number of following publications by different researchers trying to use the correlation in the form suggested by Birch et al., e.g. (BRHS, 2009; Houf and Schefer, 2008).

Birch and colleagues didn't validate the form of the correlation they publish. Instead, only the correlation between the inverse concentration (in volume fraction) and the axial displacement, x/D_{eff}, was presented in their paper (Birch et al., 1987). However, mass and volumetric fractions are changing practically linearly at values of natural gas concentrations at which measurements were carried out (6–50% by volume). This linearity provides a "good" looking correlation even without a right coefficient of proportionality.

There is another reason why Birch et al. (1984, 1987) and similar approaches cannot be applied to calculate concentration decay in jets from high pressures hydrogen equipment and storage, i.e. due to limitations for application of the ideal gas law at high pressures above 10 MPa. This is an essential problem with clear safety implications. Indeed, the ideal gas law overestimates the hydrogen mass flow rate from a 70 MPa storage by about 45% as can be estimated by the Abel-Noble equation.

Thus, the guess by Birch and colleagues about the universal character of the similarity law (Chen and Rodi, 1980) yet has to be confirmed. The procedure of the similarity law application to under-expanded jets has to be developed and validated.

5.3.3. The similarity law for expanded and under-expanded jets

If the similarity law (Chen and Rodi, 1980) is applicable in its original form (5–21) for both expanded and under-expanded jets, then the calculation of deterministic separation distances for unignited hydrogen round jets would be straight forward by equation (5–21). However, for under-expanded jets there will be one unknown parameter, i.e. a density of gas in the actual nozzle exit, ρ_N. This density can be calculated by one of justified under-expanded theories, e.g. without losses (Molkov et al., 2009) or with losses (Molkov and Bragin, 2009). For expanded hydrogen jets the application of the similarity law (5–21) is straight forward with hydrogen density at the nozzle exit ρ_N=0.0838 kg/m^3 (NTP).

The similarity law for concentration decay along the axis of the momentum-controlled jets is shown in Fig. 5–5 along with experimental data for hydrogen under-expanded releases. It is based on the hypothesis of using the original form of the similarity law by Chen and Rodi (1980) with the only unknown parameter being the density of hydrogen at the nozzle exit (Molkov, 2009a). Only 60 of total 302 experimental points in the momentum-controlled regime are presented in Fig. 5–5 to avoid overlapping of data on the graph (Molkov et al., 2010). These 60 points are the maximum and minimum values of each experiment and in some cases an additional intermediate value. The validation of the similarity law with use of the under-expanded theory for calculation of hydrogen density in the actual nozzle exit was carried out against experimental data described in details below.

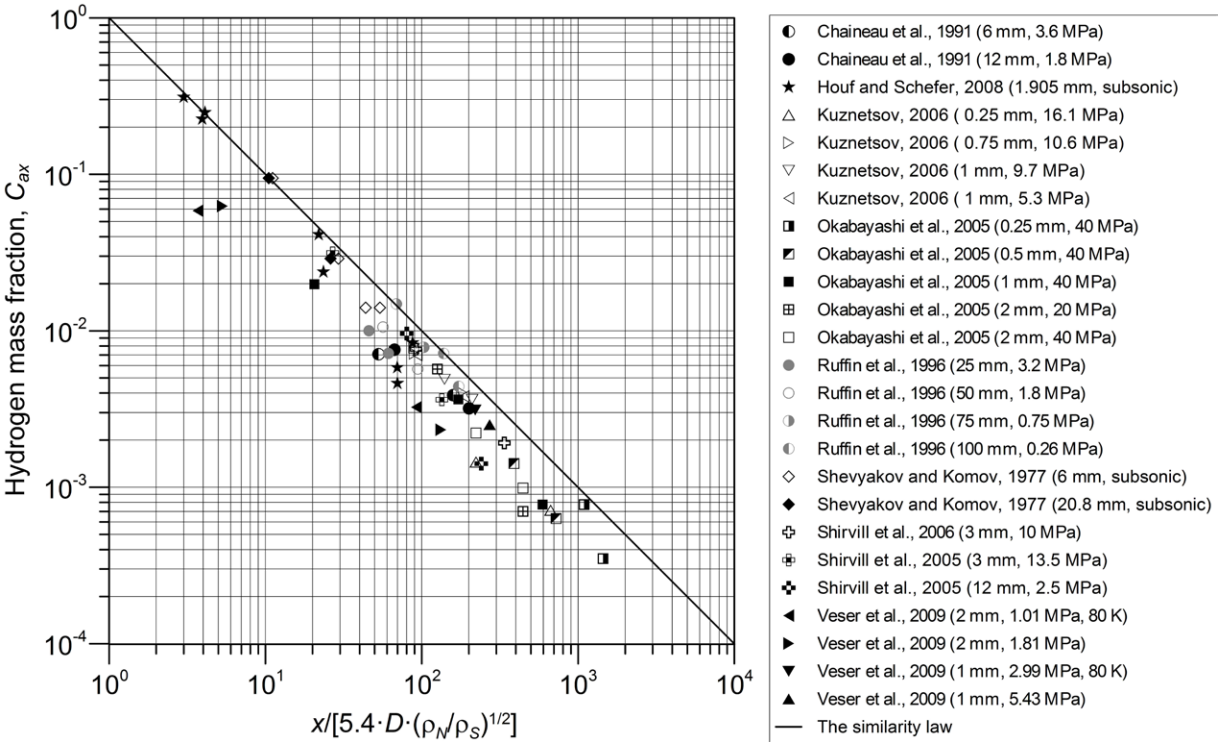

Figure 5–5. The similarity law (solid line) and experimental data on axial concentration decay in momentum-controlled expanded and under-expanded hydrogen jets.

Shevyakov et al. (1977) conducted a series of subsonic releases from nozzle diameter from 6 mm to 96 mm and hydrogen velocity in the nozzle ranging from 2.52 m/s to 861.21 m/s. The regime of each release (buoyancy- or momentum-dominated) was determined by a value of Froude number. $Fr = U_N^2/(g \cdot D)$. Only momentum-controlled jets were selected here for the validation of the similarity law. Data for 4 releases with nozzle diameter of 6 mm and 2 releases with nozzle diameter of 20.8 mm are given in Table 3–5.

Test	T_R	D	p_t	ρ_N	x	$C_{ax\text{-}v}{}^a$	$C_{ax\text{-}m}{}^b$	
	K	mm	MPa	kg·m^{-3}	m	Volume fraction	Mass fraction	$\frac{x}{5.4 \cdot D \cdot \sqrt{\frac{\rho_N}{\rho_S}}}$
Chaineaux et al. (1991)	207	6	3.6**	2.58	7.50	0.053	0.0039	158.7
Chaineaux et al. (1991)	207	6	3.6**	2.58	2.50	0.093	0.0071	52.9
Chaineaux et al. (1991)	174	12	1.8***	1.56	15	0.044	0.0032	200.6
Chaineaux et al. (1991)	174	12	1.8***	1.56	5	0.099	0.0076	66.9
Houf and Schefer (2008)	298*	1.905	-	0.08	0.24	0.108	0.0084	87.3
Houf and Schefer (2008)	298*	1.905	-	0.08	0.01	0.866	0.3108	3.0
Houf and Schefer (2008)	298*	1.905	-	0.08	0.19	0.078	0.0058	69.7
Houf and Schefer (2008)	298*	1.905	-	0.08	0.06	0.382	0.0412	21.9
Houf and Schefer (2008)	298*	1.905	-	0.08	0.01	0.826	0.2484	4.1
Houf and Schefer (2008)	298*	1.905	-	0.08	0.19	0.062	0.0046	69.8
Houf and Schefer (2008)	298*	1.905	-	0.08	0.06	0.259	0.0238	23.5
Houf and Schefer (2008)	298*	1.905	-	0.08	0.01	0.807	0.2257	3.9
Kuznetsov (2006)	287	0.25	16.1	7.68	2.25	0.010	0.0007	666.6
Kuznetsov (2006)	287	0.25	16.1	7.68	0.75	0.020	0.0015	222.2
Kuznetsov (2006)	287	0.75	10.6	5.25	1.50	0.055	0.0040	179.2
Kuznetsov (2006)	287	0.75	10.6	5.25	0.75	0.094	0.0072	89.6
Kuznetsov (2006)	287	1	9.7	4.84	2.25	0.050	0.0036	210.1
Kuznetsov (2006)	287	1	9.7	4.84	1.50	0.066	0.0049	140.0
Kuznetsov (2006)	287	1	5.3	2.73	1.50	0.052	0.0038	186.5
Kuznetsov (2006)	287	1	5.3	2.73	0.75	0.092	0.0070	93.3
Okabayashi et al. (2005)	288	2	20	9.29	13.22	0.010	0.0007	444.4
Okabayashi et al. (2005)	288	2	20	9.29	3.74	0.076	0.0057	125.9
Okabayashi et al. (2005)	288	0.25	40	16.45	7.15	0.005	0.0003	1444.4
Okabayashi et al. (2005)	288	0.25	40	16.45	5.41	0.011	0.0008	1092.6
Okabayashi et al. (2005)	288	0.5	40	16.45	7.15	0.009	0.0006	722.2
Okabayashi et al. (2005)	288	0.5	40	16.45	3.85	0.020	0.0014	388.9

Table 5–3 (Part I). Data on concentration decay in hydrogen under-expanded jets.

Test	T_R	D	p_t	ρ_N	x	$C_{ax\text{-}v}{}^a$	$C_{ax\text{-}m}{}^b$	$\frac{x}{5.4 \cdot D \cdot \sqrt{\frac{\rho_N}{\rho_S}}}$
	K	mm	MPa	kg·m^{-3}	m	Volume fraction	Mass fraction	
Okabayashi et al. (2005)	288	1	40	16.45	11.73	0.011	0.0008	592.6
Okabayashi et al. (2005)	288	1	40	16.45	3.39	0.050	0.0036	171.3
Okabayashi et al. (2005)	288	1	40	16.45	0.41	0.225	0.0198	20.6
Okabayashi et al. (2005)	288	2	40	16.45	17.59	0.014	0.0010	444.4
Okabayashi et al. (2005)	288	2	40	16.45	8.79	0.031	0.0022	222.2
Okabayashi et al. (2005)	288	2	40	16.45	3.52	0.101	0.0078	88.9
Ruffin et al. (1996)	288	25	3.24#	1.79	10.00	0.094	0.0072	61.2
Ruffin et al. (1996)	288	25	3.24#	1.79	7.50	0.127	0.0100	45.9
Ruffin et al. (1996)	288	50	1.8#	1.18	25	0.076	0.0057	94.2
Ruffin et al. (1996)	288	50	1.8#	1.18	15	0.133	0.0106	56.5
Ruffin et al. (1996)	288	75	0.75#	0.63	30	0.102	0.0078	103.3
Ruffin et al. (1996)	288	75	0.75#	0.63	20	0.178	0.0149	68.9
Ruffin et al. (1996)	288	100	0.26#	0.35	50	0.060	0.0044	172.2
Ruffin et al. (1996)	288	100	0.26#	0.35	40	0.094	0.0072	137.8
Shevyakov et al., (1977)	288	6	-	0.08	0.37	0.170	0.0141	43.8
Shevyakov et al., (1977)	288	6	-	0.08	0.46	0.170	0.0141	54.0
Shevyakov et al., (1977)	288	6	-	0.08	0.10	0.600	0.0945	11.1

Table 5–3 (Part II). Data on concentration decay in hydrogen under-expanded jets.

Test	T_R	D	p_t	ρ_N	x	$C_{ax\text{-}v}{}^a$	$C_{ax\text{-}m}{}^b$	$\frac{x}{5.4 \cdot D \cdot \sqrt{\frac{\rho_N}{\rho_S}}}$
	K	mm	MPa	kg·m^{-3}	m	Volume fraction	Mass fraction	
Shevyakov et al., (1977)	288	6	-	0.08	0.25	0.300	0.0290	29.3
Shevyakov et al., (1977)	288	20.8	-	0.08	0.77	0.300	0.0290	26.1
Shevyakov et al., (1977)	288	20.8	-	0.08	0.31	0.600	0.0945	10.5
Shirvill et al. (2006)	287	3	10	4.98	11.00	0.027	0.0019	337.2
Shirvill et al. (2006)	287	3	10	4.98	3.00	0.100	0.0076	92.0
Shirvill et al. (2005)	287	3	13.5	6.57	9.00	0.020	0.0014	240.4
Shirvill et al. (2005)	287	3	13.5	6.57	3.00	0.122	0.0096	80.1
Shirvill et al. (2005)	287	12	2.5	1.32	9.00	0.050	0.0036	134.3
Shirvill et al. (2005)	287	12	2.5	1.32	1.80	0.318	0.0315	26.9
Veser et al. (2009)	298	1	5.43	2.70	2.20	0.035	0.0025	271.8
Veser et al. (2009)	298	1	5.43	2.70	0.19	0.272	0.0253	23.5
Veser et al. (2009)	80	1	2.99	5.32	2.50	0.043	0.0031	219.9
Veser et al. (2009)	80	1	2.99	5.32	0.19	0.368	0.0389	16.7
Veser et al. (2009)	298	2	1.01	1.88	0.05	0.472	0.0585	3.70
Veser et al. (2009)	298	2	1.01	1.88	1.25	0.045	0.0032	92.44
Veser et al. (2009)	80	2	1.81	0.92	0.05	0.490	0.0627	5.29
Veser et al. (2009)	80	2	1.81	0.92	1.25	0.032	0.0023	132.19

Notes. T_R – temperature measured in the storage reservoir or nozzle (* - assumed); p_t – discharge pressure at sampling time; ** – pressure given 5 s after discharge initiation; *** - pressure given 2 s after discharge initiation; # – pressure calculated 2 s after discharge initiation using the under-expanded jets theory and blowdown model (Molkov et al., 2009); [a] – experimental data (axial volumetric fraction of hydrogen); [b] – mass fraction calculated from volumetric fraction.

Table 5–3 (Part III). Data on concentration decay in hydrogen under-expanded jets.

Chaineaux et al. (1991) conducted experiments to measure the axial concentration decay along the axis of horizontal jets of hydrogen and methane in air. They used a cylindrical vessel 0.12 m^3 (55 cm diameter and 55 cm height) pressurized to 10 MPa and placed by its rear side against a wall, with vessel axis 2.2 m above the ground. An outlet tube of 50 mm diameter was attached to the vessel. A steel plate with a hole was at the end of the tube at some distance from the pyrotechnic valve. The jet exit orifice diameters for hydrogen experiments were set at 5 mm (tests 1 and 2), 12 mm (tests 3 and 4) and 24 mm (tests 5, 6 and 7). The measurements of hydrogen concentration along jet axis were done by sampling the mixture at defined locations and times using stainless steel sampling bulbs of volume 150 cm^3 attached to vertical masts disposed along jet axis. Authors assumed the jet is "stabilized" (quasi-steady state) when the flammable cloud reaches its maximum volume. At the moment of stabilisation of the jet the pressure in the vessel has decreased from its initial value to lower pressure. For each experiment, Chaineaux and colleagues gave hydrogen concentration (% by vol.) at various locations, initial temperature in the vessel before gas venting, the minimum temperature in the vessel and the time at which this temperature was reached, as well as the residual pressure in the tank at each sampling time. For example, in test 2 the minimum temperature in the tank reached -104°C at 19 seconds after the start of release.

Among 7 tests carried out with hydrogen only 2 were considered as valid by Chaineaux et al. (tests 2 and 3). Test 1 was used for calibration, test 4 resulted in spontaneous ignition, test 5 was not valid due to displacement of a mast supporting sampling bulbs, and tests 6 and 7 were, according to authors, not "stabilized" due to large orifice diameter of 24 mm. The maximum and minimum values of measured concentrations for the tests 2 and 3 (Chaineaux et al., 1991) are presented in Table 5–3.

Ruffin et al. (1996) measured the axial concentration decay in the sub-sonic region of hydrogen and methane jets in air, where the Mach number $M<0.3$. They exploited a 5 m^3 volume tank at initial pressure and temperature prior to venting 4 MPa and 288 K respectively. The tank was vented through a horizontal pipe fitted with an orifice at its outer end. To ensure the ground had no effect on the development of the jet, the experimental rig was placed on the edge of a cliff 5 m above the ground with 100 m free space along the axis.

Four experiments with hydrogen release were carried out with different orifice diameter of 25, 50, 75 and 100 mm (Ruffin et al., 1996). Three concentration sensors used in this study, i.e. pellistors placed on a tube equipped with a vacuum pump, were located in the sub-sonic part of the jet and continuously drew the mixture at various distances from the nozzle depending on the nozzle diameter. Sensors with response time less than 1 s were mounted on thin cables positioned perpendicularly to the flow. The change in hydrogen concentration measured by different sensors as a function of time during tank's blow down was analysed. Authors suggested that it is only after the sensors have detected the maximum concentration and before the gas flow from the tank has fallen too low that a quasi-steady state can be assumed. For that reason they consider only results obtained within about 2 seconds after the onset of venting.

Unfortunately, there is no data on transient pressure within the vessel for experiments (Ruffin et al., 1996). Therefore, the under-expanded jet theory and blow-down model (Molkov et al., 2009) was applied to calculate the 2 first seconds of the blow-down of the tank for 4 experiments with different orifice diameter of 25, 50, 75 and 100 mm respectively. These calculations showed that for diameters 50, 75 and 100 mm the pressure felt after 2 seconds of release to pressures 1.79, 0.746 and 0.257 MPa respectively. The maximum and minimum values for each of the 4 experiments are given in Table 5–3, thus representing eight points. The experimental data of Ruffin et al. (1996) are partially processed using the under-expanded theory and therefore, are represented in grey in Fig. 5–5.

Okabayashi et al. (2005) investigated realistic accidental release scenarios for hydrogen refuelling stations. The experiments were performed to assess the safety of flammable gas dispersion from high pressure vessel, firstly for a steady pinhole leakage from a micro crack and secondly unsteady large-scale leakage. Five cylinders of 50 litres capacity each at pressure of 65 MPa were used, while tests were performed at lower release pressure. No data on the cylinders temperature was given in the paper. High pressure hydrogen storage of 65 MPa allowed to provide pressure 40 MPa just before the nozzle to the atmosphere.

There was a 25 mm diameter piping system between vessels and the nozzle. A valve was controlling the gas release immediately upstream of the nozzle. Four tests were performed with release pressure 40 MPa, measured just upstream of the nozzle, with different nozzle diameters: 0.25 mm (5 measurement points in different locations), 0.5 mm (3 points), 1.0 mm (21 points) and 2.0 mm (6 points), and one test at release pressure of 20 MPa with nozzle diameter 2.0 mm (5 points).

The releases (Okabayashi et al., 2005) were carried out from the nozzles located 1 m above the ground at low wind velocities less than 1 m/s. Eight sensors were located at distance 4, 6, 8, 11, 15, 20, 30 and 50 m from the nozzle and mounted on vertical poles. Authors plotted the time averaged volumetric concentrations of hydrogen along the jet axis against a non-dimensional distance from the nozzle, x/θ, where $\theta = D \cdot \sqrt{\rho_N / \rho_S}$. Unfortunately, it is not clear from the paper where density ρ_N was calculated – at actual or notional nozzle exit. In assumption that ρ_N was calculated at the actual nozzle exit, the similarity law for axial hydrogen concentration decay (5–21) can be rewritten in the form $C_{ax-m} = 5.4 \cdot \theta / x$. The maximum and minimum values for each of 5 experiments (Okabayashi et al., 2005) are plotted in Fig. 5–5. In addition, an intermediate point for 2 experiments with release diameter 1 mm and 2 mm (both at 40 MPa) are included to validate the similarity law.

In 2005–2006 a series of experiments was performed by Shell Global Solutions (UK) and Health and Safety Laboratory (UK) to characterize the hazards arising from reacting and non-reacting hydrogen release from pressurized vessels (Shirvill et al., 2005, 2006). Some experiments were carried out to investigate

the size of the flammable envelope for unignited free jets at low and high pressures. The low pressure system was composed of four multi-cylinder packs of 17 cylinders each with an initial pressure of 17.3 MPa, capable of maintaining a constant discharge pressure of 2.6 MPa for 2 minutes. The authors used two discharge orifice diameters of 6 mm and 12 mm and three discharge pressures of 0.6 MPa, 1.6 MPa and 2.6 MPa.

The high pressure system (Shirvill et al., 2005, 2006) was composed of eight multi-cylinder packs of 17 cylinders each with the same initial pressure of 17.3 MPa, capable to maintain a constant discharge pressure for a few seconds with the largest discharge orifice diameter of 12 mm. Orifice diameter of 1, 3, 4, 6 or 12 mm and discharge pressures in a range 1.1–15.1 MPa were applied in experiments. All releases were horizontal, 1.5 m above the ground. The hydrogen jet was initiated by a release valve. The pressure was recorded in the pipe on both side of the release valve and the hydrogen temperature was recorded close to the nozzle, downstream of the release valve.

The hydrogen concentration was derived (Shirvill et al., 2005, 2006) from continuous measurements of the oxygen concentration within the jet using sensors, assuming any decrease of oxygen concentration was caused by displacement by hydrogen. Oxygen concentration was measured using self-powered electrochemical oxygen sensors located 1.0, 1.5 and 2.0 m above the ground and orientated with opening perpendicular to the gas flow direction. Authors reported hydrogen concentration (% by vol.) as a function of time at each sensor location. The jet was assumed stabilized when the maximum concentration at each sensor was reached and remained steady for several seconds. The results of two experiments (2.5 MPa and 13.5 MPa) are available in (Shirvill et al., 2005) and of one experiment (10 MPa) in (Shirvill et al., 2006). The maximum and minimum values for each of the three selected experiments are shown in Table 5–3.

Kuznetsov (2006) conducted experiments to analyse hydrogen distribution in horizontal free turbulent jet in a compartment with an internal volume of 160 m^3. Experimental facility included a high pressure gas system with bundles at 30 MPa to provide hydrogen release at quasi-steady pressures in the range 2–26 MPa through a nozzle of diameter from 0.16 mm to 1 mm. The high pressure gas system with pressure and flow rate control used high speed valves and Prandtl type Pitot tubes. Hydrogen concentration profile and flow velocity were simultaneously measured at distances 0.75, 1.5, and 2.25 m from the nozzle using ultrasonic hydrogen sensor with accuracy of ±0.1%. A total of 8 experimental points from (Kuznetsov, 2006) are shown in Table 5–3 (maximum and minimum values of 4 experiments).

Veser et al. (2009) performed experiments to investigate the hydrogen distribution in a horizontal jet. The pressure, temperature and mass flow rate were regulated by using a bypass configuration. The gas was released into an attached 60 mm long pipe with inner diameter 10 mm. Pressure and temperature in the pipe were measured. The pipe fed an orifice of diameter 1, 2 or 4 mm at pressures 0.5–6.0 MPa. The exiting gas was released at temperature 35 K, 65 K, 80 K or 298 K. Orifices were positioned 0.9 m above

the ground and the jet, horizontally orientated and adjusted by laser, was released into a 5.5×8.5×3.4 m test chamber with air at ambient temperature. The temperature was measured using type K thermocouples with uncertainty ±2K and the maximum error of pressure sensors was ±0.5%. Hydrogen concentrations were measured using spherical gas probes of volume 0.3 dm^3 disposed at different locations along the jet axis. The probes content was analysed after experiments with uncertainty ±0.1%.

Houf and Schefer (2008) measured hydrogen concentration decay in small subsonic hydrogen jets. The hydrogen concentration was determined using planar laser-Rayleigh scattering. The laser sheets were imaged on a CCD camera, where concentration contours can be determined. They plot the axial time averaged hydrogen concentration along jet axis for vertical jets. The sub-sonic releases were all performed using a 1.905 mm diameter orifice and hydrogen density at the nozzle exit was 0.0838 kg/m^3. The results of 3 different experiments were published with flow velocity at the nozzle exit ranging from 49 m/s to 133 m/s. For each of 3 tests, three points (the maximum and minimum values plus one intermediate point) are presented in Table 5–3 and in Fig. 5–5.

To perform analysis of data (Veser et al., 2009) presented in the form of the reciprocal of hydrogen concentration in air by volume versus normalized distance from the nozzle, additional information on pressure in the nozzle was acquired (Kuznetsov M, 2010). Four experiments were analysed: 2 experiments with hydrogen stored at ambient temperature and released through 1 mm diameter nozzle at 5.43 MPa and through 2 mm diameter nozzle at 1.01 MPa; and 2 experiments with hydrogen stored at very low temperature of 80 K and released through 1 mm diameter nozzle at 2.99 MPa and through 2 mm diameter nozzle at 1.81 MPa.

The similarity law in its original form (Chen and Rodi, 1980) is validated here against 60 representative experimental points on axial concentration decay of pure hydrogen momentum-controlled subsonic, sonic and supersonic jets, released from vessels of different volume pressurized up to 40 MPa, and through nozzles with diameter from 0.25 mm to 100 mm. Hydrogen concentration in air was measured in the range from 1% to 86.6% by volume. The similarity law is validated for the ratio of distance from a nozzle to the nozzle diameter in the range x/D=4-28580, which is essentially beyond the maximum ratio in previous studies, e.g. expanded jets up to x/D=50 (Chen and Rodi, 1980), and under-expanded jets x/D=30-170 (Birch et al., 1984).

Laminar and turbulent, expanded and under-expanded momentum-controlled jets were used to validate the universal character of the similarity law in the original form suggested by Chen and Rodi (1980). The transition from laminar to turbulent flows for hydrogen is at Re=2000–2300 as reported by (Hawthorne et al., 1949) and (Shevyakov and Komov, 1977) respectively. Reynolds number changes in used experimental data from laminar Re=927 to highly turbulent Re=9.44×10^6.

It is worth noting that cold jets with initial storage gas temperature down to 80 K (Veser et al., 2009) obey the similarity law also. It was suggested in one of previous studies (Sunavala et al., 1957) to introduce a square root of ratio of surrounding temperature to gas temperature in the nozzle into the similarity law. This ratio does not appear to be necessary.

Figure 5–5 shows that all the experimental points are on or below the similarity law line. This is thought due to friction and minor losses in experimental equipment, which were not accounted for when the under-expanded jet theory without losses (Molkov et al., 2009) was applied. Indeed, from the similarity law equation it follows that if losses decrease pressure at the nozzle exit, and then they reduce hydrogen density and therefore the concentration in the jet for a fixed distance from the nozzle. This is equivalent to shifting experimental points down on the graph. If the spouting pressure (actual nozzle exit pressure) is applied instead of the pressure in a storage tank the difference between the similarity law curve and experimental data would reduce to zero in the limit. The universal character of the similarity law for both expanded and under-expanded jets makes it an efficient tool for hydrogen safety engineering.

5.3.4. The nomogram for concentration decay calculation in unignited jets

The nomogram for graphical calculation of hydrogen concentration decay by the similarity law and the under-expanded jet theory without losses is shown in Fig. 5–6. The nomogram includes four core graphs ("Volumetric to mass fraction", "The similarity law", "Choose leak diameter", and "Choose density in the

nozzle exit") and one additional graph "Calculate density in the nozzle exit by storage tank pressure and temperature" (based on calculations by the under-expanded jet theory without losses). Let us demonstrate how to use the nomogram to calculate the distance from the nozzle of 1 mm diameter to concentrations of hydrogen in air 4% (dash line, corresponds to the lower flammability limit of hydrogen in air) and 11% (solid line, corresponds to the average location of jet flames tip, see section "Jet fires") by volume along the axis of a release from a storage tank at pressure 70 MPa and temperature 300 K.

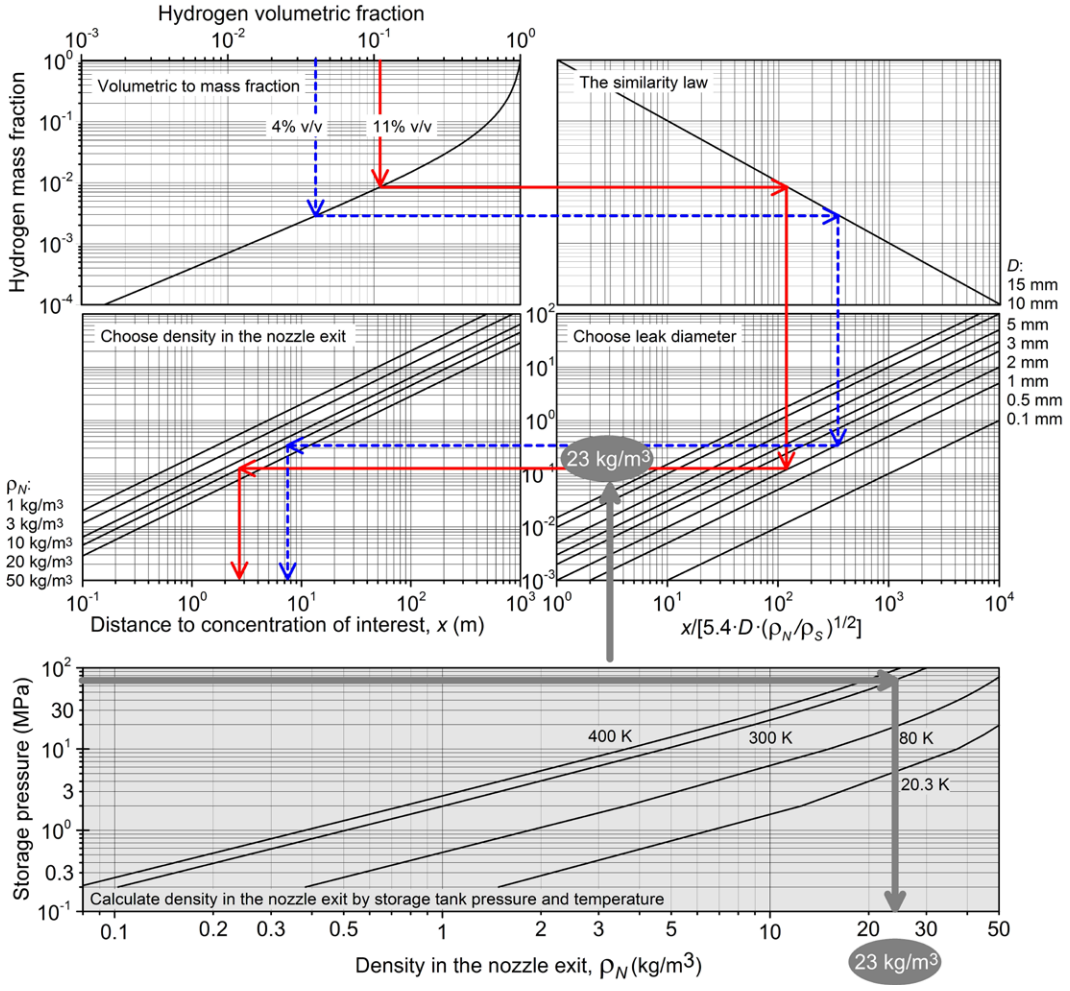

Figure 5–6. The nomogram for concentration decay calculation in unignited jets.

Firstly, the line from the axis "Hydrogen volumetric fraction" is drawn downward from the chosen concentration of interest (4% and 11% by volume in our example) until the intersection with the line of the graph "Volumetric to mass fraction". Secondly, the horizontal line from this intersection point is drawn to the intersection with the similarity law line at the right top graph "The similarity law". Thirdly, the vertical line is drawn downward until intersection with line "1 mm" at the graph "Choose leak diameter". There are eight lines on "Choose leak diameter" graph which correspond to the following leak diameters (from top to bottom): 15 mm, 10 mm, 5 mm, 3 mm, 2 mm, 1 mm, 0.5 mm, 0.1 mm). The legend is shown at the right side of the graph.

The fourth stage is to calculate the density using the additional graph "Calculate density in the nozzle exit by storage tank pressure and temperature" at the bottom of the nomogram using given pressure (70 MPa) on the ordinate axis and a line corresponding the chosen temperature (300 K). This is shown by two thick grey lines on the "Calculate density in the nozzle exit by storage tank pressure and temperature" graph. Calculated graphically density at the nozzle exit for 70 MPa and 300 K is about 23 kg/m^3.

The calculated value of density of 23 kg/m^3 is applied at the fifth stage of calculations to draw the horizontal line from the intersection with "1 mm" line at the "Choose leak diameter" graph to the left until the intersection with an imaginary line corresponding to 23 kg/m^3 at the "Choose density in the nozzle exit" graph (between two shown on the graph lines 20 kg/m^3 and 50 kg/m^3). There are five lines at the graph corresponding to densities 1 kg/m^3, 3 kg/m^3, 10 kg/m^3, 20 kg/m^3, and 50 kg/m^3 from top to bottom respectively. The legend is shown at the left side of the graph.

The final stage is to draw the vertical line downward from the intersection with the line 23 kg/m^3 to the intersection with abscissa axis of the "Choose density in the nozzle exit" graph. Thus, the calculated graphically distance from the nozzle exit to hydrogen concentration of 4% by volume is about 7.7 m, and to concentration of 11% by volume is about 2.7 m. The calculation by the equation for similarity law (5–21) with the accurate value of the density at the nozzle calculated by the under-expanded jet theory (23.95 kg/m^3) and air density of 1.205 kg/m^3 (NTP) is 8.36 m for 4% and 2.83 m for 11%. The error of graphical calculations is at the acceptable level of below 10%.

The similarity law for under-expanded jets and the nomogram are performance-based tools for calculation of deterministic separation distances for unignited releases as the alternative to prescriptive codes. For instance, the International Fire Code (2006) presents a table of prescribed separation distances between a hydrogen system and various potential targets, including air intake to building. However, this code does not provide or require any information either on the hydrogen storage parameters (pressure and temperature) and leak size from the system. This code is an example of archaic prescriptive approach that contradicts to modern requirements to codes and standards to be performance-based.

The standard NFPA 55 (2010) made one step further compared to the prescriptive International Fire Code (2010), by presenting a set of 4 equations to calculate separation distances to the axial concentration of 4% by volume of hydrogen in air. Unfortunately, there are two weak points in NFPA 55 (2010) from author's point of view. To "simplify" the use of the methodology by practitioners each of 4 equations is assigned to a quite wide range of pressures. This is resulted in "programmed" over-prediction and under-prediction of separation distance depending on the storage pressure. However, the most serious disadvantage in calculation of separation distance by NFPA 55 (2010) is the use of a leak size of only 3% of the flow area of the pipe (this choice is based on leak frequencies of other gases available to gas industry).

Indeed, the similarity law states that for the same density of hydrogen in the nozzle exit ρ_N, i.e. for the same storage pressure, the separation distance is directly proportional to leak diameter. Thus, the questionable by author choice of a leak size as 3% of cross-section area of the pipe in NFPA 55 (2010) results in the "prescribed" decrease of separation distance by reciprocal to square root from 0.03, i.e. by 5.77 times. It is clear that in case of full bore rupture of the hydrogen pipe consequences could be catastrophic if this "3%" approach is widely applied and enforced by regulators. The risk-informed approaches cannot compromise the science-informed engineering design. The alternatives to this "forced" decrease of separation distance is safety engineering design of hydrogen systems, e.g. reduction of pressure in the pipe when possible and the pipe diameter to the minimum size required by the technological reasons and/or substitution of one large pipe by a number of smaller pipes, use of PRD with enhanced safety characteristics, etc.

The conclusion can be drawn that the similarity law calculates separation distance more accurately compared to currently available standards and codes. This methodology is scientifically underpinned and can account for friction and minor losses in a leak pathway when necessary. Last but not least the hydrogen safety engineering guarantees the freedom to consider worst-credible scenario of full bore rupture rather than the questionable 3% of cross section area of pipe approach as suggested by some codes and standards.

5.4. Concentration decay in transitional and buoyancy-controlled jets

All jets can be divided into three types based on the effect of buoyancy. These jet types are shown schematically in Fig. 5–7 for a horizontal jet. Fully momentum-controlled jets are not affected by buoyancy. Fully buoyancy-controlled jets are quickly diverted from the horizontal to vertical flow

direction. Third type of jets that can be called transitional have momentum-dominated part closer to the nozzle and buoyancy-controlled flow further downstream when jet velocity drops and jet diameter increases. For hydrogen safety engineering it is important to know when this transition takes place. This has direct implication on the separation distance and thus safety and costs of hydrogen system or infrastructure.

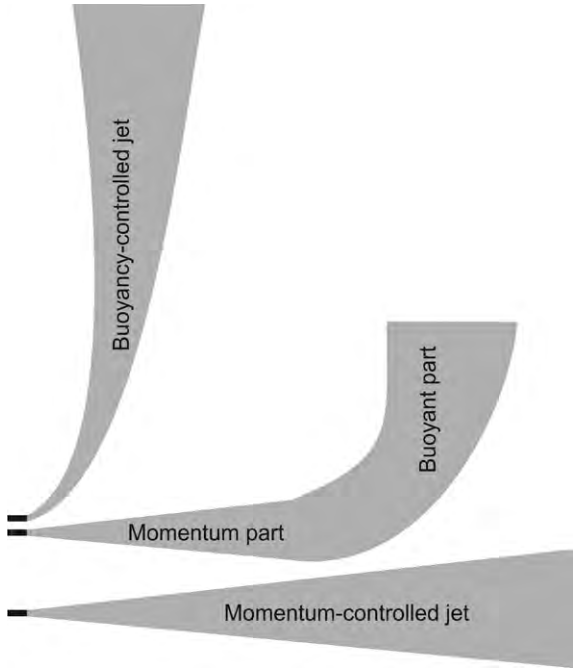

Figure 5–7. Fully momentum-controlled jet (bottom), transitional jet (middle), and fully buoyancy-controlled jet.

The engineering technique presented here to qualify a hydrogen jet (both expanded and under-expanded) or its part as momentum-controlled, and the rest of the jet downstream as buoyancy-controlled, is based on the work by Shevyakov et al. (1980, 2004) that was carried out with expanded jets only. Figure 5–8 shows in logarithmic coordinates the dependence of the distance to nozzle diameter ratio x/D (ordinate) for particular concentration of hydrogen in air on the Froude number (abscissa) in its classical form

$$Fr = \frac{U^2}{gD}, \tag{5–25}$$

where U is the velocity at the nozzle exit (notional nozzle exit for under-expanded jets) in m/s, g is the gravitational acceleration (standard acceleration of gravity on Earth is 9.80665 m/s^2), and D is the nozzle diameter (notional nozzle exit diameter for under-expanded jet) in meters. For under-expanded jets in Fig. 5–8 the notional nozzle exit diameter and velocity at the notional nozzle exit were calculated by the under-expanded jet theory (Molkov et al., 2009). Both expanded and under-expanded jets obey the same functional dependence with accuracy 20% acceptable for engineering applications.

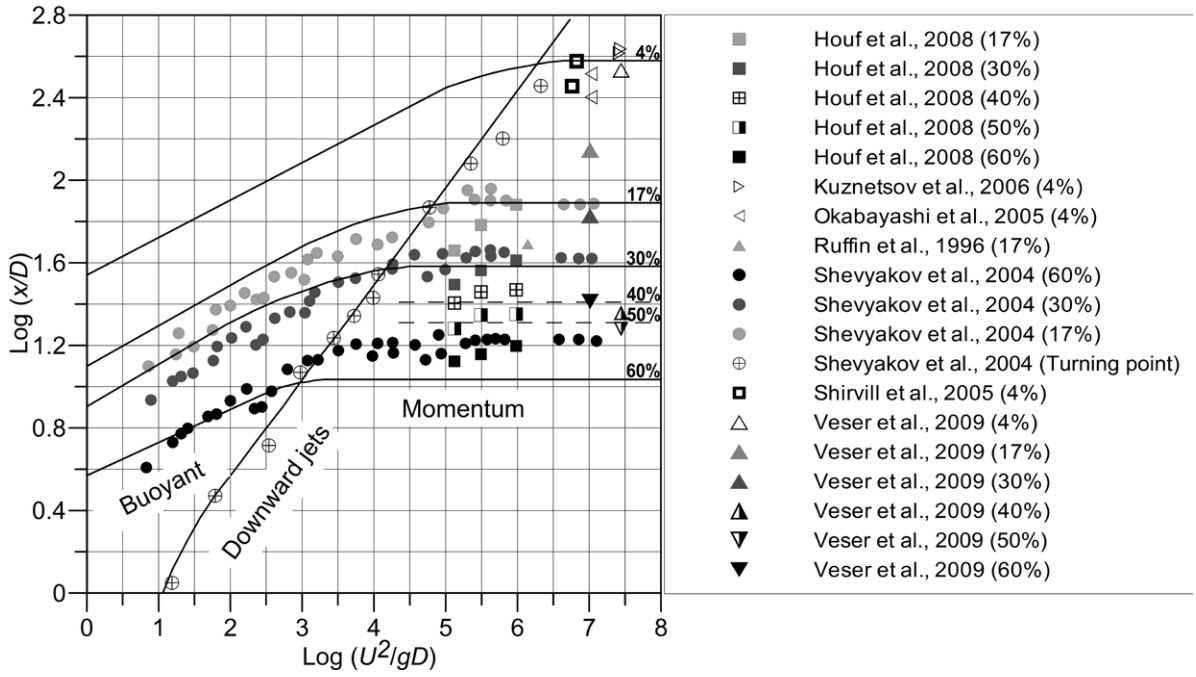

Figure 5–8. The dependence of the distance to nozzle diameter ratio for particular concentration of hydrogen in air on the Froude number.

Five theoretical curves (solid lines) by Shevyakov et al. (1980, 2004), experimental data for expanded jets (Shevyakov et al., 1980, 2004), and data of other researchers for under-expanded jets are shown in Fig. 5–8. Practically all under-expanded jets in hydrogen incidents/accidents will be in the momentum-controlled regime as follows from available tests applied to validate the correlation in Fig. 5–8. Four of five theoretical curves in the graph are related to hydrogen concentrations of 4%, 17%, 30%, and 60% by volume respectively. Each of these four curves has an ascending buoyant part and a momentum "plateau" part.

It is important to stress that the Froude number at transition from the buoyant part of the curve to the momentum part depends on the concentration of hydrogen under consideration. For example, at axial concentration of hydrogen 60% by volume the jet stays in momentum-controlled regime until *Log* (*Fr*)>3.5, while for the jet to be in the momentum-controlled regime at axial location where hydrogen concentration drops to 4% by volume (LFL) the nozzle exit Froude number has to be much higher, i.e. *Log* (*Fr*)>6.5 (three orders of magnitude higher).

The fifth curve in Fig. 5–8 "Downward jets" is of special interest for hydrogen safety engineering. It gives for a jet directed vertically downward a dimensionless distance from the nozzle to the turning point, where the jet changes direction of flow from downward to upward. To calculate the distance to turning point only knowledge of the Froude number at the nozzle (notional nozzle) is required. The fifth curve intersects each of the four other curves in Fig. 5–8 in the region of transition from momentum-dominated to buoyancy-controlled flow as expected.

The following sequence is applied in use of the correlation in Fig. 5–8. Firstly, the nozzle exit Froude number is calculated and its logarithm. The under-expanded theory is applied to calculate the notional nozzle exit diameter and the velocity in the notional nozzle exit when applicable. Then, a vertical line is drawn upward from a point on the abscissa axis equal to the calculated Froude number logarithm. The intersection of this vertical line with the line marked "Downward jets" on the graph indicates the concentration above which the jet is momentum-dominated and below which the jet is buoyancy-controlled.

For example, if a jet exit Froude number is $Log\ (Fr)=4.25$ (intersection of the vertical line with line "Downward jets" is at location of the theoretical curve corresponding to 30% by volume of hydrogen) then the jet is in momentum-dominated regime while the concentration in the jet is above 30% by volume and it becomes buoyant when the concentration on the jet axis is below 30% (further downstream of the axial concentration of 30% by volume).

This technique is quite simple to apply and at the same time can be very useful to develop cost-effective hydrogen safety solutions. For instance, the separation distance for a horizontal jet release can be essentially reduced as only a length of the momentum-dominated part of the jet can be taken as an indication of the separation distance rather than aggregated (both momentum- and buoyancy-controlled parts of the jet) distance to 4% by volume (LFL).

6 Dispersion of hydrogen in confined space

The formation of a flammable mixture is a major safety concern for indoor use of hydrogen and fuel cell systems. One of relevant questions is how safe is permeation of hydrogen from an on-board storage and its dispersion in a garage. Is natural ventilation sufficient to eliminate potential hazard of flammable hydrogen-air mixture formation? Distribution of permeated hydrogen within an enclosure, when LFL of hydrogen in air (4% by volume) is reached, is important to define maximum allowable permeation rate for hydrogen fuel cell vehicles with compressed hydrogen tanks onboard.

A unique feature of hydrogen is the pressure peaking phenomenon. It is described in detail in this chapter. Another issue considered in this chapter is a limit of hydrogen mass flow rate in an enclosure with known natural ventilation, i.e. sizes and location of vents, that will definitely followed with time by 100% by volume of hydrogen atmosphere in the enclosure.

6.1. Dispersion of permeated hydrogen in a garage

Definition of permeation could be found elsewhere (SAE J2578, 2009): *diffusion through the walls or interstices of a container vessel, piping or interface material*. It is especially pronounced for hydrogen as it is the smallest element with a highest diffusivity. It is worth noting that hydrogen permeation is atomic through metals and molecular through polymers (Schultheiß, 2007).

Compressed gaseous hydrogen (CGH_2) containers are categorised into the following four types (Commission Regulation, 2009): Type 1 – seamless metallic container, Type 2 – hoop wrapped container with a seamless metallic liner, Type 3 – fully wrapped container with a seamless or welded metallic liner, and Type 4 – fully wrapped container with a non-metallic liner. In Type 3 and 4 containers, the main purpose of the liner is containment of the hydrogen gas, while the overwrapping provides the structural strength of the container (Adams et al., 2011). Current Type 4 containers use a polymer as the liner, e.g. high-density polyethylene, typically overwrapped with carbon fibres set in a resin matrix. Other fibres such as glass or aramid may also be used, but most automotive systems use carbon fibre. The overwrap varies in thickness around the container depending on the stress distribution, as does the fibre direction. Type 3 or Type 4 containers are used for most automotive applications.

Permeation in the context of CGH_2 systems is diffusion through the walls or interstices of a container vessel, piping or interface material. Permeation may be categorised as a long term slow hydrogen release from a CGH_2 system. Controlling permeation has long been recognised as a key enabler in the development of hydrogen storage technologies (Mitlitsky et al., 2000). For metallic containers or containers with metallic liners, i.e. Types 1, 2 or 3, the permeation rate is considered to be negligible. However, hydrogen permeation is an issue for containers with non-metallic (polymer) liners, i.e. Type 4 containers.

In this section the dispersion of permeated hydrogen from a storage tank in a typical garage with adiabatic walls and still air is studied analytically and numerically. Numerical simulations are performed based on an original approach of a hydrogen mass source term introduction in the hydrogen conservation equation in control volumes around the tank surface. It is shown that the maximum hydrogen concentration in an enclosure is always on the top surface of the tank and it never reaches 100% by volume. Both the analytical analysis and numerical simulations have demonstrated that diffusion and buoyancy contributions to the hydrogen transport from the tank surface are balanced within 1 minute from the beginning of the process. The quasi-steady state conditions within the enclosure with approximately linear distribution of hydrogen from the top to the bottom are established in about 1 hour for considered permeation rates.

6.1.1. Permeation rate

The economical and technological viability of on-board hydrogen tanks depends amongst other things on their gravimetric and volumetric capacity. The gravimetric capacity is currently improved with thin walls made of light, non-metallic materials in types 4 tanks. However, they are characterized by a strong permeability. For example, at 293 K, aluminium has a low permeability 2.84×10^{-27} mol/s/m/MPa$^{1/2}$ (Korinko et al., 2001),while a polymer like Noryl has a permeability of 5.55×10^{-15} mol/s/m/MPa$^{1/2}$ (Stodilka et al., 2000), i.e. 12 orders of magnitude bigger.

The improvement of the volumetric capacity can be achieved by pressure increase from 35 MPa to 70 MPa for vehicles. However, this will increase the permeation rate. The permeation from onboard hydrogen tanks is a safety issue for enclosures where the hydrogen can accumulate over time to create a flammable mixture with air. In sealed enclosures without ventilation the lower flammability limit (LFL) of 4% by volume of hydrogen in air can be reached as a result of permeation after quite a long time. To estimate the time for reaching LFL locally, e.g. under the garage ceiling, or homogeneously throughout the garage it is important to know how hydrogen will be distributed in the enclosure.

The permeability of hydrogen for a particular material can be calculated as (Schefer et al., 2006a)

$$P = P_0 \exp(-E_0 / RT) , \tag{6–1}$$

where the pre-exponential factor P_0 (mol/s/m/MPa$^{1/2}$) and the activation energy E_0 (J/mol) are material dependent, and T is temperature, K. The permeation rate through a single material's membrane is calculated using the equation (Schefer et al., 2006a)

$$J = P\frac{\sqrt{p_r}}{l}, \tag{6–2}$$

where p_r is the reservoir pressure, MPa; and l is the reservoir wall thickness, m. The permeation rate increases with an increase of storage pressure p_r and a decrease of membrane thickness l. Equations (6–1) and (6–2) are valid for metallic and non-metallic materials (Schultheiß, 2007) and applicable to a single membrane's wall but under limited range of pressure and temperature from 10 Pa to 50 MPa and ambient temperature less than 1273 K respectively (San Marchi et al., 2007).

For serial membranes of different materials like in type 4 tanks the total permeability for z layers can be calculated using correlations found elsewhere (Crank, 1975)

$$\frac{l}{P} = \sum_{i=1}^{z} \frac{l_i}{P_i} . \tag{6–3}$$

6.1.2. Diffusion and buoyancy transport of permeated hydrogen

It is important to understand: what is the maximum concentration of permeated hydrogen at a tank surface. Let us estimate permeated hydrogen concentration in the beginning of a process when pressurised storage tank is just placed into an enclosure with still air. Molecules of hydrogen permeated from the tank are subject to Brownian motion that is a random movement of molecules suspended in a liquid or a gas. The chaotic movement is influenced by collisions between molecules of hydrogen and other molecules in the air. Following the Einstein's law (1905), which is valid for Brownian motion, the displacement in direction of the x-axis that a particle experiences on the average, or, to be more precise, the root-mean-square displacement is

$$\lambda_x = \sqrt{\overline{\Delta x^2}} = \sqrt{2 \cdot D \cdot t} , \tag{6–4}$$

where D is the diffusion of hydrogen in air (at 25°C it can be accepted as 7.79 $\times 10^{-5}$ m^2/s), and t is the time, s. As the displacement of molecules during time t is $\sqrt{2 \cdot D \cdot t}$, a volume comprising all permeated hydrogen molecules around the tank surface of area A_r is $V_{mix} = A_r \sqrt{2 \cdot D \cdot t}$. The number of moles of permeated hydrogen in this volume is $n = J \cdot t \cdot A_r$. Assuming uniform distribution of hydrogen molecules in the volume V_{mix}, the volumetric concentration of hydrogen on the tank's surface at time t is the ratio of the volume of hydrogen to the total volume V_x can be calculated as

$$[H_2]_t = 100 \frac{n \cdot V_{m25}}{V_{mix}}, \tag{6–5}$$

where V_{m25} is the molar volume of ideal gas at 25°C (0.0244 m^3/mol). The equation can be rewritten as

$$[H_2]_t = 100 \frac{J \cdot t \cdot A_r \cdot V_{m25}}{\sqrt{2 \cdot D \cdot t} \cdot A_r} = 100 \frac{J \cdot V_{m25}}{\sqrt{2 \cdot D}} \times \sqrt{t}\,. \tag{6–6}$$

It is obvious that the buoyancy effect increases with the increase of hydrogen concentration in air. Thus, the hydrogen concentration on the tank surface increases with time as $[H_2]_t \propto \sqrt{t}$ until the buoyancy will overcome diffusion transport of hydrogen. A quasi-steady state will be established when diffusion and buoyancy will balance each other.

The second Newton's Law for buoyant motion of hydrogen-air mixture of density ρ_{mix} in air of density ρ_{air} can be written as $F = m_{mix} \cdot a = (\rho_{air} - \rho_{mix}) V_{mix} \cdot g$. From mechanics a distance passed by a body moving with acceleration a is $L_x = a \cdot t^2 / 2$, and therefore

$$\rho_{mix} \cdot a = \rho_{mix} \cdot \frac{2 \cdot L_x}{t^2} = (\rho_{air} - \rho_{mix}) g , \tag{6–7}$$

Thus, the displacement of mixture by buoyancy with time is

$$L_x = \left(\frac{\rho_{air}}{\rho_{mix}} - 1 \right) \cdot \frac{g \cdot t^2}{2} , \tag{6–8}$$

where the density of mixture is by definition

$$\rho_{mix} = \frac{[H_2]_t}{100} \cdot \left(\rho_{H_2} - \rho_{air} \right) + \rho_{air} . \tag{6–9}$$

The displacement of hydrogen by buoyancy becomes of the same order as the displacement of hydrogen by diffusion, $\lambda_x = L_x$, and process reaches the quasi-steady state when

$$\sqrt{2 \cdot D \cdot t} = \left(\frac{\rho_{air}}{\frac{J \cdot t \cdot V_{m25}}{\sqrt{2 \cdot D \cdot t}} \left(\rho_{H2} - \rho_{air} \right) + \rho_{air}} - 1 \right) \cdot \frac{g \cdot t^2}{2} \cdot \tag{6–10}$$

This equation yields time 37 s for the permeation rate J=1 Ncm^3/hr/L (normal cubic centimetres of hydrogen per hour per litre of container internal volume) of tank capacity (scenario 1), and 16 s for the permeation rate J=45 Ncm^3/hr/L (scenario 2) as per SAE J2578 (2009) for a tank and a garage described in the next section.

Within the assumptions of this section, the hydrogen concentration on the tank's surface at these characteristic times can be calculated using Eq. (6–6) as 2.4×10^{-4} % by volume and 1×10^{-2} % by volume respectively. Both values of hydrogen concentrations at the tank surface are far below LFL of hydrogen in air of 4% by volume.

6.1.3. Uniformity of permeated hydrogen concentration distribution

In this section the question about an extent of uniformity of permeated hydrogen distribution within a garage-like enclosure for different permeation rates is addressed. Numerical simulations of permeated hydrogen dispersion in an enclosure were performed for the two scenarios that differ by permeation rate only. A compressed hydrogen storage tank of 0.672 m long and of 0.505 m diameter with a hemispherical ends of 0.505 m diameter with surface area of A_r=1.87 m^2 and volume of about V_r=0.2 m^3 is located in the centre of an enclosure with sizes of typical garage $L \times W \times H$=5×3×2.2 m and volume of V_g=33 m^3 with clearance between the tank and the garage floor of 0.5 m. The ambient temperature is 298 K.

In scenario 1 the permeation rate is J=1 Ncm^3/hr/L, i.e. below the allowable by the European Law (Commission Regulation, 2010) permeation rate limit of 6 Ncm^3/hr/L (at 20^{o}C). In scenario 2 the permeation rate is J=45 Ncm^3/hr/L, i.e. above the European Law limit, and is equivalent to the maximum "*normal hydrogen discharges*" (including permeation leaks) of 150 Ncm^3/min per car at normal temperature and pressure recommended by SAE J2578 (2009).

If the enclosure would be perfectly sealed then the time t_c necessary for hydrogen to reach the homogenous LFL concentration of c=4% by volume is

$$t_c = \frac{V_g \cdot c}{V_{m25} \cdot J \cdot A_r}. \tag{6–11}$$

This yields about 275 days for scenario 1 and 6 days for scenario 2. The time to create flammable mixture at LFL level would reduce if assumption about the uniformity of hydrogen distribution is not valid and permeated hydrogen would gather in a layer.

The CFD model applied to simulate permeated hydrogen dispersion and numerical details are described by Saffers et al. (2011). To decrease a simulation time the incompressible model was applied. To make the assumption of incompressibility consistent, a square vent of 0.2x0.2 m located on the floor of the garage with outflow boundary conditions was modelled. The presence of the vent creates in simulations artificial downward velocity of hydrogen-air mixture within the enclosure. This velocity is assessed using volumetric flow rate of permeated hydrogen and enclosure geometry and is about 3.62×10^{-9} m/s for scenario 1 and 1.63×10^{-7} m/s for scenario 2. For comparison the characteristic "diffusion" velocity of the order of D/H=3.54×10^{-5} m/s is much higher.

Dispersion of permeated hydrogen is a physical phenomenon essentially different from classical leaks, i.e. plumes and jets. Permeated hydrogen "leaks" in very small amounts uniformly along the surface of storage tank. Then hydrogen is driven out of the surface by diffusion and buoyancy. The source of permeated hydrogen was modelled using volumetric source of hydrogen in a thin layer of control volumes of 1 mm thickness around the tank surface. This is different modelling approach compared to artificial plumes/jets with 100% hydrogen concentration and non-physical momentum in the source.

Indeed, as demonstrate below, the permeation rate used in this study does not release enough hydrogen to cover the whole surface of the tank to form a single layer of pure hydrogen (100% by volume) as the diffusion process displaces quickly the hydrogen molecules away from the tank's surface.

One mole of ideal gas occupies 24.4 L at 25°C, i.e. there are about 41 moles of ideal gas in 1 m^3. Let us estimate a number of hydrogen moles released from the tank surface of 1.87 m^2 in a unit of time. At the permeation rate of 45 $Ncm^3/hr/L$ (scenario 2) and V_r=200 L a volume of permeated hydrogen is 25×10^{-7} m^3 in a unit of time (1 s), i.e. 1.02×10^{-4} moles are permeated in 1 s. This number of moles will occupy a volume equal to the product of the tank surface area multiplied by a characteristic distance of hydrogen transport by diffusion from the surface that can be estimated as $D^{1/2}$ in a unit of time, i.e. 8.8×10^{-3} m. This volume is 0.0165 m^3. Thus, the number of moles of permeated hydrogen per unit volume close to the surface is 0.0062 mol/m^3.

This means that the mole fraction of hydrogen is $0.0062/41=1.5\times10^{-4}$ or 0.0015% by volume. This simplified estimate is consistent with results of numerical simulations (see results for rake 01) both providing a proof that there is no 100% by volume of hydrogen concentration at the tank surface during the permeation, and it is far below LFL even for scenario 2.

The calculation domain represented a quarter of the garage (see Fig. 6–1). Profiles of the hydrogen concentration distribution across the garage height are reported below at locations of three vertical rakes: in the centre of the garage (rake 01), in the middle between the tank and the wall (rake 02) and along the wall at distance 0.1 m from the wall (rake 03).

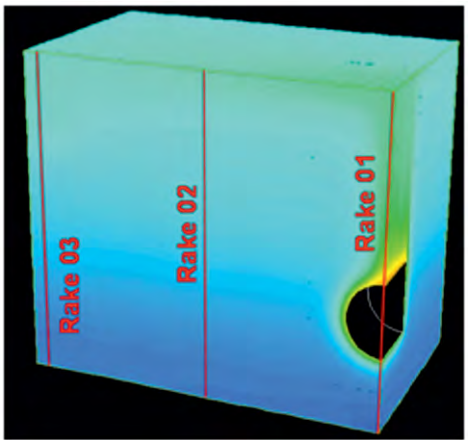

Figure 6–1. Calculation domain (garage quarter) and location of rakes.

To match the specified permeation rates, the hydrogen mass volumetric source term was equal to $S_{H2}=2.43\times10^{-6}$ kg/m^3/s for scenario 1 and to $S_{H2}=1.09\times10^{-4}$ kg/m^3/s for scenario 2. The minimum control volume (CV) size was on tank's surface and equal to $\Delta x=0.5$ mm, so the hydrogen was released in a layer of two CV thickness along the surface. The total number of CVs in the calculation domain was 194,464. SIMPLE algorithm was used for pressure-velocity coupling with 3rd order MUSCL discretisation scheme for convective terms, central difference for diffusion terms, and 2nd order implicit time stepping. It is a common practice to use implicit SIMPLE-similar procedure for incompressible flows. Hydrogen mass balance was monitored as a main indicator of acceptable numerical convergence.

The maximum hydrogen concentration in simulations is on the top of the tank as expected. The difference of 10% in thickness of hydrogen layer at the top and at the bottom of the tank surface is reached in simulations at 60 s and 12 s after the start of the process for scenarios 1 and 2 respectively. This is in an agreement with similar values obtained during the simplified analysis of the problem, i.e. 37 s and 16 s, characterising the time to the balance between contribution of diffusion and buoyancy to the hydrogen transport away from the tank surface.

The profiles of hydrogen concentration at location of rakes 01, 02 and 03 for both scenarios are shown in Fig. 6–2. The maximum concentration of hydrogen is always at the top of the tank. It reaches a negligible value of 6.24×10^{-3} % by volume for scenario 1 and 1.82×10^{-1} % by volume for scenario 2 after 133 min.

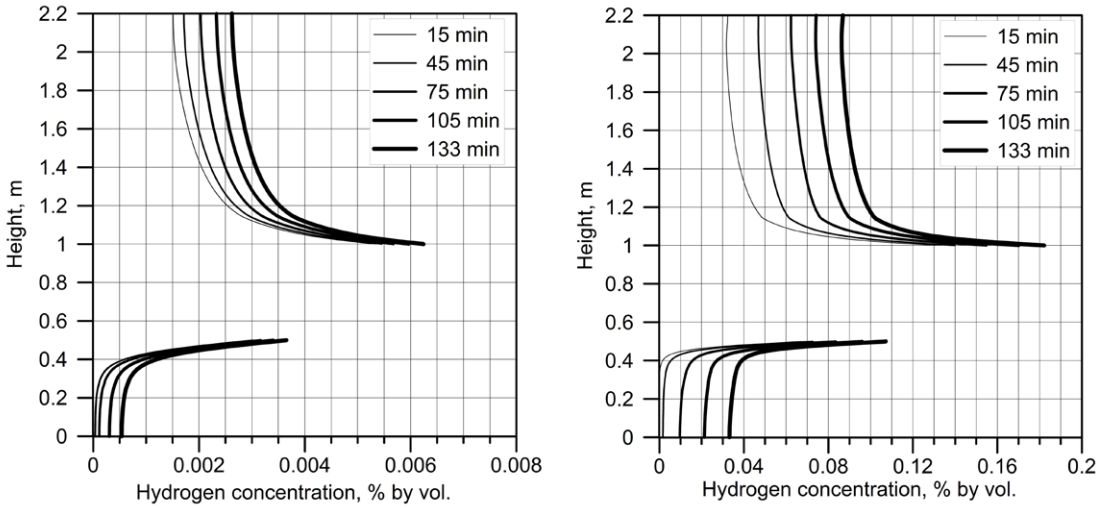

Figure 6–2. Hydrogen concentration profile across the garage height at location of rake 01 with time: left - scenario 1; right - scenario 2.

Profiles of hydrogen concentration across the garage height at rake 02 position are shown in Fig. 6–3. After about 60 minutes from the beginning of the process, a quasi-steady gradient of hydrogen concentration with height is reached. Starting from this moment the hydrogen concentration increases in time with the same increments both at the top and at the bottom of the garage thus preserving hydrogen concentration gradient. The established difference in concentration throughout the garage height obtained by numerical simulations is negligible in practical sense, i.e. 2×10^{-3} % by volume for scenario 1 and 5×10^{-2} % by volume for scenario 2. Both are essentially below the LFL of 4% by volume.

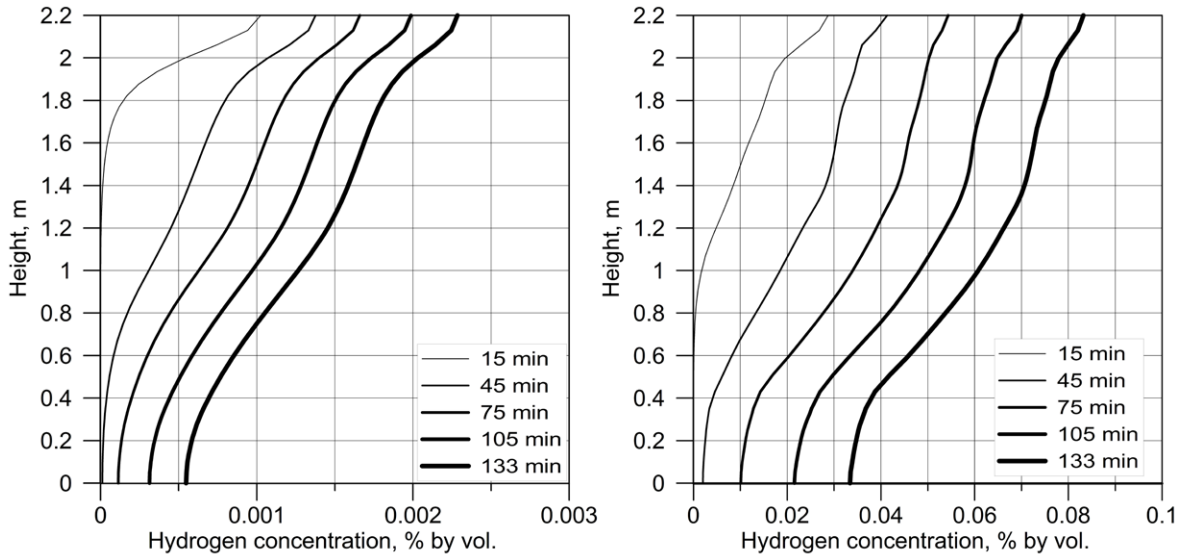

Figure 6–3. Hydrogen concentration profile across the garage height at location of rake 02 with time: left – scenario 1; right – scenario 2.

Profiles of hydrogen concentration across the garage height at rake 03 position are shown in Fig. 6–4. At 15 minutes after the start of permeation, the gradient of concentration is not linear due to the presence of the wall. The wall effect nevertheless disappears with time and the gradient linearity is established at about 60 minutes after the beginning of the process similar to rake 02.

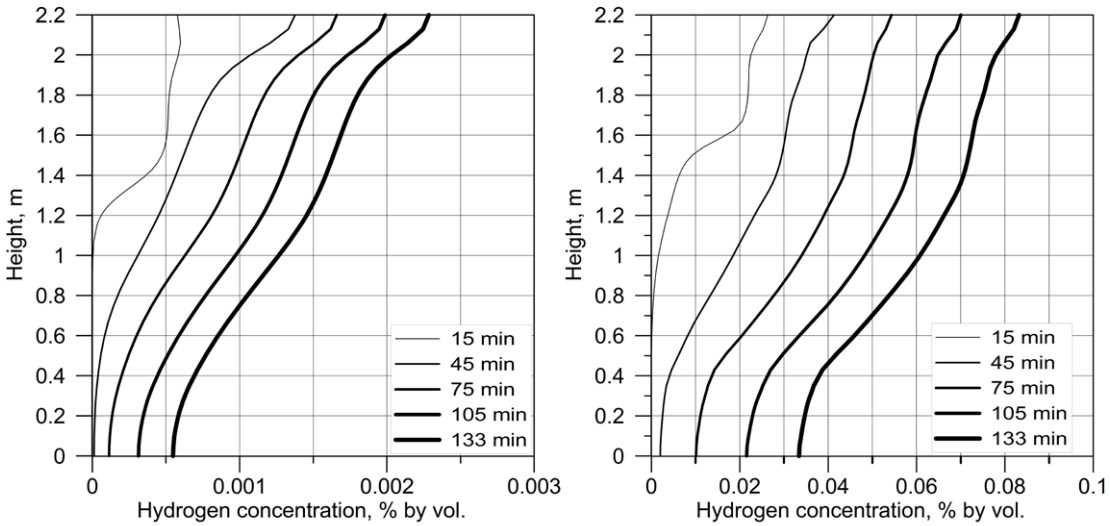

Figure 6–4. Hydrogen concentration profile across the garage height at location of rake 03 with time: left – scenario 1; right – scenario 2.

The change of the ratio of hydrogen concentration at the bottom to concentration at the top of the garage is shown in Fig. 6–5. The difference in concentration diminishes with time and the ratio tends to be 1. This proves that there is no stratification of permeated hydrogen in the garage in a practical sense. Presence of non-adiabatic walls and air movement would facilitate a perfect mixing of permeated hydrogen with air within the enclosure. The larger the permeation rate the faster the uniformity will be achieved. For example, concentration at the bottom reaches 0.1 of concentration at the top at about 80 minutes for scenario 1 and at about 55 minutes for scenario 2.

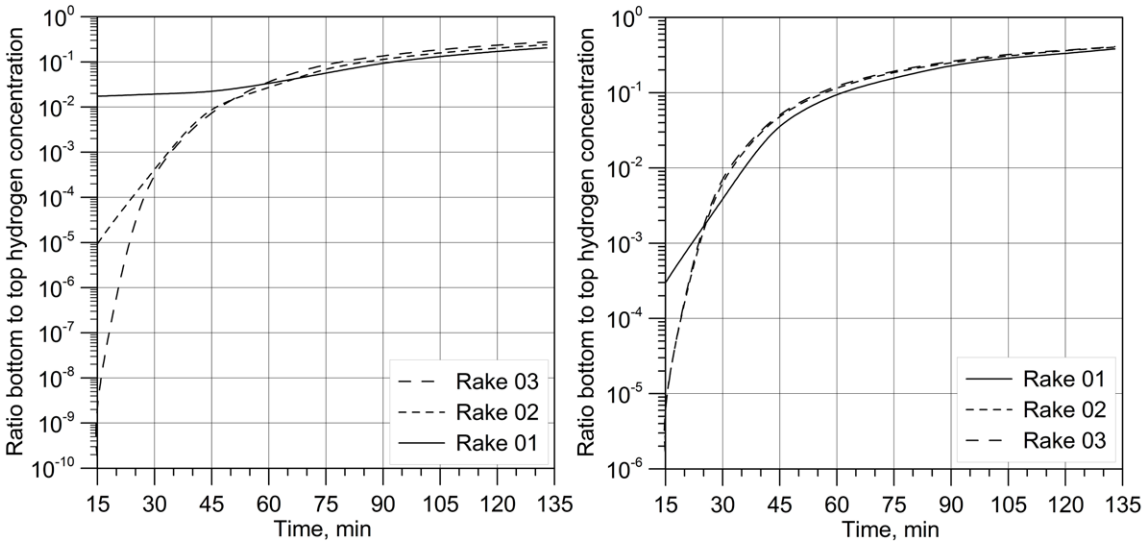

Figure 6–5. Change of the ratio of the bottom to top hydrogen concentration at the three rakes: left – scenario 1; right – scenario 2.

The following conclusions can be drawn for this section. The concentration of hydrogen on the tank's surface grows as square root of time at the initial stage of permeation. The maximum concentration of hydrogen is always on the top of the tank. However, it will never reach 100% of hydrogen by volume for any realistic enclosure (not perfectly sealed to continue accumulation). The buoyancy and the diffusion are in balance at about 37 seconds after the start of the process for 1 $Ncm^3/hr/L$ permeation rate and after 16 seconds for 45 $Ncm^3/hr/L$ rate according to the analytical estimate. This is confirmed by numerical simulations. Indeed, the 10% distortion by buoyancy of the cylindrical symmetry of hydrogen transport by diffusion is simulated at time 60 s and 12 s respectively. Numerical simulations, based on the original modelling approach of permeated hydrogen dispersion (source term of hydrogen in species equation at the tank surface rather than a plume of 100% of hydrogen with mass flow rate equal to permeation rate integrated throughout the tank surface), confirmed analytical estimate that hydrogen concentration on the surface is far below even the LFL of 4% by volume. Simulations have shown as well that distribution of hydrogen is uniform throughout the garage in the practical sense. The ratio of the bottom to the top hydrogen concentration tends to 1 with time. The uniformity of hydrogen-air mixture formed in enclosure as a result of permeation allows application of the perfect mixing equation (Marshall, 1983) to derive requirements to permeation rates (Adams et al., 2011) for the Commission Regulation (EU) No. 406/2010 of 26 April 2010.

6.1.4. Allowable permeation rate from hydrogen-powered vehicles

A long term slow hydrogen release such as that due to permeation from a vehicle into an inadequately ventilated enclosed structure is a potential hazard and associated risk of hydrogen in automotive applications. Due to its small size hydrogen permeates through the containment materials found in compressed gaseous hydrogen storage systems and is an issue that requires consideration for containers with non-metallic (polymer) liners (Adams et al., 2011). This section focuses on the development of a methodology to estimate an allowable upper limit for hydrogen permeation in automotive applications. Worst credible scenarios are identified and a maximum hydrogen permeation rate from road vehicles into enclosed garage structures is estimated. One of the key challenges in estimating an allowable hydrogen permeation rate is the very wide variation in the design, construction and ventilation requirements for enclosed structures.

Hydrogen is typically considered for use in city buses and cars with fuel cell based drivetrains and to a lesser extent internal combustion engines. Typical full size, single deck, non-articulated city bus dimensions are length 12 m, width 2.55 m, height 3 m, with a reasonable maximum hydrogen storage quantity of 50 kg according to the HyFLEET project. For a passenger car the maximum quantity of hydrogen required is in the order of 3–10 kg depending on the size and characteristics of the car, and stored at pressure 35 MPa or 70 MPa. Bus storage systems are usually roof mounted, with the fuel cells either mounted on the roof or at the back of the vehicle. For passenger cars, high pressure hydrogen storage systems are usually mounted near the rear axle as this position offers the best protection in the event of a traffic accident.

Typical enclosed structures used by road vehicles include domestic single or multi-vehicle garages, partially enclosed public parking like multi-storey parking with semi-open sides, fully enclosed public parking like underground parking, city bus garages, maintenance facilities, showrooms, covered bus stations, covered loading bays, containers for shipping vehicles, ferries, tunnels or wide over bridges, rail transport, e.g. Channel Tunnel vehicle shuttles, etc.

The methodology for estimating an allowable hydrogen permeation rate is based on the assumption that permeated hydrogen disperses homogeneously in enclosure, as shown in previous section, allowing the prefect mixing equation to be used to estimate the allowable rate. Specific focus is placed on assessing the maximum prolonged material temperature and worst credible enclosure ventilation.

With respect to hydrogen permeation, the critical cases were considered to be domestic garages for passenger cars and city bus maintenance facilities as being representative for commercial vehicles. For example, the proposed scenario for a single bus is based on the minimum maintenance volume (Adams et al., 2011). Typical working space requirements for a city bus maintenance facility are approximately 2 m to each side of the bus including the front and rear. Above the bus, 2 m is necessary to be able to lift the bus to work beneath it and a further 1.5 m is necessary for lighting and other services, giving a distance between the floor and roof of approximately 6.5 m.

6.1.4.1. Effect of temperature

One of the key parameters affecting the actual permeation rate of hydrogen through the walls of a hydrogen container is the temperature of the container materials (Mitlitsky et al., 2000). The temperature of a container wall material is influenced by thermodynamic processes inside the container, e.g. during refilling, and by the ambient temperature. All current RCS specify a maximum material temperature of 85^{0}C for container materials (Adams et al., 2011). In terms of normal usage of the system, the only time that a temperature of 85^{0}C would be experienced inside the container is immediately after fast refilling. Tests have repeatedly shown that the temperature falls rapidly after the refilling is complete so that the material temperature should drop below 50^{0}C in a few minutes (Jeary, 2001).

The hottest recorded ambient air temperature anywhere in the world is 57.8^{0}C recorded in El Azizia in Libya in 1922, while in Europe it is 48.0^{0}C recorded in Athens in 1977, lasting for 1–2 hours at most following references in (Adams et al., 2011). With respect to long term average temperatures, which are of more relevance to the permeation phenomenon, the maximum figures are somewhat lower. The average monthly maximum and minimum temperatures over a 38 year period between 1913 and 1951 for El Azizia in Libya show that for the hottest month, July, the average maximum and minimum temperatures were 37^{0}C and 20^{0}C respectively [21]. A statistical analysis of temperature loads for the StorHy project showed that in an example city (Athens) over a 30 year period average temperatures exceeded 35^{0}C for 5% of the year (Mair et al., 2007). The air temperature inside buildings will vary from the ambient outside temperature. Although no research was found on this subject the prolonged temperatures will be significantly lower than peak temperatures which will be of relatively very short duration in the context of the permeation issue (Adams et al., 2011).

It was concluded (Adams et al., 2011), a prolonged material temperature of 85^0C in an enclosed facility or beneath a vehicle is extreme and would only be experienced for short periods in comparison to the time necessary for permeation to produce hazardous concentrations of hydrogen which is in the order of weeks for a perfectly sealed enclosure. In addition, the permeation barrier, i.e. the liner, would be insulated by thick carbon fibre wrapping. Based on the above and allowing for the effect of some additional warming inside an enclosed structure, a reasonable and conservative maximum prolonged material temperature is accepted as 55^0C, which harmonises with (SAE J2579, 2009).

6.1.4.2. Worst-credible scenario

One of the key issues in determining an acceptable permeation rate is the worst-credible natural ventilation rate of enclosed structures such as garages. Life safety should be assured independent of the combination of vehicle and structure. A review of ventilation requirements undertaken within the HySafe consortium indicated that in some European countries there are no minimum requirements for natural garage ventilation (Miles, 2007). Although natural ventilation rates in many types of homes and other buildings are well studied, those for residential garages are not (Adams et al., 2011). Parameters of typical garages considered for the purpose of this section are given in (Adams et al., 2011).

Six references were identified providing detailed sets of real world natural garage ventilation measurements including two studies by the Canada Mortgage and Housing Association (2001, 2004), two studies by the Electric Power Research Institute in the USA (1991, 1996), and a study by TIAX (2001), (Waterland, 2005) in the USA. The lowest measurement identified in real world conditions was 0.03 ACH (air change per hour) from the TIAX (2001) study. It is worth noting that experiments in a well sealed experimental garage at CEA with all vents closed and doors sealed, gave a natural helium leak rate of 6 NL/min, which is equivalent to 0.01 ACH assuming that the helium leak rate corresponds to the natural ventilation rate (Cariteau et al., 2011).

The available real world measurements are shown in Fig. 6–6, excluding the data ranging from 17-47ACH from the Canadian studies which were considered to be unreasonably high for a reasonably weather proofed garage (Adams et al., 2011).

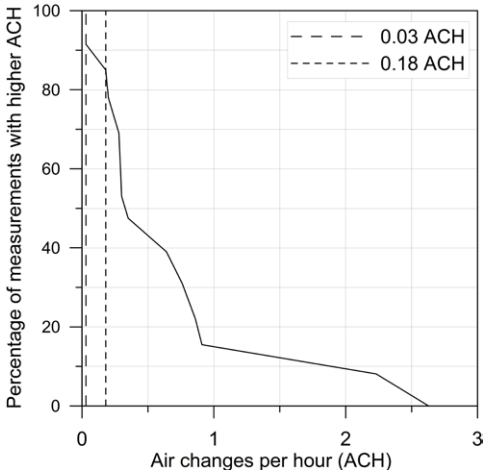

Figure 6–6. Available real world garage ventilation measurements (excluding Canadian studies): Electric Power Research Institute (1991, 1996), TIAX (2001), Waterland (2005).

Prior to this study the minimum natural ventilation rate used in other permeation studies was 0.18 ACH. However, based on research conducted for this report, the worst credible natural garage ventilation rate has now been agreed with the SAE as 0.03 ACH.

It is proposed that a worst-credible garage natural ventilation rate is 0.03 ACH (Adams et al., 2011). The value lies at a level reasonably above the lowest measured value of 0.01 ACH for the sealed CEA experimental facility and is equal to the lowest measured value for real world garages of 0.03 ACH (Waterland, 2005). This ventilation rate is also harmonised with the SAE Fuel Cell Safety Work Group.

6.1.4.3. Testing conditions

The conditions under which the test is performed represent the worst case for permeation from the container following the approach adopted in SAE J2579 (2009). If the test conditions are not representative of the worst case conditions the allowable rate must reflect the difference between the test conditions and the worst case conditions. Factors to be considered include (Adams et al., 2011): test pressure and temperature, new container or simulated end of life container. Testing should be undertaken at the nominal working pressure.

With respect to increasing material temperature, hydrogen permeation through polymer materials has been found to increase by an order of magnitude between approximately 24^0C and 82^0C (Mitlitsky et al., 1999). Material temperature/permeation characteristics are a key factor in determining the allowable permeation rate at a specified test temperature different to the maximum prolonged material temperature (Adams et al., 2011). Rothe (2009) published temperature/permeation rate data for three different materials (see Fig. 6–7). If the testing is undertaken at ambient temperature, the allowable permeation rate should be set such that the equivalent permeation at the maximum prolonged material temperature, previously proposed as 55^0C, results in a safe condition (Adams et al., 2011). The factor depends on the actual specified testing temperature and material behaviour. From Fig. 6–7, the following factor was estimated from the increase in permeation between the test temperature and maximum prolonged material temperature for the worst case material: for a test conducted at a temperature of 20^0C, a factor of 3.5 has to be used to convert from the maximum prolonged material temperature to the test temperature, and factor 4.7 if testing is at a temperature of 15^0C (conservative case of JARI Material 1).

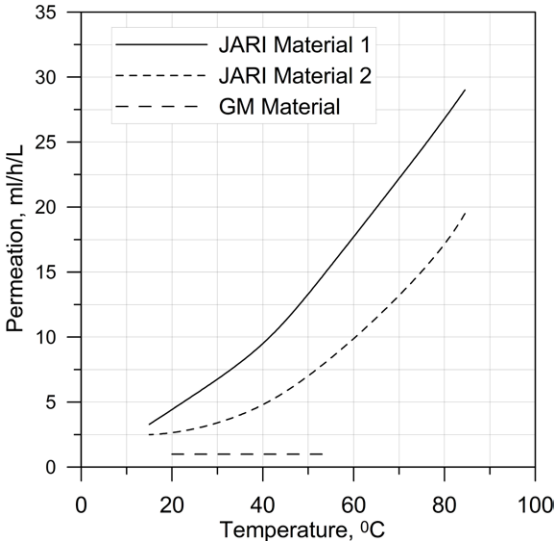

Figure 6–7. Permeation rate as a function of temperature for three materials (Rothe, 2009).

Testing is usually carried out on a new container. However, the container is a subject of aiging and permeation rate from a simulated end of life container is of interest for hydrogen safety engineering. It has been reported that the carbon fibre overwrap on new containers can significantly restrict the permeation rate (Mitlitsky, 2000). In a container that is reaching the end of its service life the carbon fibre/resin matrix will be affected by a significant amount of micro-cracking that will not affect the structural integrity, however, it could allow an increase in hydrogen permeation.

The increase in permeation for a container at end of life has been suggested to be twice that of a new container (Adams et al., 2011). Further investigations revealed conflicting opinions based on testing experience. One test centre has found that permeation does not increase significantly towards the end of life based on their test results (Webster, 2009). Other organisations suggest that increasing permeation has been observed (Novak, 2009) and also that a factor of 2 may not be adequate (Barthélémy, 2009). The investigations suggest that the effects of aging are not adequately understood and further research should be carried out, e.g. similar to the ENDEMAT project (2008). It is considered necessary to retain a factor of two reduction between end of life and new containers which would allow for unknown aging effects, use of new materials and statistical variation around limited existing data (Adams et al., 2011).

6.1.4.4. Calculation of allowable permeation rate

The following assumptions have been made (Adams et al., 2011):

- The allowable permeation rate will be specified in NmL/hr/L water capacity.
- Permeated hydrogen can be considered to disperse homogeneously.
- Worst-credible natural ventilation rate for a domestic garage is 0.03 ACH.
- Maximum permitted hydrogen concentration is 1% by volume, i.e. 25% LFL.

- Maximum long term material temperature is 55^{0}C.
- New container, with a factor of 2 to convert from the worst case end of life condition.
- For a test conducted at a temperature of 20^{0}C, a factor of 3.5 is used to convert from the maximum prolonged material temperature to the test temperature (factor 4.7 at temperature 15^{0}C).

It should not be implied that these are considered to be the best test conditions. The aim is to identify an allowable permeation rate rather than test conditions. The basic method requires the calculation of the "safe" permeation rate at the end of life condition for the container combined with the maximum prolonged material temperature, and then the value is reduced to that for a new container at the nominal test temperature, e.g. 20^{0}C. A value was also derived for an alternative test temperature of 15^{0}C.

The perfect mixing equation can be used to calculate the hydrogen release rate required to give a steady state hydrogen concentration (Marshall, 1983)

$$C_{\%} = \frac{100 \cdot Q_g}{Q_a + Q_g}, \tag{6–12}$$

where $C_{\%}$ is the steady state gas concentration, % by volume; Q_a is the air flow rate, m^3/min; and Q_g is the gas leakage rate, m^3/min.

The maximum allowable hydrogen permeation rate is then

$$Qp_x = \frac{Q_a \cdot C_{\%}}{100 - C_{\%}} \cdot \frac{60 \cdot 10^6}{V \cdot f_a \cdot f_t}, \quad (6\text{–}13)$$

where Qp_x is the allowable permeation rate at a test temperature of x^0C, mL/hr/L water capacity; V is the water capacity of hydrogen storage, L; f_a is the aging factor, taken to be 2; and f_t is the test temperature factor of 3.5 at a test temperature of 20^0C or 4.7 at a test temperature of 15^0C.

Based on the above assumptions, scenarios and methodology, the theoretical allowable permeation rates to give a hydrogen concentration less than 1% are given in Table 6-1 (Adams et al., 2011). It is proposed that the passenger car rates can be accepted for the city bus scenarios, as the worst case bus scenario is the "minimum" garage with failed forced ventilation and even in this situation the passenger car rates would still give a hydrogen concentration significantly lower than 4% by volume.

Minimum Testing Temperature (°C)	Maximum allowable permeation rate (mL/hr/L)	
	Passenger Car	City Bus
15	6.0	3.7
20	8.0	5.0

Table 6-1. Theoretical allowable permeation rates (Adams et al., 2011).

It is worth noting that an alternative value of maximum allowable permeation rate based on similar methodology at the SAE J2579 (2009) test conditions (55+ °C, simulated end of life) is 90 mL/min/std passenger vehicle. The HySafe proposals for allowable hydrogen permeation rates (Adams et al., 2011) are intended only for use in appropriate vehicle regulations and standards. The proposals are based on a range of garage scenarios that are considered to be representative of real world situations allowing the safe use of vehicles in typical enclosed structures such as domestic garages or maintenance facilities. The rates should not be applied to other situations or applications without further consideration. The proposed allowable hydrogen permeation rates are not applicable to hydrogen permeation into vehicle compartments. For hydrogen permeation into vehicle compartments the adoption of appropriate performance based requirements, or other requirements and engineering solutions as appropriate, in the relevant vehicle regulations or standards are necessary to avoid the potential development of flammable hydrogen-air mixtures and associated hazards.

In determining allowable hydrogen release rates from a vehicle, it is necessary to consider the different regulatory regimes that govern vehicles and buildings (Adams et al., 2011). The automotive industry increasingly has regulations harmonised at a global or regional level, however, vehicle regulations do not regulate the design of structures associated with vehicle use. In contrast, buildings and infrastructure are regulated at a national or local level by different authorities to those developing vehicle regulations. To achieve the safe introduction of hydrogen vehicles without unnecessary restrictions, it is necessary to ensure that vehicle and building/infrastructure regulations are compatible. Any vehicle could be driven into a wide range of garages during its life, and the discharges should be safe for all reasonable conditions. Conversely a garage can contain different vehicles. However, the structure needs to be safe regardless of the vehicle put inside. Vehicle regulations only control the approval of a vehicle and additional regulations control roadworthiness inspections.

6.2. The pressure peaking phenomenon

6.2.1. Hydrogen-powered car in a garage scenario

In vehicles hydrogen is most commonly stored today as a compressed gas in tanks which are required by the Commission Regulation (EU) No 406/2010 to be equipped with pressure relief devices (PRDs). The PRD is fitted to the fuel tank and starts to release hydrogen when high temperature of about 110°C is reached, e.g. in fire conditions. The PRD can provide rapid release of the hydrogen, if large orifice diameter is used, thus minimising the possibility of tank explosion during too long exposure to fire. High mass flow rates from PRDs are probably "acceptable" outdoors. However, the hazards resulting from a rapid release indoors are different.

Let us consider a hypothetical scenario involving a release from a typical onboard hydrogen storage tank at 35 MPa, through a 5.08 mm diameter orifice, representing a "typical" PRD (Brennan et al., 2010). The release is assumed to occur vertically upward in the centre, 0.5 m above the floor, of a small garage of size LxWxH=4.5x2.6x2.6 m (SAE J2579, 2009) and volume of 30.4 m^3 with a single vent equivalent in area to a typical brick LxH=25x5 cm located flash with the ceiling. A conservative approach is taken, i.e. a constant mass flow rate of 0.39 kg/s is applied (ignoring a pressure drop in the storage tank) after the PRD opening.

6.2.2. Phenomenological model

Let us assume that hydrogen fully occupies an enclosure to which it is released, and the steady state conditions are reached, when hydrogen mass flow rate from the enclosure through a vent is equal to mass flow rate from the nozzle of PRD to the enclosure, i.e. $\dot{m}_{vent} = \dot{m}_{nozz}$. Simple models such as the orifice equation for a subsonic regime are published elsewhere (Molkov, 1995)

$$\dot{m}_{vent} = CA\left\{\left(\frac{2\gamma}{\gamma-1}\right)P_S\rho_{encl}\left[\left(\frac{P_S}{P_{encl}}\right)^{\frac{2}{\gamma}} - \left(\frac{P_S}{P_{encl}}\right)^{\frac{\gamma+1}{\gamma}}\right]\right\}^{\frac{1}{2}} \tag{6–14}$$

and the Bernoulli's equation in the assumption of zero flow velocity in the enclosure

$$P_{encl} - P_S = \frac{1}{2\rho_{H2}}\left(\frac{\dot{m}_{nozz}}{A}\right)^2 \tag{6–15}$$

can be used to estimate the steady state overpressure within the enclosure. In this equations C is the discharge coefficient; A is the vent area, m^2; γ is the ratio of specific heats; P_S is the surrounding pressure, Pa; P_{encl} is the pressure in the enclosure, Pa; ρ_{H2S} is the density of hydrogen at the surrounding conditions, kg/m^3.

Equations (6–14) and (6–15) predict an overpressure in the enclosure of 17.9 and 15 kPa respectively for the scenario selected with C =0.6 (Emmons, 1995) and γ=1.4. It is worth noting that this is obtained in assumption of pure hydrogen within the enclosure. However, neither of two equations accounts for the injection of a lighter gas into a heavier gas and the subsequent overpressure in the garage to "push" the heavier gas air out of the garage.

The following simple system of equations is used to predict the overpressure dynamics within the enclosure with an assumption that each portion of released hydrogen is perfectly mixed with the uniform gas currently occupying the enclosure (Brennan et al., 2010)

$$m_{encl}^{t+\Delta t} = m_{encl}^{t} + \left(\dot{m}_{nozz}^{t} - \dot{m}_{vent}^{t}\right)\Delta t, \tag{6–16}$$

$$n_{encl}^{t+\Delta t} = n_{encl}^{t} + \left(\frac{\dot{m}_{nozz}^{t}}{M_{H_2}} - \frac{\dot{m}_{vent}^{t} n_{encl}^{t}}{m_{encl}^{t}}\right)\Delta t, \tag{6–17}$$

$$P_{encl}^{t+\Delta t} = \frac{n_{encl}^{t+\Delta t} RT}{V}, \tag{6–18}$$

$$\dot{m}_{vent}^{t+\Delta t} = C \cdot \left(\frac{m_{encl}^{t+\Delta t} A}{V}\right) \cdot \left(\frac{2\left(P_{encl}^{t+\Delta t} - P_S\right)V}{m_{encl}^{t+\Delta t}}\right)^{1/2}, \tag{6–19}$$

where superscripts "t" and "$t+\Delta t$" denotes previous and next time steps respectively; m is the mass of gas, kg; $\dot{m}$ is the mass flow rate, kg/s; n in the number of moles; Δt is the time step, s; V is the enclosure volume, m^3; P is the pressure, Pa.

6.2.3. Pressure load of the unignited hydrogen release (constant mass flow rate)

The transient pressure load in the vented enclosure according to the selected scenario predicted by the system of equations (6–16)–(6–19) for constant mass flow rate is given in Fig. 6–8.

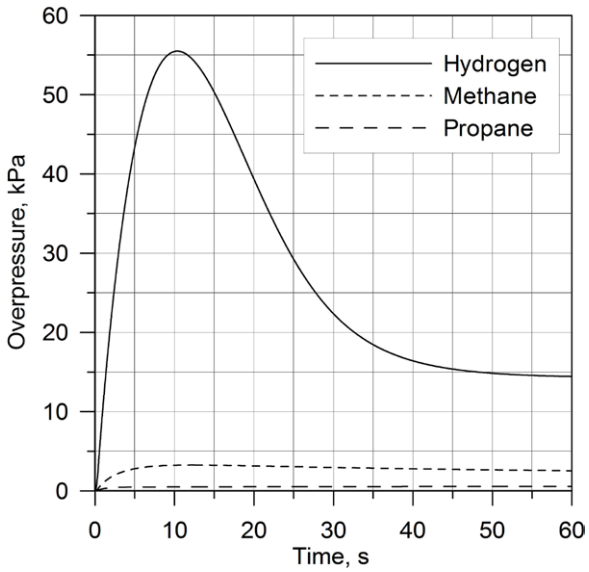

Figure 6–8. Pressure peaking phenomenon for release of hydrogen with mass flow rate 0.39 kg/s into the enclosure of 30.4 m3 with a vent of typical brick size 25x5 cm compared with pressure dynamics for releases of methane and propane at the same conditions.

The performed CFD simulation (Brennan et al., 2010) was run until just beyond the pressure maximum, after which point it was deemed unnecessary to continue the simulation. The predictions by the CFD and phenomenological models are within approximately 10%. A value of C=0.55 was found to perfectly match the CFD results.

The CFD study provided as well the dynamics of flammable hydrogen-air mixture development in the garage. It was found that almost 50% of the enclosure was engulfed by a flammable atmosphere in less than 1 s. Even after a release for 10 s the presence of the vent means that a mixture with potential to deflagrate exists in the majority of the enclosure, with the exception of a small rich region. The CFD results were shown to predict the formation of a flammable zone and mixing within the garage. This could not be shown using simple phenomenological models.

Figure 6–8 illustrates how the overpressure within the enclosure resulting from the injection of hydrogen reaches a level above 10 kPa capable of rupturing the garage (Baker et al., 1983) within only 1 s. Evacuation of people in this time is impossible and this life safety issue has to be yet addressed by car manufacturers. There is only one engineering solution that is the reduction of mass flow rate. This is turn will require higher fire resistance level of onboard storage tanks compared to current 3.5–6.5 minutes for type 4 vessels (Stephenson, 2005).

If the garage does not rupture first the pressure within the garage, for this particular scenario, reaches a maximum level in excess of 50 kPa. This maximum pressure then drops off and tends towards a steady state value, considerably lower, and equal to that predicted by the simple steady state estimations. It should be noted that this represents a worst case scenario with constant mass flow rate. Therefore, continuation of a constant mass flow rate release for 60 s is included in Fig. 6–8 purely to illustrate the time frame before a steady state conditions are reached when the garage is occupied by 100% of hydrogen.

The maximum pressure is reached in less than 10 s. Within this time the entire garage would be destroyed with missiles flying around and creating more damage. These are consequences of pressure build up without even considering the ignition of released hydrogen. Pressure peaking effect of unignited hydrogen release in vented enclosure is a new aspect of customers' safety that hydrogen safety engineers and manufacturers of hydrogen and fuel cell systems have to address.

Figure 6–8 illustrates as well the predicted overpressure values versus time for a range of fuels with different molecular mass and the same mass flow rate of 0.39 kg/s at the same garage (with discharge coefficient C=0.6): hydrogen, methane, propane with the molecular masses of 0.002, 0.016 and 0.044 kg/kmol respectively. It is clearly seen how the maximum overpressure drops with increasing molecular mass. There is a small pressure peak for methane release as its molecular mass is below that of air. The pressure peaking phenomenon is absent for propane as its molecular mass is higher than air. Instead, the pressure generated by release of hydrogen into the vented enclosure is growing monotonically to reach a steady state value. This should be taken into account when designing PRDs for use with different gases for indoor systems. Indeed, the same PRD technology used for CNG or LPG should not be assumed to behave in the same way for hydrogen. They practically have no pressure peaking (methane) or cannot have at all (propane).

The pressure peaking phenomenon for a release of gas lighter than air into vented enclosure can be explained by analysing equation (6–16)–(6–19). Indeed, from the equations it follows that volumetric mass flow rate out of the enclosure is inversely proportional to the square root from the density of gas escaping the enclosure. Thus, in the beginning of the process when the density of hydrogen-air mixture is comparatively high and close to air density the constant volumetric inflow of pure hydrogen is essentially above the volumetric outflow of heavier hydrogen-air mixture out of the enclosure. The pressure within the enclosure grows to allow mass flow rate of outgoing gas, which is a function of pressure, to match constant (for this scenario) mass flow rate entering the enclosure from the leak. Then, the molecular mass of hydrogen-air mixture decreases with time as there is no air entering the enclosure for such high mass flow rates from PRD. This implies the volumetric flow rate increase. Thus, the pressure in the enclosure can drop to match the constant volumetric flow rate from PRD.

Thus, the simple engineering methods to calculate the overpressure in an enclosure with a vent at moderate releases of hydrogen (flow is only out of the enclosure) are under predicting the steady state overpressure. This is due to existence of the pressure peaking phenomenon for releases of gases lighter than air like hydrogen and helium. Indeed, straight forward approaches like the Bernoulli's equation predict a steady state overpressure in the garage in the region of 15 kPa. However, the pressure peaking phenomenon gives far higher maximum pressures in excess of 55 kPa, which is reached within the first 10 s in the considered scenario. The phenomenological model indicates that the over pressure level predicted by the simple steady state equations would not be achieved for approximately 40–60 s at which point the building would most likely have been long destroyed. Pressure peaking reaches a maximum level in excess of 100 kPa for pressure in storage tank of 70 MPa (Brennan and Molkov, 2011).

The pressure peaking phenomenon, i.e. existence of maximum pressure peak that is above the steady state value, during a release of lighter than air gas into vented enclosure, should be accounted for when performing safety engineering for indoor use of hydrogen systems. Overall the conclusion is drawn that PRDs currently available for hydrogen-powered vehicles should be redesigned, along with the increase of fire resistance rating of onboard hydrogen storage tanks, and RCS updated if the vehicle is intended for garage parking.

6.2.4. "Safe" PRD diameter for unignited blow-down of hydrogen in a garage

This section discusses "safe" PRD diameters for enclosures of different volume with different natural ventilation level (Brennan and Molkov, 2011). The under-expanded jet theory and a blow-down model (Molkov et al., 2009) were utilised to analyse the pressure dynamics within garage-like enclosures. This model can be used to calculate decay of pressure and change of mass flow rate during a release from a storage tank of known volume through orifice of known diameter. The heat transfer during blow-down was not accounted for, and an isothermal approach which assumed a temperature of 288 K was used based on available experimental data for blow-downs at such pressures through orifices of similar size. For a given diameter, storage pressure, and hydrogen inventory, the output of the blow-down model (mass flow rate) was applied as an input to the phenomenological model to predict overpressure in a garage with a known volume and air changes per air (ACH).

A range of scenarios have been investigated whereby an unignited hydrogen release, from a PRD, is considered in a garage type enclosure with limited ventilation (Brennan and Molkov, 2011). The hypothetical events involve releases from typical onboard hydrogen storage tanks at pressures of 35 and 70 MPa. Inventory of 5 kg of hydrogen at each storage pressure is considered here. The release is assumed to occur in a garage with a vent. The volume of the garage and the size of the vent are varied. Free garage volumes of 18, 25, 30 and 46 m^3 were chosen to be representative of small, medium and large residential garages (InsHyde, 2009). A range of vent sizes were considered for each volume. The vent sizes were calculated to correspond to ACH below value of 1: 0.18, 0.3, 0.54 characteristic of residential garages (InsHyde, 2009; TIAX, 2004), and a value of 0.03 that is extremely conservative (it is the lowest measured value and representative of a worst case scenario (InsHyde, 2009)).

6.2.4.1. Air changes per hour and natural ventilation vent sizing

Let us relate garage volume and vent areas to ACH. Whilst values of ACH characteristic of residential garages can be found in the literature there was some uncertainty as to how ACH could be translated to vent area for a specific volume. By definition ACH is the ratio of volumetric air flow rate through an enclosure per hour, Q_{hr} (m^3/hr), to the enclosure volume, V (m^3),

$$\text{ACH} = Q_{hr}/V. \tag{6–20}$$

Bernoulli's equation can be used to calculate volumetric flow rate per second Q_s as a function of vent area, A (m^2), density of air, ρ (kg/m^2), discharge coefficient C, and pressure differential between the enclosure and the atmosphere, ΔP (Pa), i.e.

$$Q_s = CA\sqrt{2\Delta P / \rho} \tag{6–21}$$

The pressure differential assumed between the interior and exterior of the enclosure will obviously have an influence on the vent area calculated for a given ACH. The larger the "standard" ΔP, the smaller the corresponding vent area for a given volume and given ACH. A value of 50 Pa was accepted for ΔP in the majority of this work. This was chosen as "n50" is a standard measurement to determine the air leakage rate in a residential buildings, which is calculated based on a pressure difference of 50 Pa (The Air Tightness Testing & Measurement Association, 2010). However, a pressure difference of 5 Pa, which is close to value used by some researchers, was also used for comparison in the case of 5 kg of hydrogen at 35 MPa. This was done to demonstrate the sensitivity of the calculations to the method chosen for calculating ACH. The discharge coefficient was taken as the commonly recommended C=0.6 (Emmons, 1995).

6.2.4.2. Methodology and nomograms

The phenomenological model described in section 6.2.2 has been used in combination with models for an under-expanded jet and blow-down to examine the pressure dynamics for a range of release scenarios in a garage. For each combination of storage pressure, storage inventory, ACH and garage volume, a "safe" diameter was determined which ensures the pressure in the garage during a release does not exceed 20 kPa (and no less than 15 kPa). The mass flow rate decay data is used as an input to the phenomenological model to predict overpressure in the garage based on the garage volume and vent area, where vent area is calculated from ACH.

To provide life safety objective it is undesirable for the tank to fail, e.g. in a fire, while the pressure inside is still high. If the PRD diameter is reduced to keep pressure peak in a garage below 20 kPa the tank will take longer to blow-down, and hence the storage pressure remains higher for longer. Thus, the blow-down times through the "safe" diameters could be used to give an indication of "ideal" fire resistance rating of the hydrogen storage tanks.

Figure 6–9 gives the pressure dynamics for a release of 5 kg of hydrogen at initial storage pressure of 35 MPa, in a garage of free volume 30 m^3 with an ACH=0.18 (the minimum natural ventilation rate used in permeation studies before study of Adams et al., 2011). The figure shows the pressure dynamics for a currently typical PRD diameter of 5 mm compared with the dynamics for the "safe" diameter, found to be 0.55 mm in this case. For this specific case the PRD diameter should be reduced by an order of magnitude compared with a "typical" PRD diameter. If the storage pressure is increased, the ACH is reduced, the volume of the garage is reduced then this diameter would need to be decreased even further. This indicates the need in innovative engineering solutions for a system storage tank-PRD (the decrease of a PRD diameter means the increase of blow-down time and thus the increase of fire resistance rating of the onboard storage).

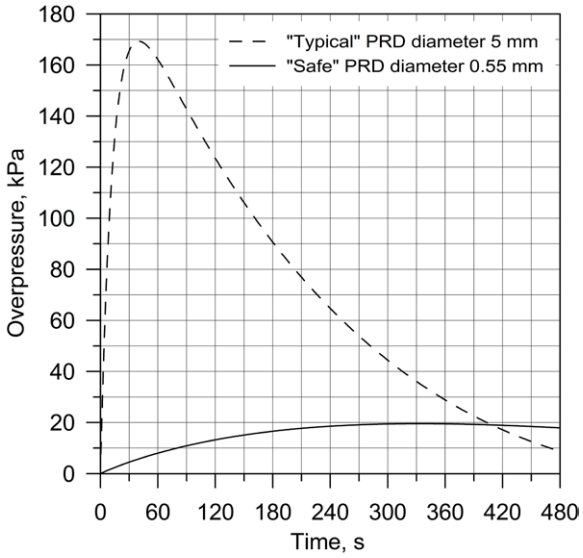

Figure 6–9. Pressure dynamics of unignited release in a 30 m^3 garage, ACH=0.18, 5 kg of hydrogen at 35 MPa, diameters of 5 mm and 0.55 mm (Brennan and Molkov, 2011).

Figure 6–10 shows a nomogram for release of 5 kg of hydrogen at initial pressures of 35 MPa in garages of different free volume and different natural ventilation. The nomogram has two graphs which have the same *x* axis (Diameter, mm). The blow-down time from initial storage pressure down to values of 10 MPa, 5 MPa, 2 MPa, 1 MPa, 0.1 MPa and 0.01 MPa storage overpressure were determined for each "safe" diameter for guidance.

The "safe" diameter can be estimated from the lower graph of the nomogram by reading horizontally across from the chosen volume until intersecting with the chosen ACH value, then read vertically up from this point of intersection to the *x* axis (values are shown for convenience at the top of the upper graph). The point of intersection with the *x* axis is the "safe" diameter for the chosen ACH, volume, inventory of hydrogen and storage pressure. Reading vertically up through/to the *x* axis to the point of intersection with the pressure curves on the upper graph can be used as a means to estimate blow-down time to that pressure for the "safe" diameter.

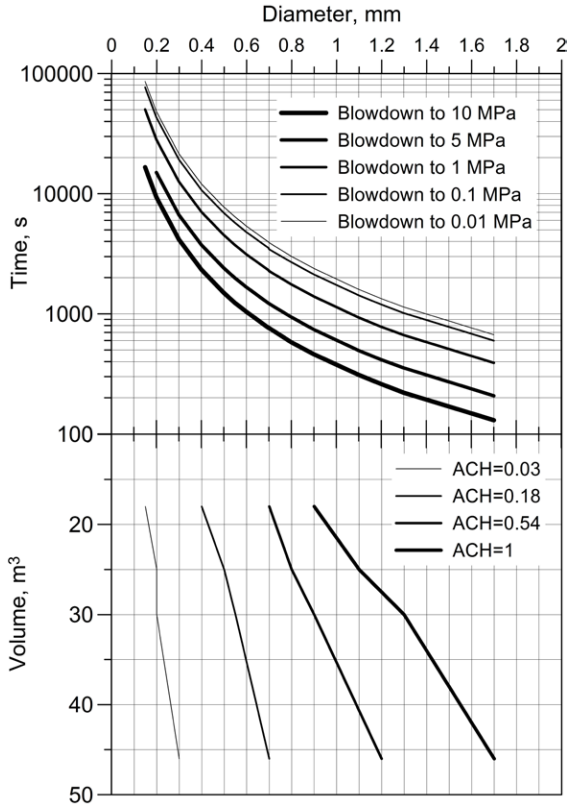

Figure 6–10. Nomogram for blow-down time of unignited release of 5 kg hydrogen in enclosures of different volume and ACH from initial pressure 35 MPa down to different residual overpressures through "safe" diameter PRD that mitigates the pressure peaking phenomenon to 15–20 kPa.

Figure 6–10 clearly demonstrates that "safe" diameter is essentially smaller than "typical" PRD diameters currently used. For lower ACH values the blow-down time through a "safe" diameter is increasing to several hours. This is an unrealistic currently requirement for fire resistance rating of type 3 and 4 tanks. More research is needed to generate innovative approaches for design of PRD and onboard storage.

Figure 6–11 represents a nomogram for calculating the "safe" diameter for 1 kg of hydrogen released at initial pressure 35 MPa or 70 MPa. The upper graph of the nomogram allows the blow-down time to an overpressure of 0.1 MPa within the tank to be calculated for each of two initial storage pressure. It is clear from comparison of Figs. 6–10 and 6–11 that storage tanks with inventories of 1kg does not present the same hazards as larger inventory of 5 kg. Thus smaller vehicles, with 1 kg tanks using "typical" PRD diameters should not cause significant problems in larger garages. As expected the "safe" diameter decreases and hence blow-down time increases with increasing hydrogen inventories and increasing storage pressure.

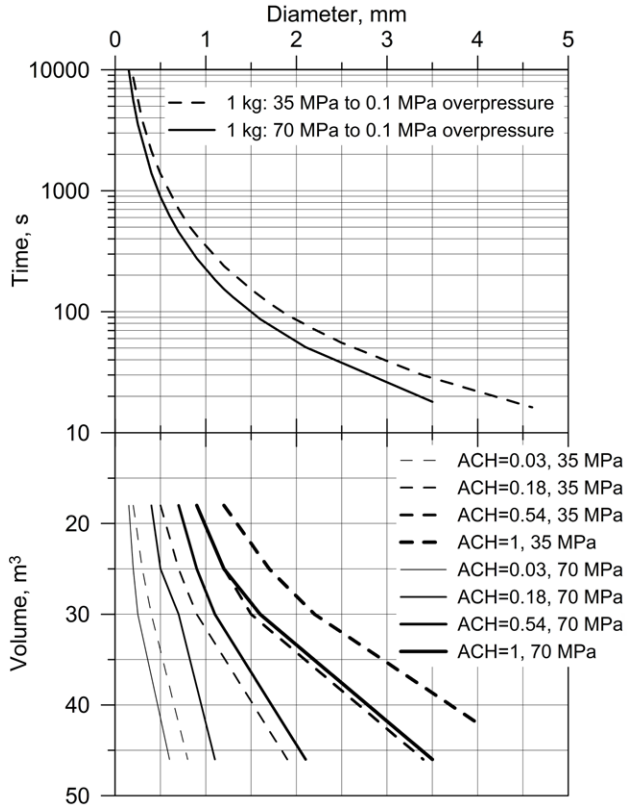

Figure 6–11. Nomogram for blow-down time of unignited release of 1 kg hydrogen in enclosures of different volume and ACH from initial pressures 35 MPa and 70 MPa down to overpressure of 0.1 MPa through "safe" diameter PRD that mitigates the pressure peaking phenomenon to 15–20 kPa.

As described previously, the relationship between vent area and ACH is dependent on the value taken for the pressure difference between the interior and exterior of the enclosure, ΔP. Figure 6–12 takes the example of 5 kg of hydrogen at 35 MPa, "safe" diameters and corresponding blow-down time to an overpressure of 0.1 MPa in the tank are compared for the cases of vent area calculated based on ΔP = 50 Pa and ΔP = 5 Pa. It can be seen that how ACH is defined has a significant impact on calculation of "safe" diameter. This would indicate that a clear consensus should be reached for similar applications and validation experiments performed. It is unclear yet which value of ΔP should be taken to calculate ACH for hydrogen applications.

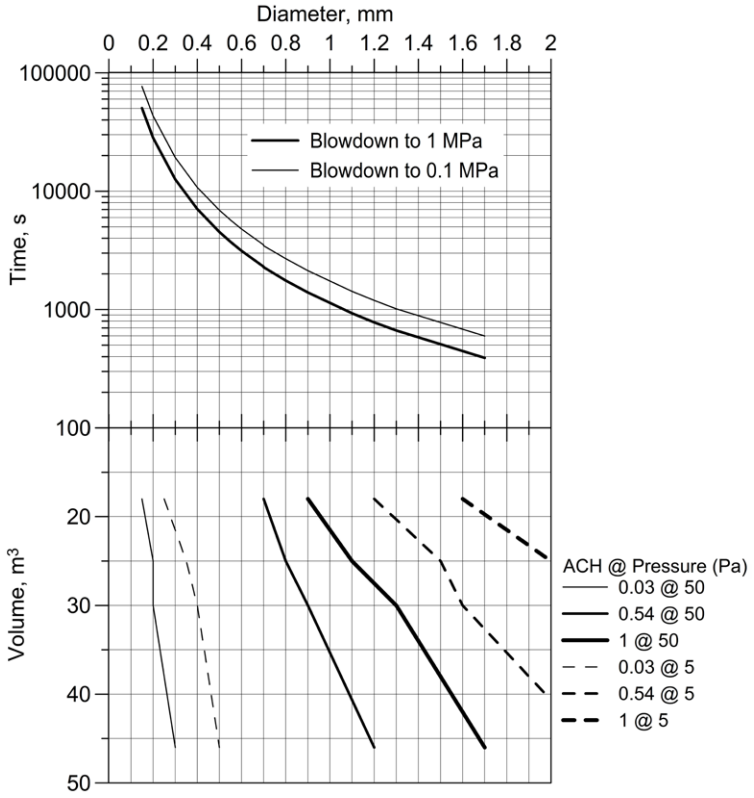

Figure 6–12. Nomogram for blow-down time of unignited release of 5 kg hydrogen in enclosures of different volume and three different ACH from initial 35 MPa down to overpressure 0.1 MPa and 1 MPa that mitigates the pressure peaking phenomenon to 15–20 kPa for ΔP = 50 Pa and ΔP = 5 Pa.

6.2.4.3. Concluding remarks

The pressure peaking is a unique phenomenon characteristic only for gases lighter than air when they are released into a ventilated enclosure. The phenomenon is the most pronounced for hydrogen which has the lightest molecule on the Earth. In practical situations it can be observed for helium and to very small extent for methane. It must be accounted for when performing hydrogen safety engineering for indoor use of hydrogen and fuel cell systems and has to be reflected in RCS.

Current approaches to fire resistance of onboard storage and parameters of PRD have a number of deficiencies. On the one hand, it is clear that existing arrangements are lacking sufficient fire resistance rating of onboard storage, and generate unacceptable safety performance of systems in enclosures if "typical" PRD of a few millimetres is activated even without combustion of release. On the other hand, simplified "redesign" of the onboard tank-PRD system to protect the garage structure from collapse puts extremely difficult to realise requirements to fire resistance of high pressure storage. Further research is needed to develop innovative safety strategies and engineering solutions to tackle the problem of fire resistance of onboard storage tanks and requirements to PRD performance, e.g. reduced flame length. Fire resistance rating of onboard storage equipment has to be provided by car manufacturers and/or other representatives of hydrogen industry as a part of permitting and certification procedures.

7 Ignition of hydrogen mixtures

7.1. Overview of hydrogen ignition mechanisms

Astbury and Hawksworth (2007) have performed an analysis of hydrogen ignition mechanisms, and stated that over the last century, there have been reports of high pressure hydrogen leaks igniting for no apparent reason, and several ignition mechanisms have been proposed. They underlined that although many leaks have ignited, there are also reported leaks where no ignition has occurred. Investigations of ignitions where no apparent ignition source was present have often been superficial, with a mechanism postulated which, whilst appearing to satisfy the conditions prevailing at the time of the release, simply does not stand up to rigorous scientific analysis. Clearly there are gaps in the knowledge of the exact ignition mechanism for releases of hydrogen. Mechanisms which have been considered by Astbury and Hawksworth (2007) are: the reverse Joule–Thomson effect, electrostatic charge generation, diffusion ignition, sudden adiabatic compression, and hot surface ignition.

The search using the Major Hazard Incident Database Service of the Health and Safety Executive (UK) Astbury and Hawksworth (2007) revealed 81 incidents involving releases of hydrogen. Of those, a delay between release and ignition was reported for only 4 releases. Authors assumed that the others ignited immediately. In 11 cases, the source of ignition was identified, but in the remainder, i.e. 86.3% of incidents, the source was not identified. This contrasts with data on the non-hydrogen releases, where 1.5% did not ignite, and only 65.5% of ignition sources were not identified. This does prove the suggestion that there is a difference in propensity for ignition between hydrogen and non-hydrogen gases when released. It is worth noting that since this is a Major Hazard Incident Database, releases of hydrogen which simply dispersed and did not involve fire, explosion, or other major hazard are not recorded, so the non-ignition being reported as zero is not necessarily an indication that all hydrogen releases ignited.

The following accidents have been described by Astbury and Hawksworth (2007) among others. From work undertaken by Nusselt in Germany several spontaneous ignitions of of hydrogen at 2.1MPa being discharged to atmosphere had been reported. Cylinders had been noted for having quantities of iron oxide (rust) in them even though they were apparently dry, and it was thought first that there was potential for electrostatic charging to occur. However, experiments on discharging hydrogen into an open funnel fitted with a long pipe showed no ignitions, except when the funnel was obstructed by an iron cap. The mechanism was not understood, so further trials were undertaken. Only when the trials were undertaken in the dark was a corona discharge observed. When the hydrogen leaked out of a flange – the corona discharge was visible, which increased when the pipe was tapped to stir up dust. An ignition followed after the tapping. Further work showed that when sharpened copper wires were used to promote corona discharges, ignition occurred when the point was bent away from the gas direction, whereas no ignition occurred when the wire was pointing in the direction of flow.

Another incident reported by Astbury and Hawksworth (2007) refers to a cylinder of hydrogen being connected to a piece of laboratory apparatus. The laboratory technician cracked the valve open to clear any dirt out of the connection, and when he did so, the escaping gas ignited immediately. Bond (1991) attributes this ignition to the phenomenon of diffusion ignition. Whilst no pressure of gas is quoted in this second incident, it can be assumed that the pressure would have been the typical full cylinder pressure of 23 MPa.

Reider et al. (1965), released a large quantity of hydrogen to determine the sound pressure levels. The hydrogen was released at an initial pressure of 23.6 MPa and an initial rate of 54.4 kg/s, for a period of 10 s. The gas was transferred through a 200 mm nominal bore pipe and a 150 mm bore ball valve to a cylindrical vessel fitted with a convergent–divergent nozzle venting to atmosphere. In the run where the gas was not deliberately ignited, after 10 s, the 150 mm diameter valve was being closed, and 3 s after starting to close the valve, ignition occurred. The three potential ignition mechanisms examined were: electrification of the gas, electrification of particles in the gas, and metal particles abrading a metal bar welded across the mouth of the nozzle. Of these, the first was discounted as pure gases are known to have negligible electrostatic charging. The second mechanism was considered, but as the system had been thoroughly cleaned out and blown down prior to the test. Yet, the velocity of the gas being discharged, at 1216 m/s, was far higher during the run than had been used before, so this potential mechanism could not be discounted. The third mechanism was considered as a possibility as the discharge velocity was high thus possibly dislodging particles and impacting them on the bar. This mechanism too could not be discounted. However, after the ignition it was found that the bar had been torn loose at one end, and this may have presented a possible ignition source which had not been foreseen.

"Unexpected" spontaneous ignition of hydrogen release in large-scale experiments was reported as well by Chaineaux et al. (1991), Groethe et al. (2005).

7.1.1. Ignition and reverse Joule–Thomson effect

Astbury and Hawksworth (2007) have disregarded the Joule-Thomson effect as potential mechanism of ignition in considered experiments. They made this conclusion using data by Michels et al. (1963) that the Joule–Thomson coefficient for hydrogen, estimated at pressures up to 250 MPa and 150°C, does not exceed 0.53K MPa at 100 MPa and temperatures up to 150°C. So, ignition by this mechanism is unlikely at the pressures in most of the incidents quoted above.

7.1.2. Electrostatic ignition

7.1.2.1. Sparks from isolated conductors

It has been mentioned that a stoichiometric mixture of hydrogen with air has a very low minimum ignition energy of 0.017 mJ (Baratov et al., 1990). There are three main types of electrostatic discharge: spark, brush, and corona discharges (Astbury and Hawksworth, 2007). The energy of a spark discharge (single plasma channel between the high potential conductor and an earthed conductor) from an isolated conductor is calculated as $E=CV^2/2$, where C is the capacitance of the item, and V is the potential (voltage).

For example, a person has a capacitance of about 100 pF, depending on body size, the area of their feet, and the construction and thickness of the soles of their footwear (Astbury and Hawksworth, 2007). Taking a typical MIE of 0.29 mJ for a hydrocarbon-air mixtures, say propane, then the voltage required to produce a spark of sufficient energy to ignite the atmosphere is given as $V=(2E/C)^{1/2}$. Substituting gives 2408 V. For air, the dielectric strength is about 30 kV/cm. So, the gap required between the charged conductor and the earthed point for breakdown to occur would be about 2400/30=0.08 cm or 800 micrometers.

People typically cannot feel an electrostatic shock of less than about 1 mJ, so would be unaware of the potential to ignite a hydrocarbon-air mixture (Astbury and Hawksworth, 2007). The gap over which the spark passes from a person to earth is rarely of a form which has pointed electrodes. Typically a finger has a tip radius of about 6 mm. So, a finger-tip approaching a flat earthed metal surface, though having a gap of 800 micrometers, would actually present a large almost flat area around the point at which the spark passes. This would tend to quench any ignition. This phenomenon of a spark not igniting a flammable mixture between two parallel plates is discussed by Metzler (1952) with relation to the prediction of MIE. The quenching of flames by parallel surfaces in close proximity has also been investigated by Potter (1960), who found that hydrocarbons have quenching distances of 2–3 mm.

Thus, theoretically, any ignition would not propagate from the plasma channel of the spark at such a "low" voltage of 2400 V. With a breakdown strength of 30 kV/cm, and a gap of 2 mm which would just allow the flame to propagate in hydrocarbon-air mixture, a potential of 6 kV would be required for a spark to occur (Astbury and Hawksworth, 2007).

If hydrogen is now considered, the corresponding voltages and gaps are much reduced (Astbury and Hawksworth, 2007). The dielectric strength of hydrogen atmospheres is only 17.5 kV/cm (Cassutt et al., 1962). Its quenching gap is only 0.64 mm (ISO/TR 15916:2004). The variation of dielectric strength with concentration of hydrogen in air mixtures is unknown, but as a simple case, it could be assumed to be linear within a specified narrow concentration range, so the theoretical dielectric strength of an about stoichiometric mixture of 30% of hydrogen in air would be (0.3x17.5 + 0.7x30) = 26.25 kV. With a quenching distance of 0.64 mm and a dielectric strength of 26.25 kV/cm the breakdown potential would correspond to a voltage of 26.25x0.064=1.68 kV, which corresponds to a stored energy of $0.5x[100x10^{-12}]$ $x[1.68x10^{3}]^{2} = 1.41x10^{-4}$ J, i.e. 0.141 mJ. This is more than sufficient to ignite the stoichiometric hydrogen–air mixture that requires only 0.017 mJ.

Thus, whilst electrostatic charging of people refuelling vehicles with petrol rarely gives rise to ignitions, it is significant that the voltage required for hydrogen to be ignited is below 2 kV. This voltage can be generated easily, without their being aware of it, on people standing on an insulating surface so there is a potential for personnel to ignite hydrogen leaks very easily, without any apparent ignition source being present (Astbury and Hawksworth, 2007).

7.1.2.2. Brush discharges

These are typified by a discharge between a charged insulator and a conducting earthed point (Astbury and Hawksworth, 2007). They are characterised by many separate plasma channels, combining at the conductor. As the charged surface is a non-conductor, a capacitance and hence energy cannot be determined. Work by Gibson and Harper (1988) introduced the term of incendivity or equivalent energy which is where the brush discharge has the ability to ignite an atmosphere, with the same minimum ignition energy as a spark which will just ignite the flammable atmosphere. Typical equivalent energies were found to be about 4mJ for brush discharges from flat polyethylene sheets. However, Ackroyd and Newton (2003) found that certain more modern plastics, and thin plastic coatings on earthed metal, had higher equivalent energies.

7.1.2.3. Corona discharges

Corona discharges are silent, usually continuous discharges which are characterised by a current but no plasma channel. A corona discharge is able to ignite a hydrogen-air mixture without there being a discrete spark or single discharge event (Astbury and Hawksworth, 2007). Cross and Jean (1987) give an equation to determine the voltage required for a corona to start from a point given its tip-radius. The prevention of ignition of hydrogen deliberately vented to atmosphere has been applied before by using a polished toroidal ring at the end of the vent to ensure that the effective tip radius is large. In practice, corrosion and dirt deposits are effectively small radius protrusions, so anything which affects the polished finish could create small radius protrusions which would still have an effect (Astbury and Hawksworth, 2007). Studies undertaken many years ago on hydrogen vents showed that ignition was rare during fine weather, but was more frequent during thunderstorms, sleet, falling snow, and on cold frosty nights (Astbury and Hawksworth, 2007).

7.1.3. Diffusion ignition

This mechanism will be discussed in more detail further in this chapter. This section is based on the mechanism analysis presented by Astbury and Hawksworth (2007). The phenomenon of diffusion ignition has been postulated by Wolanski and Wojcicki (1972), who demonstrated that ignition occurred when high pressure hydrogen was admitted to a shock tube filled with air or oxygen. They found that ignition could be achieved even if the temperature was below the autoignition temperature of the hydrogen.

Wolanski and Wojcicki calculated that gas, composed of a 3:1 mixture of hydrogen and nitrogen, would ignite in air if the shock wave exceeded a Mach number of 2.8 at a temperature of 575 K. A shock wave of this Mach number would be produced by an upstream pressure of 3.9 MPa. They also calculated that ignition would occur at a lower Mach number of only 1.7, corresponding to an upstream pressure of 1.3 MPa, when the shock wave was reflected by an obstacle.

There is no indication whether the autoignition temperature was measured in (Wolanski and Wojcicki, 1972) at the expected final pressure in the shock tube, or at atmospheric pressure. Although their shock tube experiments produced ignition, their initial temperature was rather high at 575 K (302°C), requiring an increase of only 110 K to reach their autoignition temperature of hydrogen. This clearly implies more research on this mechanism. In t addition, it worthy to note that there is no experimental work undertaken with releases to an unconfined atmosphere, such as would be the case for a leak from high pressure hydrogen storage direct to atmosphere.

7.1.4. Adiabatic compression ignition

The ideal gas laws, then compressing it at constant entropy, would increase the pressure due to the compression in accordance with the relationship $PV^{\gamma}=const$. It can be shown with use of the equation of state for the ideal gas that as well $TV^{\gamma-1}=const$. For example, for compression ratio $V_1/V_2=28$ at initial NTP ($\gamma=1.39$) the initial temperature of 293.15 K would increase to $T_2=T_1(V_1/V_2)^{\gamma-1}=1075.2$ K, i.e. the temperature rise is 782 K. In experiments conducted by Pan et al. (1995), the actual measured temperature realised by a compression ratio of 28 times was only 149 K. Based on this, Astbury and Hawksworth (2007) concluded that isentropic compression is unlikely to occur in practice.

However, work by Cain (1997) indicates that compression ignition of hydrogen–oxygen–helium mixtures occurs at a relatively constant temperature of 1050 K, at pressure rise ratios of 35–70 starting at 300K at atmospheric pressure. Reverse calculation indicates that a temperature rise from 300 to 1050K would require a pressure rise ratio of $P_2/P_1=(T_1/T_2)^{\gamma/(\gamma-1)} = (1050/300)^{1.39/0.39}=86.9$. Thus, adiabatic compression mechanism requires pressure rise ratio greater than that measured by Cain (1997), suggesting that there is another ignition mechanism present (Astbury and Hawksworth, 2007).

7.1.5. Ignition by hot surface

This is a phenomenon shared by most flammable gas or vapour air mixtures, in that providing the surroundings are at a high enough temperature, the rate of oxidation generates more heat than is being lost to the surroundings, so allowing the oxidation chain-reaction to progress (Astbury and Hawksworth, 2007). This is the usual method of determining autoignition temperatures, and the value obtained is very dependent on the apparatus used. It is known that the higher the temperature the shorter is ignition delay time. The lowest temperatures for ignition being associated with large volumes and surface areas (Snee and Griffiths, 1989).

Bulewicz et al. (1977) showed that the position and mode of heating a hot plate had an effect. They used a slow-heating method where free-convection was important, and a time delay between exposure and ignition was apparent, depending on the rate of temperature rise. The orientation of the heating surface also affected the delay, with a longer delay with the heated surface pointing down than when the heated surface was pointing up. Ungut and James (2001) reported as well that surfaces at the top of the enclosure having longer induction times.

7.1.6. Concluding remarks

From their analysis Astbury and Hawksworth (2007) concluded that no one considered mechanism is able to explain all of the recorded incidents. There is the potential for two or more potential mechanisms to work together. It is known that the minimum ignition energy of gases and vapours decreases with increases in temperature (Moorehouse et al., 1974), so expanding hydrogen would increase in temperature due to the reverse Joule–Thomson effect, and hence its ignition energy would reduce. Similarly, if particles were to be abraded from the walls of any flow path, the required energy for ignition from a corona discharge would be lower, so it is likely that less corona charging current would be required to ignite the hydrogen.

In several incidents, there is a suggestion in the reports that electrostatic effects may have been responsible. In particular, one of incidents involved only a fine stream of mercury, with no other potential ignition sources inside the closed system. The potential for drops and bursting bubbles to generate electrostatic charges has been proposed by Blanchard (1963), and the ability of such charges to ignite sensitive atmospheres has been illustrated by Pratt (1993).

It is generally recognised that pure gases do not become electrostatically charged under normal conditions (IEC, 2002), but this refers generally to low velocities and pressures. Where gases are released at very high pressures, the flow becomes sonic and the propensity of electrostatic charging occurring is not known. It is known that pure gases tend not to charge, but particles within the gas stream are known to become electrostatically charged.

The discharge path in many practical cases would probably be convoluted and not in a straight line. This would require the hydrogen to discharge through bends, which would potentially allow materials on the surface of the discharge path, e.g. piping, to be eroded and form particles which could become electrostatically charged.

In 2007 Astbury and Hawksworth suggested that the diffusion ignition mechanism to be likely only when the initial temperature is high. However, they continued that where valves on cylinders are briefly opened direct to atmosphere, presumably to clear any debris from the cylinder, ignition has occurred. The diffusion ignition effect appears to be reproducible in a shock tubes or similar closed equipment. Wolanski and Wojcicki (1972) appear to have only carried out work using a hydrogen-nitrogen mixture (Astbury and Hawksworth, 2007). Since 2007 more work both experimental and numerical has been performed on the diffusion mechanism. This is reported partially in the next section.

7.2. Spontaneous ignition of sudden releases

Many attempts have been made to explain this phenomenon over the last decades starting from pioneering study of Wolanski and Wojcicki (1972) of the so-called "diffusion ignition mechanism". Experimental data give critical conditions of the phenomenon. Unfortunately, they cannot provide a detailed insight into the dynamics of the process. For example, exact location of initial ignition spots and progression of chemical reaction within tubing downstream the rupture disk or valve can hardly be identified by experimental means at high pressures.

It is an agreed opinion that the probability of hydrogen spontaneous ignition at a sudden release from high-pressure equipment is high if mitigation measures are not undertaken. However, no references to spontaneous ignition problem or engineering design to avoid or promote it can be found in codes and standards for piping, storage and use of high-pressure systems handling compressed hydrogen.

Control of spontaneous ignition of high-pressure hydrogen release is one of the challenging problems of hydrogen safety, for which a little fundamental explanation exists.

Earlier numerical studies by Liu et al. (2005), Bazhenova et al. (2006), and Xu et al. (2008, 2009) were focused on unconfined release from high-pressure storage directly into the atmosphere. While spontaneous ignition was demonstrated by numerical simulations (Liu et al., 2005; Bazhenova et al., 2006), no experimental proof exists up to date.

7.2.1. Overview of experimental and numerical studies

7.2.1.1. Experimental observations

Experimental confirmation of spontaneous ignition by diffusion mechanism for releases from high pressure equipment to the atmosphere through a tube was obtained in "controlled laboratory environment" by Dryer et al. (2007), Golub et al. (2007, 2008), Pinto et al. (2007), and Mogi et al. (2008). To facilitate spontaneous ignition various extension tubes and attachments were positioned downstream of a burst disk. Figure 7–1 combines critical conditions for experimentally registered spontaneous ignition obtained by different research groups.

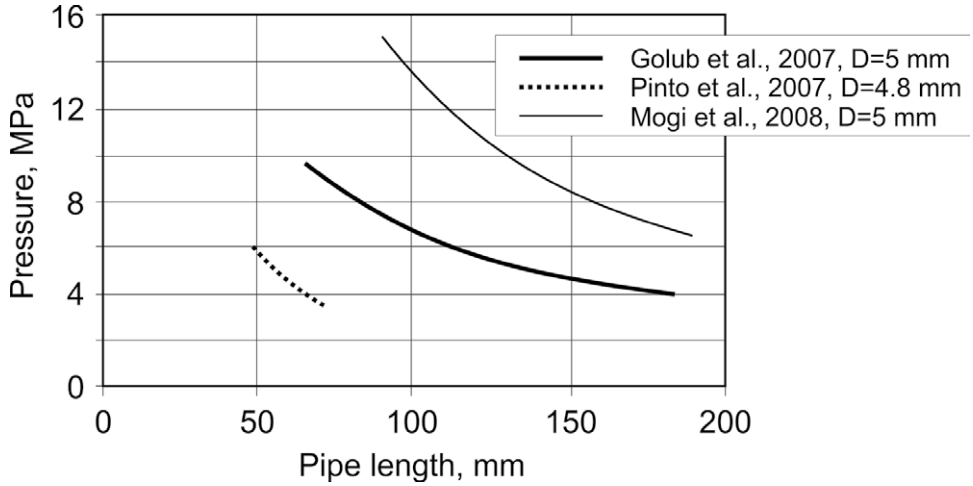

Figure 7–1. Experimental data on pressure limit of spontaneous ignition of hydrogen release into air in pipes of different length.

The data by Dryer et al. (2007) are not shown in Fig. 7–1, because of complicated internal geometry of fittings and rupture disk used which lowers the minimum pressure sufficient for spontaneous ignition down to 2.04 MPa. Although the data on spontaneous ignition of releases through practical fittings is very useful for hydrogen safety engineering, internal configurations of the fittings leaves a number of uncertainties in formulation of numerical experiments and prevents direct comparison with experimental results of other groups.

Experimental results agree in a general trend of the decrease of the critical (limit) pressure with the increase of a pipe length. However, the critical conditions of spontaneous ignition vary substantially due to difference in test arrangements. Sensitivity of spontaneous ignition to different not yet fully understood factors poses a number of issues to be studied.

Figure 7–1 shows an essential difference in critical conditions for spontaneous ignition obtained in different studies. It can be seen, for example, that for hydrogen storage pressure of 6 MPa in experiments by Pinto et al. (2007) the 50 mm pipe length is sufficient to provide spontaneous ignition. However, at the same storage pressure and practically the same internal diameter the channel length sufficient to provide spontaneous ignition in Golub et al. experiments (2007, 2008) is 110 mm, and in Mogi et al. (2008) tests the minimum length increases by four times to 200 mm. How these differences can be explained?

First of all, Golub et al. (2007, 2008) registered the onset of spontaneous ignition by monitoring the shock propagation and location of radiation from chemical reaction inside the pipe. Hence, critical conditions for spontaneous ignition in their experiments (see Fig. 7–1) represent the distance from the rupture disk to the location where ignition was captured by a radiation gauge.

Mogi et al. (2008) judged the occurrence of spontaneous ignition by optical observation of the area near the pipe exit to atmosphere. They showed that in some experiments spontaneous ignition did occur, but combustion was blown out by the flow. Unfortunately, no critical conditions for such releases were reported. Nevertheless, this fact confirms that not all spontaneously ignited releases transit into sustained jet fires. This is one likely reason for the shift of the critical curve in Mogi et al. (2008) experiments compared to Golub et al. (2007, 2008). However, the most probable reason explaining the shift of Mogi et al. (2008) data to higher pressures for the same pipe length was suggested in (Molkov, 2008). Indeed, in experiments by Mogi et al. (2008) the internal surface of the pipe between the diaphragm (rupture disk) and the exit to atmosphere was washed away by the aqueous Na_2CO_3 solution (1%) in order to allow visualization of the flame via the flame reaction of sodium. This solution could have interfered with boundary layer flow and chemistry of hydrogen combustion and draw away some heat from the process. Thus, the process happened later along the tube for the same initial pressure.

The experimental procedure applied by Pinto et al. (2007) was different as hydrogen was compressed just before the burst disk rupture using a piston combined with the shock tube. Nitrogen gas was injected into the high pressure section of the shock tube upstream of the piston to push it towards hydrogen gas in order to generate high pressure of hydrogen to burst the disk. This compression obviously caused heating of hydrogen in high-pressure chamber and the release was not at the ambient temperature, but somewhat higher. But since, neither the temperature measurements in high-pressure chamber, nor information of the time during which hydrogen was compressed are available, it is difficult to estimate accurately the initial hydrogen temperature.

The results of the Pinto et al. (2007) experiments are in full compliance with Bazhenova et al. (2006) who stated that the increase of initial hydrogen temperature stimulates spontaneous ignition to occur earlier and under lower initial pressures. Higher initial temperature of hydrogen is the most likely reason for shorter tube required for spontaneous ignition in experiments by Pinto et al. (2007) for the chosen pressure compared to experiments by Golub et al. (2007, 2008) and Mogi et al. (2008).

The way how the burst disk ruptures is probably the most important factor for spontaneous ignition as it affects the hydrogen-air mixing (Dryer et al., 2007). In experiments by Golub et al. (2007, 2008) burst disks were incised in the form of the cross to facilitate sharp "petal" opening at predetermined pressure, whereas in experiments by others a wider stochastic burst disk rupture pressure distribution was observed. Stochastic nature of an in-house made burst disk rupture produces variations in a structure and strength of the shock wave generated, even at constant burst pressure, and obviously can affect the repeatability of experimental data. Very good repeatability of experiments is stated by Golub et al. (2007, 2008) both in the measured pressure behind the generated shock wave, and the minimum initial pressure, which would provide spontaneous ignition at fixed tube length.

Pinto et al. (2007) compared results for smooth and screwed tubes. They found that the same initial pressure causing spontaneous ignition in smooth tube fails to cause ignition in case of screwed tube.

This observation, however, conflicts with the point of view of Dryer et al. (2007), who found that experiments with several tubes mated together produced ignition, where single tube (no mating unions) did not for the same initial pressure, the internal diameter and the overall tube length. These observations underline that the interaction of developing boundary layer with roughness of walls in the tube section downstream of the burst disk can promote as well as delay spontaneous ignition.

Dryer et al. (2007) reported that spontaneous ignition events are statistically distributed in a narrow pressure range of 2.04–2.21 MPa, with zero probability for membrane failure pressures less than 2.04 MPa and certain inflammation for failure pressures above 2.21 MPa, at their experimental set up. In addition to identifying a minimum pressure below which no spontaneous ignition can be observed, it is found that reducing the length of the 1.27 cm (½″) NPT pipe nipple to 3.81 cm (1.5″) led to no spontaneous ignition at all failure pressures even up to 5.66 MPa.

Experimental study by Golub et al. (2010a, 2010b) argues on a potential of spontaneous ignition in a T-shaped channel for initial hydrogen pressure in the range of pressure 1.2–2.9 MPa. However, there is some ambiguity in the interpretation of results of this study with statements of spontaneous ignition at 2.9 MPa in one communication and 2.43 MPa in another.

Dryer et al. (2007) speculate on the importance of the initial stage of a membrane rupture on the mixing and subsequent spontaneous ignition process. They concluded that at low pressures, the chemical ignition time becomes the limiting factor, while at high pressures the mixing time to achieve significant flammable mixture volume limits the process. There is a need to have a "look inside" of the pipes to clarify physics of the spontaneous ignition in order to control it.

7.2.1.2. Numerical studies

The 2D analysis of pressure-boundary rupture rate on hydrogen spontaneous ignition during release through a 3 mm hole in a wall of 0.1 mm thickness directly to atmosphere was carried out by Xu et al. (2009). Characteristic cell sizes used were 15–30 μm across the contact surface. Xu et al. (2009) found that if the rupture rate is below a certain threshold value, there would be no spontaneous ignition in the atmosphere. As the rupture rate increases, the temperature of the shock heated region grows more quickly owing to earlier flow expansion and once the rupture rate is sufficiently high, spontaneous ignition can occur. This simulation corresponds to a scenario of unconfined release for which no experimental evidence exists.

Hydrogen releases through a length of a tube 30–60 mm long and 3–6 mm internal diameter for storage pressures in a range 5–15 MPa were simulated by Wen et al. (2009). It was demonstrated that spontaneous ignition is governed by focusing of reflected from the tube wall shocks. Numerical studies by Xu et al. (2009) and Wen et al. (2009) confirmed the significance of a membrane opening time on the spontaneous ignition process.

Lee and Jeung (2009) investigated the effect of a burst disk shape on the ignition process at pressure of a burst disk rupture of 8.6 MPa and release into a pipe. Cartesian grid with a cell size of 19 μm was applied. The burst disk had a semi-spherical shape. However, an instant opening of the disk was applied in simulations. The spontaneous ignition first occurred in a boundary layer and consequently spread throughout a cross-section of the tube, i.e. through the contact surface between air and hydrogen where mixing takes place, similar to our previous 3D study with an instant opening of a flat membrane (Bragin and Molkov, 2009).

Simulations of hydrogen spontaneous ignition in air using the model accounting for viscous gas transport, multi-component diffusion, heat transfer, and incorporating a kinetic scheme of hydrogen oxidation with 9 equations were performed by Golub et al. (2008). The authors studied experimentally and numerically in 2D axisymmetric formulation the self-ignition in cylindrical and rectangular ducts and concluded that the governing mechanism for hydrogen spontaneous ignition is diffusion ignition on the contact surface assisted by the boundary layer effects. Combustion starts as kinetic one and then acquires diffusion character. Heat release and flame turbulence intensify mixing of reagents and such burning cloud may propagate along the tube far enough. Simulation with and without the boundary layer were also carried out and a conclusion is drawn that when boundary layer is not taken into account, ignition occurs at the duct axis, whereas it occurs near the wall if boundary layer is taken into account.

2D numerical simulations of the phenomenon were carried out by Pinto et al. (2007). Axisymmetric Euler equations and detailed chemical reactions mechanism were employed to simulate the behaviour of the hydrogen jet discharged from a storage vessel at pressures 10-70 MPa and temperature 300 K at an early stage of the leakage. The reduced kinetic mechanism by Petersen et al. (1999) with 9 species (H2, O2, O, H, OH, HO2, H2O2, H2O, and N2) and 18 elementary reactions was applied. Chemical reactions were treated by a point implicit way to avoid stiffness. Uniform grid with a cell size of 20x20 μm was used to carry out simulations. Dependencies of the length, where the spontaneous ignition occurs on the pressure in high-pressure chamber were obtained experimentally not only for smooth, but also for screwed tubes. It was found that screwed tubes produce some difficulty for spontaneous ignition affecting the boundary layer. Numerical simulations were reported only for one case of 10 mm diameter tube with 50 mm length and 3.8 MPa initial hydrogen pressure, but no comparison to experimental data has been presented.

In the study by Yamada et al. (2009) the model by Pinto et al. (2007) had been improved by adding viscosity effects. The governing equations used were the compressible 2D axisymmetric Navier-Stokes equations, the conservation of mass, total energy, chemical species, and the equation of state. The same reduced kinetic mechanism by Petersen et al. (1999) was applied. The governing equations were discretized in a finite difference formulation. The convective terms are evaluated using the second-order explicit Harten-Yee non-MUSCL modified-flux type TVD scheme, considering the properties of the hyperbolic equations. The viscous terms are evaluated with the standard second-order central difference formulae. The time integration method is the second-order Strang-type fractional step method. A grid with cell sizes of 20–45 μm was used to carry out simulations. Three inlet pressures were studied i.e. 3.6, 5.3 and 21.1 MPa, estimated from choked conditions at the exit resulting from initial pressure in the large hydrogen tank of 6.8, 10 and 40 MPa. The pipe had a 4.8 mm diameter and a length of 71 mm. It was found that a high-temperature area appears near the exit of the pipe. The vortex generated near the edge of the exit was observed similarly to experimental results by Mogi et al. (2008) and our numerical simulations (Bragin and Molkov, 2009). The vortex plays an important role in mixing the hydrogen provided from the pipe with surrounding air. It was shown that for a pressure of 3.6 MPa the spontaneous ignition does not occur in the vortex region; for a pressure of 5.3 MPa the shock wave retains a high temperature for spontaneous ignition, but chemical reactions do not continue long around the exit of the pipe; and only for the pressure of 21.1 MPa combusting area remains. The authors also compared release from the pipe and a hole for the same diameter. It was concluded that in the case of release from the hole, the confinement prevents the development of vortices and mixing of hydrogen with surrounding air in the recirculation zone (Yamada et al., 2009).

All described above simulations of hydrogen spontaneous ignition by the diffusion mechanism were carried out in 2D formulations, including axisymmetric, due to an understandable wish of researchers to have as fine mesh as possible to directly resolve the phenomenon. The large eddy simulation (LES) model developed and described in the next section employs “coarser” 3D grids. This “forced” increase in the mesh size is “compensated” by an advanced sub-grid scale (SGS) modelling of the combustion by the eddy dissipation concept (EDC) with a detailed chemistry and the SGS turbulence modelling by the renormalization group (RNG) theory. The aim of the LES model development at the HySAFER Centre is reproduction of experimental results obtained in complex realistic geometries, where 2D simulations cannot be applied without losing of predictive accuracy.

7.2.2. The large eddy simulation model of spontaneous ignition

The LES technique is recognised as the most promising computational fluid dynamics (CFD) approach to solve scientific and engineering problems. LES models have been successfully applied in the HySAFER Centre to model hydrogen-air deflagrations (Molkov et al., 2006a), detonations (Zbikowski et al., 2008), non-reacting under-expanded jets (Molkov et al., 2009), and jet fires (Brennan et al., 2009). The set of main governing equations can be found elsewhere (Molkov et al., 2006a). The RNG model has been employed for sub-grid scale (SGS) modelling of turbulence (Yakhot and Orszag, 1986). The reaction rate that appears in species transport equation was modelled using the eddy-dissipation-concept (EDC) model of turbulent combustion by Magnussen (1981). It incorporates detailed Arrhenius chemical kinetics. In this model the detailed 21-step chemical reaction mechanism of hydrogen combustion in air employing 37 elementary reactions by Gutheil et al. (1993) is applied. The FLUENT software has been used as the computational engine.

7.2.2.1. The governing equations

The governing equations are filtered over the control volume three-dimensional instantaneous conservation equations for mass, momentum (Navier-Stokes), energy, and species for compressible Newtonian fluid

$$\frac{\partial \overline{\rho}}{\partial t} + \frac{\partial}{\partial x_j}\left(\overline{\rho}\widetilde{u}_j\right) = 0, \qquad (7\text{–}1)$$

$$\frac{\partial \bar{\rho}\tilde{u}_i}{\partial t}+\frac{\partial}{\partial x_j}\left(\bar{\rho}\tilde{u}_i\tilde{u}_j\right)=-\frac{\partial \bar{p}}{\partial x_i}+\frac{\partial}{\partial x_j}\left(\mu_{eff}\left(\frac{\partial \tilde{u}_i}{\partial x_j}+\frac{\partial \tilde{u}_j}{\partial x_i}-\frac{2}{3}\frac{\partial \tilde{u}_k}{\partial x_k}\delta_j\right)\right)+\bar{\rho}g_i, \tag{7–2}$$

$$\frac{\partial}{\partial t}\left(\bar{\rho}\tilde{E}\right)+\frac{\partial}{\partial x_j}\left(\tilde{u}_j\left(\bar{\rho}\tilde{E}+\bar{p}\right)\right)=$$

$$=\frac{\partial}{\partial x_j}\left(\frac{\mu_{eff}c_p}{Pr_{eff}}\frac{\partial \tilde{T}}{\partial x_j}-\sum_m \tilde{h}_m\left(-\frac{\mu_{eff}}{Sc_{eff}}\frac{\partial \tilde{Y}_m}{\partial x_j}\right)+\tilde{u}_i\mu_{eff}\left(\frac{\partial \tilde{u}_i}{\partial x_j}+\frac{\partial \tilde{u}_j}{\partial x_i}-\frac{2}{3}\frac{\partial \tilde{u}_k}{\partial x_k}\delta_{ij}\right)\right)+\sum_m R_m H_C, \tag{7–3}$$

$$\frac{\partial}{\partial t}\left(\bar{\rho}\tilde{Y}_m\right)+\frac{\partial}{\partial x_j}\left(\bar{\rho}\tilde{u}_j\tilde{Y}_m\right)=\frac{\partial}{\partial x_j}\left(\frac{\mu_{eff}}{Sc_{eff}}\frac{\partial \tilde{Y}_m}{\partial x_j}\right)+R_m. \tag{7–4}$$

where bars denote: $\bar{}$ LES filtered quantity, ~ LES mass-weighted filtered quantity; E is the total energy, J/kg, $E=h-p/\rho+u^2/2$; h is the enthalpy, J/kg, $h=\int_{298.15}^{T}c_p dT$; c_p is the specific heat capacity of mixture at constant pressure, $c_p=\sum_m c_{p_m}Y_m$ (m is the m-th component of gas mixture); Y is the mass fraction; T is the temperature, K; p is the pressure, Pa; ρ is the density, kg/m^3, $\rho=pM/RT$; $u_{i,j,k}$ are velocity components, m/s, ($_{i,j,k}$ are spatial coordinate indexes); $x_{i,j,k}$ are spatial coordinates, m; t is time, s; g is the gravitational acceleration, m/s^2; H_c is the heat of combustion, J/kg.

The effective viscosity μ_{eff} is calculated using the RNG theory by Yakhot and Orszag (1986). The RNG model is capable to reproduce not only turbulent, but also transitional and laminar flows. At low Reynolds numbers the effective viscosity becomes equal to molecular viscosity. This allows the model to perform better in the vicinity of walls (Shah et al., 2001). The effective viscosity is calculated in RNG model as

$$\mu_{eff}=\mu\left[1+H\left(\mu_s^2\,\mu_{eff}/\mu^3-100\right)\right]^{1/3}, \tag{7–5}$$

where $\mu_s=\bar{\rho}\left(C_{RNG}V_{CV}^{1/3}\right)^2\sqrt{2\tilde{S}_{ij}\tilde{S}_{ij}}$; $H(x)$ is Heaviside function; C_{RNG} is the RNG LES constant, C_{RNG} = 0.157; V_{CV} is the volume of a control volume, m^3; $\tilde{S}_{ij}$ is the rate of strain tensor, s^{-1}. In highly turbulent regions of the flow $\mu_{eff}\approx\mu_s$ and the RNG model reduces to the Smagorinsky model (1963). In laminar flow regions the argument of Heaviside function becomes negative and the model recovers molecular viscosity, $\mu_{eff}=\mu$. The effective Prandtl and Schmidt numbers are calculated following the RNG theory by entirely theoretical equations (Yakhot and Orszag, 1986)

$$\left|\frac{1/N_{eff}-1.3929}{1/N-1.3929}\right|^{0.6321}\left|\frac{1/N_{eff}+2.3929}{1/N+2.3929}\right|^{0.3679}=\frac{\mu}{\mu_{eff}}, \tag{7–6}$$

where N stands for laminar Prandtl or Schmidt numbers. Laminar Prandtl and Schmidt numbers are calculated according to kinetic theory.

7.2.2.2. The EDC combustion model with full chemistry

The Eddy Dissipation Concept (EDC) model (Magnussen, 1981) with the updates that incorporates detailed Arrhenius chemical kinetics in turbulent flames was applied as the combustion sub-model (Bragin et al., 2011). EDC gives an expression for a combustion rate based on an assumption that chemical reactions occur in so-called fine structures of Kolmogorov's scale where the dissipation of turbulence energy takes place. In a flow of moderate to intense turbulence these fine structures are concentrated in isolated areas occupying only a small fraction of the flow. The characteristic size of the fine structures is much smaller than a LES filter width, i.e. a cell size in our case of "numerical LES" following the terminology by Pope (2004), and it needs to be computed as a function of flow parameters and a cell size. The EDC model adopted in FLUENT models a source term in the species transport equation as

$$R_m = \frac{\rho\left(\xi^*\right)^2}{\tau^*\left[1-\left(\xi^*\right)^3\right]}\left(Y_m^* - Y_m\right), \tag{7–7}$$

where R_m is the net rate of production of specie m by chemical reactions; ξ^* is the length fraction of the fine scale turbulent structures where the reaction occurs (* denotes fine scale quantities); Y_m^* is a fine scale species mass fraction (specie m) after reacting over the time τ^*, Y_m is a species mass fraction for specie m in the surrounding fine scales state. The multiplier in above equation with a square of the length fraction of fine scales represents the mass exchange between the surrounding and fine structure regions. The length fraction of fine structures is evaluated in this LES model similar to EDC RANS model as

$$\xi^* = C_\xi u_\eta / u_{SGS}, \tag{7–8}$$

where the volume fraction constant is taken as $C\xi$ = 2.1377 similar to RANS. The upper limit ξ^* = 1 is applied when the fine scales velocity is larger than residual SGS velocity. The scale of a LES residual velocity at the sub-grid scale (SGS) level is

$$u_{SGS} = \mu_t /(\rho \cdot L_{SGS}), \tag{7–9}$$

where μ_t is the turbulent (effective) viscosity, and the SGS length scale is determined as

$$L_{SGS} = C_{RNG} V_{CV}^{1/3}. \tag{7–10}$$

The Kolmogorov's velocity u_η is

$$u_\eta = \left(\frac{\mu \cdot u_{SGS}^3}{\rho \cdot L_{SGS}}\right)^{1/4}, \tag{7–11}$$

where μ is the laminar viscosity.

Characteristic sub-grid eddy and Kolmogorov's timescales are respectively

$$\tau_{SGS} = L_{SGS} / u_{SGS}, \text{ and} \tag{7–12}$$

$$\tau_{\eta} = \left(\frac{\mu \cdot L_{SGS}}{\rho \cdot u_{SGS}^3} \right)^{1/2}. \tag{7–13}$$

The volume fraction of the fine scales is calculated as ξ^{*3} and species are assumed to react in the fine structures over a time scale

$$\tau^* = C_{\tau} \tau_{\eta}, \tag{7–14}$$

where a time scale constant is taken equal to C_{τ} = 0.4082 similar to applied in the EDC RANS model. Magnussen (1981) assumes that all the fine scales in the cell are perfectly stirred reactors with a residence time τ^*. Combustion at the fine scales is assumed in this model to take place as a constant-pressure reactor. The reactor type is determined by the choice of a mixing rate $1/\tau^*$ and a time-step Δt. In FLUENT initial conditions at the constant pressure reactor are taken as the current species and temperature in the cell. Arrhenius reactions governed by equation (7-15) proceed over the time scale τ^*. The *in situ* adaptive tabulation ISAT algorithm (Pope, 1997), offering substantial reduction in run-time by up to three orders of magnitude, is applied.

All of the reactions considered in the chemical mechanism involved are elementary (reversible). For reversible reaction the molar rate of creation or destruction of species *i* in reaction *r* is given by equation

$$\hat{R}_{m,R} = \Gamma \cdot \left(\nu''_{m,r} - \nu'_{m,r}\right) \cdot \left(k_{f,r} \prod_{n=1}^{N} \left[C_{n,r}\right]^{\nu'_{m,r}} - k_{b,r} \prod_{n=1}^{N} \left[C_{n,r}\right]^{\nu''_{m,r}} \right), \tag{7–15}$$

where N is the number of chemical species in the system; $\nu'_{m,r}$ is the stoichiometric coefficient for reactant m in reaction r; $\nu''_{m,r}$ is the stoichiometric coefficient for product m in reaction r; $k_{f,r}$ is the forward rate constant for reaction r; $k_{b,r}$ is the backward rate constant for reaction r; $C_{n,r}$ is the molar concentration of species n in reaction r. Γ represents the net effect of third bodies on the reaction rate and is given by

$$\Gamma = \sum_{n=1}^{N} \gamma_{n,r} C_n \,, \tag{7–16}$$

where $\gamma_{m,r}$ is the third-body efficiency of n-th species in the r-th reaction. The forward rate constant for reaction r without pressure dependency is computed in conventional form of Arrhenius equation

$$k_{f,r} = A_r T^{\beta_r} \exp\left(-E_r / RT\right), \tag{7–17}$$

where A_r is the pre-exponential factor for r-th reaction; β_r is the temperature exponent; E_r is the activation energy for the reaction, J/kmol; R is the universal gas constant, 8314.4 J/K/kmol. All reactions are reversible, the backward rate constant for reaction r is calculated from the forward rate (7–17) and the equilibrium constant K_r using the equation

$$k_{b,r} = k_{f,r} / K_r \,. \tag{7–18}$$

The equilibrium constant K_r computed as

$$K_r = \exp\left(\frac{\Delta S_r^0}{R} - \frac{\Delta H_r^0}{RT} \right) \cdot \left(\frac{P_{atm}}{RT} \right)^{\sum_{i=1}^{N} \left(\nu''_{m,r} - \nu'_{m,r}\right)}, \tag{7–19}$$

where P_{atm} denotes normal atmospheric pressure (101,325 Pa). The term within the exponential function represents the change in Gibbs free energy and its components are computed as

$$\frac{\Delta S_r^0}{R} = \sum_{i=1}^{N} \left(\nu''_{m,r} - \nu'_{m,r}\right) \frac{S_m^0}{R}, \tag{7–20}$$

$$\frac{\Delta H_r^0}{RT} = \sum_{i=1}^{N} \left(\nu''_{m,r} - \nu'_{m,r}\right) \frac{h_m^0}{RT}, \tag{7–21}$$

where S_m^0 and h_m^0 are entropy and enthalpy respectively of the m-th species respectively evaluated at temperature T and atmospheric pressure. Specific heats of mixtures were approximated as piecewise-polynomial functions of temperature with polynomial coefficients calculated according to mass-weighted mixing law.

The detailed 21-step chemical reaction mechanism of hydrogen combustion in air by Gutheil et al. (1993) employing 37 elementary reactions is applied. The effect of nitrogen chemistry is taken into account by considering detailed mechanism of NO formation. The specific reaction rate constants are given in Table 7–1. The forward reaction rate constants are presented in the table, and backward rates for reversible reactions are calculated through the equilibrium constants (7-18).

No.	Reactions	*A, KJ/mol*	β_r	E_r, *mol/m³*
1	H+O2=OH+O	2.00E+14	0.00	70.30
2	H2+O=OH+H	1.80E+10	1.00	36.93
3	H2O+O=OH+OH	5.90E+09	1.30	71.25
4	H2+OH=H2O+H	1.17E+09	1.30	15.17
5	H+O2+M=HO2+M	2.30E+18	-0.8	0.00
	Third-body chaperon efficiencies H2/1./ H2O/6.5/ O2/0.4/ N2/0.4/			
6	H+HO2=OH+OH	1.50E+14	0.00	4.20
7	H+HO2=H2+O2	2.50E+13	0.00	2.93
8	OH+HO2=H2O+O2	2.00E+13	0.00	4.18
9	H+H+M=H2+M	1.80E+18	-1.00	0.00
	Third-body chaperon efficiencies H2/1./ H2O/6.5/ O2/0.4/ N2/0.4/			
10	H+OH+M=H2O+M	2.20E+22	-2.00	0.00
	Third-body chaperon efficiencies H2/1./ H2O/6.5/ O2/0.4/ N2/0.4/			
11	HO2+HO2=H2O2+O2	2.00E+12	0.00	0.00
12	H2O2+M=OH+OH+M	1.30E+17	0.00	190.38
13	H2O2+OH=H2O+HO2	1.E+13	0.00	7.53
14	O+HO2=OH+O2	2.E+13	0.00	0.00
15	H+HO2=O+H2O	5.E+12	0.00	5.90
16	H+O+M=OH+M	6.2E+16	-0.60	0.00
	Third-body chaperon efficiencies H2O:5, others 1			
17	O+O+M=O2+M	6.17E+15	-0.50	0.00
18	H2O2+H=H2O+OH	1.E+13	0.00	15.02
19	H2O2+H=HO2+H2	4.79E+13	0.00	33.26
20	O+OH+M=HO2+M	1.E+16	0.00	0.00
21	H2+O2=OH+OH	1.7E+13	0.00	200.0

	Nitrogen Chemistry			
22	O+N2=N+NO	1.82E+14	0.00	319.02
23	O+NO=N+O2	3.8E+09	1.00	173.11
24	H+NO=N+OH	2.63E+14	0.00	210.94
25	NO+M=N+O+M	3.98E+20	-1.50	627.65
26	N2+M=N+N+M	3.72E+21	-1.60	941.19
27	N2O+O=NO+NO	6.92E+13	0.00	111.41
28	N2O+O=N2+O2	1.E+14	0.00	117.23
29	N2O+N=N2+NO	1.E+13	0.00	83.14
30	N+HO2=NO+OH	1.E+13	0.00	8.31
31	N2O+H=N2+OH	7.6E+13	0.00	63.19
32	HNO+O=NO+OH	5.01E+11	0.50	8.31
33	HNO+OH=NO+H2O	1.26E+12	0.50	8.31
34	NO+HO2=HNO+O2	2.E+11	0.00	8.31
35	HNO+HO2=NO+H2O2	3.16E+11	0.50	8.31
36	HNO+H=NO+H2	1.26E+13	0.00	16.63
37	HNO+M=H+NO+M	1.78E+16	0.00	203.7

Table 7–2. Specific reaction rate constants (Gutheil et al., 1993).

7.2.3. Non-inertial rupture disk case simulations

Considering the significant scattering of available experimental data and a number of mentioned uncertainties involved, e.g. internal geometry (Dryer et al., 2007), initial hydrogen temperature (Pinto et al., 2007), presence of wetting substance (Mogi et al., 2007), it was decided to compare simulations by the LES model of spontaneous ignition against experimental data by Golub et al. (2007, 2008).

The experimental setup includes a high-pressure chamber filled with hydrogen to required pressure, and a low-pressure chamber with air at atmospheric conditions connected by a pipe of 5 mm internal diameter and variable length Golub et al. (2007, 2008). The high pressure hydrogen and air at atmospheric pressure were separated by a copper rupture disk of 0.1–0.2 mm thickness, depending on designed rupture pressure, installed at entrance from the high-pressure chamber to the pipe. When the pressure in the high-pressure chamber exceeds the critical value, the burst disk ruptures and shock wave propagates through the low-pressure pipe with air into the low-pressure chamber. Critical pressure of hydrogen in high-pressure chamber varied in the range 2.0–13.2 MPa, while a length of the tube varied between 65 mm and 185 mm. In each experiment the rupture disk completely opens in a controlled manner with its petals fully pressed to tube walls. A pair of a pressure transducer and a light sensor was installed at different distance from the rupture disk to detect shock wave propagation and radiation from the spontaneous ignition. It should be noted that in each of the experiments only one pair of sensors was present. The distance from the rupture disk to sensors pair was changed from one test to another at the same conditions to identify the location of spontaneous ignition.

From a series of experiments the test with initial hydrogen pressure of 9.73 MPa and 65 mm extension pipe was chosen in order to keep simulation time to minimum. From the experimental data it is known the spontaneous ignition occurred at distance less than 33 mm from the rupture disk. Experimentally observed pressure behind the shock wave was in the range 2.69–3.40 MPa, and the delay between the shock wave front and the chemical reaction front (spontaneous ignition) at 33 mm from the burst disk was in the range 18–24 μs.

The simulated high-pressure chamber was 140 mm long and 20 mm diameter cylinder, the simulated low-pressure chamber was 145 mm long and 5 mm diameter cylinder (Bragin and Molkov, 2009). The grid was created using GAMBIT. In order to exclude the effect of mesh irregularities on combustion in reacting flow, the low-pressure chamber was meshed with an unstructured hexahedral grid with uniform CV size of about 200 μm both along the tube and a similar characteristic CV size in the cross-section. The high-pressure chamber was meshed with the smallest CV size of about 250 μm clustered near the entrance to the pipe and rapidly increasing away from it reaching the maximum cell width of 10 mm in a far field from the rupture disk. The total number of control volumes was equal to 430,976. Non-slip impermeable adiabatic boundary conditions were used on all of the walls. The shock tube was modelled as "closed" to exclude potential effects of numerical boundary conditions on the process. This assumption is applicable as the low-pressure chamber is long enough to simulate the process of ignition without getting the reflection of the shock wave from the closed end.

Initial conditions at the high-pressure chamber were pressure 9.6 MPa, temperature 300 K, and the mole fraction of hydrogen 1. The low-pressure chamber was filled with air (0.23 mass fraction of oxygen and 0.77 of nitrogen) at atmospheric pressure and temperature of 300 K. Non-physical values were encountered in simulations due to numerical instabilities if the imaginary rupture disk, i.e. the boundary separating gases, was placed exactly at the border between the larger in diameter (20 mm) high-pressure chamber and the smaller in diameter (5 mm) low-pressure chamber. To avoid instabilities during simulation of strong discontinuity in pressure accompanied by strong discontinuity in area, the simulated "rupture disk" was moved one pipe diameter (5 mm) downstream, i.e. high-pressure hydrogen was also initially present in the first 5mm of the pipe. In simulations the maginary rupture disk was "removed instantly" and a shock wave was allowed to propagate.

The problem was simulated using FLUENT 6.3.26, which realises control-volume based finite-difference method. The solver used explicit linearization of the governing equations with explicit method for solution of linear equation set. The third order MUSCL scheme with AUSM flux splitting was applied for flow discretisation. The four step Runge-Kutta algorithm was employed for advancement of solution in time. The time step was determined from Courant-Friedrichs-Lewy condition, where the CFL number was equal to 0.5 to ensure stability.

Figure 7–2 shows the dynamics of temperature (left) and hydrogen mole fraction (right) during the first 56 μs after the rupture disk instant opening (non-inertial rupture disk). At the initial moment t=0 the "rupture disk" boundary separating high-pressure hydrogen and atmospheric air, located at x=0, is instantaneously removed and a shock wave propagates into air heating it up due to compression. The shock wave is followed by a contact surface separating cold hydrogen and heated air. It is seen that the thickness of the heated air layer between the shock front and the contact surface increases in time.

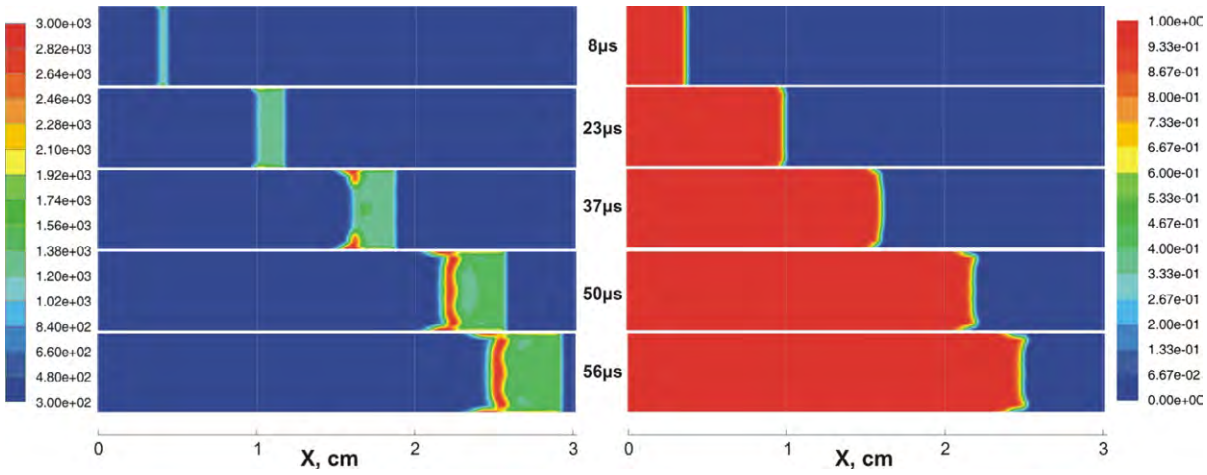

Figure 7–2. Dynamics of spontaneous ignition (Bragin and Molkov, 2009): temperature (left) and hydrogen mole fraction (right).

The shock wave propagates along the tube as a plane wave without any curvature outside the boundary layer. The shape of the contact surface changes from plane to slightly convex in the beginning due to non-slip conditions at the pipe walls. The highest temperature is observed in the boundary layer due to velocity decrease (stagnation conditions). Owing to counter diffusion of hydrogen and air the contact surface, and heat diffusion from hot air to cold hydrogen through the contact surface the spontaneous ignition occurs when critical conditions for chemical reaction are reached. The chemical reaction propagates in the direction from the wall to the tube axis as the contact surface propagates downstream. After 45 μs from the start of the process at distance 20 mm from the non-inertial "rupture disk" location the combustion occupies the whole cross-section area of the pipe. Initiation of the chemical reactions in the boundary layer accelerates propagation of the reaction front along the wall compared to the axial part leading to change of the convex shape of the contact surface in the most of the tube cross-section to a slightly concave form.

In numerical simulations the reaction front is established throughout the pipe cross-section at distance 20 mm from the burst disk at time 45 μs after the instant rupture. In the experiment by Golub et al. (2007, 2008) the light sensor was located 33 mm from the burst disk. Unfortunately, the time of the shock arrival at this location in experiment was not reported. In numerical simulations the shock reached the light sensor location of 33 mm at 58 μs, and the reaction front followed the shock with a delay of 7–10 μs. In the experiment the sensor started to register light 18–24 μs after the shock arrival. The deviation in delay of the flame front arrival after the shock could be explained by the inertial (not instant) opening of the real rupture disk, which was not accounted for in the simulations. Another factor, which could explain the deviation, could be the absence of heat transfer from the reaction zone to walls in the simulations.

7.2.4. Mechanism of flame separation by vortex

A sequence of photographs showing the flame exiting from a pipe, where spontaneous ignition has happened, was published by Mogi et al. (2008) using high-speed digital colour video camera. Initial pressure of hydrogen in chosen for numerical simulations experiment was 14.5 MPa and the pipe length was 185 mm. The pipe wall thickness was 4 mm. This sequence of snapshots shows combustion of spontaneously ignited hydrogen-air mixture emerging outside and stabilizing in the vicinity of the pipe exit. The authors observed that once the emerged from the pipe flame is stabilized near the nozzle, it acts as a pilot flame and ignites/sustains the jet fire afterwards. Therefore, the numerical observation of flame "stabilization" near the pipe exit may be taken as an indication of the transition from the spontaneous ignition to the sustained jet fire.

In this series of simulations (Bragin and Molkov, 2009) we have shifted the focus from the resolution of spontaneous ignition towards the transition from ignition within the pipe to combustion outside the pipe in the atmosphere. Therefore, it was decided to sacrifice resolution in the channel further in order to reduce CPU time to practically reasonable. The characteristic size of control volumes was twice larger than in simulations described in previous section and it was of the order of 400 μm. The larger cell size attached to the wall makes the boundary layer "wider" and thus, due to reducing the heat dissipation from the initial ignition spot, facilitates faster ignition.

The area in the immediate vicinity of the tube exit in the atmosphere was initially coarsely meshed with cells clustered around the anticipated under-expanded jet shock structure. Just before the initial shock wave and the spontaneously ignited mixture reached the end of the pipe, the grid outside the pipe was refined for the first time. As the process evolved and the jet flow increased in size, the second grid refinement was performed at 220 μs after the rupture disk opening. The number of control volumes increased due to the grid refinement from 261,640 to 478,528 during the simulation.

Since temperature of hydrogen and surrounding air were not reported in the experimental paper, they were accepted as 300 K in simulations. Atmospheric pressure of air (23% of oxygen and 77% nitrogen by volume) was taken as 101,325 Pa. At time t=0 the imaginary rupture disk was instantaneously removed to commence the discontinuity decay. Non-reflecting "far field" boundary conditions were set downstream and at radial boundaries of the calculations domain.

Figure 7–3 shows the dynamics of temperature, velocity, hydrogen and hydroxyl mole fractions. The field of view in all numerical snapshots is kept constant, where the channel length shown corresponds to 66.5 mm, and the external to the pipe area is 148 mm long and 130 mm wide. All snapshots represent 2D cross-section along the pipe axis. The maximum and minimum values in each series were fixed in order to lock the relation between colours and corresponding parameters in all frames. Minimum and maximum values in each set of frames were fixed to 0–2400 K for temperature, 0–3000 m/s for velocity, 0–1 for hydrogen mole fraction, and 0.001–0.01 for hydroxyl mole fraction. If values fall out of these limits, they are coloured according to the colour of limits – red for values above the upper limit and blue for values below the lower limit.

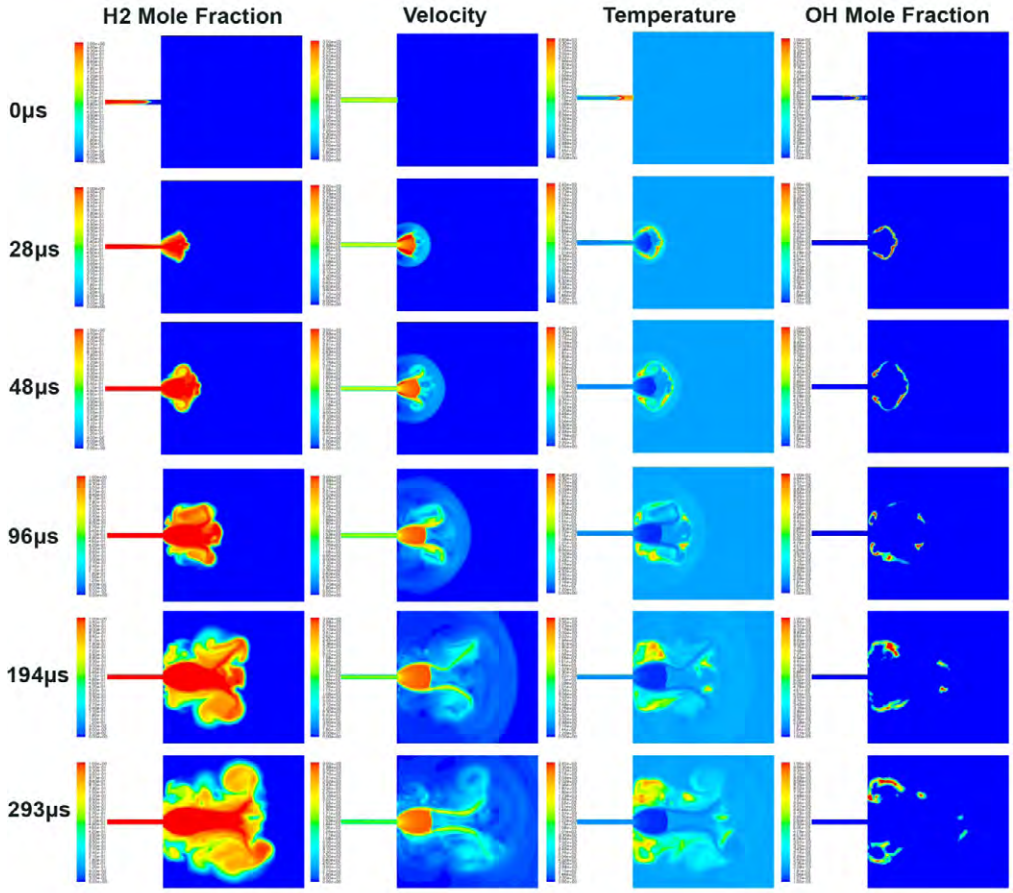

Figure 7–3. Dynamics of the velocity, temperature and mole fractions of hydrogen and hydroxyl in 2D slice along the pipe axis (Bragin and Molkov, 2009).

The dynamics of spontaneous ignition in the pipe was similar to the one described in previous section and is not shown here. The resulting flame front tip gets behind the shock wave by about 7 mm by the end of the pipe. The flame front width is about 3 mm near the pipe axis, while near the wall it extends as long as 35 mm. Combustion is more pronounced near walls, having wider regions with high temperature. The first frame in time series corresponds to the time 131.5 μs from the instant opening of the "rupture disk". For ease of interpretation of the transition process the reference time was set to 0 μs at this moment (see Fig. 7–3).

Figure 7–3 shows that as the shock wave emerges from the pipe exit it diffracts and transforms from a plane to a hemispherical form. The shock propagates outwards and quickly loses the strength. It is followed by the flame front pushed by the expanding hydrogen. Once hydrogen leaves the tube, hemispherical expansion starts and the flame front follows the expansion. The formation of Mach disk commences shortly after (see "28 μs" frame in Fig. 7–3) and the expansion of hydrogen is held back increasing the separation distance between the leading shock and the contact surface. Sudden deceleration of hydrogen stimulates turbulent mixing and the contact surface becomes turbulent.

In parallel to the Mach disk formation, the outer annular flow at the Mach disk's periphery forms. Owing to viscous forces this supersonic annular flow generates a large-scale vortex, which turns the flow back towards the pipe exit. The formation of vortex breaks the combusting gas (48 μs) into two parts – downstream and upstream parts (see comparison with experimental snapshots below).

Meanwhile, the shock barrel is not yet stabilized. Upstream combustion region is pushed back by the vortex tip (96 μs), while downstream combustion region in the vicinity of jet axis is forced out. As the vortex straightens, the supply of hydrogen to the recirculation area dies out and reduction of flow velocity allows necessary induction time for intensification of combustion. It can be seen that combustion affects the gas dynamic evolution of the jet and results in non-axis-symmetrical to some extent flow beyond the Mach disk (194 μs). Shock barrel is stabilized around 200 μs. The annular vortex increases in size widening distance from the axis where hydrogen is present. By the time of the last frame in Fig. 7–3 (293 μs) the downstream combustion is fully ceased, while the upstream combustion in the recirculation zone is sustained.

Unlike 2D CFD slices of reacting flow parameters, experimental snapshots give a side-view on the 3D combusting jet. Therefore, it is impossible to see the jet to the level of details the numerical experiments can produce, including profiles of all the parameters of interest. Experimental data on the flame size by Mogi et al. (2008) were critically analysed. The uncertainty in published snapshots lies in the scale of frames presented. The scale given should be reconsidered, since the inner diameter of the tube is known to be 5 mm, but according to the scale given on photographs (Mogi et al., 2008) an outer diameter of the tube is equal to 4.5 mm. From a private communication from Dr Mogi, it was clarified that the tube wall width was 4 mm. Thus, outer diameter of the tube shown in photographs was equal to 13 mm. Therefore, field of view in experimental photographs corresponds to 104 x 76.4 mm with pipe bulging out by 14.6 mm.

While some works base their estimation of the visible flame length on temperature, e.g. Brennan et al. (2009), in this study the flame is identified by the mole fraction of hydroxyl. Hydroxyl concentration coupled with high-temperature is widely acknowledged as an indication of combustion taking place. Here we identify visible flame by the hydroxyl mole fraction higher than 0.001. Figure 7–4 shows comparison between experimental and simulated snapshots. Numerical flame propagation can be referenced to experimental dimensions by vertical lines, which are positioned 10 mm apart.

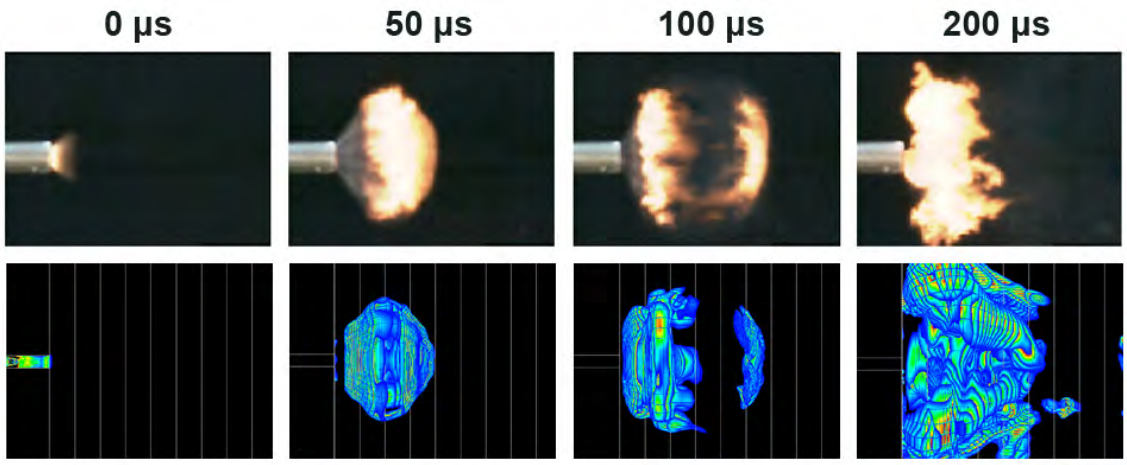

Figure 7–4. Comparison of high-speed video camera experimental photographs (Mogi et al., 2008) with numerical 3D snapshots (Bragin and Molkov, 2009).

The ignited within the pipe jet exits to atmosphere at 0 µs. It develops into a cocoon of combusting mixture (50 µs). Shortly after this the annular vortex, which cannot be seen here (see previous Fig. 7–3) causes the cocoon to break into upstream and downstream combusting regions (100 µs). As the downstream combustion region is blown away, the upstream region is stabilized near the tube exit (200 µs). The size of this region, however, is bigger in simulations. This can be explained by three potential reasons. Firstly, the chosen limit for the numerical visualisation of the flame front of 0.001 of OH (it is often is taken as 0.01 of OH). Secondly, there are difference conditions for air entrainment in the experiment and simulations. Indeed, simulations of hydrogen release were carried out not for the pipe with 5 mm internal diameter and 4 mm wall thickness, but for the channel of 5 mm in a wall with "infinite" dimension. Third reason for deviation in size of stabilised flame could be the wetting of the inside surface of the tube between the burst disk and the exit to the atmosphere by the aqueous Na_2CO_3 solution (1%) in order to allow visualization of the flame. This solution could have interfered with heat transfer and chemistry of hydrogen combustion and decreases the visible flame size.

The mechanism of transition from spontaneous ignition inside of the tube into sustained jet fire is described in this section within the computational limitations. It is assumed, following the experimental observations and numerical simulations, that the transition to the sustained jet flame is largely dependent on the initial jet formation stage, where developing annular vortex pushes combusting mixture upstream into the recirculation zone. Once the flame is stabilised near the pipe exit, it can act as a pilot flame to jet fire later on.

7.2.5. Lower pressure limit of spontaneous ignition in a T-shaped channel

7.2.5.1. Experimental set up

The geometry of the experimental set up, including a T-shaped channel mimicking PRD, is taken from Golub et al. (2010a) and is shown in Fig. 7–5. The high pressure system consists of a 210 mm long tube with 16 mm internal diameter (ID) followed by a 280 mm long tube with 10 mm ID at the end of which a flat rupture disk, made of copper or aluminium with cuts facilitating failure, is located followed by a mock-up PRD (T-shaped channel) open to the atmosphere.

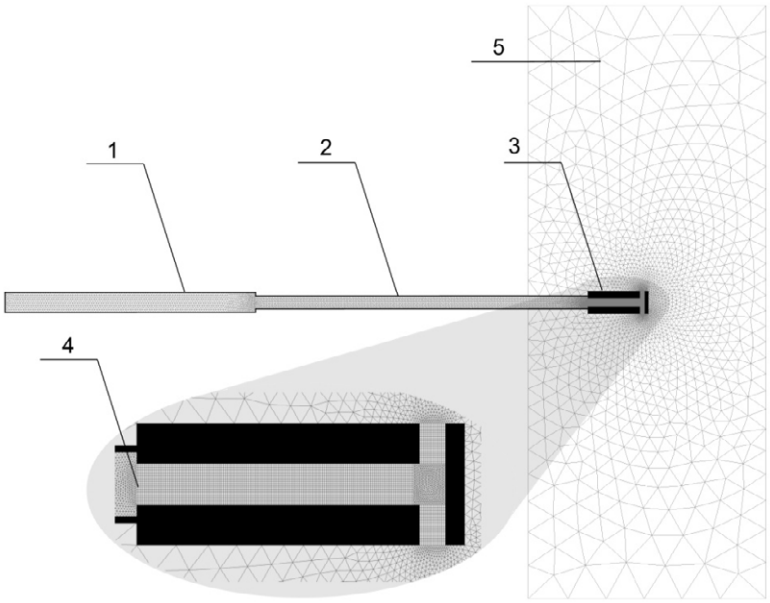

Figure 7–5. The geometry and computational domain: 1 and 2 – high pressure tubes, 3 – mock-up PRD (T-shaped channel), 4 – burst disk, 5 – external computational domain.

The PRD has a 48 mm long axial channel of 6.5 mm ID with a flat end, and two radial channels on opposite sides of the axial channel to vent hydrogen to atmosphere. Each radial channel has 6.25 mm length and 4 mm ID (distance from the end connected to the atmosphere of one radial channel to the end of another is 19 mm). Radial channels are flushed with the axial channel end wall and positioned so that the edge of each side channel touches tangentially the flat end wall of the axial channel. The rupture disk opening was estimated by Golub et al. (2010a) as about ten microseconds thus creating conditions for better mixing of hydrogen with air during the opening as compared to not realistic instant opening. To register spontaneous ignition a light sensor was installed along the axis of radial channels of the PRD. Temperature behind the shock wave reflected from the flat end wall was estimated by authors as more than twice higher than the temperature behind the incident shock wave. Golub et al. (2010a) stated that when the initial pressure in high pressure chamber did not exceed 1.2 MPa the light sensor did not record any signal, and when pressure was 2.9 MPa the ignition was registered. Unfortunately, there is no published experimental information on spontaneous ignition at storage pressures in between these two values. However, it has been stated by Golub (2010b) that light was registered at storage pressure 2.43 MPa as well.

7.2.5.2. Numerical details

The 3D grid was created using GAMBIT tool of FLUENT 6.3.26, which realises control-volume based finite-difference method (Bragin et al., 2011). The axial and radial channels of the PRD were meshed with a hexahedral grid with a uniform control volume (CV) size of about 400 μm both along the axial channel and in its cross-section, excluding the intersection zone. The intersection area of the axial and the radial channels was meshed with tetrahedral CVs with size of about 200 μm. This is the largest CV size used in numerical simulations of the spontaneous ignition phenomenon. This is due to the application of the LES technique requiring 3D domain and thus larger CV size to simulate a problem in reasonable computation time. The high-pressure chamber was meshed by tetrahedrons with the smallest CV size of about 250 μm clustered near the membrane of the PRD and rapidly increasing away from it reaching the maximum cell width of 10 mm at the far end. The total number of control volumes in the computational domain was equal to a moderate number of 417,685 cells.

Non-slip impermeable adiabatic boundary conditions were used on walls. Non-reflecting open "pressure-far-field" boundaries were used outside of the PRD. The high pressure system was modelled as closed to exclude potential effects of inlet boundary conditions on the process. This assumption is valid because the observation time in simulation is less than a time required for rarefaction wave to reach the far end of the high-pressure system. Four cases are presented below to illustrate changes in the process dynamics with initial hydrogen pressure in the high-pressure system of 1.35, 1.65, 2.43 and 2.90 MPa. Initial temperature of 300 K and the mole fraction of hydrogen equal to 1 were assumed in the high-pressure system before the start of inertial rupture disk opening in all four cases. Low pressure chamber was filled with air (0.23 mass fraction of oxygen and 0.77 of nitrogen) at pressure 0.101 MPa and temperature 300 K.

The solver used explicit linearisation of the governing equations with explicit method for solution of linear equation set. A second order upwind scheme with AUSM flux splitting was applied for flow discretisation. The four step Runge-Kutta algorithm was employed for advancement of simulations in time. The time step was determined from Courant-Friedrichs-Lewy condition, where the CFL number was equal to 0.2 to ensure stability.

7.2.5.3. Modelling of rupture disk opening

The rupture disk opening is expected to play an important role in the process of spontaneous ignition by diffusion mechanism due to its effect on the mixing between hydrogen and air. A modelling strategy is described below. The following formula is applied to calculate an opening time of a diaphragm (Spence and Woods, 1964)

$$t = k\left(\rho bd / p\right)^{1/2}, \tag{7–22}$$

where ρ is the density of the diaphragm material, b and d are thickness and diameter of the diaphragm respectively, and the values of k are found to be in a range 0.91–0.93 (Wen et al., 2009). Density of annealed copper is 8900 kg/m^3. For example, for 2.9 MPa case, the opening time can be calculated as

$$t = 0.92\left(8900 \cdot 5 \cdot 10^{-5} \cdot 6.5 \cdot 10^{-3} / 2.9 \cdot 10^{6}\right)^{1/2} = 29.1 \text{ µs}. \quad (7\text{–}23)$$

The opening of a membrane was approximated in simulations by 10 step-like process (see Fig. 7–6) with a time for each section given in Table 7–2 for four investigated cases.

Section	1	2	3	4	5	6	7	8	9	10
Opening time, µs [1.35 MPa case]	0	4.7	9.4	14.2	18.9	23.6	28.4	33.1	37.8	42.6
Opening time, µs [1.65 MPa case]	0	4.3	8.6	12.8	17.1	21.4	25.6	29.9	34.3	38.5
Opening time, µs [2.43 MPa case]	0	3.5	7.1	10.6	14.2	17.7	21.3	24.8	28.3	31.9
Opening time, µs [2.9 MPa case]	0	3.2	6.5	9.7	12.9	16.2	19.4	22.6	25.9	29.1

Table 7–2. Opening times of sections for simulated cases (Bragin et al., 2011).

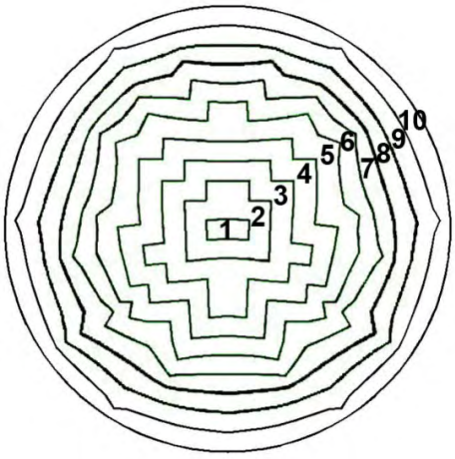

Figure 7–6. Step-like approximation of a burst disk rupture process: 1-10 are sections that open in series.

7.2.5.4. Initial stage following the membrane rupture

Figure 7–7 shows dynamics of temperature and hydrogen mole fraction at an initial stage of hydrogen release into air in the mock up PRD with instant opening (left) and inertial opening (right) of the rupture disk for initial pressure 1.35 MPa in the high-pressure chamber (Bragin et al., 2011). The inertial rupture disk opening is accompanied by formation of an under-expanded jet from increasing with time open area of the disk. A barrel-like structure can be seen for the case of inertial membrane opening (Fig. 7–7, right).

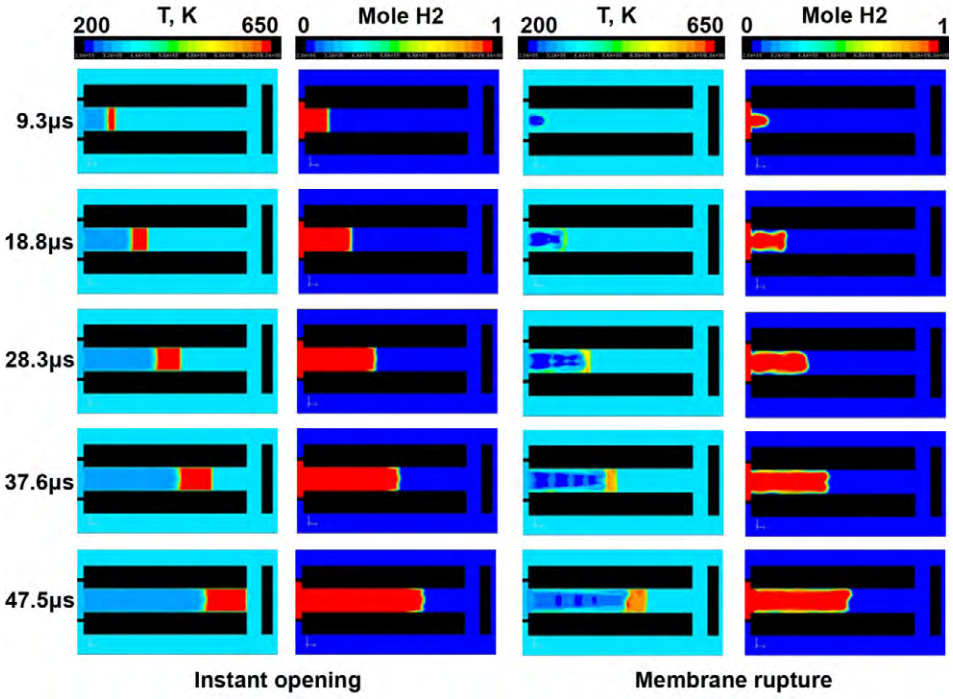

Figure 7–7. Dynamics of temperature and hydrogen mole fraction at the initial stage following an instant rupture disk opening (left) and inertial ten-step rupture disk opening (right) for the 1.35 MPa high-pressure chamber case.

The one by one opening of each of 10 sections of the rupture disk changes the barrel diameter to a larger one and the flow pattern looks similar to the multiple diamond-like pattern, which is characteristic for this range of pressures. For the case of instant opening of an imaginary non-inertial membrane the shock heated zone in air (red colour) is almost three times thicker compared to the inertial membrane rupture case at the same moment of time. It is obvious, that the inertial opening of the membrane generates more intense mixing of hydrogen and air, including in the boundary layer of the axial channel walls. Maximum temperature in the shock-heated air is 50 K lower for the inertial membrane opening case. Thus, modelling of the inertial rupture disk opening is an important part of predictive simulations of spontaneous ignition in complex geometries.

7.2.5.5. Shock reflection

Shock wave reflections can play an important role in the triggering of spontaneous ignition process. Reflected pressure at the flat end of the axial channel of the T-shaped PRD can be estimated using 1D gas dynamic equations that can be found elsewhere (Bragin et al., 2011). First, we estimate the Mach number M_S of the shock wave generated by the discontinuity

$$\frac{p_4}{p_1} = \left(1 + \frac{2\gamma_1}{\gamma_1 + 1}\left(M_S^2 - 1\right)\right) \Big/ \left(1 - \frac{\gamma_4 - 1}{\gamma_1 + 1} \cdot \frac{a_1}{a_4} \cdot \frac{M_S^2 - 1}{M_S}\right)^{\frac{2\gamma_4}{\gamma_4 - 1}}, \tag{7–24}$$

where p_4/p_1 is initial hydrogen to atmospheric air pressure ratio when the membrane is removed, γ_1 and γ_4 are specific heat ratio for air and pushing gas respectively (for our case $\gamma_1 = \gamma_4 = 1.4$), a_1/a_4 – ratio of air to hydrogen speed of sound. Knowing M_S, pressure p_2 behind the leading shock wave (propagating in air) can be calculate

$$p_2 = p_1\left(\frac{2\gamma_1 M_S^2}{\gamma_1 + 1} - \frac{\gamma_1 - 1}{\gamma_1 + 1}\right). \tag{7–25}$$

Finally, the pressure p_5 following normal reflection of leading shock wave can be calculated as

$$\frac{p_5}{p_2} = \frac{(3\gamma_1 - 1)p_2 / p_1 - (\gamma_1 - 1)}{(\gamma_1 - 1)p_2 / p_1 + (\gamma_1 + 1)}. \tag{7–26}$$

Table 7–3 gives results of calculations by 1D theory using Eqs. (7-24)-(7-26) and 3D numerical simulations (LES) for the reflected shock pressure. Results of LES simulations are close to the theoretical 1D prediction yet are by 8-10% above the theory. It is worth to note that, as numerical simulations have demonstrated, spontaneous ignition at the flat end of the axial channel, where reflection takes place, is impossible as there is no hydrogen at this location for considerable time.

Initial hydrogen pressure, MPa	1.35	1.65	2.43	2.9
Mach number of leading shock wave Eq. (7–24)	2.47	2.64	2.98	3.15
Pressure behind leading shock wave Eq. (7–25), MPa	0.7	0.8	1.04	1.16
Calculated reflected pressure Eq. (7–26), MPa	2.96	3.61	5.15	6.0
Simulated reflected pressure (LES), MPa	3.25	3.9	5.56	6.6

Table 7–3. Calculated parameters for normal shock wave reflection using Eqs. (7–24)–(7–26).

Applicability of 1D theories is limited to simple scenarios, e.g. propagation of a shock wave through uniform hydrogen-air pre-mixture and normal reflection from a flat surface. If the mixture is not uniform or the shock is oblique and surface is not flat then simple methods are hardly applied. The case of T-shaped channel is even more complicated due to absence of hydrogen-air mixture in an area of first reflection, i.e. at the flat end of the axial channel, and presence of multiple reflections from curved surfaces of the channels.

7.2.5.6. Effect of storage pressure on spontaneous ignition in a T-shaped channel

Temperature and hydroxyl mole fraction profiles in the axial cross-section for cases with initial pressure of 2.9 MPa and 2.43 MPa in the high-pressure chamber are presented in Figs. 7-8 and 7-9 respectively.

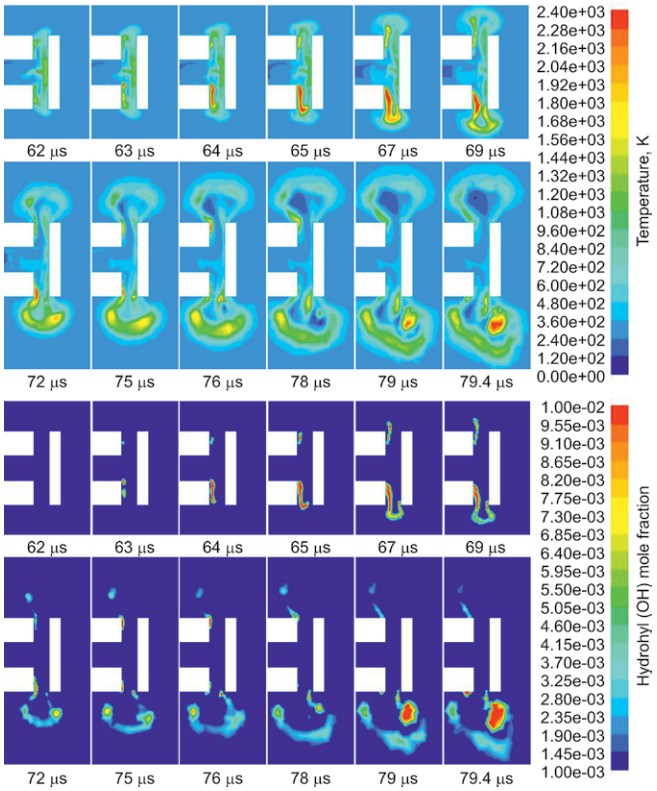

Figure 7–8. Temperature and hydroxyl mole fraction for 2.9 MPa storage pressure.

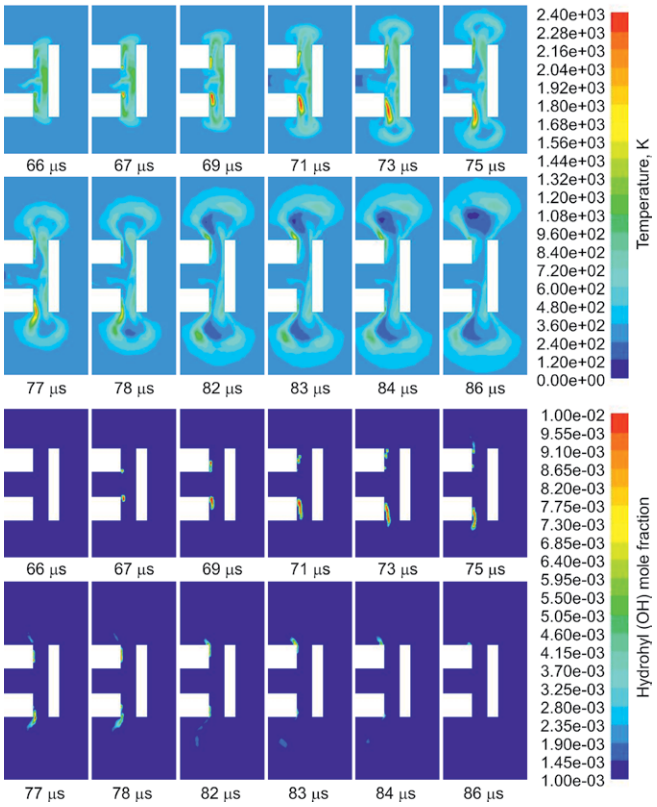

Figure 7–9. Temperature and hydroxyl mole fraction for 2.43 MPa storage pressure.

It is clear that ignition is not possible at location of the leading shock reflection on the flat end of the axial channel since hydrogen is not supplied to this area yet. Once the hydrogen flow diffracts around the edge from the axial into radial channels, it starts mixing with heated by shocks air. This provides the necessary conditions for ignition of the hydrogen-air mixture. It can be seen that for both initial pressures chemical reaction is initiated in the radial channel in a location close to the upstream wall.

Larger high temperature regions can be observed for storage pressure 2.9 MPa (Fig. 7–8) compared to pressure 2.43 MPa (Fig. 7–9). The difference becomes obvious when combusting mixture is pushed outside. At pressure 2.9 MPa a semi-spherical cocoon of a heated to critical conditions flammable hydrogen-air mixture is formed outside the PRD being followed by expanding hydrogen. Combustion is initiated in a number of spots within the cocoon (see snapshots of temperature and OH mole fraction at 79 μs). The concentration of hydrogen in these spots outside the PRD just before the ignition is in the range 29-36% by volume. Thus, a conclusion can be drawn that the ignition by the diffusion mechanism takes place in the most reacting hydrogen-air mixtures.

At storage pressure 2.43 MPa (Fig. 7–9) the combustion is rather weak, compared to the case of pressure 2.9 MPa, and the reacting mixture is dragged with the adjacent hydrogen flow, which leads to the elongation of combusting regions. Upon exit from the radial channels of the PRD, the flow undergoes an expansion and high-temperature regions disappear thus ceasing reaction and OH concentration, including the cooling role of expanding pure hydrogen jet on the flammable mixture.

The whole process from combustion initiation to self-extinction (disappearance of high temperature and OH mole fractions region, Fig. 7–9) takes a little more than 10 μs. This is sufficient to register the chemical reaction by a light sensor in the experiments. This explains the uncertainty in interpretation of experimental observations by Golub et al. (2010a, 2010b). Indeed, at pressure 2.9 MPa the combustion quite pronounced but at pressure 2.43 MPa the spot of spontaneous ignition is weak and disappears due to self-extinction. However, the light sensors still registered a signal during the spontaneous ignition. Thus, in full compliance with experimental observations the simulations confirmed the spontaneous ignition at storage pressure of 2.43 MPa.

Figures 7-8 and 7-9 demonstrate that the process is asymmetrical, i.e. the ignition in the upper radial channel is weaker than in the lower channel. At pressure 2.9 MPa the ignition survives the expansion from only the lower radial channel, while the upper part is extinguished. This is sought due to the asymmetrical opening of the rupture disk in simulations. This result demonstrates the sensitivity of spontaneous ignition to the membrane rupture process that should be investigated further along with effect of other factors such as air humidity, etc.

Figures 7-10 demonstrates temperature (left) and hydroxyl (OH) mole fraction (right) dynamics in 3D view for the case of storage pressure 1.65 MPa. This type of visualisation of simulation results is chosen because an ignition spot is located in this case not in the symmetry 2D plane. The ignition takes place on the wall within the axial channel when reflected from the flat end of the axial channel pressure wave enters the channel again. The combustion follows the flow behind the reflected pressure wave and propagates along the wall upstream of the release direction. When oxygen of air in the boundary layer is consumed the chemical reaction is self-extinguished. Thus, simulations can explain why the ignition was not reported in the experimental paper for the test at storage pressure of 1.65 MPa. Indeed, the light sensor can register only the ignition in the radial channels and cannot "see" the weak combustion process inside the axial channel unless special arrangements are done, e.g. the axial channel is made of transparent walls.

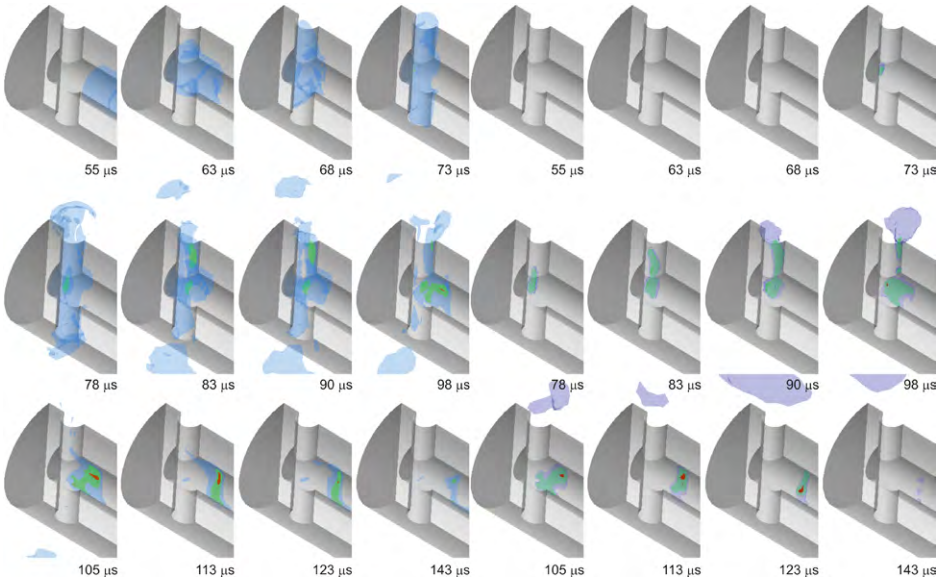

Figure 7–10. Temperature (left) and hydroxyl mole fraction (right) dynamics for 1.65 MPa storage pressure. Temperature colours: blue – 550 K, green – 1500 K, red – 2400 K. Hydroxyl mole fraction colours: blue – 0.0002, green – 0.002, red – 0.02.

Figure 7–11 shows temperature dynamics in T-shaped channel after inertial opening of the rupture disk at storage pressure of 1.35 MPa. The hydroxyl mole fraction dynamics is not presented as OH concentration is of the order of 10^{-9}–10^{-10} indicating that there is no combustion in the domain. Temperature scale is 0–1100 K in Fig. 7–11. This is different from the scale 0–2400 K applied in higher pressure when spontaneous ignition has been observed in simulations (1.65, 2.43, and 2.9 MPa) and experimentally (2.43, and 2.9 MPa).

Figure 7–11 is convenient to analyse the flow pattern and get insight into the process of the spontaneous ignition in T-shaped channel. Snapshot "60 μs" shows the contact surface between hydrogen at close to room temperature (in blue) and heated by pressure wave air (in green-yellow). The contact surface is inside the axial channel at this moment and it is disturbed by Rayleigh-Taylor instability. Close to the flat end of the axial channel there is a volume of air that is heated further by the reflected shock (in red). New areas of heated air (in red) in radial channels are seen in the next snapshot "63 μs" along with the increasing volume of hot air at the axial channel end. These new areas are probably due to the second reflection from a wall of the radial channel that is opposite to the flan end of the axial channel. At time 67 μs "cold" hydrogen starts to exit the axial channel and flows along one side of the radial channel. Hot air temperature in front of hydrogen reduces (snapshots from "67" to "77"). There is a drop in heated air temperature when hot air exits the radial channel to the atmosphere. Reflected shock is weak at storage pressure of 1.35 MPa and hot air in flow following the reflected pressure wave cannot enter the axial channel (only to small extent at the axial channel axis). At time 77 μs hydrogen starts exit to atmosphere and its temperature drops further down during this expansion.

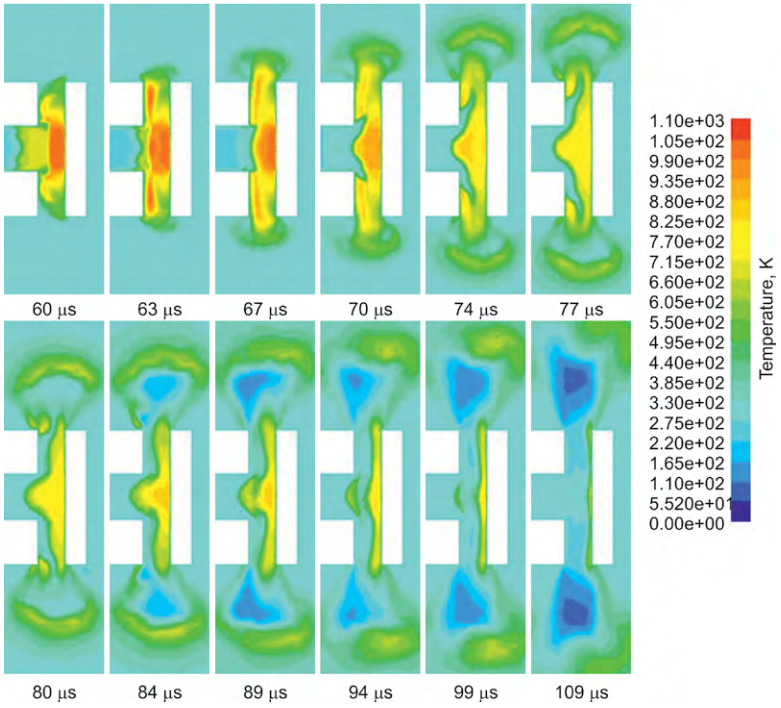

Figure 7–11. Temperature 2D profiles across the symmetry plane for storage pressure 1.35 MPa.

Thus, the conclusion can be drawn that the LES model based on the eddy dissipation concept (EDC) with detailed Arrhenius kinetics for the modelling of SGS combustion, and the renormalization group (RNG) theory for the modelling of SGS turbulence has been successfully applied to reproduce experimental data (Golub et al., 2010a, 2010b) and get an insight into the phenomenon of spontaneous ignition by diffusion mechanism in the T-shaped channel filled with air. It is confirmed that the modelling of a realistic inertial rupture disk opening is important to simulate properly the mixing process between heated by shock air and cold expanding hydrogen, and thus to find out the lower pressure limit of spontaneous ignition for particular geometry. The numerical efficiency of the EDC LES model as a tool for hydrogen safety engineering is confirmed at 3D grids with mesh size not less than 200 μk.

Numerical simulations have demonstrated that there is no ignition in T-shaped channel at storage pressure of 1.35 MPa. There is an ignition followed by a self-extinction of reaction at storage pressures 1.65 and 2.43 MPa. The minimum storage pressure at which the ignition has been observed numerically is 1.65 MPa. However, the initial spot of combustion is quickly self-extinguished in numerical test at storage pressure of 1.65 MPa. The "sustainable" ignition, when chemical reaction is clearly seen outside the mock-up PRD, has been achieved at storage pressure of 2.9 MPa. Multiple spots of combustion are developing in the cocoon of the flammable mixture outside the PRD at this pressure.

The ignition by the diffusion mechanism is located in the most reacting hydrogen-air mixtures in the range of hydrogen concentrations 29–36% by volume. The pressure range 1.65–2.9 MPa can be considered as the lower pressure limit for spontaneous ignition of hydrogen in the studied T-shaped geometry. Only pressure at the upper part of this range is able support transition from spontaneous ignition to the sustained jet flame.

8 Microflames

The scenario of concern is that a small leak in a hydrogen system could ignite, burn undetected for a long time, and potentially degrade surrounding materials or ignite any hydrogen release that may occur nearby (Butler et al., 2009). The technical information report SAE J2579 (2009) states that a localised hydrogen leak from a typical compression fitting cannot sustain a flame (that can subsequently weaken material and cause a loss of containment), when mass flow rate is below 28 μg/s. The lowest leak possible sustain a flame from a miniature burner configuration is 5 μg/s.

Images of hydrogen diffusion microflames near their quenching limits in air (left) and in oxygen (right) are shown in Fig. 8–1 (Lecoustre et al., 2010). The hydrogen flow was directed downward. To give an impression about the real flame size the word "WE" from a US dime is shown at the same scale as the flames. The burner was a stainless steel hypodermic tube with an internal diameter of 0.15 mm and an outside diameter of 0.30 mm. The flames and any glowing of the burner tip were not visible even in a darkened laboratory and hence were detected with a thermocouple. A shutter time for a camera used to make images in Fig. 8–1 was 30 s. Buoyancy was found by detailed experiments and computations to be insignificant for hydrogen microflames (Cheng et al., 2005).

Figure 8–1. Hydrogen diffusion microflames near their quenching limits (Lecoustre et al., 2010): in air (left) and in oxygen (right). A shutter time is 30 s.

Near their quenching limits these flames had hydrogen flow rates of 3.9 μg/s and 2.1 μg/s in air and oxygen, respectively (Lecoustre et al., 2010). Assuming complete combustion, the associated heat release rates are 0.46 W and 0.25 W (based on hydrogen's lower heating value of 119.9 kJ/g). These are the weakest self-sustaining steady flames ever observed. Hydrogen leaks support combustion at flow rates much lower than leaks of other gaseous fuels. Uncertainties in the quenching limit flow rates measurements are estimated by authors at ±10%.

Microflames are associated with small flow rates of subsonic laminar flows from cracks. The equation for volumetric flow rate from the orifice casts (see equation 6-14)

$$\dot{V}_{vent} = CA\left\{\left(\frac{2\gamma}{\gamma-1}\right)\frac{P_S}{\rho_{encl}}\left[\left(\frac{P_S}{P_{encl}}\right)^{\frac{2}{\gamma}} - \left(\frac{P_S}{P_{encl}}\right)^{\frac{\gamma+1}{\gamma}}\right]\right\}^{\frac{1}{2}}. \qquad (8\text{–}1)$$

Thus, for the same supply pressure the highest volumetric flow rate through leaks is expected for a gas with lowest density, i.e. hydrogen.

8.1. Quenching and blow-off limits

There is generally a limited range of flow rates for which a flame can be established on the present burners (Sunderland, 2010). Below this range, the flow is said to be below the quenching limit. Quenching occurs when there is too much heat loss for combustion to be sustained. On the other extreme, blow-off limit occurs when the flow rate is reached beyond which the flame blows off the burner. Quenching and blow-off limits bound the leak flow rates that can support combustion.

Quenching and blow-off limits of different gases were measured by Kalghatgi (1981), (Matta et al., 2002), Baker et al. (2002), Cheng et al. (2006) measured blowoff limits for a variety of fuels including propane, methane and hydrogen on circular burners. Flame is not able to exist when its predicted length is less than the measured stand-off distance (Matta et al., 2002). Experiments verified this method of finding the quenching flow rate by establishing a propane flame over a hypodermic stainless steel tube and decreasing the fuel flow rate until extinction. These studies showed that hydrogen mass flow rate blow-off limits are higher than those for methane and propane. For a given leak size, there is a range of mass flow rates where hydrogen is able to support a stable flame but methane and propane would be blown off.

8.1.1. Round burners

Three different types of round burners were considered by Butler et al. (2009): pinhole, curved-wall pinhole, and tube burners, as depicted in Fig. 8–2. The pinholes diameters ranged from 0.008 mm to 3.18 mm. The *pinhole burners* were stainless steel nozzles that are manufactured for solid-stream spray generation, the top of each burner (except the two smallest ones) is a slightly curved surface with a hole passing through its axis, the two smallest burners had holes in planar, not curved, surfaces. The *curved-wall pinhole burners* were constructed of stainless steel tubes with two outside diameters, i.e. 1.59 mm (holes 0.41–1.02 mm) and 6.35 mm (holes 0.41–3.12 mm), in which a radial hole was drilled. The *tube burners* were made from stainless steel hypodermic tubes of inside diameters ranged from 0.051 mm to 2.21 mm. These burners resemble microinjectors that may be used in future small-scale microelectro-mechanical power generators (Lee et al., 2003).

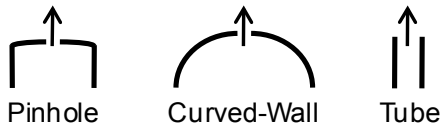

Figure 8–2. Round-hole burners used to find quenching limits (Butler et al., 2009).
Arrows show hydrogen flow direction.

The small flow rates required special flow measurement procedures (Sunderland, 2010). For tests with round burners a glass soap-bubble meter was installed upstream of the burners. Quenching flow rates were measured by first establishing a small flame, decreasing the flow rate until the flame extinguished, and then introducing a soap bubble in the meter for flow rate measurement.

Tests performed at different burner temperatures, from room temperature and up to about 200°C, found quenching flow rate to be largely independent of burner temperature provided condensation was avoided (Butler et al., 2009). Tests were also conducted with varying ambient humidity, and quenching limits were found to be generally independent of the relative humidity of the air in the range of 46–90%.

Hydrogen flow rate at blow-off was measured with a soap bubble meter (Butler et al., 2009). A stable flame was established and then the flow rate was increased until the flame first lifted and then extinguished. For blow-off tests the flames were detected visually. Hearing protection was required for the blow-off tests for the larger burners.

Butler et al. (2009) performed additional tests to consider buoyancy effects. To this end quenching flow rates were found for pinhole and tube burners in the vertical, horizontal, and inverted orientations.

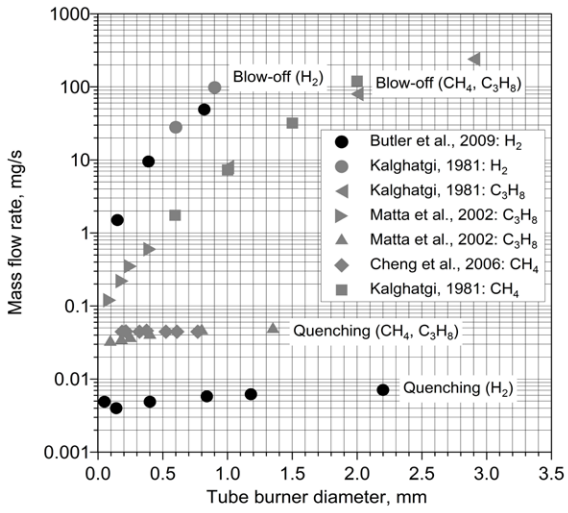

Figure 8–3. Quenching and blow-off limits as a function of tube burner internal diameter.

Figure 8–3 demonstrates that while blow-off flow rates increases with tube internal diameter the quenching flow rates are practically independent of diameter. The combustion limits are much wider for hydrogen than for methane and propane. Quenching and blow-off limits for methane and propane are very similar.

8.1.1.1. Quenching limit and round burner type

Figure 8–4 shows the hydrogen quenching limits for three types of burners (Butler et al., 2009). The simple theory predicts that the quenching flow rate is independent of burner diameter as 0.008 mg/s. Figure 8–4 shows that the scaling analysis performed by Butler et al. (2009) approximately predicts the average quenching flow rate for hydrogen, especially at burner diameters greater than 1.5 mm. For smaller burners, there are clearly other mechanisms that are affecting quenching limits that are not accounted for in the simple model.

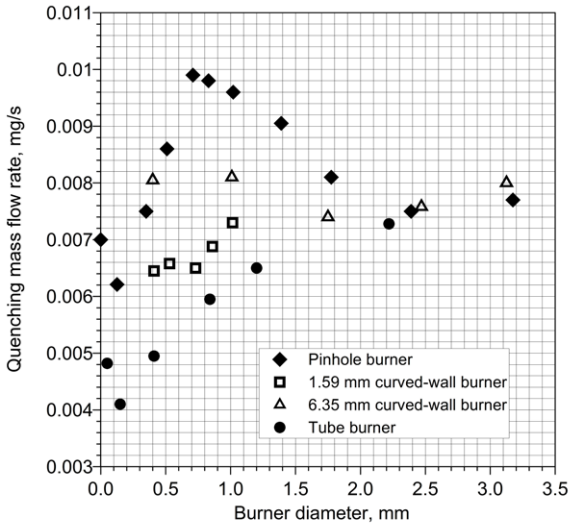

Figure 8–4. Quenching limits as a function of burner internal diameter and round burner type (Butler et al., 2009).

Heat loss contributes to the differences in limits for different round hole burners. For small burner diameters, the pinhole burners show the highest quenching flow rates, while the tube burners show the lowest. The 6.35 mm curved-wall burners act more like pinhole burners, whereas the 1.59 mm curved wall burners act more like tube burners, and thus the 6.35 mm curved-wall burners have higher average quenching flow rates than the 1.59 mm curved-wall burners.

Butler et al. (2009) investigated the effect of burner orientation (vertical, horizontal, inverted) on quenching limit. The results reveal that the quenching flow rate for pinhole and tube burners is nearly independent of orientation. The weakest was an inverted flame with a hydrogen flow rate of 3.9 μg/s. With no mechanism other than radiative heat losses, and this being low for hydrogen flames, it is the weakest ever observed flames (Butler et al. 2009). During these experiments, the burner was found to be warmer during non-vertical tests. If burner temperature does not affect temperature and the quenching limit is independent of orientation, then the flow field must also be constant with varying orientation. Hence, flames near extinction are driven by mechanisms other than buoyancy concluded authors.

8.1.1.2. Pressure dependence

Let us consider isentropic choked flows of different gases through round holes at the quenching limits of three gases under consideration given in Fig. 8–3. The fuel mass flow rate is linear with pressure upstream of the hole P_0 and area of the leak A

$$\dot{m} = CAP_0\left(\frac{\gamma M}{RT_0}\right)^{\frac{1}{2}}\left(\frac{2}{\gamma+1}\right)^{\frac{\gamma+1}{2(\gamma-1)}}. \tag{8–2}$$

Equation (8–2) is applied to predict the hole diameter associated with the quenching limit for a given fuel and upstream pressure (Butler et al., 2009). The results of these calculations are shown in Fig. 8–5 for hydrogen, methane, and propane. Each line in Fig. 8–5 starts at the minimum upstream pressure for choked flow and ends at the maximum pressure anticipated in alternative fuel vehicles. This plot predicts that for a given storage pressure, hydrogen is susceptible to leak flames for hole diameters that are smaller than those for methane or propane. Furthermore, at hydrogen's maximum anticipated storage pressure of 69 MPa (10,000 psi), a hole diameter of just 0.4 μm is predicted to support a flame.

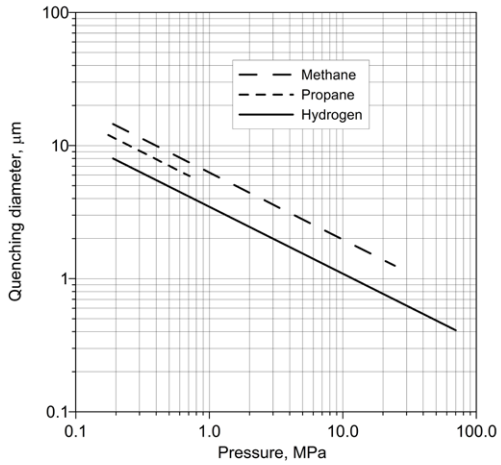

Figure 8–5. Quenching diameter as a function of upstream absolute pressure assuming isentropic choked flow (Butler et al., 2009).

8.1.2. Leaky fittings

Ge and Sutton (2006) conducted research on hydrogen interface leakage in national pipe thread (NPT) fittings. They found that the best threaded fittings investigated leaked hydrogen with rates of 1 μg/s. Leak rates under non-ideal conditions were far higher. They found as well that a larger tightening torque is not as important in sealing the threads as the Teflon material and properties. The tests were run at a pressure drop of 7 MPa. It was determined that two wraps of Teflon had better performance than one wrap and the Swagelok™ anaerobic pipe thread sealant outperformed the Teflon.

Compression fittings are used often with gases at high pressure (Sunderland, 2010). Compression fittings are a reliable method that allows fittings to be taken apart and attached with ease. A benefit of using compression fittings over pipe thread fittings is the lack of Teflon tape that is necessary to prevent leakage. Any time a pipe thread fitting is taken apart, it must be cleaned and rewrapped before it can be used again.

Figure 8–6 shows a cross-sectional schematic of a compression fitting (Sunderland, 2010). The steel tube, nut, fitting body and ferrules are shown. Leak paths seen in the experiments are shown with the dotted line. The leak travels from the tube exit, around the front and back ferrule, and exits between the nut and the tube. Leaks were not seen coming from threads of the compression fitting.

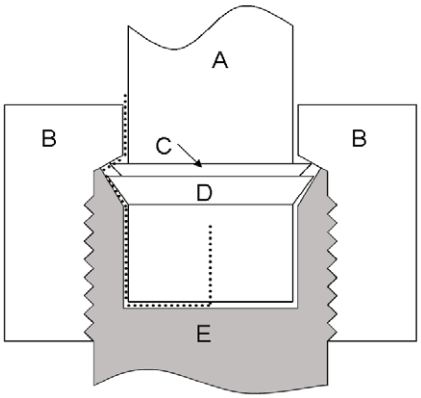

Figure 8–6. Cross-sectional view of the fitting connection with proposed leak path:
A – steel tube, B – Swagelok nut, C – back ferrule, D – front ferrule, E – fitting body (Sunderland, 2010).

Over-tightening a fitting damages the ferrule in the compression fitting, allowing leaks to occur. This method was done only for the 6.33 mm fitting (it is difficult to over tighten a 12.66 mm fitting as it is so large that a high torque is required). The fittings were made using the manufacturer's instructions and confirmed to be leak free at 0.689 MPa (100 psig) using hydrogen. The fitting between the steel tube and union was taken apart and then retightened to finger tight. The fitting was then tightened one full turn (¾ turn past manufacturer's instructions). The fitting was then taken apart again and tightened until the ignition flow rate limit was found for several different pressures. Scratched fittings simulate a ferrule being damaged by insertion into a fitting and was done only for the 6.33 mm fitting. The fittings were made using the manufacturer's instructions and confirmed to be leak free at 0.689 MPa (100 psig) using hydrogen. The ferrule on the steel tube was then scratched using a small triangular file. The fitting was then reassembled properly and the ignition flow rate limit was found by slowly tightening the fitting.

Figure 8–7 (left) shows the measured ignition flow rates for hydrogen, methane, and propane for a leaky fitting in the vertical orientation (Butler et al., 2009). The minimum flow rate necessary for sustained ignition is plotted versus pressure. For each fuel, the measurements at increased pressures are associated with an increase in torque on the fitting. The upper limit on pressure for propane is lower than that of the other gases because the vapor pressure of propane at 21°C is 0.76 MPa (110 psig).

Butler et al. (2009) converted the measured ignition mass flow rates of Fig. 8–7 (left) to volumetric flow rates using the measured current temperature and pressure of the laboratory. The resulting volumetric flow rates are plotted in Fig. 8–7 (right) with respect to upstream pressure. Within experimental uncertainties, the minimum fuel mass and volumetric flow rates are independent of pressure. Propane requires the lowest volumetric flow rate for ignition while methane requires the highest. The volumetric flow rates for hydrogen, methane and propane are 0.337, 0.581, and 0.187 mL/s, respectively.

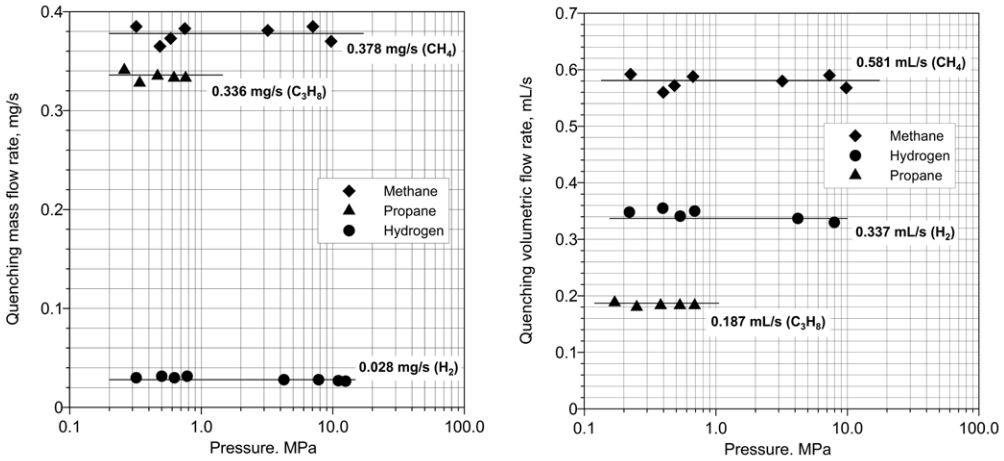

Figure 8–7. Quenching mass flow rate limit (left; Butler et al., 2009) and quenching volumetric flow rate (right; Sunderland, 2010) as functions of upstream pressure in the vertical orientation of fittings.

Although hydrogen has the lowest mass flow rate necessary to sustain fittings microflame, propane has the lowest volumetric flow rate to sustain fittings microflame.

9 Jet fires

A critical review and rethinking of hydrogen jet flames is presented in this chapter. It is demonstrated that Froude number only based correlations are deficient for the prediction of flame length of under-expanded jet fires. The novel dimensionless flame length correlation is described. It accounts for effects of Froude, Reynolds, and Mach numbers. The correlation is validated for a wide range of pressures 0.1–90.0 MPa, temperatures 80–300 K, and leak diameters 0.4–51.7 mm. Three distinct jet flame regimes are identified: traditional buoyancy-controlled, momentum-dominated "plateau" for expanded jets, and momentum-dominated "slope" for under-expanded jets.

The former statement "calculated flame length may be obtained by substitution the concentration corresponding to the stoichiometric mixture in equation of axial concentration decay for non-reacting jet" is shown to be incorrect. The correct average value for non-premixed turbulent flames is found to be 11% by volume of hydrogen in air (the range is from 8%–16%) not stoichiometric 29.5%. Three separation distances for jet fire are introduced and discussed. All three conservative separation distances for jet fire are shown to be longer than separation distance for a non-reacting jet (to LFL of 4% by volume) from the same source.

9.1. Introduction to hydrogen jet fires and safety issues

The use of hydrogen and fuel cell systems at pressure up to 100 MPa brings new engineering challenges to provide public safety for these emerging technologies. To formulate the principles of hydrogen safety engineering a proper understanding of underlying physical phenomena is needed including jet fires.

Safety is often mistakenly called a "non-technical" barrier to the emerging hydrogen economy. In fact, the hydrogen safety is a challenging area of science and engineering, technological development and innovation. There is a number of demanding engineering issues to be resolved before rolling out hydrogen and fuel cell technologies to the market. These unresolved issues include the reduction of the under-expanded jet flame length from current 10–15 m from the hydrogen-powered vehicle onboard storage to allow evacuation of passengers and their safeguarding by first responders when relevant.

Another important safety issue to be addressed by car manufacturers is the increase of fire resistance rating of onboard storage tanks from present 1–7 minutes for type 4 vessels to allow longer time for blow-down of tanks. This in turn would prevent severe destruction of civil structures like garages during accidental release, and exclude even a potential for formation of large hydrogen-air clouds in tunnels able to make fatalities throughout the whole length of the tunnel. Higher fire resistance rating on hydrogen storage tanks would permit safe evacuation of civilians from the accident scene, etc.

One of challenges for safety engineering is determination of science-informed separation distance from a hydrogen system or infrastructure. The separation distance can be defined (European Industrial Gas Association, 2007) as the minimum separation between a hazard source and an object (human, equipment or environment) which will mitigate the effect of a likely foreseeable incident and prevent a minor incident escalating into a larger incident/accident. The following definitions can be used to distinguish between incident and accident. Incident is something that occurs casually in connection with something else, and accident is an unforeseen and unplanned event or circumstance causing loss or injury.

Depending on incident scenario the minimum separation distance could be determined either by characteristics of an unignited release, or parameters of a jet fire, or pressure effects from deflagration and detonation. This chapter addresses in particular the question which of two separation distances, i.e. based on hazards from a non-reacting jet (unignited leak) or hazards from a reacting hydrogen release (jet flame) from the same source, is longer. Due to current lack of knowledge only free jets are considered.

Hydrogen jets from storage tanks and equipment at pressures up to 100 MPa will be mainly in a form of under-expanded jet. The under-expanded jet is defined as a jet with pressure at the nozzle exit is above the atmospheric pressure. Unfortunately, under-expanded hydrogen flames can reach tens of meters from current pressure relief devices (PRD) installed on onboard storage of hydrogen-fuelled vehicles, and up to hundreds of meters for large diameter high pressure industrial hydrogen pipes. This raises an important issue of a link between safety and cost-effectiveness of the technology applications through reduction of separation distances by the innovative engineering design.

The prediction of laminar and turbulent non-premixed hydrogen jet flame length has been the subject of studies starting from the seminal work of Hawthorne et al. (1949). Analysis of previous publications shows that practically all former correlations of the dimensionless flame length, i.e. the flame length normalized by the burner nozzle diameter, are based on the Froude number (*Fr*) in one or another form. This statement is applicable to both former works mainly on expanded jets and recent studies on highly under-expanded jets. It is quite obvious that *Fr*-based correlations, ignoring theoretically predicted and experimentally proved dependence on Reynolds (*Re*) and Mach (*M*) numbers, cannot be of general nature in a wide range of parameters.

The former correlations distinguish two regimes of jet fires. The first regime is buoyancy-controlled jet fire. This regime is characterised by lower *Fr* number. In this regime the dimensionless flame length, L_F/D, where L_F is the flame length and D is the nozzle exit diameter, grows with *Fr* number. The second regime is momentum-dominated jet flame. This regime is characterised by larger *Fr* numbers compared to the buoyancy-controlled regime. The dimensionless flame length is independent of *Fr* for momentum-dominated expanded jet flames. It is worth noting that this was derived for expanded jets only. Here we expand the current classification of jet fires to include under-expanded jet fires through the development of a novel correlation for jet fires that comprises dependence on *Fr, Re* and *M* numbers.

Jet fire is a typical scenario for hydrogen accidents. Statistics proves that in the most situations unscheduled high pressure hydrogen release will be ignited (Astbury and Hawksworth, 2007). Knowledge of the jet flame length and related separation distances is of key importance for hydrogen safety engineering. Science and research are extremely challenging areas of human activities and no one is assured against possible errors and incorrect conclusions.

Sunavala et al. (1957) stated that "calculated flame length may be obtained by substitution the concentration corresponding to the stoichiometric mixture in equation of axial concentration decay for non-reacting jet". The statement was reiterated later. For instance, Bilger and Beck (1975) "for convenience" defined the flame length as the length on the axis to the point having a mean composition which is stoichiometric (hydrogen concentration is twice of oxygen). Bilger (1976) repeated that, for reaction rates limited by diffusion, the pioneering work of Hawthorne et al. (1949) showed that the flame problem is analogous to an equivalent non-reacting mixing problem with the reaction zone appearing at the contour, where the nozzle fluid concentration has been diluted to stoichiometric.

However, these statements can be questioned if the Hawthorne's concept of the concentration fluctuations in turbulent flame or local "unmixedness", producing a statistical smearing of reaction zone and a consequent lengthening beyond the point where the mean composition of mixture is stoichiometric, is applied. Indeed, our preliminary study (Molkov, 2009b) and results shown below demonstrate that hydrogen non-premixed turbulent jet flame tip is located much farther from the nozzle as will be shown below, i.e. from 2.2 times (for shortest flame limit of 16% by volume of hydrogen in air mixture) to 4.7 times (for longest flame limit of 8%), compared to the axial location of stoichiometric concentration of hydrogen in air in non-reacting momentum-dominated jet. The existing misinterpretations of the hydrogen flame length based on former studies could have serious safety and economical implications and will be clarified further in this chapter.

The ultimate aim of this chapter is the advancement of hydrogen jet flames understanding and the development of reliable tools for hydrogen safety engineering, including a general dimensionless correlation for predicting the length of expanded and under-expanded hydrogen jet flames from round nozzles of arbitrary size at different storage pressures and temperatures.

9.2. Chronological overview of hydrogen jet flame studies

Hawthorne et al. (1949) concluded at their seminal study on expanded hydrogen flames that the flame length, L_F, is proportional to the nozzle diameter, D, only. The fuel gas flow rate was found to have no effect on flame length as long as it is great enough to produce a fully developed turbulent flame. The following equation describing the dimensionless length of free turbulent flame jets was derived

$$\frac{L_F - s}{D} = \frac{5.3}{C_{st}} \sqrt{\frac{T_{ad}}{\alpha_T T_N} \left[C_{st} + (1 - C_{st}) \frac{M_S}{M_N} \right]}, \tag{9-1}$$

where s is the distance from the breakpoint to the nozzle (see Fig. 9–1 from Hottel and Hawthorne, 1949), α_T is the ratio of reactant moles to product moles for stoichiometric mixture, T_{ad} is the adiabatic flame temperature, T_N is the temperature of fluid in the nozzle, C_{st} is the mole fraction of the nozzle fluid in stoichiometric mixture with air and M_S/M_N is the ratio of molecular masses of the surrounding and nozzle fluids.

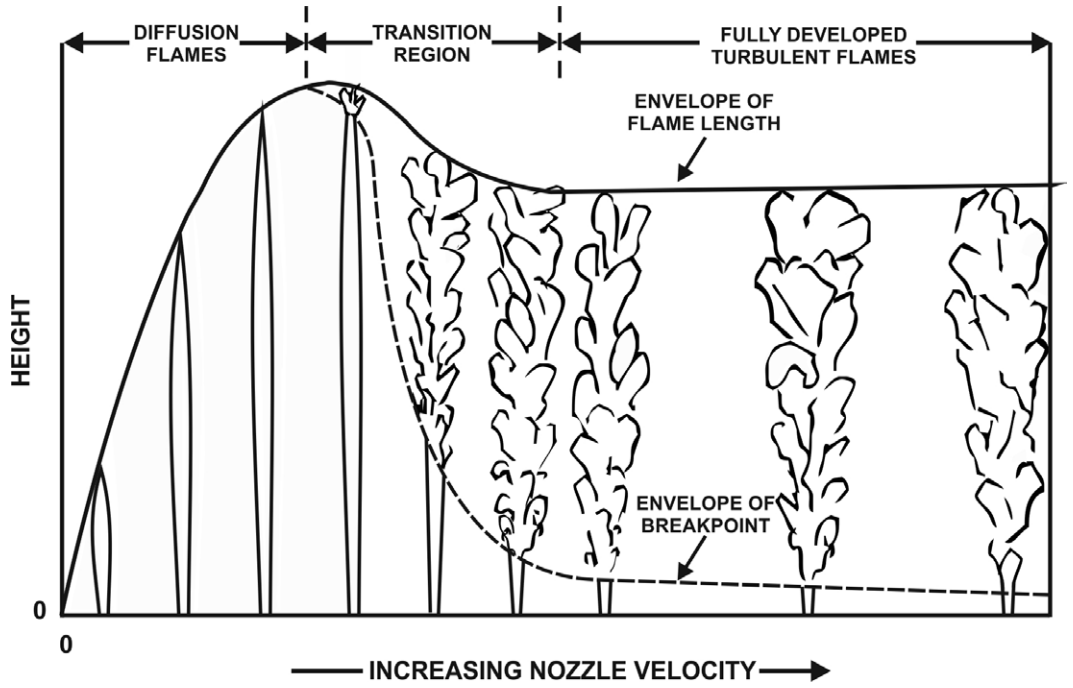

Figure 9–1. Progressive change from laminar diffusion flame to fully developed turbulent non-premixed flame (Hottel and Hawthorne, 1949).

Equation (9-1) computes L_F/D=152 for a free turbulent expanded hydrogen flame in air with parameters (Hawthorne et al., 1949): α_T =1.173, T_{ad}/T_N=8.04, C_{st}=0.296, M_S/M_N=14.45. Two experiments with vertical subsonic hydrogen jet fire were reported by Hawthorne et al. (1949). Each experiment was repeated in a darkened and lit room. The first experiment consisted of a rounded nozzle of 4.76 mm diameter with L_F/D=134 in a lit room (Re=2,870; $Fr=U_N^2/gD$=92,000, where U_N is the velocity in the nozzle and g is the acceleration due to gravity; the flame width to length ratio was reported as W_F/L_F =0.21). The second experiment investigated a sharp-edged nozzle orifice of 4.62 mm diameter with L_F/D=147 (Re=3,580; Fr=158,000). The visible flame length observed in the darkened room was 10% greater than that observed in the lit room (Hawthorne et al., 1949).

Figure 9–1 shows progressive change of the flame height with the nozzle velocity during transition from laminar diffusion to fully developed turbulent non-premixed flame as observed by Hawthorne et al. (1949). In the beginning the increase of nozzle velocity leads to the increase of flame length for laminar flames. Then, at some velocity the laminar flame height reaches its maximum and starts to decline as the flame becomes turbulent at its tip first. The transition from vertical laminar diffusion flame to turbulent flame starts to occur at Reynolds number of around Re=2000 when considering the release of hydrogen into still air. Finally, Hawthorne et al. (1949) concluded, based on their experiments with expanded jets, that fuel gas flow rate has no effect on the flame length as long as it is great enough to produce a fully developed turbulent flame.

It is important to stress that Hawthorne et al. (1949) pointed out that it does not follow that burning will proceed as far as ideal mixing would allow since actually the sample has a rapid time variation in constitution so that excess oxygen and excess hydrogen can alternate to produce a mixture capable of further combustion (1953). They showed as well that the actual variation of hydrogen concentration (normalised by axial concentration) over a cross-section of jet fire (normalised by a jet width where concentration is half of maximum concentration) is independent of distance from the nozzle. This result can be used for verification/validation of computational fluid dynamics (CFD) simulations of expanded jet fires.

It is not obvious that conclusions of study by Hawthorne et al. (1949) on expanded jet fires, especially about the independence of flame length on the nozzle velocity for turbulent jets, can be extended to under-expanded jet fires. For instance, the turbulence and velocity fluctuation at the under-expanded jet axis downstream of the Mach disk is known to be quite high compared to sub-sonic flows, i.e. the ratio of root mean square (r.m.s.) to average axial velocity is 0.25±10% as derived in 1953 by Thring and Newby (1953) from experiments of Corrsin (1943). This high level of turbulence in under-expanded jets has been confirmed recently by the application of the large eddy simulation (LES) technique by Brennan et al. (2009) during processing the experimental data on large-scale hydrogen jet fires by Sandia National Laboratories.

Golovichev and Yasakov (1972) theoretically predicted the maximum flame length to nozzle diameter ratio L_F/D=220. The maximum measured value for a subsonic release, i.e. expanded jet, was in their experiments L_F/D=205 at velocity 365 m/s. Baev et al. (1974a, 1974b) undertook the first systematic attempt to investigate flame length over the whole applicable range of operation from forced convection (jets) to natural convection (plumes), as stated by Becker and Liang (1978). The basic flame length equation derived by these studies resembles that of Hawthorne et al. (1949) but is more general in that it allows for effects of compressibility, i.e. Mach number above 1 (Becker and Liang, 1978). More than 70 experiments were performed with nozzle diameters ranging from 1 mm to 16.65 mm, investigating both subsonic and supersonic jets with Mach number from 0.25 to 3.08 (outflow velocities up to 2600 m/s). Experimental error was ±15%. In spite of the understanding of the role of *Fr, Re, M* numbers, the experimental flame length data were presented as a function of the Froude number $Fr=U_N^2/gD$ only, similar to the approach used for the first time to our knowledge by Shorin and Ermolaev (1952).

Baev et al. (1974a) theoretically derived that at the momentum-controlled limit the flame length $L_F \sim Re$, or dimensionless flame length $L_F/D \sim U_N\rho/\mu$, where ρ is the gas density and μ is the viscosity. This means that the dimensionless flame length, L_F/D, has to be a constant for sonic (choked) expanded jets if both the density and the viscosity remain unchanged. In the presence of lifting (buoyancy) forces they derived that $L_F \sim Re^{2/3}Fr^{1/3} \sim u^{4/3}D^{1/3}$. The largest experimental ratio L_F/D=230 was observed for subsonic flow.

In the same year Baev and Yasakov (1974b) showed theoretically that depending on *Fr* there will be a characteristic peak in $L_F(Re)$ function, mentioned by Hottel and Hawthorne (1949), or there will be no peak for nozzles of larger diameter (Fig. 9–2).

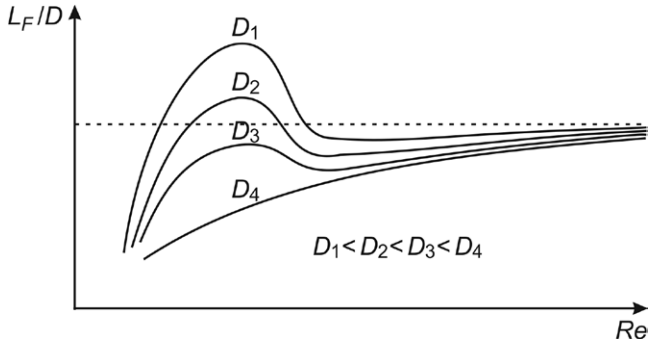

Figure 9–2. The theoretical dependence of the flame length to diameter ratio, L_F/D, as a function of Reynolds number, *Re*, for different nozzle diameters, *D*. Dotted horizontal line indicates a turbulent flame length limit L_t (Baev and Yasakov, 1974b).

Baev and Yasakov (1974b) derived within the assumptions of their theory that the ratio of maximum laminar to maximum turbulent flame length is L_l/L_t=1.74 and is independent of fuel type. This ratio decreases with the increase of diameter *D* (see Fig. 9–2). There is a critical diameter above which the flame length in a whole range of *Re* is below the value L_t. They suggested that the limit of turbulent flame length L_t can be reached at $Re \to \infty$. The relationship $L_F \sim Re^{2/3} Fr^{1/3} \sim u^{4/3} D^{1/3}$. was used in their discussion about the turbulent limit for jet fire length L_t. Their experimental data gave a maximum L_F/D=230 for laminar jet flames and a limit L_F/D=190 for turbulent jet fires.

Three years later the theoretical conclusions by Baev et al. (1974a, 1974b) were confirmed by experiments carried out by Shevyakov and Komov (1977) that are reproduced in Fig. 9–3. The experimental dependence of L_F/D on *Re* up to *Re*=20,000 is presented for nine stainless steel tubular burners of diameter 1.45–51.7 mm. Burner length to diameter ratio was changing from 50 for smaller diameter burners to 10 for the largest one. The visual length of on-port subsonic flames was measured in a darkened room. The hydrogen density of 0.0899 kg/m^3 and the temperature of 273 K were assumed in the nozzle exit during the processing of the Shevyakov's data in our studies.

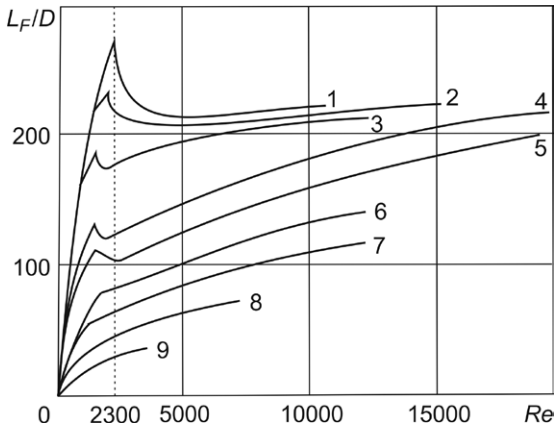

Figure 9–3. The experimental flame length to diameter ratio, L_F/D, as a function of Reynolds number, *Re*, for different nozzle diameters, *D*, mm: 1 – 1.45; 2 – 1.9; 3 – 2.9; 4 – 4.0; 5 – 6.0; 6 – 10.75; 7 – 15.5; 8 – 21; 9 – 51.7 (Shevyakov and Komov, 1977).

The experimental dependence of L_F/D on *Re* for smaller diameter (below 6 mm) burners has a characteristic peak (Shevyakov and Komov, 1977, see Fig. 9–3) predicted theoretically in (Baev et al., 1974b, see Fig. 9–2). This peak magnitude is decreasing with the increase of burner diameter in the area of transition from laminar to turbulent flow (Re<2,300). Then L_F/D increases again with *Re* approaching a limit L_F/D=220-230 at high Reynolds numbers. This experimental data is above a turbulent jet flame limit L_F/D=190 measured by Baev and Yasakov (1974b). The similar limit L_F/D=230 was measured by Baev et al. for laminar jet flames (1974a). It is worth noting that for the same Reynolds number L_F/D decreases with the diameter increase (see Fig. 9–3).

Lavoie and Schlader (1974) published the experimental study from which information on flame length for the momentum-controlled regime can be extracted partially. All tests were performed at constant *Re*=4500. Two of four experiments were performed within the momentum-controlled limit: *D*=0.48 mm (Fr=1.6·10^8), *D*=0.96 mm (Fr=2.1·10^7). Other two tests were in the transitional area closer to the momentum-controlled limit: *D*=2.2 mm (Fr=1.8·10^6), *D*=3.3 mm (Fr=5.0·10^5). The length was estimated by the most remote location of flame sampling (x/D=200, except x/D=180 for nozzle *D*=3.3 mm). Thus, actual flame lengths can be a bit longer than reported.

Bilger and Beck (1975) conducted experiments with vertical jet diffusion hydrogen flame at constant *Fr* so that fluid dynamics similarity is obtained. They carried out the study using a principle of fluid dynamics stating that a jet issuing into still surroundings will exhibit main flow similarity independent of viscosity if the Reynolds number based on jet diameter and velocity at exit is sufficiently high. This phenomenon was called by Townsend (1956) "Reynolds number similarity". Bilger and Beck (1975) highlighted that the flames should exhibit Reynolds number similarity if the Froude number, the nozzle fluid density and composition are kept constant. Only three experiments were carried out for measurements of flame length dependence on the Froude number with Fr=0.6·10^6, 1.5·10^6, and 5.2·10^6. There is an indication of the flame length saturation for *Fr* above 1.5·10^6 in their experiments.

However, the flame length "for convenience" was defined by Bilger and Beck (1975) incorrectly (from author's point of view) as the length on the axis to the point having a mean composition which is stoichiometric (hydrogen concentration is twice of oxygen). No experimental data on actual flame lengths was reported. Bilger and Beck (1975) did not give details on how visible flame lengths in Hawthorne et al. (1949) study, i.e. L_F/D=134 and 147, were transformed into "stoichiometric hydrogen/oxygen flame length" of about 79 and 89 respectively. It is interesting to note that if the same ratio (134/79=1.69) would apply to the momentum-dominated limit of the dimensional flame length associated with Lavoie and Schlader (1974) experiments (in Fig. 8 from paper by Bilger and Beck, 1975), then the value L_F/D =125·1.69=212 for visible flame length could be derived from the Bilger and Beck's (1975) paper. Bilger and Beck (1975) noted as well that the experiments of Lavoie and Schlader (1974) were made for constant jet Reynolds number and exhibit no basic similarity due to the variation of the Froude number.

Bilger (1976) stated, with reference to the pioneering work of Hawthorne et al. (1949), that for reaction rates limited by diffusion the flame problem is analogous to an equivalent non-reacting mixing problem with the reaction zone appearing at the contour, where the nozzle fluid concentration has been diluted to stoichiometric. It is not clear laminar or turbulent diffusion was meant. This statement differs from our conclusion below that the flame tip is located farther downstream of the location of the stoichiometric concentration in a non-reacting turbulent jet from the same leak source. It is thought that our conclusion is in line with the Hawthorne et al. (1949) concept of concentration fluctuations in the turbulent non-premixed flame or local "unmixedness", producing a statistical smearing of reaction zone and a consequent lengthening beyond the point where the mean composition of mixture is stoichiometric.

In 1977 Shevyakov, whose group's studies of hydrogen non-reacting and reacting jets are barely known and thus not cited in English literature on the subject, had published with Komov probably the only paper translated into English (Shevyakov and Komov, 1977, see Fig. 9–3). Later the group published more results on unignited hydrogen jets (Shevyakov et al., 1980), and for expanded hydrogen jet fires (Shevyakov and Saveleva, 2004) both in Russian. Shevyakov et al. (1977, 1980) carried out and summarised in coordinates L_F/D versus $Fr=U_N^2/gD$ probably the largest number of experiments on subsonic hydrogen jet fires in still air (more than 70).

The momentum-dominated limit L_F/D=220-230 for subsonic hydrogen jet fires was reached at $Fr>2\cdot10^6$ (Shevyakov et al., 1977, 1980). This limit is substantially above the value L_F/D=152 reported by Hawthorne et al. (1949). In spite of the difference between these numbers there is no contradiction. Indeed, two experiments reported by Hawthorne et al. (1949) were performed with nozzle diameters 4.62 mm and 4.76 mm (Re=2,870 and 3,580 respectively) and were in the buoyancy-controlled flow regime. For similar experimental conditions, i.e. nozzle diameter and velocity, the dimensionless flame length in Hawthorne et al. (1949) tests is practically exactly reproduced in Shevyakov et al. study (1980) as will be demonstrated in more detail below.

Probably the most validated correlation for calculation of the dimensionless flame length of vertical subsonic hydrogen jet fires is developed by Shevyakov and Komov (1977) and updated by Shevyakov and Saveleva (2004). The correlation is in coordinates L_F/D versus $Fr=U_N^2/gD$ and covers the range of conditions from buoyancy-controlled (lower Fr) to momentum-dominated (higher Fr) subsonic hydrogen jet flames. To account for the conservative increase of the momentum-dominated limit from L_F/D=220 in study (Shevyakov and Komov, 1977) to L_F/D=230 in work (Shevyakov and Saveleva, 2004), and to achieve continuous piecewise linearity of the correlation in the whole range of Fr the following modification of the original correlation has been obtained here using linear regression analysis

$$\begin{aligned} &L_F / D = 15.8 \cdot Fr^{1/5} \ (Fr < 10^5); \\ &L_F / D = 37.5 \cdot Fr^{1/8} \ (10^5 < Fr < 2 \cdot 10^6); \\ &L_F / D = 230 \ (Fr > 2 \cdot 10^6). \end{aligned} \tag{9–2}$$

This correlation can be used to explain the "scattering" of experimental data on L_F/D measured by different authors. For example, experimental value L_F/D=147 by Hawthorne et al. (1949) is substantially below the experimental limit L_F/D=230 established in work (Shevyakov and Saveleva, 2004). Nevertheless, these results are in agreement. Indeed, the substitution of Fr from two experiments by Hawthorne et al. (1949) into the correlation (9–2) yields L_F/D=152 for the rounded nozzle (experimental Fr=92,000; measured in the illuminated room L_F/D=134, Hawthorne et al., 1949), and L_F/D=164 for sharp-edged nozzle orifice (Fr=158,000; measured L_F/D=147, Hawthorne et al., 1949). The correlation (9–2) overestimates the measured values of L_F/D by 15%. This is of the same order of magnitude as 10% difference in hydrogen flame length measured in lit and darkened room.

The comparison between the modified Shevyakov's correlation (9–2) at the momentum-controlled limit and the similarity law for concentration decay in non-reacting expanded jets (Chen and Rodi, 1980) has revealed recently (Molkov, 2009b) that the concentration of hydrogen in a non-reacting expanded jet at a distance equal to the flame tip location is about 8.5% by volume. This is "surprisingly" close to the flammability limit of 8.5–9.5% for downward and spherically propagating premixed hydrogen-air flames. This result contradicts to previously published point of view by Sunavala et al. (1957), Bilger and Beck (1975), and Bilger (1975) that the flame length may be calculated by substitution of the concentration corresponding to the stoichiometric mixture (29.5% by volume of hydrogen in air) into the equation of axial concentration decay for non-reacting jets.

Becker and Liang (1978) validated previous findings by Baev et al. (1974a, 1974b) and Shevyakov and Komov (1977) that in buoyancy-controlled regime (under the natural convection conditions) flames of large base diameter would be rather short (smaller L_f/D compared to the momentum-dominated limit, see Figs. 9–2 and 9–3). This observation was used by authors to explain the behaviour of large pan fires of Blinov and Khudyakov (1957). They reported that observed flames in the forced convection limit are around 50% longer than previously suspected for subsonic releases. By this reasoning they increased the coefficient in Eq. (9–1) suggested by Hawthorne et al. (1949) from 5.3 to 11. This is an equivalent to more than 100% increase of the flame length! Hydrogen of comparatively low 99% by volume purity was used in their experiments, despite the fact that presence of hydrocarbons can strongly affect hydrogen combustion in air (Azatyan et al., 2009). It is known as well that in the momentum-controlled regime the flame length of hydrocarbons is longer: methane jet flame is about 130% of hydrogen jet flame length, and propane is about 200% (Heskestad, 1999).

They (Becker and Liang, 1978) developed the overall flame length model and gave general correlations for predicting flame length for the whole range of operations from full forced convection to full natural convection. The correlations are built on the Richardson number, *Ri*, which in thermal convection problems represents the importance of natural convection relative to the forced convection. The characteristic source momentum flux was embedded into *Ri.*

Kalghatgi (1984) published experimental data of more than 70 tests with nozzle diameters in the range 1.08–10.1 mm, both with subsonic and sonic hydrogen jet flames. The maximum measured flame lengths agree well with the modified Shevyakov's correlation (9–2). However, all data are below that recommended by the Becker and Liang formula (1978). Kalghatgi undoubtedly stated that his results disagree with the Becker and Liang's (1978) predictions.

The original experimental data (Kalghatgi, 1984) are reproduced in Fig. 9–4. Two important conclusions can be drawn from Kalghatgi's experimental study. The conclusions are valid for both subsonic and sonic flows: 1) flame length grows with mass flow rate at fixed diameter (*D*=const), and 2) flame length grows with diameter at fixed mass flow rate ($\dot{m}$ =const). These conclusions put under doubt the generality of the statement by Hawthorne et al. (1949), made by the analysis of expanded subsonic jets only, that jet flame length is proportional to nozzle diameter only and hydrogen flow rate is not a factor.

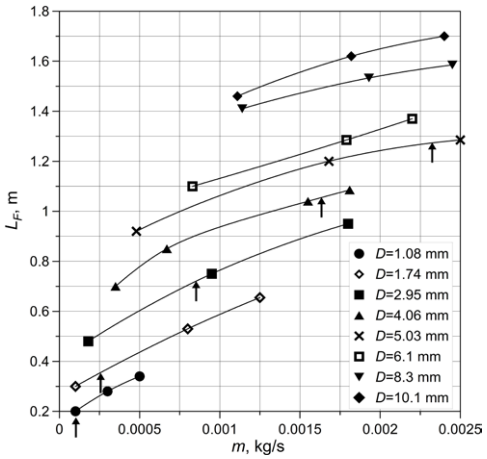

Figure 9–4. The original experimental data by Kalghatgi (1984) on hydrogen jet flame length for subsonic and sonic jet fires for different nozzle diameters and different mass flow rates. Arrows indicate the transition from subsonic (to the left from the arrow) to sonic flow.

The conclusions by Kalghatgi (1984) can be applied to question the generality of recent correlation of the flame length with the mass flow rate only (Mogi et al., 2005) that obviously is missing the revealed by Kalghatgi dependence on the nozzle diameter at $\dot{m}$ =const. It was also showed (Kalghatgi, 1984) that the lift-off height varies linearly with the jet exit velocity and is independent of the burner diameter for a given gas.

The dependence of flame height on mass flow rate implies that non-ideal behaviour of hydrogen at high pressures should be accounted for in the development of jet flame length correlations. Here we assume that hydrogen temperature in the storage tank in the Kalghatgi's (1984) experimental set-up was 273 K and the density of hydrogen in the nozzles for cases of subsonic flows was 0.0899 kg/m^3. For under-expanded jets in experiments (Kalghatgi, 1984) the initial temperature in the container was assumed to be the same, i.e. 273 K, and the density of hydrogen at the nozzle exit was calculated using the under-expanded jet theory (Molkov et al., 2009) described in chapter 5.

Delichatsios (1993) studied flame height relationships in the range from buoyancy- to momentum-controlled turbulent non-premixed expanded jet flames. The "fire Froude number" for reacting flows similar to Ricou and Spalding (1961) was applied. For the momentum-dominated limit it was suggested that $L_F/D=23(S+1)(\rho_N/\rho_S)^{1/2}$, where S is the air to fuel mass stoichiometric ratio. This gives the maximum value of $L_F/D=210$ for expanded hydrogen jets into still air ($S=33.72$), that is somewhat below the value $L_F/D=220$-230 published sixteen years earlier (Shevyakov and Komov, 1977).

Blake and McDonald (1993) showed that for upward turbulent diffusion flames the dimensionless flame length L_F/D is a function of a density weighted Froude number (inverse Richardson number) and a flame density to ambient density ratio. Authors commented that in the momentum-controlled limit, the length of horizontal flame is identical to the length of vertical flame from the same source. While in the buoyancy limit, the vertical size of a horizontally directed jet flame approaches the length of a vertical flame.

Cheng and Chiou (1998) observed that an increase of the lift-off velocity increases the lift-off height without significantly altering the hydrogen flame height. For example, an increase of lift-off velocity from 530 to 1120 m/s for a nozzle of 1.8 mm diameter increases the flame height from 37 to 49 cm.

Heskestad (1999) published a paper on "consolidation of flame height data for turbulent jet diffusion flames". Assuming the subsonic discharge, he concluded that the momentum-controlled limit for hydrogen is $L_F/D=175$. This limit is below the limit $L_F/D=220–230$ established by Baev et al. and Shevyakov et al. in 1974–1977 and confirmed in our studies.

Mogi et al. (2005) studied horizontal hydrogen jet flames from convergent nozzles of 0.1–4.0 mm exit diameter in the range of overpressures 0.01–40 MPa. The experimentally measured dimensionless flame length increases with the spouting pressure (static pressure measured close to nozzle exit) as $L_F/D=524.5\cdot P^{0.436}$, where P is the pressure in MPa. This experimental correlation implies that the momentum-controlled "plateau" in the coordinates L_F/D versus Fr would have extremely large scattering of experimental data if these coordinates to be used (similar to previous studies of mainly expanded jets). The correlation by Mogi et al. (2005) gives for subsonic flows the maximum value of $L_F/D=254$ (at the spouting pressure 0.19 MPa), which is somewhat above the maximum value $L_F/D=230$ obtained for expanded jets.

The correlation gives an extremely high ratio L_F/D=3344 at 70 MPa (Mogi et al., 2005). Convergent nozzles are characterised by smaller hydraulic losses and consequently larger flame lengths can be expected. The nozzle in this study was positioned 1 m above a floor and 1 m from a wall. The proximity of a jet to the floor and/or wall can affect the flame length due to change in air entrainment. It is well known that a fire plume along a wall has longer axial decay of temperature with distance from the source compared to a free plume with the same parameters.

The increase of a hydrogen jet flame length up to 1.8 times, when released along a ground, has been observed recently in experiments by Royle and Willoughby (2009). The effect of a surface, along which the jet is released, on the concentration decay in the jet is not yet fully explained and formalised through engineering correlations.

Under-expanded jet flames cannot be self-sustained at some conditions. For example, no stable flames were observed by Mogi et al. (2005) for nozzle diameters 0.1 and 0.2 mm – flame blew off although the spouting pressure increased up to 40 MPa.

Mogi et al. (2005) assumed as well that the flame length can be expressed as a function of mass flow rate only as L_F=20.25$\cdot \dot{m}^{0.53}$ regardless of the nozzle diameter. However, it is easy to see from Fig. 5 in paper (Mogi et al., 2005) that the experimental data attributed to different nozzle diameters are distributed in exactly the same manner as in Kalghatgi's work (1984).

Schefer et al. (2006b) studied open-flame hydrogen vertical jets for both subsonic and sonic (choked) flows at pressures up to 17.2 MPa. They confirmed Kalghatgi's conclusion (1984) that flame length increases with mass flow rate and jet nozzle diameter. Two sets of jet flame data are presented by Schefer et al. (2006b): subsonic laboratory scale hydrogen releases (*Fr* from transitional $4.1 \cdot 10^5$ to momentum-controlled $6.5 \cdot 10^6$, *Re* from laminar 1569 to turbulent 6247) from a 1.91 mm diameter nozzle; and a blow-down test at an initial pressure of 17.2 MPa through a stainless steel tubing of 7.94 mm diameter ($Fr=2.6 \cdot 10^6$-$1.9 \cdot 10^7$, turbulent $Re=(1.9\text{-}9.8) \cdot 10^5$). It is worth noting that there was a 3.175 mm internal diameter manifold near the cylinder outlets to a 7.6 m straight section tubing of 7.94 mm diameter. This set-up could have reduced flame length due to pressure losses in the flow pathway.

The blow-down time of two cylinders of 49 litres each was about 100 s (Schefer et al., 2006b). An attempt was made to present data for both expanded and under-expanded jet fires in coordinates "dimensionless flame length" versus "Froude number". Dimensionless flame length was defined by Schefer et al. (2006b) in a manner similar to Delichatsios (1993) as $L^* = L_F \cdot f_S / D^*$, where the jet momentum diameter is $D^*=D_j(\rho_e / \rho_S)^{0.5}$, ρ_e / ρ_S is the ratio of jet gas density to ambient gas density, D_j is the jet exit diameter, and f_S is the mass fraction of fuel at stoichiometric conditions. The Froude number form employed was

$$Fr_f = \frac{U_e f_S^{3/2}}{(\rho_e / \rho_S)^{1/4}[(\Delta T_f / T_S) g d_j]^{1/2}}, \tag{9–3}$$

where U_e is the jet exit velocity, ΔT_f is the peak flame temperature rise due to combustion heat release, and T_S is the ambient air temperature. The momentum-dominated regime is defined as $L^*=23$ ($Fr_f > 5$). Unfortunately, only limited number of experimental data was processed to validate the correlation (Schefer et al., 2006b).

Infrared, visible, and ultraviolet flame lengths were found to be related through the following equations $L_F/L_{IR}=0.88$, $L_F/L_{UV}=0.78$ (Schefer et al., 2006b). For turbulent jet flames the flame width was assessed as $0.17 \cdot L_F$ that is somewhat narrower than $0.21 \cdot L_F$ in the study by Hawthorne et al. (1949).

Later Schefer et al. (2007) published results of experiments with a nozzle diameter of 5.08 mm at higher pressures up to 41.3 MPa, where departures from ideal gas behaviour become more evident. Authors stated that lower-pressure engineering correlations for dimensionless flame length based on *Fr* apply to pressures up to 41.3 MPa, if the notional nozzle diameter and flow properties at the notional nozzle exit were substituted into the *Fr*-based correlation and non-ideal behaviour is accounted for. This is not confirmed in our studies as will be demonstrated below. The blow-down of two hydrogen storage tubes of 617 litres volume each at initial pressure of 41.3 MPa through the experimental hydraulic system, including stagnation chamber, with 5.08 mm nozzle at the exit took approximately 500–600 s.

Schefer et al. (2007) were the first to calculate notional nozzle exit parameters taking into account the non-ideal behaviour of hydrogen at high pressures. Their approach is analogous to Birch et al. (1987) and is based on the conservation of mass and momentum, assumes no viscous forces, the ambient pressure and uniform velocity profile across the notional nozzle, sonic (choked) flow at the jet exit from actual nozzle, and isentropic flow relations. The previous correlation for flame length (Schefer et al., 2006b) was expanded in (Schefer et al., 2007) and a new equation for the notional nozzle, $D_{eff}=D(\rho_N U_N/\rho_{eff}U_{eff})^{0.5}$, where "*N*" denotes actual nozzle exit parameters and "*eff*" effective (notional) nozzle parameters, was applied. It is important to note that flow properties at the notional nozzle exit were used to build the correlation for the flame length in the coordinates L^*-Fr_f.

Imamura et al. (2008) carried out a series of experiments to understand the thermal hazards of hydrogen jet flames and more specifically temperature field of hot currents in the downstream region. They used hydrogen release system composed of a hydrogen cylinder, a stop valve, a regulator, an air-operated ball valve and a nozzle located 1 m above the ground. Experiments investigated the dependence of flame shape on: nozzle diameter of 1, 2, 3 and 4 mm and spouting pressure of 0.5, 1.0, 1.5, 2.0, 2.5 and 3.0 MPa. The hydrogen flame was visualized by spraying NaCl aqueous solution. The spouting pressure was measured at the pressure transducer close to the nozzle. The assumption of temperature in the container equal to 273 K, and the under-expanded jet theory (Molkov et al., 2009) were applied to calculate flow parameters at actual nozzle to add experimental data of Imamura et al. (2008) to flame length correlations presented further in this chapter.

Proust et al. (2009) published experimental results on horizontal hydrogen jet flame in the widest range of pressures 1-90 MPa and leak diameters 1, 2, 3 and 10 mm. They used a type 4 tank of 25 liters capacity with hydrogen being released horizontally 1.5 m above the ground via a 10 m long pipe with internal diameter 10 mm with a valve (opening time 0.1 s) just upstream of the nozzle, and ignited by a continuous propane-air burner. The system was installed in an open gallery of 12 m^2 cross-section and 80 m long. The pressure was measured at the head of the tank, the temperature - inside the tank using K-Type thermocouples, and the mass flow rate was deduced from a numerical weighting device where the tank was located. There were some doubts about the accuracy of the mass flow rate provided. By this reason the experimental data on pressure and temperature (Proust et al., 2009) were used here to calculate the mass flow rate and other flow parameters at actual nozzle exit by the under-expanded jet theory described in chapter 5. It is found that calculated mass flow rates are in an excellent agreement with the experimental ones.

Studer et al. (2009) published results of experimental study on hydrogen jet fires. Hydrogen was stored in a 25 liter type 4 tank at 10 MPa and released horizontally through a 5 m long flexible pipe with internal diameter of 15 mm. The hydrogen was released 1.5 m above the ground and ignited immediately after release by an electric spark. Pressure and temperature were recorded in the pipe just prior to the nozzle but were not given in the publication. Releases through orifices of diameter 4, 7 and 10 mm were studied. The experimental data on pressure history, jet flame length and time of sampling were published elsewhere (HYPER, 2008). The flow parameters at actual nozzle exit were calculated using the under-expanded jet theory without losses described in chapter 5 in the assumption that hydrogen temperature in the tank was 273 K.

9.3. The drawback of Froude-based correlations

Nearly all correlations for jet flame length are based on the Froude number in one or another form, including recently published correlations by Schefer et al. (2006b, 2007) that incorporate data on under-expanded jet fires. To include under-expanded jet fires into the dimensionless correlation Schefer et al. (2006b) substituted actual nozzle diameter by effective (notional) nozzle diameter. In their subsequent study (Schefer et al., 2007) the effective diameter was taken as mentioned above in the form $D_{eff}=D(\rho_N U_N/\rho_{eff}U_{eff})^{0.5}$, and is accepted here to build a correlation presented in Fig. 9–5.

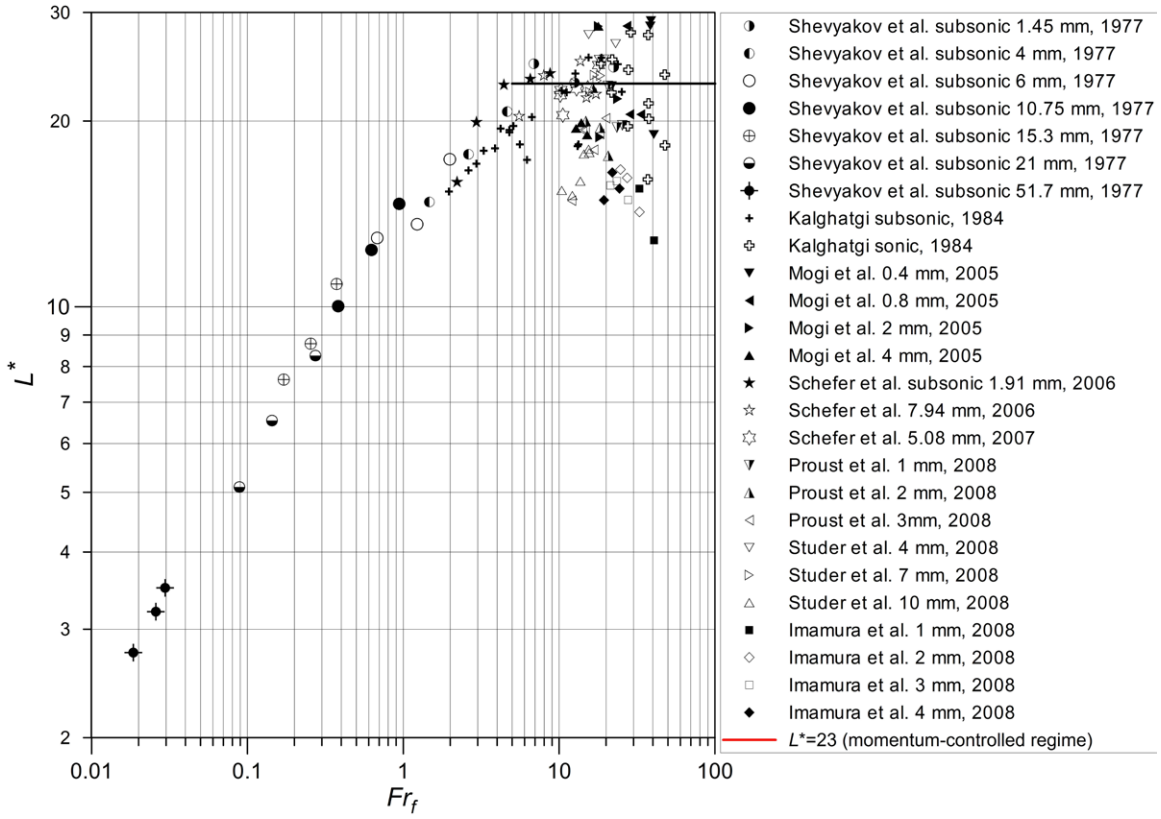

Figure 9–5. The *Fr*-based flame length correlation in coordinates used by Schefer et al. (2007) with the extended range of experimental data on under-expanded jet fires.

Unfortunately, only limited number of own experiments with under-expanded jet fires was included to validate the *Fr*-based correlations in papers (Schefer et al., 2006b, 2007). In this section we investigate the predictive capability of *Fr*-based correlations for flame length of highly under-expanded hydrogen jets fires by inclusion into the analysis a wider range of experimental data reported by different authors (see Fig. 9–5).

Parameters at the notional nozzle exit are used to build the correlation in Fig. 9–5 for the flame length, following the approach applied by Schefer et al. (2007). These parameters were calculated for the correlation shown in Fig. 9–5 using the under-expanded jet theory by Schefer et al. (2007). The dimensionless flame length and Froude number coordinates in the correlation (Fig. 9–5) are the same as in Schefer et al. (2007)

$$L^* = \frac{L_F f_S}{d_{eff}(\rho_{eff}/\rho_S)^{1/2}} \quad \text{and} \quad Fr_f = \frac{U_{eff} f_S^{3/2}}{(\rho_{eff}/\rho_S)^{1/4}[(\Delta T_f/T_S) g d_{eff}]^{1/2}}, \tag{9–4}$$

where f_S is introduced to unify the correlation for different fuels similar to other studies. The following constants are accepted: f_S=0.0281 (29.5% by volume of hydrogen in air), ρ_S=1.2 kg/m^3, ΔT_f=2092 K, T_S=298 K, g=9.82 m/s^2.

Figure 9–5 demonstrates that flame length data is unacceptably scattered in the momentum-dominated area of the correlation with large Froude numbers, which are typical for leaks from high pressure hydrogen equipment. It is clear that the simplification of flame length correlations to functional dependence on Froude number only, i.e. with ignoring the theoretically predicted and experimentally observed dependence on Reynolds and Mach numbers, does not make it work well when under-expanded jets are included.

9.4. The similitude analysis and a dimensional correlation

Kalghatgi (1984) proved experimentally that the flame length of a hydrogen jet into still air is affected by both nozzle diameter and mass flow rate. This experimental observation was confirmed later by Schefer et al. (2006b) and implies that jet flame length correlations, which take into account dependence on the diameter only, e.g. Hawthorne et al. (1949), or the mass flow rate only, e.g. Mogi et al. (2005), are lacking physical reasoning. In this section a dimensional correlation, which includes the dependence of flame length on both nozzle diameter and mass flow rate, is discussed (Molkov, 2009a).

Let us apply the similitude analysis to correlate the flame length, L_F, with the actual nozzle diameter, D, the density of hydrogen in the actual nozzle exit, ρ_N, the density of surrounding air, ρ_S, the viscosity, μ_N, and the velocity in the actual nozzle exit, U_N. The Buckingham Π theorem states that for a problem with 6 physical quantities and 3 dimensions, the quantities can be arranged into (6–3)=3 independent dimensionless Π parameters. These three Π parameters can be easily derived by the repeating variables or other methods as e.g. $\Pi_1 = D/L_F$, $\Pi_2 = \rho_N / \rho_S$, and $\Pi_3 = \rho_N D U_N / \mu_N$. To develop the flame length correlation with both the diameter, D, and the mass flow rate, $\dot{m}$, it is convenient to modify some of the Π parameters to form a new dimensionless group $\Pi_1 \times \Pi_3^{1/2} = (\dot{m} \cdot D)^{1/2} / [L_F \cdot (\pi \mu_N / 4)^{1/2}]$. From this dimensionless group the following functional dependence can be suggested for the validation against experimental data

$$L_F = f\left[(\dot{m} \cdot D)^{1/2} \sqrt{\frac{4}{\pi \mu_N}} \right], \tag{9–5}$$

where the parameter in brackets has the length dimension similar to the left hand side of Eq. (9–5), L_F.

The experimental data by Kalghatgi (1984) shown in Fig. 9–4 in the original coordinates L_F– $\dot{m}$ are quite scattered. Contrary, Fig. 9–6 shows a convergence of the Kalghatgi's experimental data onto the same curve (black circles for subsonic jet fires, and black diamonds for sonic (choked) flames) in the obtained by the similitude analysis coordinates L_F–$(\dot{m} \cdot D)^{1/2}$, as well as the same data in the original coordinates L_F– $\dot{m}$ (hollow circles, abscissa axis is on the top).

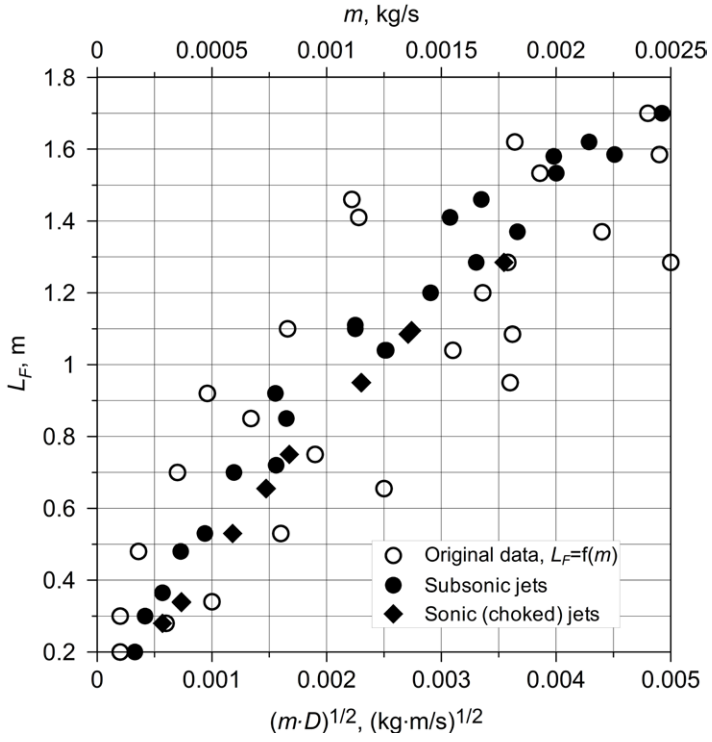

Figure 9–6. The experimental data by Kalghatgi (1984): scattered in the original coordinates L_F– $\dot{m}$ (hollow circles), and converged in the coordinates L_F–$(\dot{m} \cdot D)^{1/2}$ (black circles – subsonic, diamonds – sonic jet fires).

The use of new similarity group $(\dot{m} \cdot D)^{1/2}$ has essentially improved the convergence of the flame length data by Kalghatgi (1984) for both subsonic and sonic jets (see Fig. 9–6). Following this encouraging result, let us expand the analysis and include into the dimensional correlation along with experimental data by Kalghatgi (1984) data obtained by other researchers: Mogi et al. (2005), Schefer et al. (2006b, 2007), and experimental data obtained by researchers from INERIS in France (Proust et al., 2009), (Studer et al., 2009), including through the HYPER (2008) project. Figure 9–7 consolidates, in coordinates L_F–$(\dot{m} \cdot d)^{1/2}$, 95 experimental data points on hydrogen jet flame length in a wide range of pressures up to 90 MPa and nozzle diameters 0.4–10.1 mm (Molkov, 2009a).

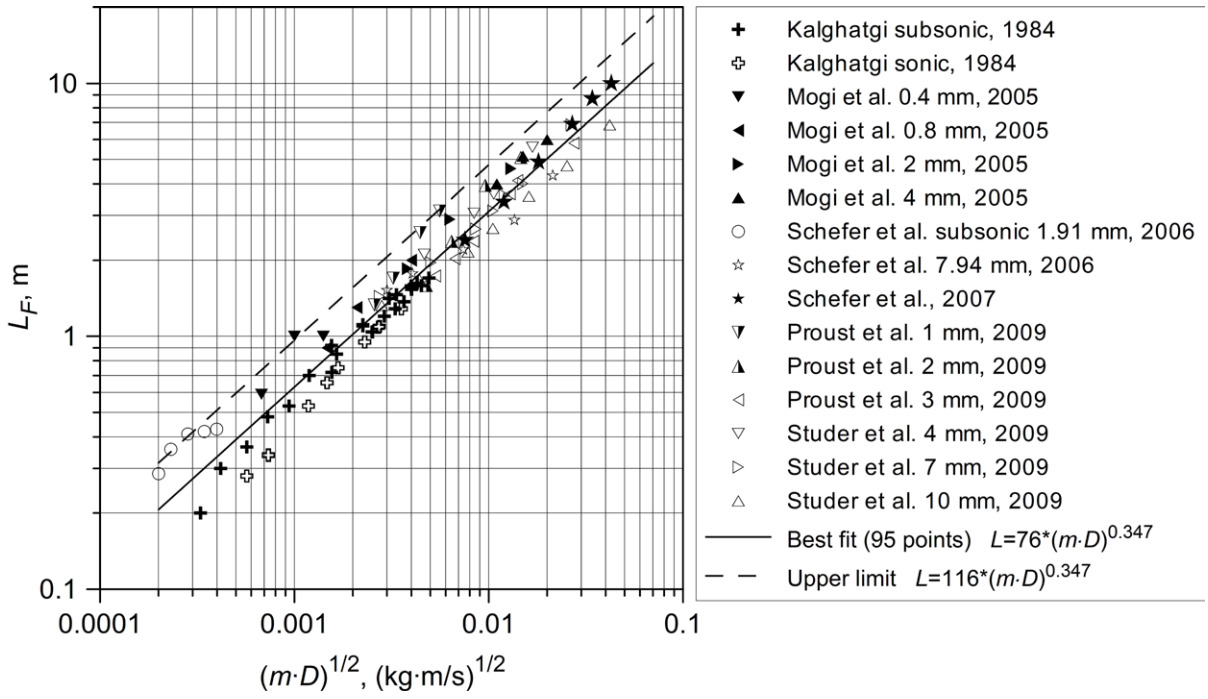

Figure 9–7. The dimensional correlation for hydrogen jet flame length (Molkov, 2009a).

The experimental data obtained by different research groups are collapsed onto the same curve, with the best fit line in Fig. 9–7 being described by the following dimensional equation (L_F is in meters)

$$L_F = 76 \cdot (\dot{m} \cdot D)^{0.347}, \tag{9–6}$$

where D is the actual nozzle diameter, m; and $\dot{m}$ is the mass flow rate, kg/s. This equation requires knowledge of the actual leak diameter and the mass flow rate only. The mass flow rate can be calculated using any validated under-expanded jet theory. The advantage of this methodology is that it does not require substituting the actual nozzle diameter by the notional nozzle diameter. This excludes additional uncertainty in determination of parameters at notional nozzle exit related to particular assumptions of an under-expanded theory applied. The correlation is validated against subsonic, sonic, and supersonic hydrogen jet flames (see Fig. 9–7).

The upper limit curve for the experimental flame lengths in Fig. 9–7 (conservative estimate), is represented by equation

$$L_F = 116 \cdot (\dot{m} \cdot D)^{0.347} \tag{9–7}$$

that yields 50% longer flame length compared to the best fit line described by Eq. (9–6).

Correlations (9–6) and (9–7) give practically a linear dependence of the flame length on the nozzle diameter, $L_F \sim D$. In contrast, the correlation shows a weaker dependence of the flame length on the density and the velocity in the nozzle, $L_F \sim (\rho_N \cdot U_N)^{1/3}$. There could be a contribution to data scattering in Fig. 9–7 of hydraulic losses which are expected to be different for each particular experimental set-up.

Predictive capability of the dimensional correlation in Fig. 9–7 is quite good for high debit jet fires (20%), and yet it is only about 50% for smaller debit flames, where the characteristic peak in the dependence L_F/D=f(Re) for small diameters (see Figs. 9–2 and 9–3) is one of possible reasons of the larger scattering in the experimental data. While the correlation is a convenient and reliable tool for hydrogen safety engineering at large mass flow rate leaks it is not shedding a light on the underlying the correlation physics, and its low predictive capability at smaller leaks.

It should be emphasized that the correlation must be applied to small diameter leaks with caution. Indeed, experiments published elsewhere (Mogi et al., 2005), (Okabayashi et al., 2007) showed that a sustained hydrogen flame is possible only when a leak size is above the limit for a particular storage pressure. As have been mentioned above, no stable flames were observed for nozzle diameters 0.1–0.2 mm by Mogi et al. (2005) at pressures up to 40 MPa. In line with this, a stable jet flame can exist at a pressure of 35 MPa if only the orifice diameter is above 0.3 mm (Okabayashi et al., 2007).

9.4.1. A simple nomogram for graphical flame length estimation

Figure 9–8 presents a nomogram designed to simplify the use of the dimensional correlation (9–6). The graphical estimation of jet flame length using the nomogram requires only two parameters of a leak, e.g. storage pressure and actual diameter of the leak, which are usually available and do not require any calculations (Molkov, 2009a).

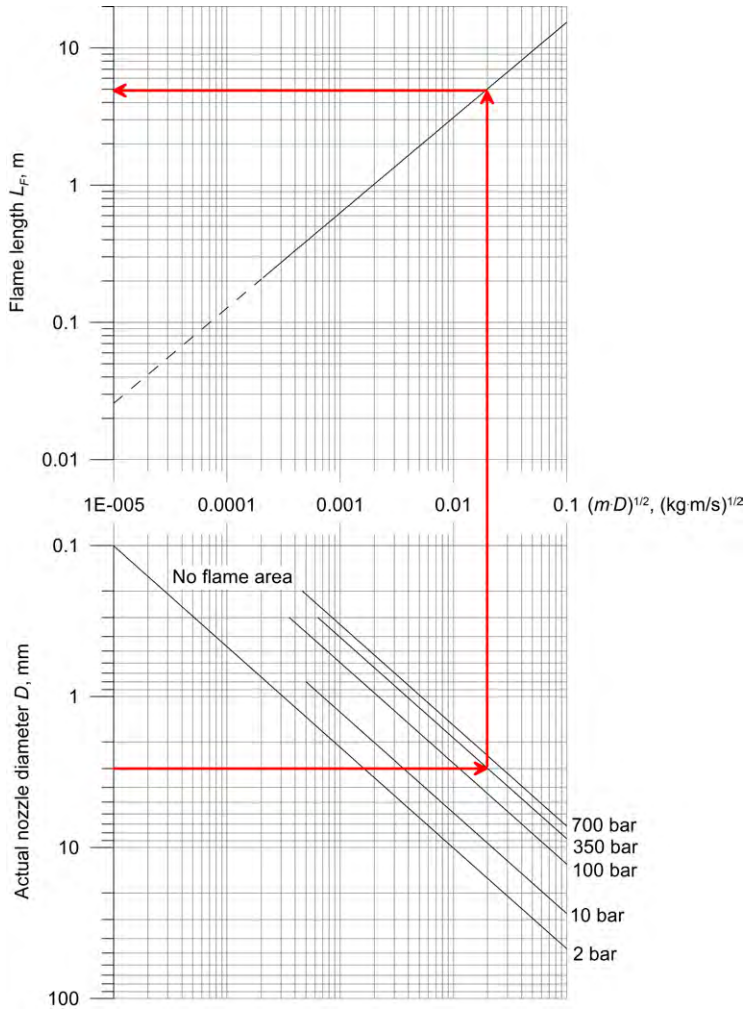

Figure 9–8. The nomogram for hydrogen jet flame length (Molkov, 2009a).

The nomogram is derived from the best fit line of the dimensional flame length correlation shown in Fig. 9–7. The use of the nomogram for calculation of flame length is demonstrated in Fig. 9–8 by thick lines with arrows. Firstly, an actual nozzle diameter of a leak, e.g. D=3 mm in this example, and a storage pressure, e.g. 35 MPa, are chosen. Secondly, a horizontal line is drawn from the diameter axis at point 3 mm to the right until it intersects with the pressure line denoted as 35 MPa. Thirdly, a vertical line is drawn from the intersection point upward until the second intersection with the only line available in coordinates (L_F, $(m{\cdot}D)^{1/2}$). Finally, to get a flame length a horizontal line is draw from the second intersection to the left until the final intersection with the axis denoted "Hydrogen flame length L_F, m". In the example considered, the leak of hydrogen at pressure 35 MPa through the orifice of 3 mm diameter will result in the flame length of 5 m. The conservative estimate of the flame length, as discussed above, is 50% longer, i.e. 7.5 m.

The nomogram incorporates a special feature based on the results by Mogi *et al.* (2005), Mogi and Horiguchi (2009), Okabayashi *et al.* (2007) and others, i.e. no stable flame was observed for nozzle diameters 0.1-0.2 mm as the flame blew off although the spouting pressures were as high as 40 MPa (denoted as "No flame area" in Fig. 9–8). For example, a stable jet flame cannot exist at pressures equal or below 35 MPa if the leak orifice diameter is below 0.3 mm.

It should be noted that the nomogram doesn't account for conditions when flow losses in a leakage pathway cannot be ignored. In such cases a straight forward use of the nomogram gives a conservative result. A more accurate prediction of the flame length in equipment with essential friction and minor losses can be obtained if a method is available allowing calculation of the density in the nozzle exit affected by the losses. The nomogram can be used for a quick estimate of the hydrogen jet flame length. However, the use of the novel dimensionless flame correlation is recommended for more accurate calculation of the flame length (see next section).

9.5. The jet flame blow-off phenomenon

Figure 9–9 (left) shows a region of flame blow-off in the coordinates "release pressure – nozzle diameter" (Mogi and Horiguchi, 2009). The blow-off implies that the flame extinguishes as soon as the pilot burner is switched-off. Authors observed that when the release pressure was less than the critical pressure, which is 1.9 times of the atmospheric pressure, the flame was found to be lifted, irrespective of the nozzle diameter. The lower limit of the pressure for the blow-off is weekly dependent of the nozzle diameter. However, the upper limit for blow-off is strongly affected by both the release pressure and the nozzle diameter. The decrease of the release pressure increases the nozzle diameter at the upper blow-off limit. For diameters 0.1–0.2 mm no self-sustained flames were observed, the blow-off occurs even the spouting pressure increases up to 40 MPa. The flame blow-off is impossible for diameters above 1 mm (first experimental point with no blow-off is at diameter a bit above 1 mm) at any pressures.

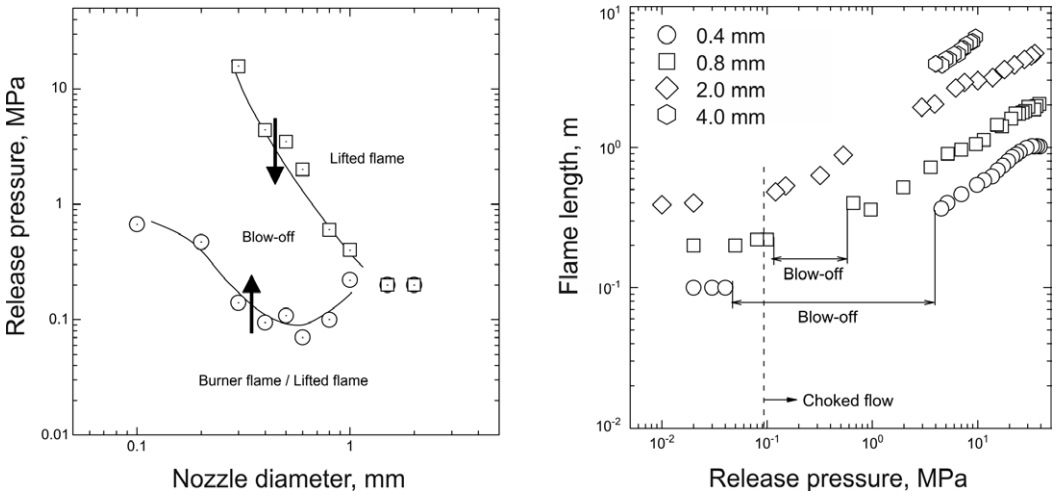

Figure 9–9. Hydrogen jet flame blow-off region (left) and flame length (right) as a function of different leak diameters and release pressures (Mogi and Horiguchi, 2009).

Figure 9–9 (right) demonstrates the flame length (distance from the nozzle exit to the visible flame tip) as a function of various release pressures and nozzle diameters. The measurements for nozzle diameter 4 mm are made in the pressure range of 4–10 MPa. There is no flame blow-off for nozzle diameters 4 mm and 2 mm. The blow-off region exists for nozzles with diameter 0.4 mm and 0.8 mm. The flame length remains approximately constant, irrespective of the release pressure, when the release pressure is below the critical pressure. However, the flame length grows proportional to the release pressure when it is higher than the critical pressure.

Figure 9–10 shows similar results on the blow-off limits obtained by Okabayashi et al. (2007) with more experiments carried out at high pressures and small diameters. They confirmed that even at very high release pressures it is impossible to sustain jet flame from nozzles with diameters below 0.1 mm.

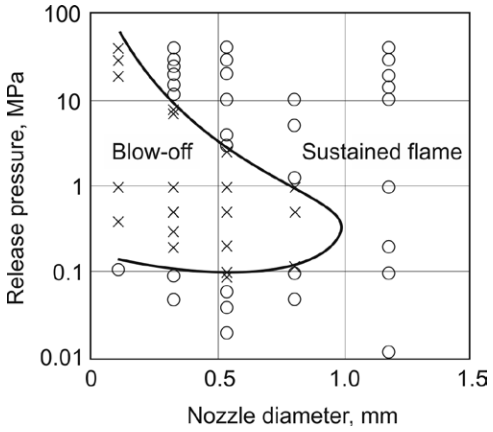

Figure 9–10. Regions of flame blow-off and sustained hydrogen jet flames (Okabayashi et al., 2007).

9.6. The novel dimensionless flame length correlation

Practically all former flame length correlations are *Fr*-based and built on experimental data for subsonic buoyant jet/plume fires with a limited number of momentum-controlled jet fires at moderate pressures. Figure 9–11 shows that the *Fr*-based "correlation" is lacking physical commonality when a large number of experimental data on under-expanded jet fires are included (all in the momentum-dominated regime).

Theoretical and experimental results indicate that the flame length has to be a function of not only the Froude number (*Fr*) but also the Reynolds (*Re*) number and the Mach (*M*) number. The analysis of previous research resumes that it is impossible to build a universal correlation applicable to both expanded and under-expanded jet fires based on only one of these three similarity groups. A new in principle approach is needed to correlate the experimental data properly with physical underpinning.

Dimensional correlations like one in the previous section (see Fig. 9–7) are convenient engineering tools yet do not make a distinction between different jet fire regimes. This section aims to advance our understanding of hydrogen jet flame behaviour, and develop a dimensionless correlation for non-premixed flames that will differentiate between traditional buoyancy-controlled and momentum-dominated jet flames, as well as between expanded and under-expanded jet fires.

The dimensional correlation (9–6) can be approximated as $L_F \propto (\dot{m} \cdot D)^{1/3}$. The mass flow rate is by definition $\dot{m} \propto D^2$. Thus, a conclusion can be drawn after substitution of $\dot{m} \propto D^2$ into the above relationship for L_F that the dimensional flame length, L_F/D, does not depend explicitly on the diameter, D. This is a basic hypothesis behind the development of a novel dimensionless correlation for the jet flame length, which is supported by the experimental data analysis. The only dependence of the dimensionless flame length, L_F/D, is then on the "residual" parameters in the mass flow rate, i.e. density ρ_N and velocity U_N at the nozzle exit, which are assumed uniform for the simplicity.

The density and velocity can be normalized as ρ_N/ρ_S and U_N/C_N respectively, where C_N is the speed of sound at conditions of gas in the nozzle and ρ_S is the density of the surrounding gas (air). In assumption of the kinetic energy flux in the nozzle exit to be a conserved scalar of the process a relation between the density and the velocity in the dimensional group can be suggested as $(\rho_N/\rho_S)(U_N/C_N)^3$.

Figure 9–11 presents a novel dimensionless hydrogen flame length correlation. In this correlation the experimental data on flame length are normalized by the actual (not notional) nozzle diameter, and are correlated with the product of the dimensionless density ratio ρ_N/ρ_S and the Mach number (ratio of the flow velocity to the speed of sound at the actual nozzle exit) to the power of three $M^3=(U_N/C_N)^3$.

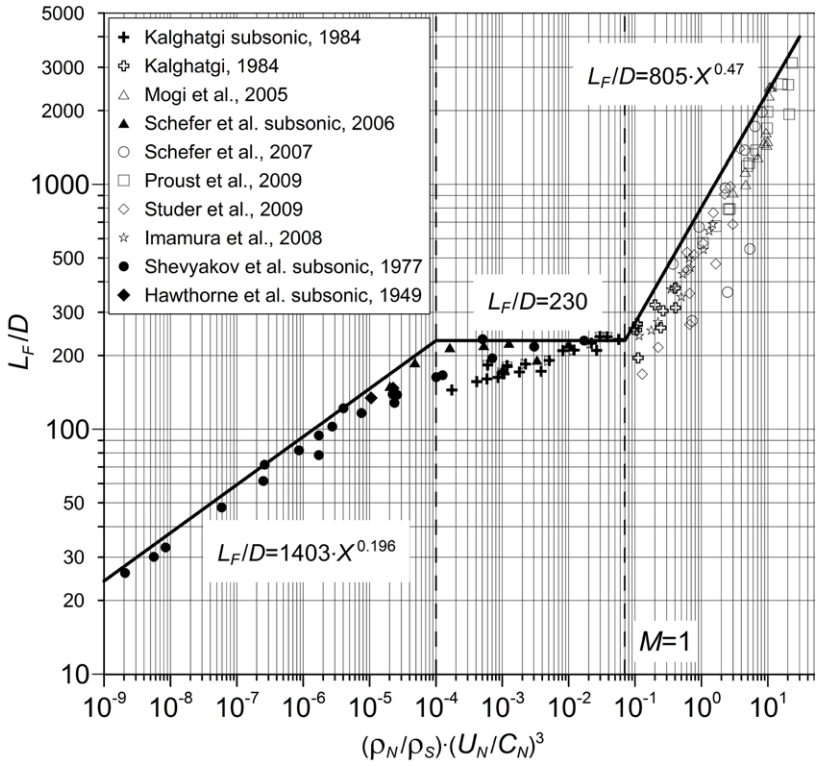

Figure 9–11. The dimensionless correlation for hydrogen jet flames (in formulas "*X*" denotes the similarity group $(\rho_N/\rho_S)(U_N/C_N)^3$).

One of the advantages of this correlation is the absence of parameters at the notional nozzle exit. The parameters needed to predict the flame length are those at the actual nozzle exit only: diameter, hydrogen density and flow velocity, the speed of sound at pressure and temperature at the nozzle exit. The use of the correlation requires application of an under-expanded jet theory to calculate these parameters. There is lesser uncertainty in calculation of flow parameters in the actual nozzle exit compared to uncertainties at the notional nozzle. Indeed, it is well known that there is a strong non-uniformity of velocity immediately downstream of the Mach disk that deviates from the common for all under-expanded jet theories assumption of uniform velocity at the notional nozzle exit. By this fact, the developed methodology excludes from consideration the questionable issue of use of flow parameters at the notional nozzle exit.

The hydrogen flow parameters at the nozzle exit for experiments in Fig. 9–11 are taken either directly from the experiments or calculated by the under-expanded jet theory (Molkov et al., 2009). The details of experiments used to underpin the dimensionless correlation are given in (Molkov and Saffers, 2011). The novel correlation covers the whole spectrum of hydrogen reacting leaks, including laminar and turbulent flames, buoyancy- and momentum-controlled fires, expanded (subsonic and sonic) and under-expanded (sonic and supersonic) jet fires.

The dimensionless group derived for correlating the dimensionless flame length can be rewritten in terms of *Re* and *Fr* numbers as follows

$$\frac{\rho_N}{\rho_S}\cdot\left(\frac{U_N}{C_N}\right)^3=\frac{g\cdot\mu_N}{\rho_S\cdot C_N^3}\cdot \mathrm{Re}\cdot Fr\,, \tag{9–8}$$

where the viscosity was calculated as $\mu_N=\mu_{293}\cdot\left((293+K_{Suth})/(T_N+K_{Suth})\right)\cdot\left(T_N/293\right)^{3/2}$ (Sutherland constant for hydrogen was taken as K_{Suth} = 72 K and the dynamic viscosity as μ_{293} = 8.76×10^{-6} Pa·s), and *Re* and *Fr* are determined by parameters of hydrogen flow in the actual nozzle exit as $\mathrm{Re}=(\rho_N\cdot U_N\cdot D)/\mu_N$ and $Fr=U_N^2/(g\cdot D)$.

The form of the dimensionless group in the left hand side of Eq. (9–8) suggests that for subsonic flows, when Mach number M<1 and the density ratio ρ_N/ρ_S is a constant for expanded jets (in assumption of constant temperature in the nozzle), the dimensionless flame length depends on the nozzle Mach number only. For choked flows in the nozzle exit (M=1) the dimensionless flame length depends only on the hydrogen density in the nozzle exit ρ_N. The density increases with the increase of storage pressure and the decrease of hydrogen temperature.

The form of the right hand side of Eq. (9–8) indicates that at a constant temperature of hydrogen in the nozzle exit (that provides the constancy of the speed of sound C_N) the dimensionless flame length depends on both *Fr* and *Re* numbers. This is contrary to the former correlations built on *Fr* number only.

There are three distinct parts in the novel dimensionless correlation in Fig. 9–8 (from the left to the right): traditional buoyancy-controlled, traditional momentum-dominated "plateau" (expanded jets), and a new momentum-dominated under-expanded jet fire "slope". These three parts can be approximated by the following equations (conservative curves) respectively

$$\begin{aligned}
&L_F/D=1403\cdot X^{0.196}, && \text{for} \quad X=\frac{\rho_N}{\rho_S}\left(\frac{U_N}{C_N}\right)^3<0.0001;\\
&L_F/D=230, && \text{for} \quad 0.0001<X=\frac{\rho_N}{\rho_S}\left(\frac{U_N}{C_N}\right)^3<0.07;\\
&L_F/D=805\cdot X^{0.47}, && \text{for} \quad X=\frac{\rho_N}{\rho_S}\left(\frac{U_N}{C_N}\right)^3>0.07.
\end{aligned} \tag{9–9}$$

There is a saturation of L_F/D for expanded jet fires as the flow velocity in the actual nozzle exit is approaching the speed of sound. The value of this saturation limit L_F/D =230 reproduces results of a number of previous studies with expanded jets, though in the new coordinates. However, there is no saturation of the dimensionless flame length for choked under-expanded jet flames. Reported in recent under-expanded jet fire experiments (Proust et al., 2009) values up to L_F/D=3000 are significantly higher compared to the limit L_F/D =230 for expanded jets.

There are some experimental points of Schefer et al. (2006b) in Fig. 9–11 that are below the rest of the data. It is thought due to losses in this particular experimental set-up, which is not described in detail sufficient to allow the application of the under-expanded jet theory with losses. Indeed, the losses would decrease the density in the nozzle exit and those points would be shifted to the left along the abscissa axis closer to the correlation. The experimental set-up that was used in another study of Schefer et al. (2007) had obviously lesser flow losses and pressure given was measured closer to the nozzle.

The shape of correlation in Fig. 9–11 has a physical meaning based on the knowledge of jet flame behavior. For example, the dimensionless flame length, L_F/D, increases for laminar and transitional flames (usually identified as "buoyancy-controlled" regime, low *Re*), then it is practically constant for transitional and fully developed turbulent expanded flames (traditionally named as "momentum-dominated" regime, moderate *Re*), and it increases again for under-expanded jets (momentum-controlled under-expanded jet regime, high *Re*). The growth of dimensionless flame length in the under-expanded regime is due to the fact that the dimensionless flame length is defined through the actual nozzle exit diameter, which is a constant, while in reality the under-expanded jet expands to atmospheric pressure at the notional nozzle exit which increases with the increase of density in the nozzle.

Figure 9–12 demonstrates changes of dimensionless numbers *Re, Fr, M*, for the experiments used for the development of the dimensionless correlation, as a function of the similarity group $(\rho_N/\rho_S)(U_N/C_N)^3$. The analysis of *Re, Fr, M* functional dependence on the similarity group shows that for under-expanded jets the dimensionless flame length growth depends practically on *Re* only. Indeed, the nozzle flow for under-expanded jets is choked, i.e. local *M*=1, and the nozzle *Fr* number is practically constant also (the scattering of *Fr* is due to the difference in nozzle diameters of about one order of magnitude).

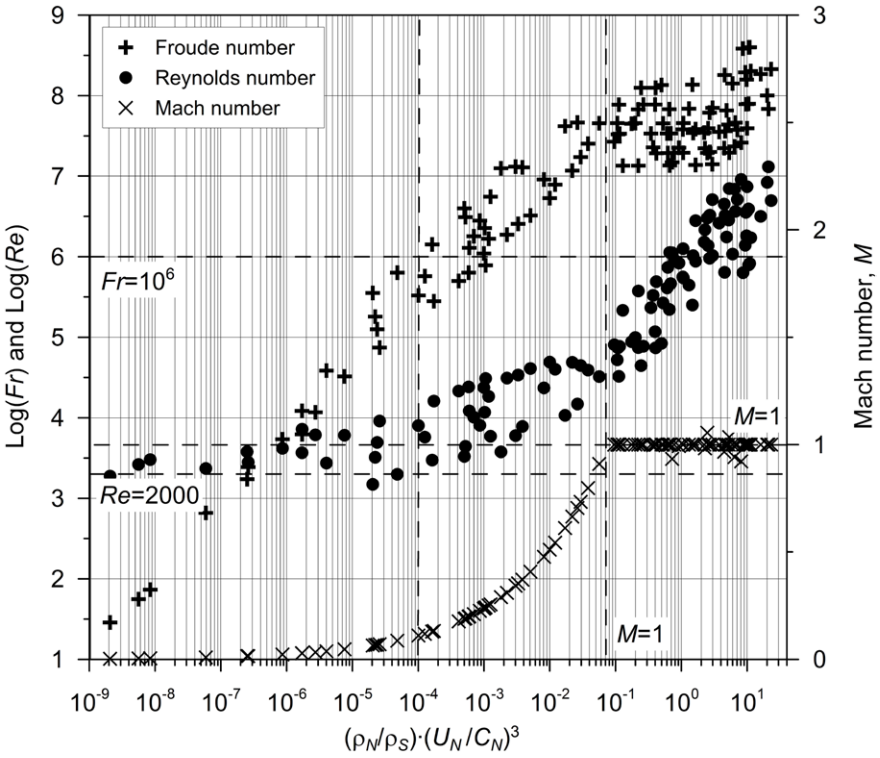

Figure 9–12. Dimensionless numbers *Re, Fr, M* as a function of the similarity group $(\rho_N/\rho_S)(U_N/C_N)^3$ for experiments used to build the dimensionless correlation.

There are five dashed thick lines in Fig. 9–12. Line *Re*=2000 indicates the start of transition from laminar to turbulent nozzle flow. Close to (or immediately above) this line there are experimental points representing laminar jet flames and jet flames in the transitional regime. Horizontal line *M*=1 indicates a choked flow limit. Subsonic expanded jets have *M*<1 and sonic and supersonic (the last is relevant to notional nozzle flows only) under-expanded jets have *M*=1 in the nozzle exit. There is some scattering of data around *M*=1 due to measurements and data processing errors. Horizontal line $Fr=10^6$ is an approximate division between buoyancy-controlled ($Fr<10^6$) and momentum-dominated ($Fr>10^6$) jets established previously for expanded jets. A vertical line at a value of the similarity group $(\rho_N/\rho_S)(U_N/C_N)^3=0.0001$ conditionally separates buoyant jet fires (to the left from the line) and momentum jet fires (to the right from the line). Finally, a vertical line denoted *M*=1 divides subsonic (to the left) and sonic or chocked in the nozzle exit jets (to the right).

In log-log coordinates in Fig. 9–12 the *Fr* number increases linearly with the similarity group $(\rho_N/\rho_S)(U_N/C_N)^3$ for expanded jet fires. There is practically no change of *Fr* for under-expanded jets in this new system of coordinates (scattering is mainly due to difference in nozzle sizes). There is a slight growth of *Re* with the similarity group for buoyant jets, moderate increase in traditional momentum-dominated area, and comparatively steep growth of *Re* number in the area of under-expanded jet fires that are all momentum-dominated.

The novel dimensionless correlation is validated in the range of hydrogen storage pressures from nearly atmospheric up to 90 MPa, temperatures down to 80 K, and nozzle diameters from 0.4 to 51.7 mm. The predictive capability of this dimensionless correlation exceeds that of *Fr*-based only correlations, and it clearly distinguishes three regimes of jet fires, i.e. buoyancy-controlled, momentum-dominated (expanded), momentum-dominated (under-expanded).

9.7. Flame tip location and equivalent unignited jet concentration

There is an incorrect point of view that had been published for the first time by Sunavala et al. (1957) and repeated later at least by Bilger and Beck (1975) and Bilger (1976) that the calculated flame length may be obtained by substitution the concentration corresponding to the stoichiometric mixture (29.5% by volume of hydrogen in air) in equation of axial concentration decay for a non-reacting jet.

The experimental data demonstrates that the longest, and thus the most hazardous, flames are associated with under-expanded jets. This is important to underline that all experimental data on under-expanded jet fires are in the momentum-dominated regime (high *Fr*). This is due to high velocity of chocked flows and comparatively small diameters of piping for equipment working at pressures up to 100 MPa. Recently the similarity law for axial concentration decay in round unignited expanded momentum-dominated jets, suggested by Chen and Rodi (1980), has been extended and thoroughly validated for under-expanded hydrogen jets (Molkov, 2009b)

$$\frac{C_{ax}}{C_N} = 5.4\sqrt{\frac{\rho_N}{\rho_S}}\frac{D}{x}, \tag{9–10}$$

where C_{ax} is the mass fraction of gas at axial distance x from the nozzle, C_N is a mass fraction of gas in the nozzle (C_N=1 for pure gas release), x is the axial distance from the nozzle, and density at the nozzle exit ρ_N is the only unknown parameter.

The application of the similarity law (Eq. 9–10) to axial concentration decay in expanded jet is straight forward with the use of a constant hydrogen density in a nozzle, e.g. ρ_N=0.0838 kg/m^3 at normal temperature and pressure (NTP). However, for under-expanded jets the knowledge of density in the nozzle exit, ρ_N, as a function of storage pressure and losses in a leak pathway is necessary. The density in the nozzle can be calculated using the under-expanded jet theory described in chapter 5.

Figure 9–13 presents a correlation between location of hydrogen jet flame tip (flame length) and location of hydrogen concentration in unignited jet originating from the same leak source. Points in Fig. 9–13 represent the dimensionless experimental flame length, L_F/D. The diagonal curves in the graph correspond to the dimensionless distance x/D to location of particular axial hydrogen concentration, C_{ax}, as a function of the density in the nozzle exit, ρ_N, (recalculated to the storage pressure, p in atmospheres, in Fig. 9–13) and calculated using the similarity law (9–10).

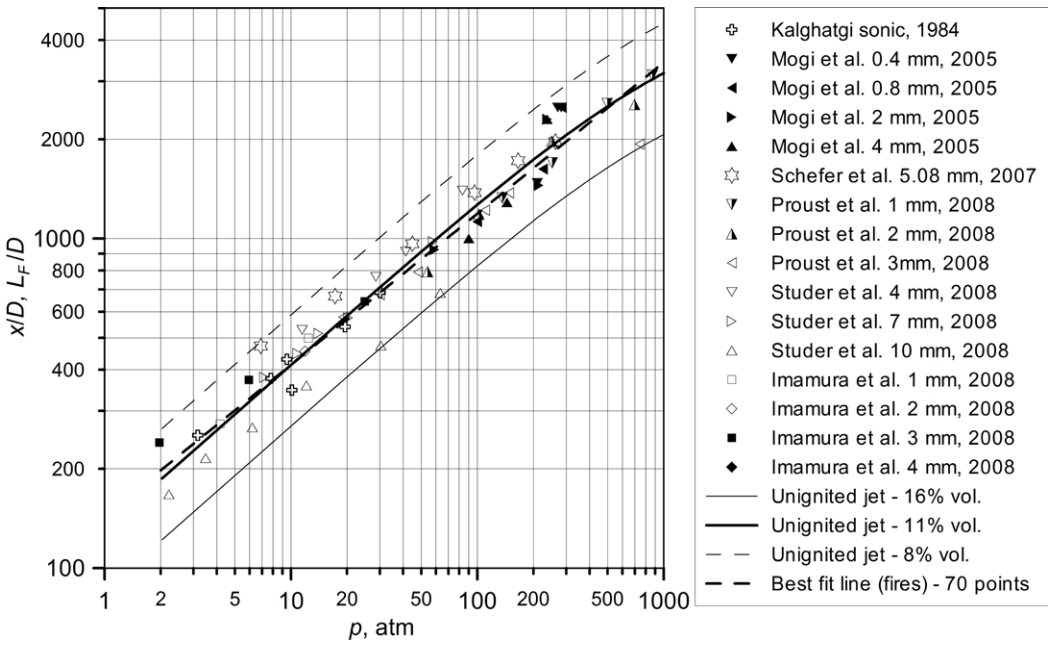

Figure 9–13. The correlation between the dimensionless flame length, L_F/D, and the distance to a particular concentration in a non-reacting jet, x/D, from same leak source for different storage pressures, p.

The conclusion can be drawn from Fig. 9–13 that for momentum-controlled round jet fires the flame tip is located where the axial concentration of hydrogen in an unignited jet from the same leak source is in the range between 8% and 16% by volume, depending on experimental conditions. The best fit line of 70 experimental points for hydrogen flame length of momentum-dominated jet fires is close to 11% by volume of hydrogen in air in unignited jet.

These concentrations (8% to 16%) are far below the stoichiometric concentration of 29.5% by volume of hydrogen in air as was stated previously by Sunavala et al. (1957), Bilger and Beck (1975), and Bilger (1976). Distances to these concentrations from the nozzle are longer by 2.2 time (16%) to 4.7 times (8%) than a distance to axial concentration 29.5% (stoichiometric hydrogen-air mixture). This obviously could have serious safety and economic implications.

9.8. Separation distances from a hydrogen leak

Different engineering tools to calculate hydrogen jet flame length are developed and described above. They include the dimensional and dimensionless correlations for the jet flame length, as well as the methodology to calculate hydrogen axial concentration decay to 11% by volume in an unignited jet to evaluate the flame tip location (flame length). However, the question about separation distances from a leak source based on comparative analysis of hazards from unignited jet and jet fire is not yet finalised.

British standard (BSI, 2004) recommends 115°C as the threshold for pain from an elevated air temperature for exposure longer than 5 minutes. This is in line with the previously published classification (DNV, 2001) of elevated temperature effects on occupants: below 70°C, no fatal issue in a closed space except uncomfortable situation; between 70°C and 150°C, the impact is dominated by difficulties to breath; above 150°C, skin burns occur in less than 5 minutes and this is a limiting temperature for escape. Time to incapacitation in minutes as a function of air temperature (°C) can be estimated by the following equations recommended by DNV (2001) and BSI (1997) respectively

$$t_{incap} = 5.33 \cdot 10^{8} \cdot T_{air}^{-3.66}, \tag{9–11}$$

$$t_{incap} = 5 \cdot 10^{7} \cdot T_{air}^{-3.4}. \tag{9–12}$$

For temperature 115°C Eq. (9–11) gives the incapacitation time 5 minutes of exposure and Eq. (9–12) gives 15 minutes. Temperature 115°C is assumed here as the acceptance criteria for pain limit in hot air when considering an escape from an elevated temperature gas flow generated by a hydrogen jet fire. More details on physiological response of humans to air at elevated temperature are as follows (Bryan, 1986; DNV, 2001): 127°C – difficult breathing; 149°C – mouth breathing difficult, temperature limit for escape; 160°C – rapid, unbearable pain with dry skin; 182°C – irreversible injuries in 30 seconds; 203°C – respiratory systems tolerance time less than four minutes with wet skin; 309°C – third degree burns for a 20 seconds exposure, causes burns to larynx after a few minutes, escape improbable.

Harm criteria for people can be expressed in terms of injury or death (LaChance, 2010). It is possible to use a "no harm" criterion which limits the level of acceptable consequences to a low enough level that no injury would occur. Temperature 70°C is taken as "no harm" criterion in this study. Exposures to flames, hot air or radiant heat fluxes can result in first, second, or third degree burns. The resulting level of harm is dependent upon several factors: the amount and location of exposed skin, the person's age, the exposure time, the speed and type of medical treatment, etc.

Figure 9–14 shows measured axial temperature of hydrogen flame (Barlow and Carter, 1996; Imamura et al., 2008; LaChance, 2010) as a function of distance from the nozzle, x, normalised by the flame length, L_F. Three accepted here criteria are presented by horizontal lines: 70°C – "no harm" limit; 115°C – pain limit for 5 min exposure; 309°C – third degree burns for a 20 s ("death" limit). Comparison between the axial temperature profile and named criteria provides the separation distances: x=3.5L_F for "no harm" separation (70°C), x=3L_F for pain limit (115°C, 5 min), x=2L_F for third degree burns (309°C, 20 s).

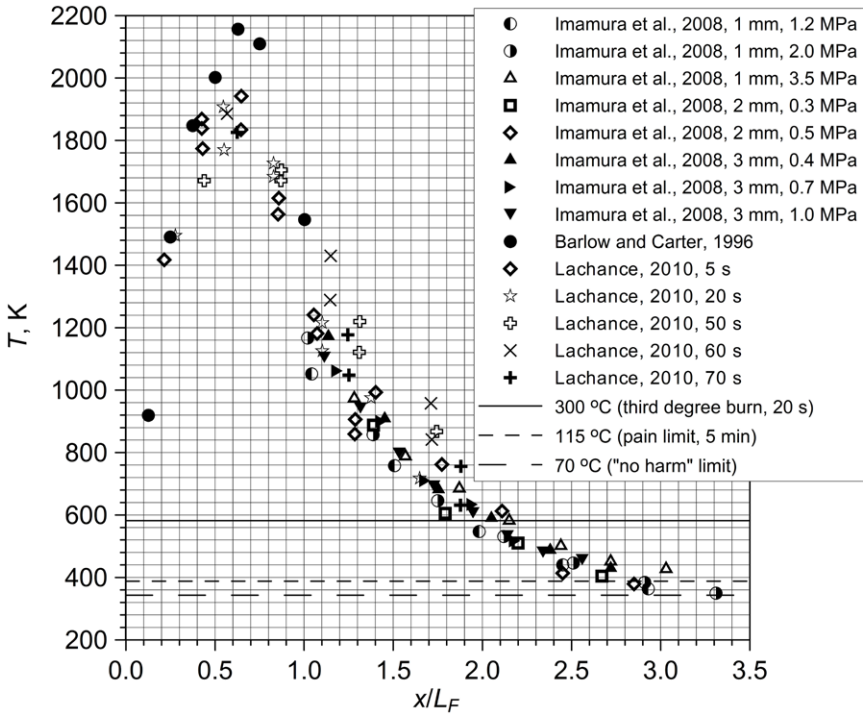

Figure 9–14. Measured axial temperature as a function of distance expressed in flame calibres, and three criteria for jet fire effects (lines).

Let us compare for the same leak source three separation distances for momentum-controlled jet fire and a separation distance for momentum-dominated unignited release (distance to the lower flammability limit, LFL, of 4% by volume of hydrogen in air). It is demonstrated above that the statistically averaged flame length is equal to the distance from the nozzle to an axial location where hydrogen concentration decays to 11% by volume in unignited jet (data are scattered from 8% to 16% by volume).

The similarity law (9–10) for concentration decay in unignited momentum-controlled jets requires the use of hydrogen mass fraction and not volumetric fraction as mistakenly applied in some published works. The mass fraction (C_M) can be calculated by the volumetric (mole) fraction (C_V) by equation $1/C_M=1+(1/C_V -1)$ M_S/M_N, where M_S and M_N are the molecular mass of surrounding gas and nozzle gas respectively. For air composition of 21% by volume of oxygen and 79% of nitrogen the mass fraction of hydrogen C_{ax}=0.002881 corresponds to 4% of hydrogen by volume in air, 0.008498 corresponds to 11% of hydrogen by volume (0.005994 – 8%, 0.013037 – 16%), and mass fraction of stoichiometric mixture is 0.0282 (29.5% by volume).

The ratio of distances from the nozzle to axial concentration 11% by volume (correct flame tip location obtained in this study) and to 29.5% by volume (incorrect location of the flame tip suggested in some studies) can be estimated by dividing the similarity laws (9–10) for these two concentrations by each other (in assumption that the similarity law is applicable up to concentrations as high as stoichiometric), i.e. $x_{11\%}/x_{29.5\%}=C_{ax(29.5\%)}/C_{ax(11\%)}$=0.0282/0.008498= 3.3. This increases calculated flame length by an order of magnitude compared to that based on the previous incorrect knowledge (attributing flame length tip location to location of 29.5% by volume concentration in unignited jet from the same source).

The ratio of distances to LFL of 4% by volume and to the averaged flame tip location of 11% by volume is (it has to be stressed that flame length is not equal to separation distance from the flame source): $x_{4\%}/x_{11\%}$=0.008498/0.002881=2.95 (LFL distance to longest flame length ratio is $x_{4\%}/x_{8\%}$=2.08, and LFL to shortest flame ratio is $x_{4\%}/x_{16\%}$=4.53). Thus, ratios of the separation distance to LFL (unignited jet) to three separation distances based on the choice of harm criteria from reacting hydrogen jet are (for average flame tip location at concentration in unignited jet of 11% by volume): $x_{4\%}/x_{T=70C}=x_{4\%}/(3.5\cdot x_{11\%})$=2.95/3.5=0.84; $x_{4\%}/x_{T=115C}$= 2.95/3=0.98; $x_{4\%}/x_{T=309C}$ =2.95/2=1.48.

However, in the conservative case of the flame tip location at the concentration of 8% by volume in unignited jet, these three ratios will change to the following values respectively:

$x_{4\%}/x_{T=70C(8\%)}$=0.005994/0.002881/3.5=2.08/3.5=0.59;
$x_{4\%}/x_{T=115C(8\%)}$=2.08/3=0.69;
$x_{4\%}/x_{T=309C(8\%)}$ =2.08/2=1.04.

As a result an "unexpected" conclusion can be drawn from the performed analysis that in the conservative case all three separation distance for reacting release (jet fire) are longer or equal to the separation distance based on the LFL (unignited release). In particular, the separation distance from a hydrogen leak source to a location with axial concentration equal to the LFL, e.g. to prevent ingress of flammable mixture into a ventilation system of building, is practically equal to the "death" separation distance for reacting release (exposure to 309°C during 20 s). Two other separation distances for jet fires ("no harm" and "pain" limits) are longer than separation distance to LFL (unignited release).

The revealed "longest" location of the hydrogen jet flame tip at axial distances from the nozzle corresponding to 8% by volume of hydrogen in unignited jet is a physically sound result. Indeed, this value is within the measurements and theoretical assumptions error to the lower flammability limit for downward and spherically propagating premixed hydrogen-air flames of 8.5–9.5% by volume. Thus, any combustion beyond this distance (at smaller concentrations) is "detached" from the area of "continuous" vertical flame.

Radial separation distance from hydrogen jet fire requires an analysis of radiative heat transfer rather than flow temperature. Relevant information can be found elsewhere (Schefer et al., 2007).

9.9. Effect of nozzle shape on flame length

Mogi and Horiguchi (2009) carried a series of experiments at release pressure of 40 MPa on effect of the nozzle shape on hydrogen flame length and width. Three nozzles of the same cross-section area were tested: the round nozzle of 1 mm diameter, the plane nozzle of LxW=2x0.4 mm (aspect ratio AR=5), the plane nozzle of LxW=3.2x0.25 mm (AR=12.8). Figure 9–15 shows nozzles photographs (left), side view of hydrogen flame from each of three nozzles (centre), and front view of these jet flames. The round nozzle flame shape is axisymmetric as in many other experiments. The reacting flow is in the momentum-dominated regime as the effect of buoyancy is not pronounced. However, flames from plane nozzles are flattened in the direction perpendicular to the major axis. This is due to the switch-of-axis phenomenon (Makarov and Molkov, 2013).

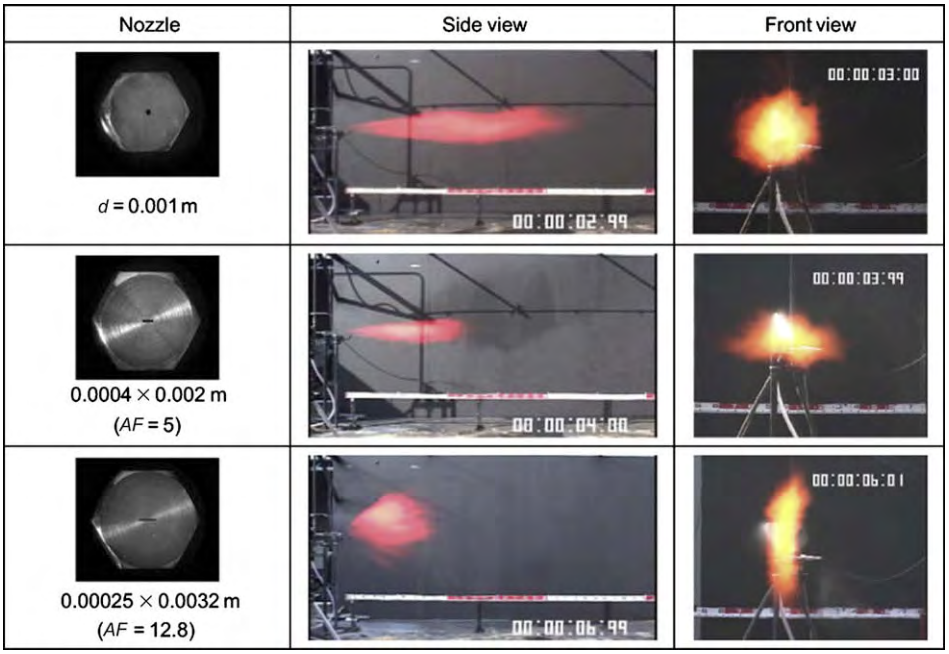

Figure 9–15. Photographs of three nozzles shape (left), side hydrogen flame view (centre), and front hydrogen flame view (right) for release pressure of 40 MPa (Mogi and Horiguchi, 2009).

The measured flame lengths and widths are presented in Fig. 9–16 (Mogi and Horiguchi, 2009). For plane nozzles the flame length is about half of that for the round nozzle of the same cross-section area, whereas the maximum flame width is approximately twice of that for the round nozzle. The results demonstrated that the width of the plane nozzle (shorter dimension) affects the flame length. The smaller is the width the shorter is the flame length. On the other hand, in authors' opinion the length of the plane nozzle (longer dimension) affects the maximum flame width.

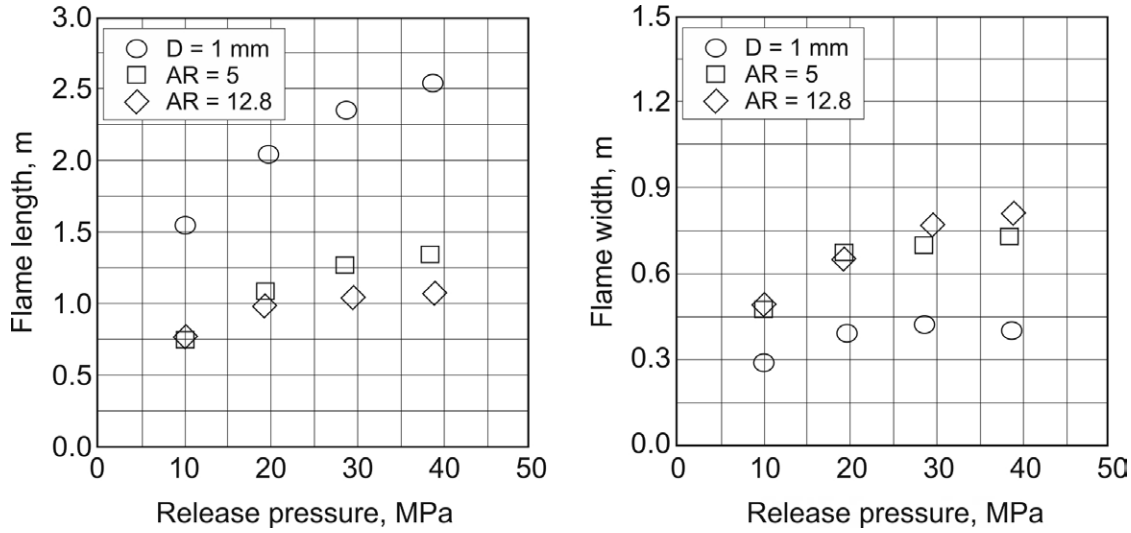

Figure 9–16. Flame length (left) and flame width (right) for three different nozzles of the same cross-section area: round nozzle of 1 mm diameter, plane nozzle with aspect ratio AR=5, plane nozzle with AR=12.8 (Mogi and Horiguchi, 2009).

9.10. Effect of jet attachment of flame length

It is known from fire safety science that the flame length of fire increases when the fire source is attached to wall. The effect is even stronger if the same fire is placed in a corner. The phenomenon is explained by the change in the air entrainment rate.

Royle and Willoughby (2009) measured the increase of the flame length due to attachment to ground. The flame length of free unattached horizontal jet from storage at 20.5 MPa through a nozzle located 1.2 m above the ground depends on the nozzle diameter. The flame length is 3 m for the nozzle diameter D=1.5 mm, 6 m – for D=3.2 mm, 9 m – for D=6.4 mm, and 11 m – for D=9.5 mm. For attached jet from the nozzle located only 0.11 m above the ground the flame length increases as follows: from 3 m to 5.5 m (nozzle diameter D=1.5 mm), from 6 m to 9 m (D=3.2 mm), from 9 m to 11 m (D=6.4 mm), and from 11 m to 13 m (D=9.5 mm). The effect of jet flame attachment on its length growth decreases with the increase of the nozzle diameter. In addition to change of air entrainment conditions probably the effect of momentum losses of the high velocity jet on the surface due to non-slip conditions should be accounted for to explain this experimental observation.

9.11. Pressure effects of hydrogen jet fires

There is an unsteady stage in the jet establishment immediately after leak initiation from the high pressure hydrogen equipment. Delayed ignition and consequent combustion of the unsteady highly turbulent hydrogen-air cloud formed at this stage can lead to significant overpressure in the near field able to harm people. This process is basically the deflagration and takes place before the quisi-steady jet fire is established.

9.11.1. Delayed ignition of non-premixed turbulent jets (Japan)

Takeno *et al.* (2007) studied the effects of an ignition delay and location of ignition source on deflagration pressure following the release of hydrogen from the storage at pressures between 40 MPa and 65 MPa through a 10 mm diameter nozzle (pressure in the nozzle was 40 MPa). In the open atmosphere the flame propagation velocity was assessed to be over 300 m/s at a distance of approximately 4 m. The increase of ignition delay from 0.85 s to 5.2 s, when an ignition source was located at distance 4 m from the nozzle, led to a decrease in the maximum deflagration overpressure in the near field (about 2 m from the nozzle) from 90 kPa to 15 kPa. It was concluded that the shorter the ignition delay, the greater is the overpressure. Takeno *et al.* (2007) also concluded that the turbulence has a greater effect on the "explosiveness" than the total amount of leakage or the premixed volume has.

Tanaka *et al.* (2007) investigated also the ignition of jets from a refuelling dispenser in the open. The horizontal jet from a 8 mm diameter nozzle was ignited at a distance of 4 m. It was found that the logarithm of the peak overpressure decreases linearly with increased logarithm of time to ignition. The largest overpressure was found for a 1.2 s ignition delay. This conclusion is in line with the HySAFER blind simulations of the HSL experiment on delayed ignition. The simulations demonstrated that the maximum volume of near-stoichiometric mixture is formed at time about 1 s after the release start.

9.11.2. Delayed ignition of non-premixed turbulent jets (UK)

The UK Health and Safety Laboratory (HSL) of the Health and Safety Executive performed a series of over 40 experiments with high pressure releases of hydrogen as a part of the project HYPER (2008) and published later by Royle and Willoughby (2009). The effects on overpressure of varying the jet exit diameter, the ignition delay and position were determined and presented here.

Hydrogen was stored in two 50 litres cylinders at pressure 20.5 MPa. There was the stainless steel tubing of internal diameter 11.9 mm, and a series of ball valves with internal bore of 9.5 mm between the storage and the nozzle exit. Restrictors of the same 2 mm length and different diameter of 1.5, 3.2, and 6.4 mm were used in the nozzle to vary the jet exit diameter. The release point is 1.2 m above the ground. The jet was ignited by a match head with small amount of pyrotechnic material 1.2 m above the ground. The ignition point location varied in the range 2-10 m from the release point. Piezo-resistive transducers were pointed out upwards except for wall mounted. Transducers were located at axial distance 2.8 m from the nozzle, 1.5 m (then +1.1 m and +1.1 m) perpendicular to the axis, at height 0.5 m.

Time 260 ms was needed to fully open the valve, 140 ms for hydrogen to reach 2 m. Thus, 400 ms is the shortest possible ignition delay of the unsteady jet. Jets from hydrogen storage at 20.5 MPa were predominantly momentum-controlled, i.e. the floow was relatively non-buoyant up to the lower flammability limit (Royle and Willoughby, 2009).

9.11.2.1. Effect of the ignition delay and the varying ignition position

The effect of the ignition delay was studied for the nozzle diameter 6.4 mm and the ignition location of 2 m from the nozzle (see Table 9–1). It can be concluded that ignition in a close to the flammability limits region of the jet cloud (ignition delay of 400 ms) results in a relatively slow burn and hence a small overpressure. The maximum overpressure of 19.4 kPa is observed for the ignition delay of 600 ms. Maximum overpressures were observed when the jet was ignited at a time which coincided with the area of maximum turbulence within the front portion of the jet, reaching the ignition point.

Ignition delay, ms	Max overpressure, kPa
400	3.7
500	18.4
600	19.4
800	15.2
1000	11.7
1200	12.5
2000	9.5

Table 9–1. Effect of the ignition delay on the maximum overpressure generated by deflagrating jet (Royle and Willoughby, 2009).

A single nozzle with diameter 6.4 mm was chosen with a fixed release pressure of 20.5 MPa and a fixed ignition delay 800 ms. The ignition position varied from 2 m to 10 m. The maximum overpressures were seen by transducer No.1 located 2.8 m from the nozzle and 1.5 from the jet centre line (see Table 9–2). The deflagration overpressure reduces drastically with the increase of the ignition position from the jet source. There was no ignition of jet with the location of the ignition source 10 m from the nozzle.

Ignition position, m	Max overpressure, kPa
2	15.2
3	5.0
4	2.1
5	2.1
6	Not recordable
8	Not recordable
10	No ignition

Table 9–2. Effect of the ignition delay on the maximum overpressure generated by deflagrating jet (Royle and Willoughby, 2009).

9.11.2.2. Effect of the nozzle diameter

Table 9–3 shows experimental measurements of the unsteady hydrogen jet deflagration overpressure for two ignition delays (minimum possible 400 ms and 800 ms) and nozzle diameters from minimum 1.5 mm to maximum 9.5 mm. The nozzle diameter has a crucial effect on the maximum overpressure generated by ignited jet.

Nozzle diameter, mm	Ignition delay, ms	Max overpressure, kPa
1.5	800	Not recordable
1.5	400	Not recordable
3.2	800	3.5
3.2	400	2.1
6.4	800	15.2
6.4	400	2.7-3.7
9.5	800	16.5
9.5	400	3.3–5.4

Table 9–3. Effect of the nozzle diameter and the ignition delay on the maximum overpressure generated by deflagrating jet (Royle and Willoughby, 2009).

There was no overpressure for release through the nozzle of 1.5 mm diameter. The overpressure for 400 ms ignition delay, when jet just reached the ignition point located 2 m downstream from the nozzle, is always below the overpressure for the ignition delay of 800 ms corresponding to a larger turbulent flammable hydrogen-air cloud formed. It is worth noting that there is a wall in the experiments behind the nozzle. The maximum registered overpressure of free hydrogen jet was 16.5 kPa.

There is an important conclusion from this series of experiments: the leak diameter has to be reduced as low as reasonably possible (ALARP) for a particular hydrogen and fuel cell technology. The inclusion of flow restrictors in hydrogen supply lines reduces the flame lengths observed, therefore reducing safety distances required. This is thought due to reduction of mass flow rate and pressure losses on the restrictor and thus lower pressure at the jet exit from the pipe.

Royle and Willoughby (2009) concluded that the jet turbulence and size had a greater effect on a deflagration pressure than the total amount of hydrogen leaked. The total amount of hydrogen released is not always important, especially at open atmosphere, as buoyancy continues to drive dilution of hydrogen by entrained air until it reaches the LFL of 4% by volume and beyond. Thus, portions of hydrogen released in the beginning in many practical scenarios will not contribute to combustion as they form a part of cloud which is below the LFL.

It can be assumed, based on the presented results, that the spontaneous ignition of a sudden hydrogen release by the diffusion mechanism could reduce overpressure of self-ignited release compared to the delayed ignition (the ignition delay is minimised in this case). It is worth noting that the spontaneous ignition was observed during sudden release in case of rupture disk burst and author is not familiar with any results of spontaneous ignition of jet by the diffusion mechanism when valves were used to initiate the high pressure hydrogen release.

9.11.2.3. Effect of barrier wall

To reduce flame the hydrogen flame length the barriers are often considered as a mitigation measure. However, there is cost for reduction of flame length by barriers. For example, in case of vertical 90° barrier the deflagration overpressure peak after delayed ignition (0.8 s) of the turbulent jet from 9.5 mm nozzle at storage pressure 20.5 MPa increases from 16.5 kPa for free jet to 42 kPa.

Figure 9–17 shows a sequence of snapshots (from top to bottom) after the delayed ignition of hydrogen jet impinging a 90° barrier. Before the jet flame reaches the quasi-steady state conditions (bottom snapshot) there is seen a deflagrative combustion of the non-uniform mixture in the confined space between the barrier and ground (see top and middle snapshots).

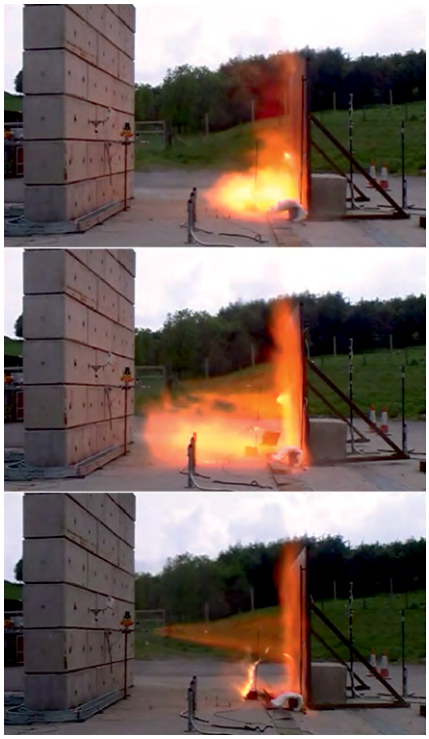

Figure 9–17. The delayed (0.8 s) ignition of hydrogen jet (20.5 MPa pressure storage, 9.5 mm diameter nozzle) impinging a 90 degree barrier: deflagration stage (top and middle snapshot), steady-state impinging jet fire stage (bottom snapshot), HSL test (HYPER, 2008).

The inclined to 60° barrier increases overpressure further to 57 kPa. Figure 9–18 shows a sequence of two snapshots after the delayed ignition of hydrogen jet impinging a 60° barrier.

Figure 9–18. The delayed (0.8 s) ignition of hydrogen jet (20.5 MPa pressure storage, 9.5 mm diameter nozzle) impinging a 60° barrier: deflagration stage (top snapshot), steady-state impinging jet fire stage (bottom snapshot), HSL test (HYPER, 2008).

9.11.2.4. Harmful pressure effects on human

Highest overpressures registered in experiments with delayed ignition of hydrogen jets for larger nozzle diameters can be a reason for serious injuries. Indeed, peak values of overpressure and associated level of injury to people outdoor are (Barry, 2003):

- 8 kPa – no serious injury to people;
- 6.9–13.8 kPa – threshold of skin lacerations by missiles;
- 10.3-20 kPa – people are knocked down by pressure wave;
- 13.8 kPa – possible fatality by being projected against obstacles;
- 34 kPa – eardrum rupture;
- 35 kPa – 15% probability of fatality;
- 54 kPa – fatal head injury;
- 62 kPa – severe lung damage;
- 83 kPa – severe injury or death.

9.12. Summary

- The Froude (*Fr*) number only based correlations are not applicable to under-expanded jets due to their inability to replicate the strong dependence of the dimensionless flame length on Reynolds number.
- The application of the similarity group in the form of a product of the mass flow rate and the actual nozzle diameter provided the essential reduction of experimental data scattering for both subsonic and sonic jet flames in the coordinates $L_F - \dot{m} \cdot D$ compared to the original coordinates of Kalghatgi (1984) $L_F - \dot{m}$. The dimensional correlation for hydrogen jet flame length
  $L_F = 76 \cdot (\dot{m} \cdot D)^{0.347}$ has been developed as a best fit line for 95 experimental data published by different research groups at pressures up to 90 MPa and nozzle diameters up to 10 mm. The conservative equation for the flame length is $L_F = 116 \cdot (\dot{m} \cdot D)^{0.347}$ (50% longer flame compared to the best fit line equation).
- The nomogram for graphical estimation of the flame length by only storage pressure and leak diameter is presented. This is built on the best fit line of the dimensional correlation. The nomogram includes "no flame" area informed experimental studies by Mogi et al. (2005, 2008) and Okabayashi et al. (2007) on the flame blow-off for different nozzle diameters and release pressures.
- The under-expanded jet theory accounting to non-ideal behaviour of hydrogen at high pressures as well as friction and minor losses in the leak pathway is presented. It is demonstrated that losses could strongly affect the mass flow rate (hydrogen density in the nozzle exit, ρ_N) and has to be accounted for in carrying out hydrogen safety engineering when relevant.
- The novel dimensionless correlation for hydrogen jet flame length in still air in the coordinates $L_F/D - (\rho_N/\rho_S) \cdot (U_N/C_N)^3$ is developed and described in detail. The correlation is validated against experimental data on laminar and non-premixed turbulent flames, buoyancy- and momentum-dominated flows, expanded and under-expanded hydrogen jet flames in the widest known to authors range of pressures 0.1–90.0 MPa, temperatures 80–300 K, and leaks diameters 0.4–51.7 mm.

- Three regimes of jet fires are identified, changing from the traditional buoyancy-controlled at low values of the dimensionless group $(\rho_N/\rho_S)\cdot(U_N/C_N)^3$, to the traditional momentum-dominated "plateau" at moderated values, and finally to the momentum-controlled under-expanded jet fire regime at higher values of $(\rho_N/\rho_S)\cdot(U_N/C_N)^3$.
- The statement of Sunavala et al. (1957) "calculated flame length may be obtained by substitution the concentration corresponding to the stoichiometric mixture in equation of axial concentration decay for non-reacting jet" was applied for more than 50 years and was repeated by Bilger and Beck in 1975 and by Bilger in 1976. It is proved that this statement is not valid for non-premixed turbulent jets in the momentum-dominated regime. The locus of average location of hydrogen jet flame tip in the range of pressures 0.2–90 MPa is matched by a line with an average axial concentration in unignited jet of 11% by volume of hydrogen in air (data are scattered in the range of axial hydrogen concentration in non-reacting jets from 8% to 16% by volume). Location of these axial concentrations is farther from the nozzle compared to location of stoichiometric concentration of 29.5% by volume to which the location of the flame tip was attributed before. This conclusion has serious safety and economic implications, e.g. distance from a leak source to axial concentration 11% by volume is 3.3 times longer than distance to the axial concentration 29.5% by volume (2.2 times longer for 16% by volume, and 4.7 times longer in the conservative case of 8% by volume).
- Three separation distances for jet fire include: "no harm" distance to temperature 70°C, which is about 3.5 times of the flame length; "pain limit" (115°C, 5 min), which is 3 times of the flame length; and "death limit" (309°C, 20 s), which is 2 times longer than the flame length.
- In the conservative case of the flame tip location at the location of concentration of 8% by volume in unignited jet, the ratios of a distance to the axial concentration 4% by volume (LFL) in non-reacting jet to the three separation distances for a jet fire are: $x_{4\%}/x_{T=70C(8\%)}=0.59$; $x_{4\%}/x_{T=115C(8\%)}=0.69$; $x_{4\%}/x_{T=309C(8\%)}=1.04$. Thus, all three separation distances for reacting jet are longer (within 4% error for the "death" limit) compared to the separation distance for non-reacting jet from the same leak source.
- The results of study by Mogi and Horiguchi (2009) on the effect of nozzle shape on the flame length and width are presented. The experiments demonstrated that the flame length from plane nozzle can be shorter compared to the flame length from round nozzle of the same cross-section area.
- Pressure effects of delayed ignition of hydrogen high pressure under-expanded jets are discussed following the studies by Takeno et al. (2007) and Royle and Willoughby (2009). The main conclusion is the reduction of the potential leak diameter ALARP. The maximum overpressures are observed at ignition delays less than 1 s. The removal of ignition source further than 10 m excluded the ignition of investigated realistic releases.

Please find the second part of this book by downloading
"**Fundamentals of Hydrogen Safety Engineering II**"